

Aerodynamic performance of bluff bodies with openings on side surface

Jiaqi Wang

Abstract

The objective of this research is to investigate the effects of discretely distributed side-surface openings on the aerodynamic performance of the bluff bodies. The research is based on the experimental investigations on the aerodynamic instabilities of the recently introduced butterfly web girder, which is a box-shaped girder with discretely distributed openings along the span-wise direction, and the rectangular cylinder, which is usually utilized as the simplified configuration for the box girder or high-rise building to reach more general conclusion. The research covers a wide range of aerodynamic phenomena, i.e. vortex-induced vibration, vertical one-degree-of-freedom (1DOF) flutter or the galloping, torsional 1DOF flutter, focusing on the galloping instability.

Firstly, it is assumed that the flow could get through the inner space of butterfly web girder into the wake owing to the side-surface openings, potentially affecting the aerodynamic instabilities. To investigate the effects of the side-surface openings on the aerodynamic instabilities, two butterfly web girders with side ratio $B/D = 3.24$ and 5, where B is the girder width and D is the girder height, were examined through a series of wind tunnel tests. The side-surface openings stabilized the vortex-induced vibration and galloping when $B/D = 3.24$, whereas the vortex-induced vibration and torsional flutter were stabilized when $B/D = 5$.

Secondly, the $B/D = 3.24$ butterfly web girder is widely applied in the parallel bridges, the aerodynamic performance of which is sometimes more unstable. To investigate the effects of the side-surface openings on the aerodynamic performance of the butterfly web girder in tandem arrangement, the $B/D = 3.24$ butterfly web girder was duplicated and a series of wind tunnel tests was carried out for these two girders in the tandem arrangement. The upstream girder was more unstable in galloping owing to the fixed downstream girder and the downstream girder was more unstable in the vortex-induced vibration owing to the fixed upstream girder. The side-surface openings stabilized the upstream girder against the vortex-induced vibration and the galloping, while the side-surface openings stabilized the downstream girder against the vortex-induced vibration.

Thirdly, the rectangular cylinder with different-sized openings was applied in a series of wind tunnel tests to investigate the mechanism related to the stabilization against the galloping owing to the openings. The Opening-area Ratio (OR), the ratio between the area of the total openings and half the side-surface area, played a dominant role in stabilizing the galloping. At high wind velocities, with an increase in OR , the aerodynamic damping increased and the separated flow gradually approached the side surface. Increasing OR above a certain value (75%) resulted in a decrease of aerodynamic damping and the separated flow reattaching itself to the model. Despite the complicated relationship between the aerodynamic damping and OR , with the increase of OR , the galloping response decreased, and the galloping onset increased accompanied by the decrease in the Strouhal number and the approaching of the separated flow to the side surface. Therefore,

the side-surface openings stabilized the galloping by promoting the reattachment of the separated flow on the side surfaces.

These findings confirm the feasibility of the side-surface openings to stabilize the box girders against different aerodynamic instabilities and especially to stabilize the galloping by promoting the reattachment of the flow on the side surface. The implication is also practical for more general rectangular cylinder-like bluff bodies, i.e. high-rise buildings.

Acknowledgments

Pursuing a Ph.D. degree at a world recognized university in a foreign country is not an easy task. Without help, I would not have accomplished this objective, and I am sincerely thankful for all the support and assistance I had from a number of people.

I would like to thank my supervisor, Professor Tomomi Yagi, for the scientific and financial support he provided during the last four and a half years. He always taught me to look at the problem from different perspectives by asking the enlightening questions. He also helped me to widen the sight to have a comprehensive view by merging our experience into the whole knowledge schema. The long conversations and discussions we had regarding the research, i.e., experimental plan, interpretation of the results and etc., taught me a lot. I also greatly appreciate that Professor Yagi provided many valuable opportunities to attend international academic conferences and a contract to me for one year after the expire of the scholarship to finish my research. Many thanks to Professor Tomomi Yagi for all he has done for me.

I thank as well the late Professor Hiromichi Shirato from the Laboratory of Bridge Engineering of Kyoto University for his help and valuable suggestions on this research. Also, Professor Junji Kiyono from the Laboratory of Earthquake and Lifeline Engineering of the Department of Urban Management and Professor Yoshikazu Takahashi from the Laboratory of Structural Dynamics of Department of Civil and Earth Resources Engineering, both from Kyoto University, are thankfully acknowledged for the valuable questions and comments to the draft of this thesis. They taught me to look at my research from different perspectives.

I wish to extend my thanks and gratitude to Dr. Kyohei Noguchi, who gave valuable suggestions and guidance regarding writing journal papers, presentation skills, wind tunnel tests and etc. Dr. Kyohei Noguchi, as the assistant professor in the lab, took care of me as a student of the lab and helped me to address the obstacles in both daily life and the research.

I also would like to thank the Sumitomo Mitsui Construction co., Ltd., for the opportunity to participate in their interesting project. Dr. Naoki Nagamoto and Mr. Hiroyuki Uchibori from Structural Engineering Service Dept., Sumitomo Mitsui Construction co., Ltd., also provided valuable suggestions on this research.

The lovely students of the Laboratory of Structural Dynamics and the Laboratory of Bridge Engineering were essential components for the development of my research. Special thanks to members of the butterfly web girder research team, Mr. Jun Ushioda, Mr. Hidekazu Ichikawa, and Mr. Soichiro Yamamoto, not only for their hardwork but also for the happy time together. They enormously contributed to the wind tunnel tests, data analysis, and reference review. Former graduate student, Mr. Satoshi Ogawa, Mr. Yuta Sasaki, Mr. Takahiro Komatsu and other students cannot list here, also helped a lot regarding the wind tunnel tests and daily life. Regarding the experiments, I should mention Mr. Yasuhiro Miyasaka, who contributed his experience in the

preparation of wind tunnel tests. To all the students of the laboratory, my thankful feelings are extended.

Ms. Yachiyo Mitsushima, the secretary in the Laboratory of Structural Dynamics, and Ms. Tomoko Souda, the secretary in the Laboratory of Bridge Engineering are deeply thanked for their help regarding daily life and the bureaucratic procedures.

I would like to thank the Ministry of Education, Culture, Sports, Science and Technology of the Japanese government for providing the scholarship, which made it possible for me to study in Japan.

Finally, I would like to thank my girlfriend Tianqi Gao and my family in China: dad, mom, brother, nephews. The support they gave all the time were determinant in my accomplishments in Japan.

To all people mentioned above and those who were not mentioned but also accompanied me through this journey, I sincerely thank you.

Contents

Acknowledgments.....	iii
List of Figures.....	ix
List of Tables.....	xvii
List of Symbols.....	xix
1 Introduction.....	1
1.1 Motivation.....	1
1.2 Objective of the thesis.....	2
1.3 Organization.....	3
Reference.....	4
2 General background.....	5
2.1 Introduction.....	5
2.2 Classification of the aerodynamic instabilities.....	5
2.2.1 Flow pattern of rectangular cylinder with different side ratio B/D	5
2.2.2 Vortex-induced vibration.....	6
2.2.3 Galloping.....	8
2.2.4 Torsional flutter.....	11
2.3 Stabilization against the galloping.....	12
2.3.1 Unsteady effects of galloping response at low wind velocities.....	12
2.3.2 Asymptotic behavior of the aerodynamic response/damping at high wind velocities.....	13
2.3.3 Importance of the afterbody.....	13
2.3.4 Importance of vortex shedding.....	15
2.3.5 Lesson from effects of turbulence on galloping.....	17
2.4 Outline of the wind tunnel tests.....	19
2.4.1 Wind tunnel.....	19
2.4.2 Aerodynamic force measurement system.....	20
2.4.3 Aerodynamic force tests on the stationary model.....	21
2.4.4 Forced vibration tests.....	23
2.4.5 Free vibration tests.....	25

2.4.6	Wind velocity measurement.....	26
2.5	Conclusion remarks.....	27
	Reference.....	27
3	Aerodynamic performance of single box girders with side-surface openings	33
3.1	Introduction	33
3.2	Wind tunnel test details	34
3.2.1	Model details	34
3.2.2	Free vibration tests	36
3.2.3	Aerodynamic force tests on stationary girder.....	37
3.2.4	Forced vibration tests	37
3.3	Aerodynamic performance of a butterfly web girder with side ratio $B/D = 3.24$	38
3.3.1	Aerodynamic forces	38
3.3.2	Vertical 1DOF aerodynamic performance	39
3.3.3	Torsional 1DOF aerodynamic performance.....	41
3.4	Flow field characteristics in the wake and inner space of the $B/D = 3.24$ girder	42
3.4.1	Wind velocity measurement around the girder	42
3.4.2	Time-averaged flow in the girder wake and side-surface openings.....	43
3.5	Aerodynamic performance of a butterfly web girder with side ratio $B/D = 5$	45
3.5.1	Torsional 1DOF aerodynamic performance.....	45
3.5.2	Vertical 1DOF aerodynamic performance	49
3.6	Conclusion remarks.....	50
	Reference.....	51
4	Aerodynamic performance of parallel box girders with side-surface openings.....	55
4.1	Introduction	55
4.2	Details of wind tunnel tests	56
4.2.1	Background	56
4.2.2	Spring-supported free vibration test.....	60
4.2.3	Aerodynamic force test on the stationary girder and forced vibration tests.....	61
4.3	Aerodynamic force of stationary girders in tandem arrangement.....	63
4.3.1	Aerodynamic force of upstream girder	63

4.3.2	Aerodynamic force of downstream girder.....	65
4.4	Aerodynamic performance of the upstream girder.....	67
4.4.1	Effects of fixed downstream girder	67
4.4.2	Effects of side-surface openings.....	69
4.5	Aerodynamic performance of the downstream girder.....	73
4.5.1	Effects of fixed upstream girder	73
4.5.2	Effects of side-surface openings.....	76
4.6	Conclusion remarks	79
	Reference.....	81
5	Effects of side-surface openings on galloping instability of rectangular cylinder	83
5.1	Introduction	83
5.2	Set-up of wind tunnel tests	84
5.2.1	The detail of the model and case list	84
5.2.2	Free vibration test.....	86
5.2.3	Aerodynamic force test on stationary girder	87
5.2.4	Forced vibration test.....	88
5.3	Opening size and galloping instability	88
5.3.1	Vertical 1DOF aerodynamic response	88
5.3.2	Aerodynamic force characteristics	91
5.3.3	Critical wind velocity of galloping and Strouhal number	97
5.4	Flow field around rectangular cylinder with side-surface openings	101
5.4.1	PIV measurement	102
5.4.2	Through-body flow in X - Z plane.....	105
5.4.3	Separated flow in X - Y plane	111
5.5	Conclusion Remarks.....	117
	Reference.....	119
6	Conclusion and the future topic.....	123
6.1	Conclusion.....	123
6.2	Future topics	126
Appendix A	131

Appendix B	145
Appendix C	167

List of Figures

Chapter 1

Fig. 1-1 Butterfly web girder (Takubogawa Bridge)	2
---	---

Chapter 2

Fig. 2-1 The flow pattern of the motion-induced vortex vibration for the rectangular cylinder. LV represents the vortices from the leading edge, while TV represents the vortices from the trailing edge.	7
Fig. 2-2 Resonance or onset reduced velocity for bluff bodies (Shiraishi and Matsumoto, 1983).	8
Fig. 2-3 Stability boundaries for galloping of rectangular cylinders (Nakamura and Hirata, 1994)	9
Fig. 2-4 Mechanism of galloping	9
Fig. 2-5 Aerodynamic force working on the stationary model	11
Fig. 2-6 Change of Strouhal number with side ratio B/D .	14
Fig. 2-7 Change of drag force coefficient with side ratio B/D	15
Fig. 2-8 Vibration amplitude for rectangular cylinder with different side ratio (Parkinson and Wawzonek, 1981). (U_{kv} represents the resonance wind velocity, equaling to fD/St ; A_{η} is the oscillation amplitude; B and D are the body width and body height respectively).	15
Fig. 2-9 Stability boundaries for galloping of rectangular cylinders with the splitter plate in the wake (Nakamura and Hirata, 1994).	16
Fig. 2-10 Aerodynamic force coefficient of the rectangular cylinder with splitter plate in the wake: (a) drag force coefficient; (b) fluctuating lift force coefficient (Matsumoto et al., 2006).	17
Fig. 2-11 Illustration for the role of splitter plate on the time-averaged flow (Horitsu, 2007).	17
Fig. 2-12 Flow separation on the bluff body: smooth flow (plain line), turbulent flow (dashed line) (Andrienne, 2012).	18
Fig. 2-13 Aerodynamic response of $B/D = 1.5$ rectangular cylinder in the turbulence flow (I_u represents the turbulence intensity; $Sc = 28$ is the mass damping parameter) (Mannini et al., 2018a).	18

Fig. 2-14 Variation in critical wind velocity of galloping and Strouhal number with turbulence intensity. (Data is from Mannini et al., 2018a)	19
Fig. 2-15 Sketch of the wind tunnel (unit: mm)	20
Fig. 2-16 Apparatus for forced vibration tests	21
Fig. 2-17 Definitions of aerodynamic forces.	23
Fig. 2-18 Free vibration test supporting system.	26

Chapter 3

Fig. 3-1 Section of the $B/D = 3.24$ side ratio model and side-surface opening detail (unit: mm).	34
Fig. 3-2 Section of the $B/D = 5$ model and side-surface opening detail (unit: mm).	35
Fig. 3-3 Models used in the experiment: (a) open girder ($B/D = 3.24$); (b) open girder ($B/D = 5$); (c) closed girder ($B/D = 3.24$, side-surface openings covered); (d) closed girder ($B/D = 5$, side-surface openings covered).	35
Fig. 3-4 Equivalent size of the model. (a) shows the case at $\alpha = 0^\circ$. (b) shows the case at $\alpha = +3^\circ$. α is the angle of attack due to mean wind.	36
Fig. 3-5 Aerodynamic force coefficients ($B/D = 3.24$ model, $U = 6$ m/s, smooth flow) for (a) lift force C_{Fy} ; (b) drag force C_{Fx} ; (c) pitching moment C_M .	38
Fig. 3-6 Fluctuating lift force coefficient C_{Fy}' ($B/D = 3.24$ model, $U = 6$ m/s, smooth flow).	39
Fig. 3-7 Aerodynamic response of the $B/D = 3.24$ model ($B'/D' = 2.6$, vertical one degree of freedom (1DOF), $\alpha = +3^\circ$, smooth flow).	40
Fig. 3-8 Aerodynamic derivative H_1^* of the $B/D = 3.24$ model ($B'/D' = 2.6$, vertical 1DOF, $\alpha = +3^\circ$, $f = 2.0$ Hz, $2A\eta = 20$ mm, smooth flow).	41
Fig. 3-9 Aerodynamic derivative A_2^* of the $B/D = 3.24$ model ($B'/D' = 2.6$, torsional 1DOF, $\alpha = +3^\circ$, $f = 2.6$ Hz, $2A\varphi = 4^\circ$, smooth flow).	41
Fig. 3-10 Aerodynamic derivative A_2^* of the $B/D = 3.24$ model ($B'/D' = 3.24$, torsional 1DOF, $\alpha = 0^\circ$, $f = 2.6$ Hz, $2A\varphi = 4^\circ$, smooth flow).	42
Fig. 3-11 Measurement points ($B/D = 3.24$ model) in the X - Y plane (unit: mm).	43
Fig. 3-12 Mean wind velocity vector distribution in the wake of the $B/D = 3.24$ model ($\alpha = 0^\circ$, $U = 6$ m/s, smooth flow). The black arrow represents the wind velocity vector of the closed girder. The red arrow represents the wind velocity vector of the open girder.	44

Fig. 3-13 Aerodynamic response of the $B/D = 5$ model ($B'/D' = 4.1$, torsional 1DOF, $\alpha = +3^\circ$, smooth flow).	46
Fig. 3-14 Aerodynamic derivative A_2^* of the $B/D = 5$ model ($B'/D' = 4.1$, torsional 1DOF, $\alpha = +3^\circ$, $f = 2.6$ Hz, $2A\phi = 4^\circ$, smooth flow).	46
Fig. 3-15 Aerodynamic response of the $B/D = 5$ model ($B'/D' = 5$, torsional 1DOF, $\alpha = 0^\circ$, smooth flow).	47
Fig. 3-16 Aerodynamic derivative A_2^* of the $B/D = 5$ model ($B'/D' = 5$, torsional 1DOF, $\alpha = 0^\circ$, $f = 2.6$ Hz, $2A\phi = 4^\circ$, smooth flow).	47
Fig. 3-17 Relationship between A_2^* of closed girder and equivalent side ratio B'/D' .	48
Fig. 3-18 A_2^* of the rectangular cylinder with different side ratios (Matsumoto 1996).	49
Fig. 3-19 Aerodynamic response of the $B/D = 5$ model ($B'/D' = 5$, vertical 1DOF, $\alpha = 0^\circ$, smooth flow).	50

Chapter 4

Fig. 4-1 Duplicated $B/D = 3.24$ butterfly web girders in the wind tunnel.	55
Fig. 4-2 (a) Variation of Strouhal number with center distance; (b) Variation of maximum amplitude of vortex-induced vibration with center distance (c) Disposition of two girders. (Park et al., 2017a)	57
Fig. 4-3 Variation of Strouhal number St with spacing ratio S/D . (Sakamoto et al, 1987)	58
Fig. 4-4 Aerodynamic response of the downstream $B/D = 3$ rectangular cylinder. (Okajima et al., 1990a)	58
Fig. 4-5 Aerodynamic response: (a) upstream girder; (b) downstream girder with an elastically supported upstream girder; (c) downstream girder with a rigidly supported upstream girder. D_2 is the body height of the upstream girder. D_1 is the body height of the downstream girder. FR is the frequency ratio of upstream girder frequency to the downstream girder frequency. (Park and Kim, 2017b)	59
Fig. 4-6 Free vibration system for: (a) upstream girder; (b) downstream girder.	61
Fig. 4-7 Disposition of two girders in the wind tunnel: (a) the upstream girder is under measurement with a fixed girder at the downstream side; (b) the downstream girder is under measurement with a fixed girder at the upstream side.	62
Fig. 4-8 (a) Comparison between the aerodynamic response of the upstream closed girder and the single closed girder; (b) comparison between the aerodynamic response of the upstream	

open girder and the single open girder. (Vertical one-degree of freedom [1DOF], $\alpha = 3^\circ$, smooth flow) 68

Fig. 4-9 (a) Comparison between the aerodynamic derivative H_1^* of the upstream closed girder and the single closed girder; (b) comparison between the aerodynamic derivative H_1^* of the upstream open girder and the single open girder. (Vertical 1DOF, $\alpha = 3^\circ$, $f = 2.0$ Hz, $2A\eta = 20$ mm, smooth flow) 68

Fig. 4-10 Vortex-induced vibration for (vertical 1DOF, $\alpha = 0^\circ$, smooth flow) (a) upstream closed girder with a fixed downstream closed girder; (b) upstream closed girder with a fixed downstream open girder; (c) upstream open girder with a fixed downstream closed girder; (d) upstream open girder with a fixed downstream open girder. 70

Fig. 4-11 Aerodynamic response for (vertical 1DOF, $\alpha = +3^\circ$, smooth flow): (a) upstream closed girder with a fixed downstream closed girder; (b) upstream closed girder with a fixed downstream open girder; (c) upstream open girder with a fixed downstream closed girder; (d) upstream open girder with a fixed downstream open girder. 71

Fig. 4-12 Aerodynamic derivative H_1^* for (vertical 1DOF, $\alpha = 3^\circ$, $f = 2.0$ Hz, $2A\eta = 20$ mm, smooth flow): (a) upstream closed girder with a fixed downstream closed girder; (b) upstream closed girder with a fixed downstream open girder; (c) upstream open girder with a fixed downstream closed girder; (d) upstream open girder with a fixed downstream open girder. 72

Fig. 4-13 (a) Comparison between the aerodynamic response of the downstream closed girder and single closed girder; (b) comparison between the aerodynamic response of the downstream open girder and single open girder. (Vertical 1DOF, $\alpha = 3^\circ$, smooth flow) 74

Fig. 4-14 (a) Comparison between the aerodynamic derivative H_1^* of the upstream closed girder and the single closed girder; (b) comparison between the aerodynamic derivative H_1^* of the upstream open girder and the single open girder. (Vertical 1DOF, $\alpha = 3^\circ$, $f = 2.0$ Hz, $2A\eta = 20$ mm, smooth flow) 75

Fig. 4-15 (a) Comparison between the vortex-induced vibration of the downstream closed girder and single closed girder; (b) comparison between the vortex-induced vibration of the downstream open girder and single open girder. (Vertical 1DOF, $\alpha = 0^\circ$, smooth flow) 75

Fig. 4-16 Vortex-induced vibration for (vertical 1DOF, $\alpha = 0^\circ$, smooth flow): (a) downstream closed girder with a fixed upstream closed girder; (b) downstream closed girder with a fixed upstream open girder; (c) downstream open girder with a fixed upstream closed girder; (d) downstream open girder with a fixed upstream open girder. 77

Fig. 4-17 Aerodynamic response for (vertical 1DOF, $\alpha = +3^\circ$, smooth flow): (a) downstream closed girder with a fixed upstream closed girder; (b) downstream closed girder with a fixed upstream open girder; (c) downstream open girder with a fixed upstream closed girder; (d) downstream open girder with a fixed upstream open girder. 78

Fig. 4-18 Aerodynamic derivative H_1^* for (vertical 1DOF, $\alpha = 3^\circ$, $f = 2.0\text{Hz}$, $2A\eta = 20\text{mm}$, smooth flow): (a) downstream closed girder with a fixed upstream closed girder; (b) downstream open girder with a fixed upstream closed girder; (c) downstream closed girder with a fixed upstream open girder; (d) downstream open girder with a fixed upstream open girder. 79

Chapter 5

Fig. 5-1 Model information: (a) main body; (b) model section (unit: mm). 85

Fig. 5-2 Detail of side-surface openings 85

Fig. 5-3 Aerodynamic response of: (a) Case 1 ($OR=0$); (b) Case 2 ($OR=0.25$, $RER=1.07$); (c) Case 4 ($OR=0.75$, $RER=1.07$); (d) Case 10 ($OR=1$); (e) Case 6 ($OR=0.25$, $RER=2.14$); (f) Case 6 ($OR=0.75$, $RER=2.14$). (Vertical one degree of freedom (1DOF), $\alpha = 0^\circ$, smooth flow). U_{rc0} is the critical wind velocity of galloping corresponding to $2A\eta$ of 0mm. U_{rc10_fre} represents the wind velocity corresponding to $2A\eta$ of 10mm. f is the frequency of the system. 89

Fig. 5-4 Change of lift force coefficients with OR ($OR = 0, 0.25, 0.5, 0.75, 0.875$ and 1) for $RER = 1.07$ ($U = 6\text{m/s}$, smooth flow). 93

Fig. 5-5 Change of lift force coefficients with OR ($OR = 0, 0.25, 0.5, 0.75, 0.875$ and 1) for $RER = 2.14$ ($U = 6\text{m/s}$, smooth flow). 93

Fig. 5-6 Lift slope at angle of attack $\alpha = 0^\circ$. ($U = 6\text{m/s}$, smooth flow) 94

Fig. 5-7 Change of H_1^* with OR ($OR = 0, 0.25, 0.5, 0.75, 0.875$ and 1) for $RER = 1.07$ (smooth flow, $\alpha = 0^\circ$, $f = 2.6\text{Hz}$, $2A\eta = 10\text{mm}$). 95

Fig. 5-8 Change of H_1^* with OR ($OR = 0, 0.25, 0.5, 0.75, 0.875$ and 1) for $RER = 2.14$ (smooth flow, $\alpha = 0^\circ$, $f = 2.6\text{Hz}$, $2A\eta = 10\text{mm}$). 95

Fig. 5-9 Comparison between H_1^* of cases of $RER = 1.07$ and 2.14 for (a) $OR = 0.25$; (b) $OR = 0.5$; (c) $OR = 0.75$; (d) $OR = 0.875$ (smooth flow, $\alpha = 0^\circ$, $f = 2.6\text{Hz}$, $2A\eta = 10\text{mm}$). 96

Fig. 5-10 (a) Change of Strouhal number (St) with OR ($RER = 1.07$, $U = 6\text{m/s}$, smooth flow). (b) Change of reduced critical wind velocity of galloping with OR ($RER = 1.07$, smooth flow). U_{rc0} is the reduced critical wind velocity of galloping corresponding to $2A\eta$ of 0mm (decided from free vibration tests). 98

- Fig. 5-11 Change of Strouhal number with side ratio B/D . 98
- Fig. 5-12 Change of fluctuating lift force coefficients: (a) with OR ($RER = 1.07$, $U = 6\text{m/s}$, smooth flow); (b) with side ratio B/D . 99
- Fig. 5-13 (a) Change of drag force coefficient C_{Fx} with OR ($RER = 1.07$, $U = 6\text{m/s}$, smooth flow); (b) change of drag force coefficient C_{Fxr} with OR ($RER = 1.07$, $U = 6\text{m/s}$, smooth flow); (c) change of C_{Fx} with side ratio B/D . (C_{Fx} was calculated based on the total front/rear surface, while C_{Fxr} was calculated based on the real area of the front/rear surface). 100
- Fig. 5-14 Model for flow visualization tests 102
- Fig. 5-15 Set-up for the flow visualization test the X - Y plane. The X -direction is the approaching wind velocity. Y -direction is the vertical direction. Z -direction is the span-wise direction. The origin of coordinate is at the span center and upside leading edge. 103
- Fig. 5-16 Set-up for the flow visualization test in X - Z plane for (a) the inner space of model; (b) the wake of the model. The laser sheet is set in the X - Z plane through the center of the model section. 104
- Fig. 5-17 Measurement position (X - Y plane) for: (a) closed section ($z = 0\text{mm}$); (b) open section ($z = 18.73\text{mm}$). 104
- Fig. 5-18 Distribution of the measurement points for the wind velocity of the flow getting through the inner space of the rectangular cylinder. 105
- Fig. 5-19 Contour map of non-dimensional X -direction wind velocity (U_{1x}/U) in X - Z plane of: (a) Case 1 ($OR = 0$); (b) Case 2 ($OR = 0.25$, $RER = 1.07$); (c) Case 3 ($OR = 0.50$, $RER = 1.07$); (d) Case 4 ($OR = 0.75$, $RER = 1.07$); (e) Case 5 ($OR = 0.875$, $RER = 1.07$), (f) Case 10 ($OR = 1$) ($U = 1.5\text{m/s}$, smooth flow). 107
- Fig. 5-20 Non-dimensional X -direction wind velocity (U_{1x}/U) of the flow through the model of: (a) Case 2 ($OR = 0.25$, $RER = 1.07$); (b) Case 3 ($OR = 0.50$, $RER = 1.07$); (c) Case 4 ($OR = 0.75$, $RER = 1.07$); (d) Case 5 ($OR = 0.875$, $RER = 1.07$); (e) Case 10 ($OR = 1$) (PIV tests: $U = 1.5\text{m/s}$, smooth flow; wind velocity measurement: $U = 6\text{m/s}$, smooth flow). 108
- Fig. 5-21 (a) Side view (span-wise direction) of the flow rate Q through the total front surface S_{fro} of the model, the flow rate Q_1 through the total opening area S_{op} and the flow rate Q_2 into the separated flow. (b) Sketch for S_{fro} and S_{op} (n is 24 for $RER = 1.07$; $S_1 = D_0^2 \times OR \times RER$). 110
- Fig. 5-22 Time-averaged streamline in X - Y plane around: (a) section of Case 1 ($OR = 0$); (b) closed section of Case 2 ($OR = 0.25$, $RER = 1.07$); (c) open section of Case 2; (d) closed section of Case 3 ($OR = 0.50$, $RER = 1.07$); (e) open section of Case 3; (f) closed section of Case 4 ($OR = 0.75$, $RER = 1.07$); (g) open section of Case 4; (h) closed section of Case 5 (OR

= 0.875, $REr = 1.07$); (i) open section of Case 5; (j) section of Case 10 ($OR = 1$) ($U = 1.5\text{m/s}$, smooth flow).

113

List of Tables

Chapter 3

Table 3-1 Characteristic parameters for the model (side ratio $B/D = 3.24$) used in free vibration experiments; the model has one vertical degree of freedom (1DOF) and the experiment is in smooth flow.	36
Table 3-2 Characteristic parameters for the model ($B/D = 5$) used in free vibration experiments (torsional 1DOF, smooth flow).	37
Table 3-3 Characteristic parameters for the model ($B/D = 5$) used in free vibration experiments (vertical 1DOF, smooth flow).	37
Table 3-4 Strouhal number identified from fluctuating lift force ($B/D = 3.24$ model, $U = 6$ m/s, smooth flow, $\alpha = 0^\circ$).	39

Chapter 4

Table 4-1 Characteristic parameters for the upstream girder used in free vibration experiments (vertical 1DOF, smooth flow).	62
Table 4-2 Characteristic parameters for the downstream girder used in free vibration experiments (vertical 1DOF, smooth flow).	63
Table 4-3 Aerodynamic force coefficients of the upstream girder ($\alpha = 0^\circ$, $U = 6$ m/s)	64
Table 4-4 Strouhal number of the upstream girder ($\alpha = 0^\circ$, $U = 6$ m/s)	64
Table 4-5 Aerodynamic force coefficients of the single girder ($\alpha = 0^\circ$, $U = 6$ m/s)	64
Table 4-6 Strouhal number of the single girder ($\alpha = 0^\circ$, $U = 6$ m/s)	64
Table 4-7 Aerodynamic force coefficients of the downstream girder ($\alpha = 0^\circ$, $U = 6$ m/s)	66
Table 4-8 Strouhal number of the downstream girder ($\alpha = 0^\circ$, $U = 6$ m/s)	66

Chapter 5

Table 5-1 Case lists of wind tunnel tests	86
Table 5-2 Characteristic parameters for free vibration tests of different cases (vertical one degree of freedom 1DOF, smooth flow)	87

Table 5-3 Flow rate Q_1 through the total opening area ($RER = 1.07$, $n = 24$, $U = 6\text{m/s}$; $Q = 0.378\text{m}^3/\text{s}$)

111

List of Symbols

OR : Opening-area Ratio;

$REER$: Repeating Element-size Ratio;

$A\eta$: amplitude in vertical direction;

$A\phi$: amplitude in torsional direction;

l : the span length;

l_1 : the width of the openings;

l_2 : the width of the plastic plate;

D_0 : the height of the side-surface openings;

D_1 : the upside/downside girder depth;

D : the girder depth;

D' : the effective girder depth owing to the change of angle of attack or the side surface openings;

B : the girder width;

B' : the effective girder width owing to the change of angle of attack or the side-surface openings;

b : half the girder width ($B/2$)

S_1 : the opening area;

S_2 : the plate area;

C_{Fy} : lift force coefficient defined on the structural axis;

C_{Fx} : drag force coefficient defined on the structural axis;

C_{Fxr} : drag force coefficient considering the real windward surface area of the model;

C_{Fy}' : fluctuating lift force coefficient defined on the structural axis;

C_M : pitching moment coefficient

St : Strouhal number;

F_y : the lift force (N) defined on the structural axis;

F_x : the drag force (N) defined on the structural axis;

ρ : the air density (kg/m^3);

U : the approaching wind velocity (m/s);
 f : the natural frequency of the system (for both the free vibration tests and forced vibration tests)
 f_{st} : the dominant frequency (Hz) of the Kármán-vortex shedding;
 $F_y(t)$: the fluctuating lift force time series defined on the structural axis;
 $F_y'(t)$: the lift force component fluctuating in the frequency of f_{st} defined on the structural axis;
 $F_y'(t)_{std}$: the standard deviation of $F_y'(t)$ defined on the structural axis;
 $dC_{Fy}/d\alpha$: the lift slope ($dC_{Fy}/d\alpha$) indicates the galloping instability.
 S_{cn} : Scruton number in the vertical direction;
 $S_{c\varphi}$: Scruton number in the torsional direction;
 U_r : reduced wind velocity; $U_r = U/fD$;
 U_{rc0} : reduced critical wind velocity of the galloping identified from the free vibration tests;
 $U_{rc_{for}}$: reduced critical wind velocity of the galloping identified from the forced vibration tests;
 U_{kv} : critical wind velocity of Kármán-vortex vibration (m/s)
 U_{ckv} : reduced critical wind velocity of Kármán-vortex vibration ($1/St$)
 U_{cmv} : the reduced critical wind velocity of the vertical motion-induced vortex vibration;
 U_{cmt} : the reduced critical wind velocity of the torsional motion-induced vortex vibration;
 m : model mass per unit (kg/m);
 I : moment of inertia per unit (kg·m);
 δ_η : the vertical structural damping quantified by logarithmic decrement;
 δ_φ : the torsional structural damping quantified by logarithmic decrement;
 L_{se} : the self-excited lift force per unit span (N/m) (downward lift is positive);
 M_{se} : the self-excited pitching moment per unit span (N·m/m) (nose-up moment is positive);
 η : the vertical displacement (m);
 φ : the torsional displacement (°);
 $(\dot{\cdot})$: indicates the time differentiation;
 b : the half-length of the body width (m);
 k : the reduced frequency ($b\omega/U$);
 ω : the angular frequency (rad/s);
 H_i^* and A_i^* ($i = 1\sim 4$): aerodynamic derivatives;

F : measured force working on the oscillating model;
 F_t : the amplitude of measured force under wind;
 Ψ_t : the phase lag between the displacement and the measured force F ;
 F_a : the amplitude of the aerodynamic force working on the model under wind;
 Ψ_a : the phase lag between the displacement and the aerodynamic force
 η_0 : the displacement amplitude of vertical forced vibration;
 $\Psi_{L\eta}$: the phase lag between unsteady lift and vertical displacement;
 $L_{\eta 0}$: the amplitude of the lift working on the vertical 1DOF sinusoidal vibration model per unit
(downward direction is positive);
 $M_{\eta 0}$: the amplitude of the pitching moment working on the vertical 1DOF sinusoidal vibration
model per unit (nose-up direction is positive);
 $\Psi_{M\eta}$: the phase lag between the pitching moment and vertical displacement;
 φ_0 : the torsional displacement amplitude;
 $\Psi_{L\varphi}$: the phase lag between unsteady lift and torsional displacement;
 $L_{\varphi 0}$: the amplitude of the lift working on the torsional 1DOF sinusoidal vibration model per unit
(downward direction is positive);
 $M_{\varphi 0}$: the amplitude of the pitching moment working on the torsional 1DOF sinusoidal vibration
model per unit (nose-up direction is positive);
 $\Psi_{M\varphi}$: the phase lag between the pitching moment and the torsional displacement.
 S_{fro} : total front surface area;
 S_{op} : total opening area;
 U_1 : measured wind velocity of the flow field around the model;
 Q : flow rate through the total front surface area S_{fro} ;
 Q_1 : flow rate through the total front surface area S_{op} ;
 Q_2 : flow rate into the separated flow from Q ;
 $Q_2 = Q - Q_1$;
 α : angle of attack owing to the mean wind;
 α_0 : relative angle of attack between the body vibration velocity and the approaching wind velocity.

1 Introduction

1.1 Motivation

The long-span bridge always calls for the light, strong bridge girder with good wind-resistance ability. The bridge serves humankind as an important tool to conquer the complex terrain, promoting the commercial and cultural communications between different societies for centuries. Associated with the greed for the even longer bridge to conquer the more complex terrain, the researches and engineers have contributed a lot to achieve the good balance between the lightness and the structural performance of the girder, the main part of the bridge. In the history of pursuing this balance, the tragic and famous episode of old Tacoma Narrows Bridge failure (1942) reminds us of the sensitivity of the bridge to the natural wind and the importance of the aerodynamic performance of the girder (Billah and Scanlan, 1991). Therefore, this research mainly focuses on the **aerodynamic performance** of the girder.

A new type of girder, the butterfly web girder, is recently introduced owing to the advantages in terms of structure, construction, and maintenance (Kasuga, 2017). This girder can be viewed as a box girder with discretely distributed openings on the windward and leeward surfaces (Fig. 1-1). The openings on the side surface are named the side-surface openings. The side-surface openings reduce the weight of a butterfly web girder bridge by almost as much as a corrugated steel web girder bridge without the loss of the stiffness. As a successful design in achieving a good balance between the lightness and structural performance, the side-surface openings also shows good potential in upgrading the aerodynamic performance of the box girder based on one case study (Kasuga, 2015). However, the lack of wide discussion based on different box girders brings concerns for what effects the side-surface openings will bring to the different types of aerodynamic phenomena.

Additionally, a bridge is sometimes added in parallel to an existing bridge to accommodate the increase of traffic (Honda et al. 1993; Irwin et al. 2005; Meng et al. 2011; Kim et al. 2013). Compared with the aerodynamic performance of the single stand-alone bridge to the natural wind, the aerodynamic performance of two bridges in tandem is complicated and even more unstable (Honda et al. 1993; Meng et al. 2011; Kim et al. 2013). This raises another concern whether the box girder with side-surface openings can show good aerodynamic performance in the tandem arrangement.

Among all the aerodynamic phenomena, the galloping is the main concern for the current research. From the perspective of the aerodynamic phenomena, the box girder generally could be regarded as the rectangular cylinder-like bluff body. The rectangular cylinder-like bluff body with a proper ratio of the girder width to girder depth usually has the problem of the galloping instability, which is a self-excited one degree of freedom vibration in a direction normal to the oncoming wind (Parkinson, 1989; Nakamura and Hirata, 1994). Galloping vibration is potentially catastrophic

since the amplitude increases continuously with the flow velocity above a critical value. The accurate apprehension on the mechanism related to the effects of the side-surface opening on the galloping is essentially important to apply the method in the practical design of the box girder. In this sense, more fundamental discussion utilizing the rectangular cylinder would result in more general conclusions related to the effects of the different sized side-surface openings on the galloping instability. The rectangular cylinder also brings convenience to monitor how the flow field around the body was manipulated by the side-surface openings to benefit the stabilization against the galloping. All those discussions would reveal the mechanism related to the effect of the side-surface openings on the galloping instability.

In this context, this research attempts to bring contributions to the expansion of the knowledge frontiers regarding the design of light, strong box girder with a good aerodynamic performance by introducing the side-surface openings. The focus is put on revealing the mechanism related to the effects of the side-surface openings on the galloping instability of the box girder and more general rectangular cylinder-like bluff bodies. Therefore, the contribution of the current research is not limited to the box girder but also more general rectangular cylinder-like bluff bodies, indicating the potential application for other slender structures, such as the high-rise building.



Fig. 1-1 Butterfly web girder (Takubogawa Bridge)

1.2 Objective of the thesis

This research is inserted in a context in which the feasibility of a novel method to stabilize the rectangular cylinder-like bluff bodies against the aerodynamic instabilities by introducing the side-surface openings is assessed. The complete development of such a method is a very complex task, which demands a huge effort. So the main objective is restricted to two parts. The principal objective for the present work was to evaluate the aerodynamic performance of the box girder with the side-surface openings in a single stand-alone situation and in a tandem arrangement. For the evaluation of the performance of the box girder with side-surface openings to different kinds of aerodynamic phenomena, two box girders with different ratios of girder width to girder depth were

utilized. One of the motioned two girders was further utilized to evaluate the aerodynamic performance of the box girder with side-surface openings accompanied by the other adjacent box girder. The focus has been put on the galloping instability. The second objective was to reveal the mechanism related to the effects of side-surface openings on the galloping instability of the rectangular cylinder-like bluff bodies. To accomplish this, the configuration of the box girder is simplified as the rectangular cylinder. Extensive experimental studies are carried out in the wind tunnel, focusing on monitoring the aerodynamic response and the aerodynamic damping. Then the general relationship between the different sized side-surface openings and the galloping instability is summarized. The flow field is additionally monitored through flow visualization tests in the wind tunnel to qualitatively explain the effects related to the side-surface openings.

1.3 Organization

The thesis consists of six chapters, each one preceded by a short introduction denouncing the aims of the relative content, and finalized by a brief summary recalling the main findings. This thesis is generally divided into two parts: the first part consists of Chapters 1 and 2, explaining the general background of this research; the second part consists of Chapters 3, 4 and 5, presenting the results and discussion. Then, the findings and future works are summarized in Chapter 6. Other results and discussions are summarized in the appendix.

In the present chapter, the scope of this thesis is introduced.

In Chapter 2, the general background for different aerodynamic phenomena necessary to understand the research is illustrated at first. Then the important lessons related to the stabilization against the galloping are outlined. Finally, Chapter 2 illustrates the wind tunnel tests and the methodology.

In Chapter 3, to investigate the effects of side-surface openings on the aerodynamic performance of the single box girder, two butterfly web girders with side ratio $B/D = 3.24$ and 5, where B is the girder width and D is the girder height, are examined through a series of wind tunnel tests. The results of the butterfly web girders and those of the conventional box girders of the same shape as the aforementioned butterfly web girders are compared, regarding the aerodynamic response and aerodynamic damping. Then the effects of the side-surface openings on the vortex-induced vibration, galloping instability, and torsional flutter are evaluated and discussed.

In Chapter 4, to investigate the effects of the side-surface openings on the aerodynamic performance of the box girders in the tandem arrangement, the $B/D = 3.24$ butterfly web girder is duplicated and the aerodynamic performance of these two girders in the tandem arrangement are investigated through a series of wind tunnel tests. The effects of side-surface openings of a box girder on the aerodynamic instabilities of itself are evaluated when it is accompanied by another adjacent girder. Additionally, the relationship between the aerodynamic instabilities of one girder and the side-surface openings of the other adjacent girder is evaluated and discussed.

In Chapter 5, by simplifying the $B/D = 3.24$ butterfly web girder as the rectangular cylinder, the aerodynamic performance of the rectangular cylinder with the different-sized openings is

experimentally examined to investigate the mechanism related to the stabilization against the galloping owing to the openings. The relationship between the opening size and galloping instability, i.e., aerodynamic response and aerodynamic damping, is evaluated and discussed. The flow field around the rectangular cylinder with different-sized openings is described and explained. Based on the change of flow field owing to the side-surface openings, the mechanism related to the stabilization against the galloping is explained.

Finally, the last chapter provides a summary of the results with the conclusions of the study. Then the future work regarding the effects of side openings on aerodynamic performance is recommended.

Reference

Billah, K.Y., Scanlan, R.H., 1991. Resonance, Tacoma Narrows bridge failure, and undergraduate physics textbooks. *Am. J. Phys.* 59, 118–124.

Kasuga, A., 2015. Multi-span extradosed bridge. *Proceeding of International Conference on Multi-span Large Bridges*, Porto, Portugal.

Kasuga, A., 2017. Effects of butterfly web design on bridge construction. *Struct. Concr.* 18(a), 128–142.

Honda, A., Shiraishi, N., Motoyama S., 1990. Aerodynamic stability of Kansai International Airport Access Bridge. *J. Wind Eng. Ind. Aerodyn.* 33, 369-376.

Irwin, P. A., Stoyanoff, S., Xie, J., Hunter, M., 2005. Tacoma Narrows 50 years later-Wind engineering investigations for parallel bridges. *Bridg. Struct.* 1, 3–17.

Meng, X. L., Zhu, L. D., Guo, Z. S., 2011. Aerodynamic interference effects and mitigation measures on vortex induced vibrations of two adjacent parallel bridges. *Front. Archit. Civ. Eng. China.* 5(4), 510–517.

Kim, S. J., Kim, H. K., Calmer, R., Park, J., Kim, G. S., and Lee, D. K., 2013. Operational field monitoring of interactive vortex-induced vibrations between two parallel cable-stayed bridges. *J. Wind Eng. Ind. Aerodyn.* 123, 143–154.

Parkinson, G. V., 1989. Phenomena and modelling of flow-induced vibrations of bluff bodies. *Prog. Aerosp. Sci.* 26, 169–224.

Nakamura, Y., Hirata, K., 1994. The aerodynamic mechanism of galloping. *Trans. Jpn. Soc. Aeronaut. Space Sci.* 36, 257-269.

2 General background

2.1 Introduction

In this chapter, a brief overview of the background necessary for reading this thesis is given, including the general classification of the aerodynamic instabilities, the basic knowledge related to the stabilization against the galloping, the outline of the wind tunnel tests and description of the methodology. Because this research deals with the rectangular cylinder-like bluff bodies, i.g., the box girder, the general background mainly focus on the aerodynamic instabilities of the rectangular cylinder.

2.2 Classification of the aerodynamic instabilities

Simiu and Scanlan (1996) proposed a general list of the aerodynamic instabilities of the rectangular cylinder-like bluff bodies based on three global categories: vortex-induced vibration, galloping, and torsional flutter. These phenomena strongly depend on the side ratio B/D , where B is the body width and D is the body depth, owing to the change of the flow pattern.

2.2.1 Flow pattern of rectangular cylinder with different side ratio B/D

The flow filed around the rectangular cylinders generally can be separated into four groups based on the reattachment of the time-averaged flow and interaction between the side surface and the shear layer (Nakaguchi et al., 1968; Mizota and Okajima, 1981):

The rectangular cylinder with side ratio $B/D < 0.6$ shows the flow field of steady detachment type. The shear layer separates from the leading edge and flows into the wake without interfering with the side surface of the rectangular cylinder.

The $0.6 < B/D < 2.8$ rectangular cylinder shows the flow field of unsteady detachment type. The shear layer separates from the leading edge and intermittently reattaches on the side surface, while the time-averaged flow shows the detachment type.

The $2.8 < B/D < 6$ rectangular cylinder shows the flow field of the unsteady reattachment type. The shear layer separates from the leading edge and intermittently reattaches on the side surface, while the time-averaged flow shows the reattachment type.

The $6.0 < B/D$ rectangular cylinder shows the flow filed of steady reattachment type. The shear layer separates from the leading edge and travels along the side surface without intermittently reattaching on the side surface. The time-averaged flow shows the reattachment type forming a separation bubble at the leading edge.

Owing to the change of flow pattern, the characteristics of the aerodynamic instabilities vary with the side ratio B/D .

2.2.2 Vortex-induced vibration

Vortex-induced vibration, which may cause fatigue damage and unacceptable vibration, is one of the major issues concerning flexible structures subjected to the wind. Vortex-induced vibration can be roughly divided into two types: the Kármán-vortex and motion-induced types (Komatsu and Kobayashi, 1980; Shiraishi and Matsumoto, 1983; Nakamura and Nakashima, 1986; Naudascher and Wang, 1993; Wu and Kareem, 2012; Nguyen et al. 2018).

The Kármán-vortex vibration is a wind-velocity restricted vibration occurs at the wind velocity that the Kármán-vortex shedding frequency is the same as the natural frequency of the system. Irrespective of the section of the bluff body, when the flow past around the bluff body, the shear layer separates and alternately sheds the vortices from the two sides of the body. The time-periodic vortices stagger in a two-row configuration in the wake to form a laminar vortex street, which is well known as Kármán-vortex Street. The vortex shedding exerts in turn fluctuating forces on the bluff body sides, exciting the bluff body to vibrate. The vortex shedding phenomenon follows the relation:

$$St = \frac{f_{st}D}{U} \quad \text{Eq. 2-1}$$

f_{st} is the dominant frequency (Hz) of the Kármán-vortex shedding, D is the characteristic dimension of the body projected on a plane normal to the mean flow velocity, U is the velocity of the approaching wind. If the structure is elastic with a natural frequency of f , when f_{st} approaches f with the increase of wind velocity, it will tend to develop a resonant response in the form of heaving vibration to the wind direction. If the velocity of the approaching wind is non-dimensionalized as U_r :

$$U_r = \frac{U}{fD} \quad \text{Eq. 2-2}$$

the onset reduced wind velocity of Kármán-vortex vibration is $1/St$.

As illustrated in Fig. 2-1, the motion-induced vortex vibration occurs owing to that the motion-induced vortices at the leading edge travels with a velocity of 60% approaching wind velocity along the side surface and coalesces with the vortices from the trailing edge (Kiya and Nozawa, 1987; Shiraishi and Matsumono, 1983; Nakamura and Nakashima, 1986). During the motion, the pressure fluctuates owing to the traveling of the motion-induced vortices. With the increase of the wind velocity, when the motion-induced vortices travel along the side surface in a frequency f_{mv} that is $1/N$ times ($N = 1, 2 \dots$) the natural frequency f , the resonance vibration in the heaving direction will occur. While, when the motion-induced vortices travel along the side surface in a frequency of f_{mv} that is $2/(2N-1)$ times ($N = 1, 2 \dots$) the natural frequency f , the resonance vibration in the torsional direction will occur. Therefore, the onset reduced wind velocity in motion-induced vortex vibration can be expressed by the following equations (Matsumoto et al. 2008):

Vertical motion:

$$U_{cmv} = \frac{1}{N} \frac{1}{0.6} \frac{B}{D} = \frac{1}{N} 1.67 \frac{B}{D} \quad \text{Eq. 2-3}$$

Torsion motion:

$$U_{cmt} = \frac{2}{2N-1} \frac{1}{0.6} \frac{B}{D} = \frac{2}{2N-1} 1.67 \frac{B}{D} \quad \text{Eq. 2-4}$$

where $N = 1, 2, \dots$; B is the body width; D is the body depth.

The type and onset wind velocity of vortex-induced vibration significantly depend on the side ratio B/D of the rectangular cylinder (Fig. 2-2). The $B/D < 2$ rectangular cylinder shows the Kármán-vortex vibration, excited by the Kármán-vortex shedding from the leading edge. The vortex-induced vibration of the $2 < B/D < 6$ rectangular cylinder is more complicated owing to the intermittent reattachment of the shear layer on the afterbody. The $2 < B/D < 2.8$ rectangular cylinder shows both the Kármán-vortex vibration and the motion-induced vortex vibration as indicated by the discrepancy between the onset wind velocities of these two vibrations (Fig. 2-2). The onset wind velocity of these two vibrations is almost the same for the $2.8 < B/D < 6$ rectangular cylinders (Fig. 2-2), which mainly shows the motion-induced vortex vibration. The $6 < B/D$ rectangular cylinder mainly shows the Kármán-vortex vibration, excited by the Kármán-vortex shedding from the trailing edge.

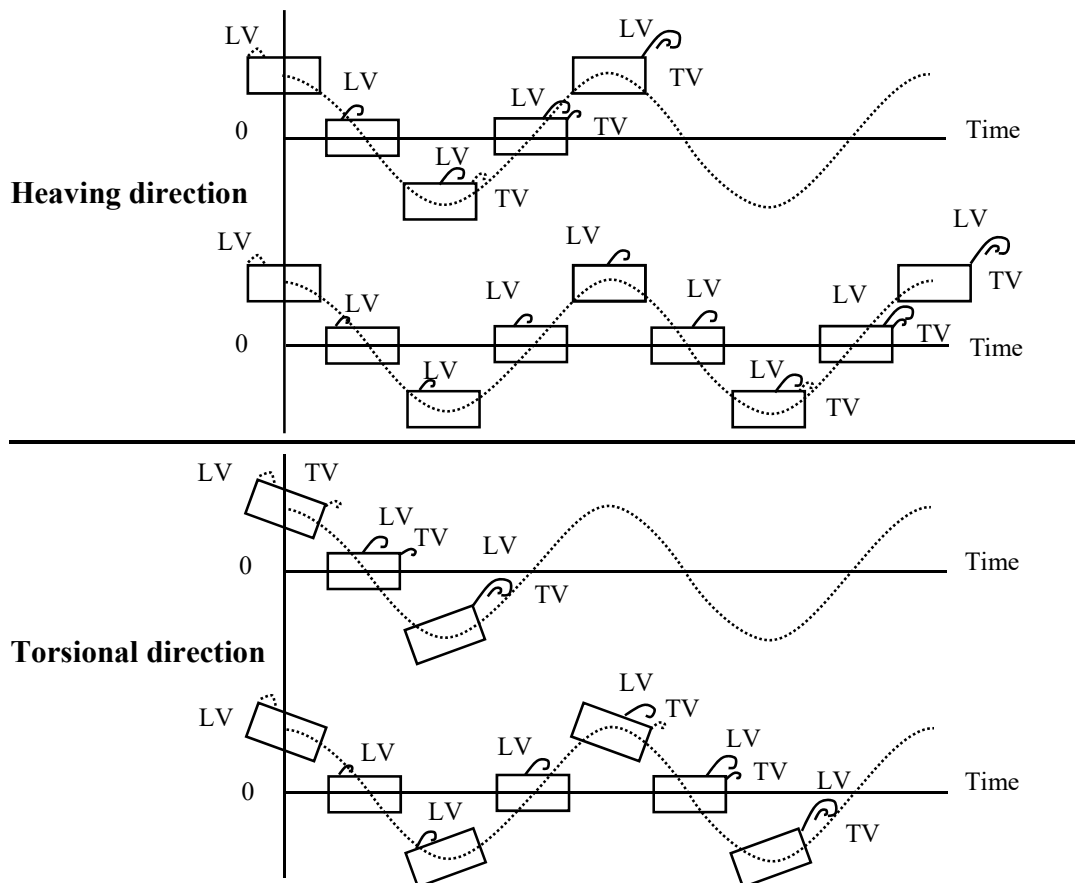


Fig. 2-1 The flow pattern of the motion-induced vortex vibration for the rectangular cylinder. LV represents the vortices from the leading edge, while TV represents the vortices from the trailing edge.

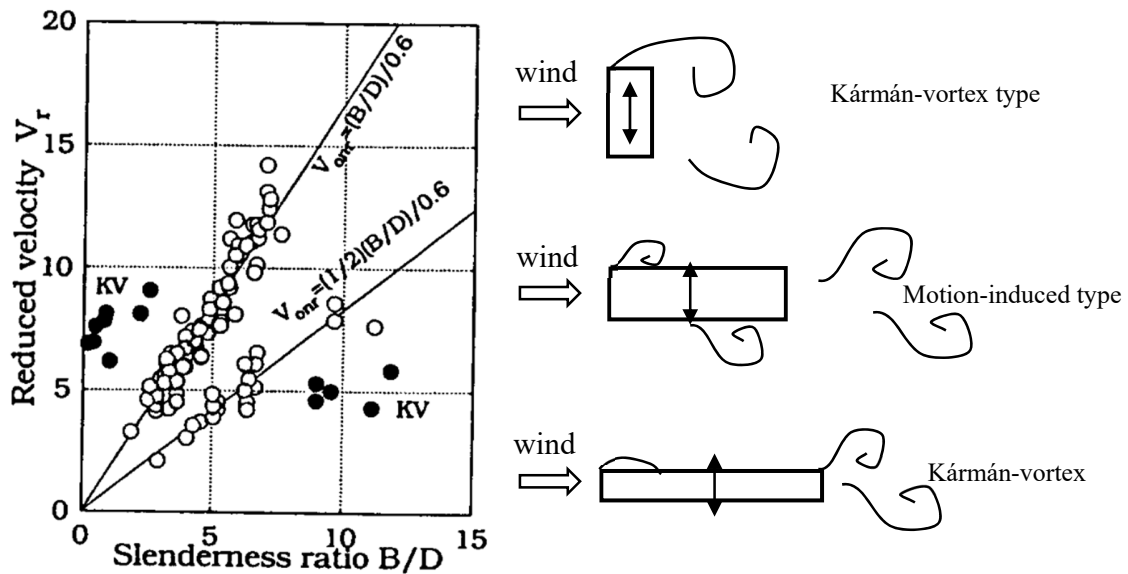


Fig. 2-2 Resonance or onset reduced velocity for bluff bodies (Shiraishi and Matsumoto, 1983).

2.2.3 Galloping

The galloping is the self-excited one-degree of freedom vibration in the direction normal to the approaching wind (Nakamura et al. 1991 and 1994; Parkinson and Smith 1964, Naudascher et al. 1981, Hu et al. 2016). The structures can exhibit large amplitude galloping oscillation at frequencies that are much lower than the vortex shedding frequency. The bridge girder, tall buildings and high-rise structures (i.e., bridge tower, lighting pole and isolated structural elements) are typical examples of structures prone to galloping when the wind velocity exceeds certain critical velocity thresholds, although the origins of its study comes from older evidence on different structures, such as ice-coated power lines cables (Parkinson and Brooks, 1961; Parkinson, 1989). Two common characteristics of the cross-section of those structures are the non-axisymmetric property and the sufficient afterbody, defined as the portion of the body downstream the separation point or the entire cross-section.

Galloping greatly depends on the side ratio B/D (Fig. 2-3) (Parkinson, 1989; Massai, 2016; Nakamura et al. 1991; Nakamura and Hirata, 1994; Hu et al. 2016). For $B/D < 0.6$, the rectangular cylinder shows hard galloping or low-speed galloping, which needs a high initial amplitude to trigger the vibrations, because the afterbody is totally free from interfering with the shear layer. For $0.6 < B/D < 2.8$, the rectangular cylinder shows soft galloping or high-speed galloping, which gallops spontaneously from rest because the afterbody intermittently interferes with the shear layer. With the increase of side ratio from 0.6 to 2.8, the vibration amplitude at a certain wind velocity gradually decreases and the critical wind velocity of galloping also gradually increases (Parkinson, 1989; Parkinson and Wawzonek, 1981; Parkinson and Brooks, 1961). For $B/D > 2.8$, the galloping is stabilized owing to the complete reattachment of the shear layer to the afterbody. Because the

box girders or rectangular cylinders applied in this research have a side ratio large than 0.6, the galloping in this research refers to the high-speed galloping.

The basic mechanism of galloping is that for the rectangular cylinder-like bluff bodies with time-averaged flow field of non-reattachment type, at high enough wind velocities, the downward motion causes the lower shear layer to move closer to the downside surface and hence to become more curved; while the upper shear layer moves further away from it and hence becomes less curved; as a result, the pressure recovery is observed at the upside surface and/or the reduction in the negative pressure is observed at the downside surface, forming a downward force (Fig. 2-4) (Parkinson and Sullivan, 1979; Mizota and Okajima, 1981; Nakamura et al., 1991 and 1994; Hu et al., 2016).

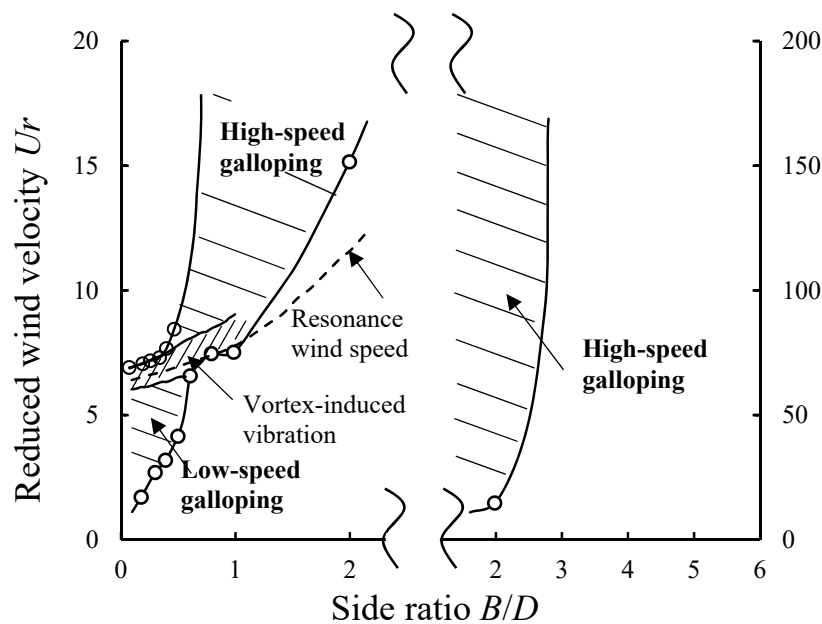


Fig. 2-3 Stability boundaries for galloping of rectangular cylinders (Nakamura and Hirata, 1994)

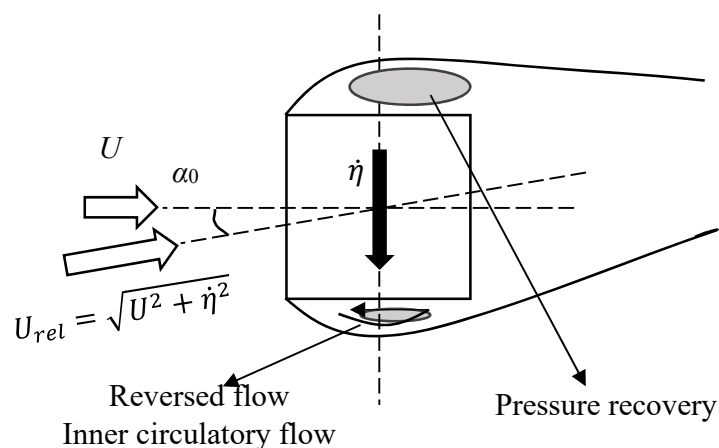


Fig. 2-4 Mechanism of galloping

At high wind velocities, where the natural vortex shedding has a higher frequency than the natural frequency of the system, the transverse force working on the oscillating body can be decided by the pressure distribution on the side surface of the body at the instance. Den Hartog (1985) assumed that the instantaneous transverse force working on the heaving oscillating body with a velocity of $\dot{\eta}$ can be regarded as the transverse force working on the stationary body under the relative angle of attack (α_0) defined as the angle between the chord line and the approaching flow direction (Fig. 2-4). The relative angle of attack can be expressed as:

$$\alpha_0 = \arctan\left(\frac{\dot{\eta}}{U}\right) \quad \text{Eq. 2-5}$$

where U is the approaching wind velocity, $\dot{\eta}$ is the body motion velocity positive in the downward direction. α_0 is positive in the nose-up direction. When the body vibrates in the downward direction, it has a relative angle of attack in the nose-up direction. Therefore, α_0 is positive when $\dot{\eta}$ is positive.

As shown in Fig. 2-5, F_y is the lift force working on a stationary body in the structural axis and positive in the upward direction. F_y can be expressed as:

$$F_y = \frac{1}{2} \rho U^2 B l C_{Fy}(\alpha) \quad \text{Eq. 2-6}$$

where l is the span length, ρ is the air density, α is the angle of attack between the mean wind (U) and the chord line, C_{Fy} is the lift force coefficient. If the body vibrates with a velocity of $\dot{\eta}$, the lift force working on the oscillating body can be expressed as:

$$F_y = \frac{1}{2} \rho U_{rel}^2 B l C_{Fy}(\alpha_0) = \frac{1}{2} \rho U^2 B l C_{Fy}(\alpha_0) \sec^2(\alpha_0) \quad \text{Eq. 2-7}$$

where $U_{rel} = U/\cos(\alpha_0)$. If the relative angle of attack α_0 is small, α_0 , the lift force coefficient C_{Fy} , and U_{rel} can be expressed as the power series:

$$C_{Fy}(\alpha_0) = C_{Fy}|_{\alpha=0^\circ} + \left. \frac{dC_{Fy}}{d\alpha} \right|_{\alpha=0^\circ} \cdot \frac{\alpha_0}{1!} + O(\alpha_0^2) + \dots \quad \text{Eq. 2-8}$$

$$U_{rel}(\alpha_0) = U + O(\alpha_0^2) \quad \text{Eq. 2-9}$$

$$\alpha_0 = \frac{\dot{\eta}}{U} + O(\alpha_0^2) \quad \text{Eq. 2-10}$$

Therefore, the lift force coefficient is

$$C_{Fy}(\alpha_0) = C_{Fy}(0^\circ) + \left. \frac{dC_{Fy}}{d\alpha} \right|_{\alpha=0^\circ} \cdot \alpha_0 \quad \text{Eq. 2-11}$$

For the axisymmetric section, $C_{Fy}(\alpha)$ is the odd function of α and $C_{Fy}(0^\circ) = 0$. Subsequently, take Eq. 2-10 into Eq. 2-11, the lift force coefficient is:

$$C_{Fy}(\alpha_0) = \left. \frac{dC_{Fy}}{d\alpha} \right|_{\alpha=0^\circ} \cdot \frac{\dot{\eta}}{U} \quad \text{Eq. 2-12}$$

Substitute Eq. 2-9 and Eq. 2-12 to Eq. 2-7, the lift force working on the stationary body at α_0 is:

$$F_y = \frac{1}{2} \rho U B l \left. \frac{dC_{Fy}}{d\alpha} \right|_{\alpha=0^\circ} \cdot \dot{\eta} \quad \text{Eq. 2-13}$$

The aerodynamic lift force working on the oscillating body is defined positive in the downward direction. Therefore, the linear quasi-steady lift force working on the oscillating body is

$$L_{qs} = -\frac{1}{2}\rho U_{rel}^2 B l C_{Fy}(\alpha_0) = -\frac{1}{2}\rho U B l \left. \frac{dC_{Fy}}{d\alpha} \right|_{\alpha=0^\circ} \cdot \dot{\eta} \quad \text{Eq. 2-14}$$

The equation of motion for the system subject to the linear quasi-steady force can be written as:

$$m\ddot{\eta} + c\dot{\eta} + k_0\eta = -\frac{1}{2}\rho U B l \left. \frac{dC_{Fy}}{d\alpha} \right|_{\alpha=0^\circ} \cdot \dot{\eta} \quad \text{Eq. 2-15}$$

where, m is the mass per meter; c is the structural damping coefficient, k_0 is the structural stiffness. The aerodynamic damping is characterized by the lift slope $dC_{Fy}/d\alpha$, when

$$\left. \frac{dC_{Fy}}{d\alpha} \right|_{\alpha=0^\circ} < 0 \quad \text{Eq. 2-16}$$

the downward motion creates a positive relative angle of attack, resulting in a downward lift force and negative aerodynamic damping. Subsequently, the lift force working on the oscillating body acts as an exciting force. Eq. 2-16 is the widely known den Hartog criterion, according to which the negative lift slope indicates the galloping instability.

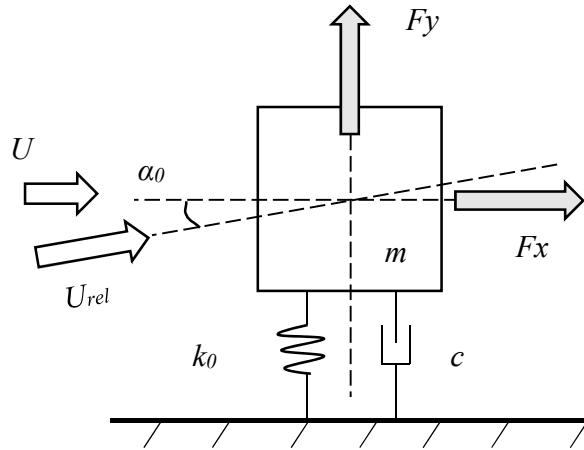


Fig. 2-5 Aerodynamic force working on the stationary model

2.2.4 Torsional flutter

The torsional flutter is an aeroelastic instability in the pitch degree of freedom. Structures with sharp edges and an afterbody are prone to undergo torsional flutter oscillations. It is worth mentioning that the torsional flutter has been found responsible for the destruction of the Tacoma Narrows bridge in 1940 (Billah and Scanlan, 1991). Like galloping, torsional flutter vibration is also potentially catastrophic owing to the continuous increase of the amplitude with the flow velocity above a critical value.

The torsional flutter also greatly depends on the side ratio (Matsumoto et al., 1996 and 1997). For the rectangular cylinder with a small side ratio such as 2, which shows the intermittent

reattachment type of unsteady flow and steady reattachment type of time-averaged flow, the torsional flutter shows the wind-velocity-restricted characteristic. The phase difference between the flow to torsional displacement plays a significant role in the excitation for this type of torsional flutter. For a slender rectangular cylinder with a side ratio larger than 2.8, the torsional flutter can separate into two stages: the first stage is called “low-speed torsional flutter”, which is initiated by vortex convection on side surface at the relatively low wind velocity range; consistently following the former one, “high-speed torsional flutter” is caused by the local separated flow near the leading edge at high wind velocities. With further increase of the side ratio, the rectangular cylinder just shows the “high-speed torsional flutter”. With the side ratio larger than 10, the rectangular cylinder shows the “coupled flutter”, which is of the same mechanism as the “high-speed torsional flutter” owing to the local separated flow at the leading edge.

2.3 Stabilization against the galloping

In the last subsection, the general classification of the aerodynamic phenomena has been laid out. This subsection deals with what are the lessons from the past researches to stabilize the galloping. Firstly, to successfully stabilize the galloping, the contribution should be put on controlling two factors, i.e., the onset wind velocity of galloping and the aerodynamic damping that excites the vibration. Then the roles of the side ratio, vortex shedding and turbulence on the galloping are illustrated separately to provide a basic understanding of the stabilization mechanism against the galloping.

2.3.1 Unsteady effects of galloping response at low wind velocities

The most important goal in stabilizing the galloping is to increase the critical wind velocity of the galloping. However, the quasi-steady theory does not work well for the prediction of the aerodynamic response and aerodynamic damping at the low-wind velocity range owing to the complicated combined effects between the vortex-induced vibration and galloping or the unsteady effects (Bokaian and Geoola, 1984; Parkinson, 1989; Otsuki et al., 1974; Washizu et al., 1978; Novak, 1972; Massai, 2016; Mannini et al., 2014, 2016, 2018a and b; Gao and Zhu, 2016 and 2017). Many pieces of research tried to describe these effects by the nonlinearity quasi-steady theory. Parkinson and Brooks (1961) initially proposed a fifth-order polynomial function for the curve of the lift force coefficient C_{Fy} vs the angle of attack α to predict the critical wind velocity of galloping and the response for the square section. Other researchers also proposed mathematical models to describe the interaction between vortex-induced vibration and galloping by modifying the quasi-steady theory or introducing the mathematical model of vortex-induced vibration (Parkinson and Smith, 1964; Corless and Parkinson, 1988 and 1993; Novak, 1972; Tamura and Shimada, 1987; Mannini et al., 2018b). Even though these models can predict aerodynamic response at high wind velocities, it failed to accurately predict the onset wind velocity of galloping and the aerodynamic response at the low wind velocity range. Recently, Gao and Zhu (2017) effectively considered the unsteady effects in the coefficient of the nonlinear quasi-steady force

model and pointed out the contribution of each term to the total exciting force. Rather than the complicated combination effects between the vortex-induced vibration and galloping at low wind velocities, one interesting phenomenon is that the vortex shedding can stabilize the galloping until the resonance reduced wind velocity characterized as the reciprocal of the Strouhal number for the low-mass damping system. Therefore, the relationship between the Strouhal number and the critical wind velocity of galloping provides the first important clue for stabilizing the galloping by manipulating the Strouhal number.

2.3.2 Asymptotic behavior of the aerodynamic response/damping at high wind velocities

Even though the non-linear quasi-steady theory does not work well for predicting the critical wind velocity of galloping, it is valid in predicting the galloping response or linear increase of galloping response with wind velocity at high wind velocities (Parkinson and Brooks, 1961; Parkinson and Smith, 1964; Novak, 1972; Mannini et al., 2016). By directly measuring the force working on an elastically supported body, Gao and Zhu (2017) also showed the asymptotic behavior of the parameters in their unsteady aerodynamic force model to those of the nonlinear quasi-steady force model at high wind velocities. Meanwhile, the unsteady linear aerodynamic damping was also observed to be asymptotic to the linear quasi-steady aerodynamic damping at high wind velocities through the forced vibration tests, which can reduce the variables to only the amplitude and frequency (Nakamura and Mizota, 1975; Obasaju, 1983; Washizu et al., 1978; Yagi et al., 2013). The linear quasi-steady aerodynamic damping and the linear unsteady aerodynamic damping are mainly utilized in current research to evaluate the aerodynamic damping at the high wind velocities.

2.3.3 Importance of the afterbody

As indicated by the fact that all the aerodynamic phenomena greatly depend on the side ratio and the flow pattern changes with the side ratio, the afterbody, defined as the portion of the body downstream the separation point or the entire cross-section, plays an important role in the aerodynamic performance. As shown in Fig. 2-6 and Fig. 2-7, both the Strouhal number (St) and drag force coefficient (C_{Fx}) varies obviously with the side ratio for the rectangular cylinder. The first notable feature of Fig. 2-6 and Fig. 2-7 is that C_{Fx} dramatically increases while St barely varies for $0 < B/D < 0.6$. According to Bearman and Trueman (1971), the increase in the drag coefficient C_{Fx} is owing to that the size of the “base cavity” from which the fluid entrainment takes place by the shear layer forming a discrete vortex, and the base pressure is accordingly lowered. When the body width B is small and the shear layer is free from the interference with the side surface of the bluff body, the vortex of full strength will lie closer to the rear surface with the increase of girder width B , resulting in the lower base pressure. The lack of interference between the shear layer and the afterbody is also the reason for the minor change of St at $0 < B/D < 0.6$. At $0 < B/D < 0.6$, the rectangular cylinder shows the hard-type galloping also because of that the shear layer is free from the interference with the afterbody. However, with a further increase of girder width B , the

afterbody starts to interfere with the shear layer. According to Bearman and Trueman (1971), the interference between the shear layer and the afterbody leads to the vortex forming further downstream, raising the base pressure and resulting in a decrease in the frequency of vortex shedding. Therefore, as the second notable feature of Fig. 2-6 and Fig. 2-7, the drag force coefficient C_{Fx} and St decrease at $0.6 < B/D < 2.8$. At $0.6 < B/D < 2.8$, the rectangular cylinder shows the soft galloping owing to the intermittent interference between the shear layer and the afterbody. As shown in Fig. 2-8, owing to the low mass and damping of the system, for the rectangular cylinders with side ratio from 0.3~2.5, the galloping generally occurs from the resonance wind velocity characterized by reciprocal of Strouhal number ($1/St$). Especially for the $0.6 < B/D < 2.8$ rectangular cylinders, the increase of $1/St$ with B/D indicates that the critical wind velocity of galloping increase with B/D . Furthermore, with the increase of B/D from 0.6 to 2.8, the vibration amplitude of galloping gradually decreases. This is because that the interference between the shear layer and the afterbody turns stronger with the increase of side ratio. Like the abrupt change of C_{Fx} at $B/D = 0.6$, St abruptly changes at $B/D = 2.8$ accompanied by switching of the time-averaged flow field from detachment type to the reattachment type. For $B/D > 3$, St and C_{Fx} decrease with B/D , while another abrupt change is observed in St at $B/D = 6$ owing to the change of flow pattern. Owing to the strong interference between the shear layer and the afterbody, the $B/D > 3$ rectangular cylinders cannot show the galloping. Therefore, it is clear that the occurrence of the galloping instability and the galloping response greatly depend on the side ratio of the bluff body owing to the interference between the shear layer and the afterbody. The qualitative judgment of the interference between the shear layer and the afterbody can be obtained based on the time-averaged flow field around the body.

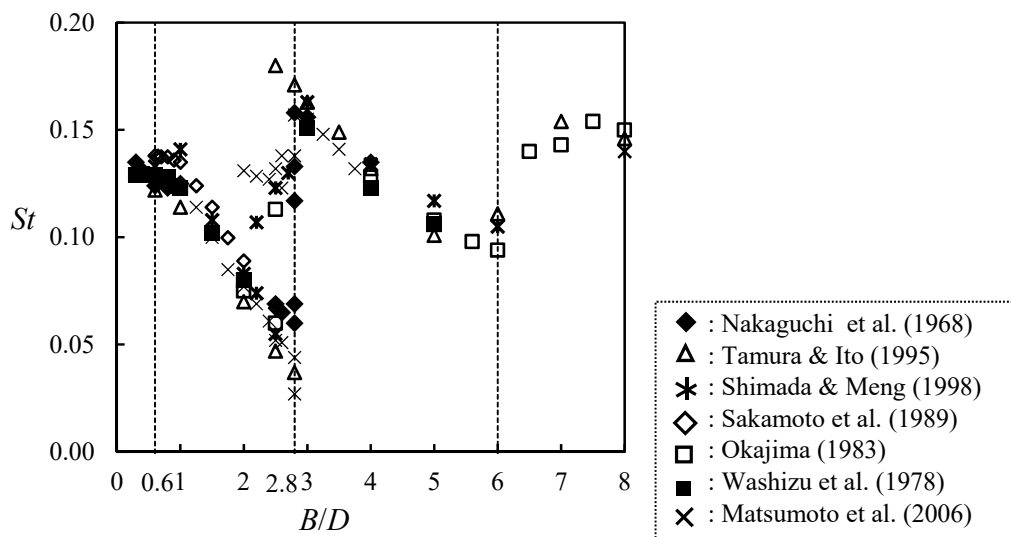


Fig. 2-6 Change of Strouhal number with side ratio B/D .

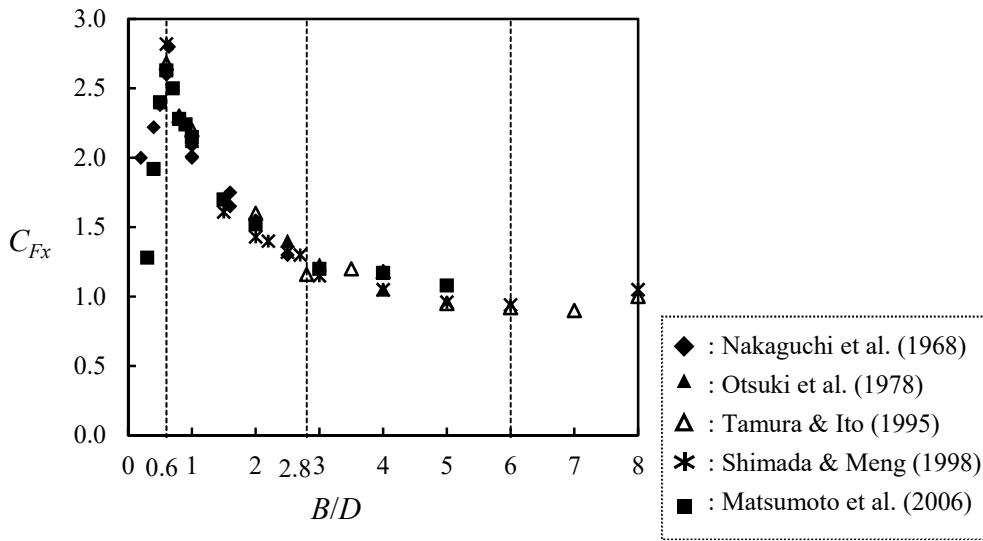


Fig. 2-7 Change of drag force coefficient with side ratio B/D

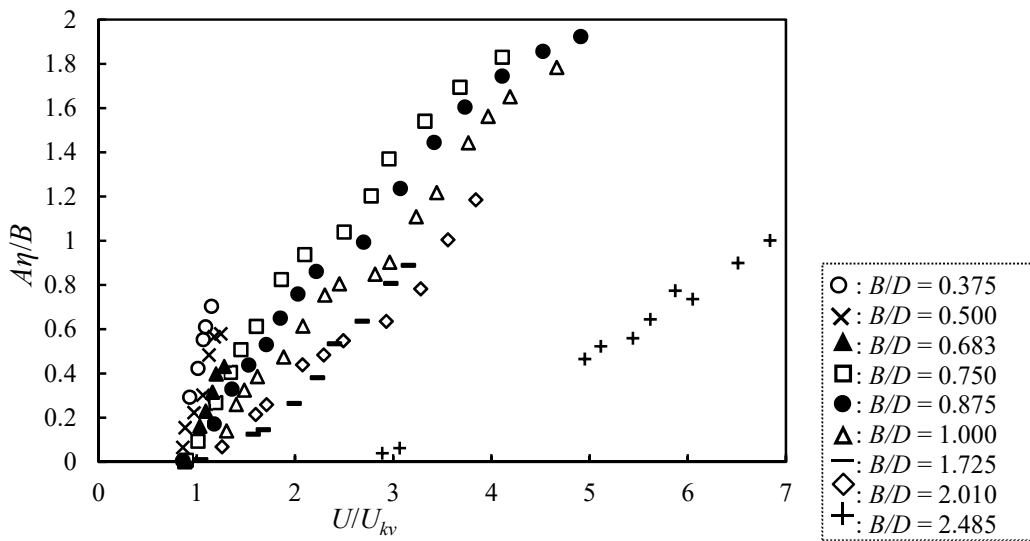


Fig. 2-8 Vibration amplitude for rectangular cylinder with different side ratio (Parkinson and Wawzonek, 1981). (U_{kv} represents the resonance wind velocity, equaling to fD/St ; $A\eta$ is the oscillation amplitude; B and D are the body width and body height respectively).

2.3.4 Importance of vortex shedding

The vortex shedding plays an important role in stabilizing the galloping according to past researches (Yagi, et. al., 2013; Nakamura et al., 1991 and 1994; Horitsu, 2007; Matsumoto et al., 1990, 2001, 2010). As shown in Fig. 2-9, the splitter plate can make the rectangular cylinder with side ratio up to about 5 prone to the galloping instability. The suppression of the vortex shedding in the wake by the splitter plate is assumed to be the reason for the excitation of the galloping

instability for the rectangular cylinder of the time-averaged flow of reattachment type. Furthermore, the intense secondary flow was observed in the near wake of the inclined circular cylinder firstly by Shirakashi (1986) and believed to suppress the vortex shedding in a similar way as the splitter plate (Matsumoto et al., 1990, 2001, 2010). As a result, even the circular cylinder, which does not have the galloping problem, was observed to show the large amplitude of galloping vibration (Matsumoto et al., 1990, 2001, 2010). The suppression of the vortex shedding was qualitatively explained by the change of the aerodynamic force coefficients (Matsumoto et al., 2006; Horitsu, 2005). As shown in Fig. 2-10, the splitter plate in the wake reduced the drag force coefficient C_{Fx} and fluctuating lift force coefficient C_{Fy}' . The fluctuating lift force coefficient C_{Fy}' is the vortex shedding intensity, which indicates the strength of the vortex shedding. According to Horitsu (2007), suppression of the vortex shedding by the splitter plate in the wake can effectively decrease of curvature of the time-averaged shear layer. This illustration was also validated by other researches (Chauhan, et al., 2018). In this sense, to suppress the vortex shedding in the wake by splitter plate can effectively change the flow pattern to more detachment type and make the bluff body more galloping instability. Therefore, the vortex shedding or the flow entrainment in the near wake plays an important in controlling the galloping instability.

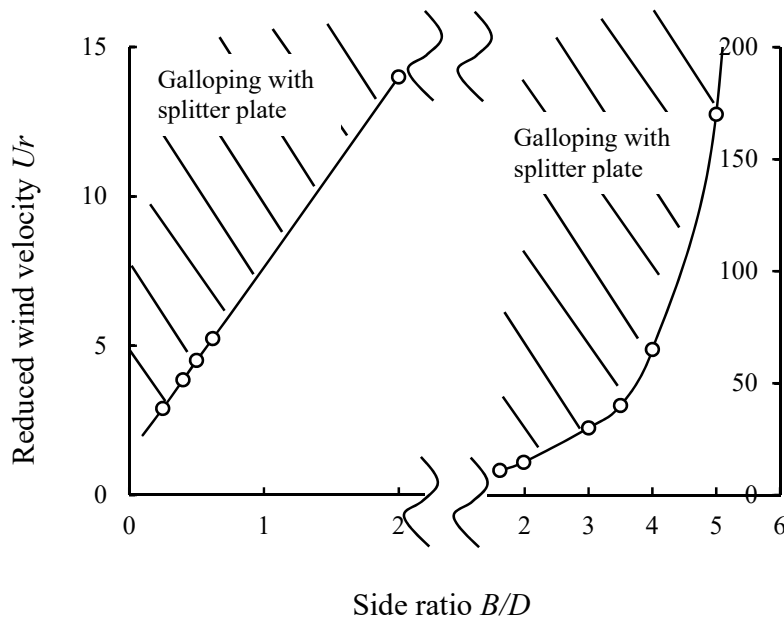


Fig. 2-9 Stability boundaries for galloping of rectangular cylinders with the splitter plate in the wake (Nakamura and Hirata, 1994).

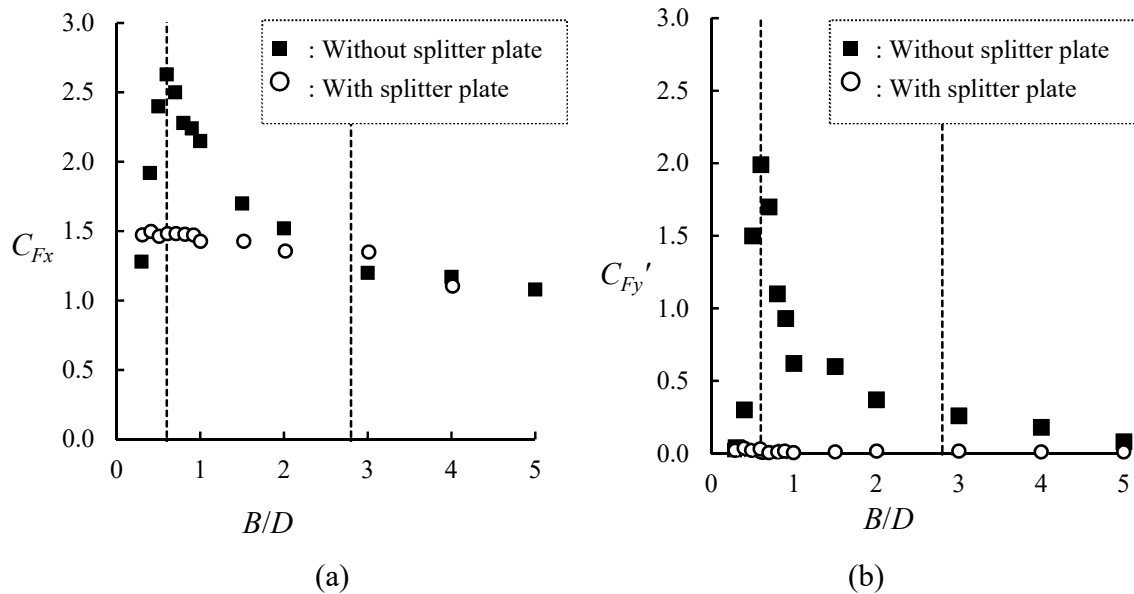


Fig. 2-10 Aerodynamic force coefficient of the rectangular cylinder with splitter plate in the wake: (a) drag force coefficient; (b) fluctuating lift force coefficient (Matsumoto et al., 2006).

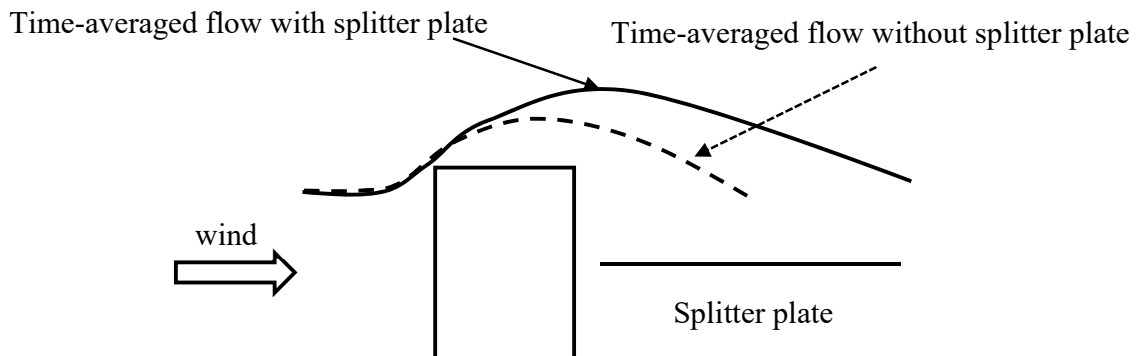


Fig. 2-11 Illustration for the role of splitter plate on the time-averaged flow (Horitsu, 2007).

2.3.5 Lesson from effects of turbulence on galloping

The galloping instability is very sensitive to the effects of turbulence and Parkinson (1989) gave a detailed explanation for these effects. According past researches (Kwok and Melbourne, 1977 and 1980; Hillier and Cherry, 1980, Parkinson, 1989; Nakamura and Tomonari, 1977), compared with the smooth flow, the high turbulence intensity can increase the fluid entrainment of the shear layer and promote the interference between the shear layer and the afterbody (Fig. 2-12). As a result, the turbulence intensity effectively elongates the side ratio of the rectangular cylinder by increasing the curvature of the shear layer and promoting the shear layer to reattach on the side surface. However, the turbulence scale seems to be less important (Parkinson, 1989). It is widely realized that the increases in the side ratio and the turbulence intensity have an identical effect and

result in a similar shear layer (Parkinson, 1989; Hu et. al, 2016). In another word, the promotion of the reattachment of shear layer on the afterbody owing to the turbulent flow makes the response resemble a rectangular cylinder with a larger side ratio: in the turbulent flow, the hard-type galloping ($B/D < 0.6$) switched to the soft-type galloping, and the soft-type galloping ($B/D < 0.6$) became weaker and eventually stable (Laneville and Parkinson, 1971; Novak et al., 1970, 1972, 1974, Mannini et al., 2018a). Even though the stabilization effects of the turbulence intensity on the galloping depend on the mass-damping system (Bearman et al., 1987; Mannini et al., 2018a), for the flow mass-damping system, the turbulence intensity obviously reduced the vibration amplitude (Fig. 2-13). Meanwhile, the reduced critical wind velocity of galloping (U_{rc0}) and the reciprocal of Strouhal number ($1/St$) both increased with the increase of turbulence intensity. In summary, one important lesson from the stabilization of the turbulence against the galloping is to promote the reattachment of the shear layer on the side surface and strengthen the interference between the shear layer and the afterbody.

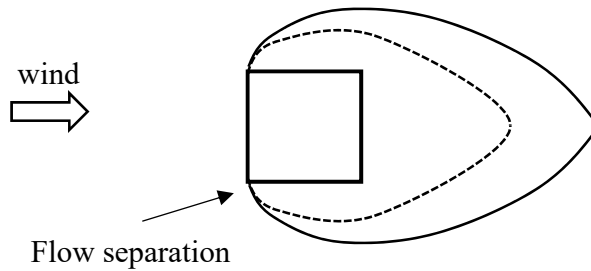


Fig. 2-12 Flow separation on the bluff body: smooth flow (plain line), turbulent flow (dashed line) (Andrienne, 2012).

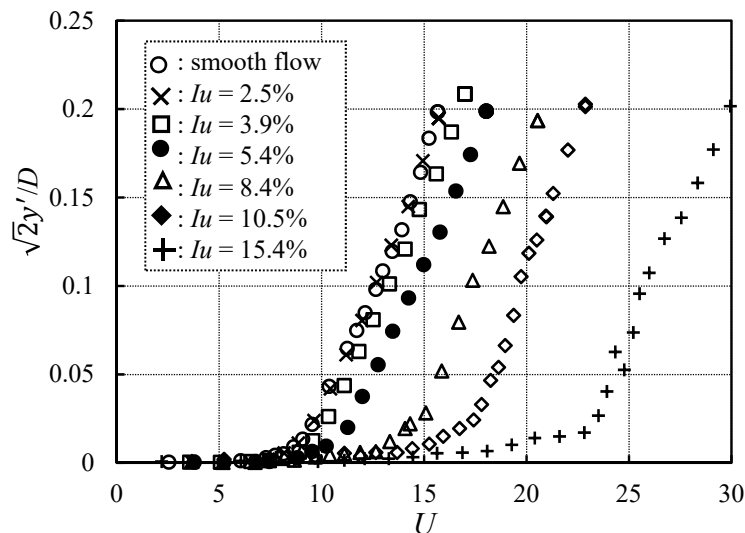


Fig. 2-13 Aerodynamic response of $B/D = 1.5$ rectangular cylinder in the turbulence flow (I_u represents the turbulence intensity; $Sc = 28$ is the mass damping parameter) (Mannini et al., 2018a).

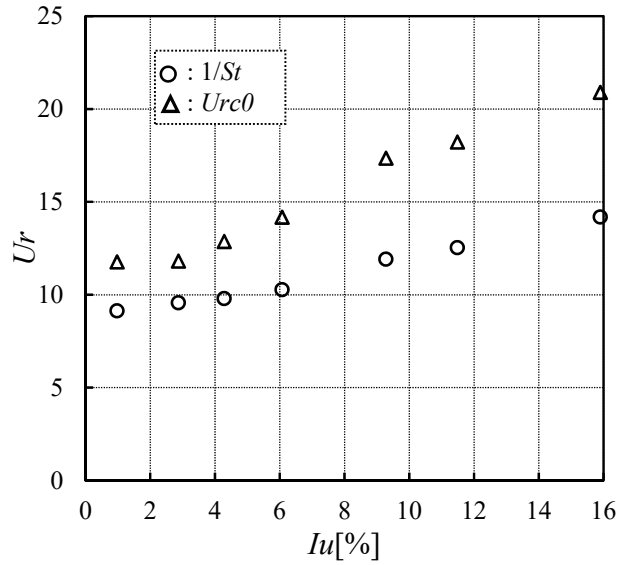


Fig. 2-14 Variation in critical wind velocity of galloping and Strouhal number with turbulence intensity. (Data is from Mannini et al., 2018a)

2.4 Outline of the wind tunnel tests

This subsection illustrates the wind tunnel tests and analysis method applied in this research. The wind tunnel tests include free vibration tests, aerodynamic force tests, forced vibration tests, and wind velocity measurements.

2.4.1 Wind tunnel

The wind tunnel tests were all carried out in the room-circuit Eiffel type wind tunnel (KWT-81) at Kyoto University (Fig. 2-15). The measurement section of the wind tunnel has a height of 1.8m and a width of 1.0m. The wind velocity can continuously vary from 0.2m/s to 30m/s. In order to avoid the disturbance of the boundary turbulence on the side wall and the supporting arm, the guide wall was put in the wind tunnel 35mm far from the wind tunnel wall. The distribution of the wind velocity is uniform along the measurement section of the wind tunnel, and the turbulence intensity in the approaching flow is less than 0.3% for the mean wind velocity of 10m/s.

The wind velocity in the wind tunnel was adjusted based on the relationship between the rotational speed of the wind tunnel motor and the wind velocity. The relationship was calibrated based on the wind velocity calculated (Eq. 2-17) by the difference ΔP between the total pressure and the static pressure measured by the NPL Pitot tube.

$$U = \sqrt{\frac{2\Delta P}{\rho}} \quad \text{Eq. 2-17}$$

where ρ is the air density (kg/m^3).

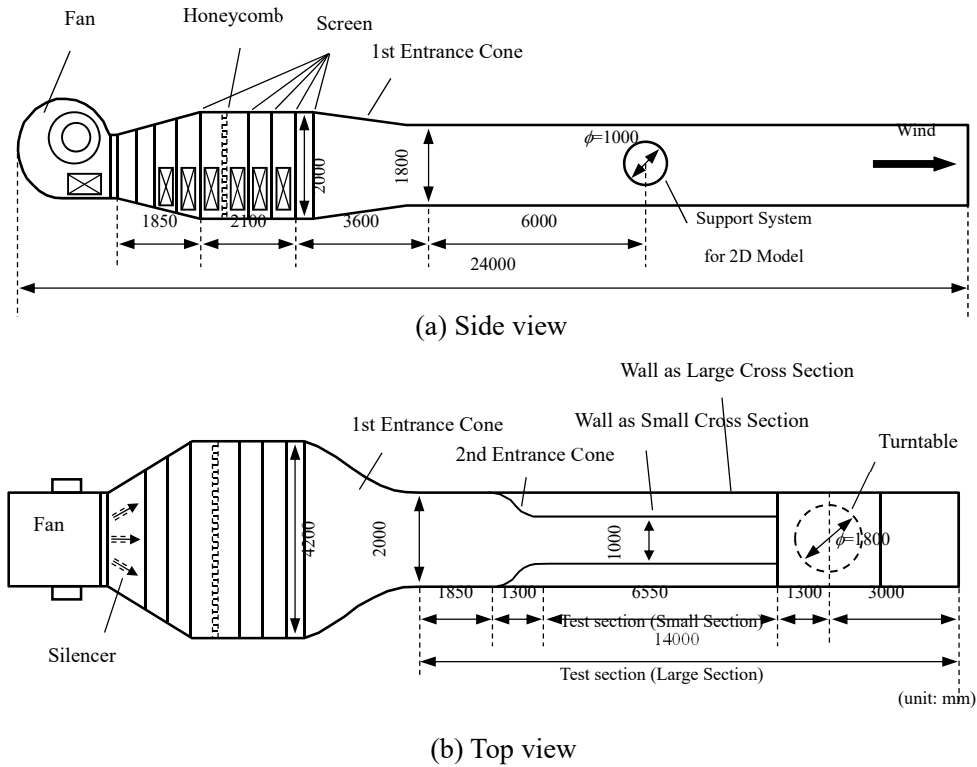
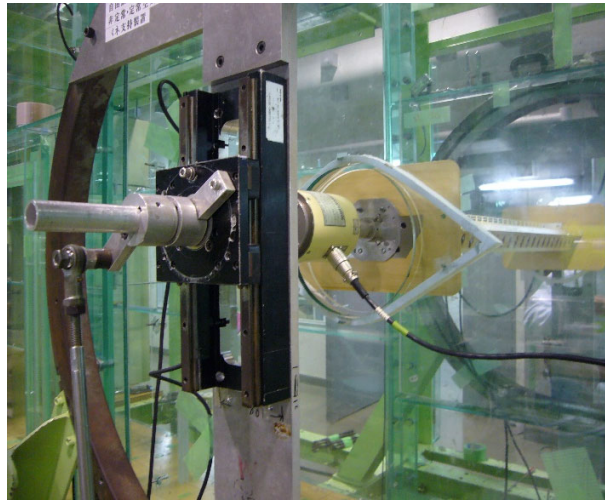


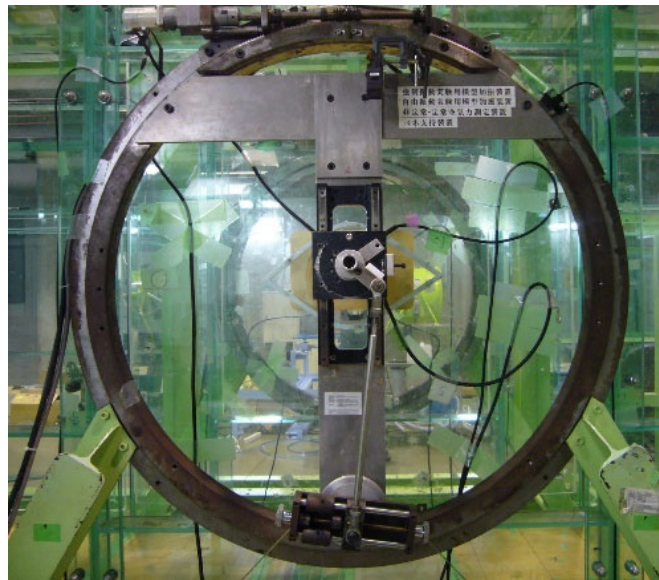
Fig. 2-15 Sketch of the wind tunnel (unit: mm)

2.4.2 Aerodynamic force measurement system

The load cell (NISHO ELECTRIC WORKS CO.LTD MULTI COMPONENT LOADCELL MODL LMC-3501-50N) (Fig. 2-16 (a)) was utilized to measure the aerodynamic force working on the model. The digital data from the load cell was put on the 100Hz low pass filter in the dynamic-strain measuring instrument (KYOWA, MCD-8A) and transferred to the A/D adapter. The sampling frequency is 1000Hz. The time length of the data measurement was 60s for the aerodynamic force working on the stationary model and 180s for the force working on the oscillating model. The model was rigidly connected to the load cell, which was rigidly connected to the supporting system at the outside of the wind tunnel (Fig. 2-16 (a) (b)). The supporting system can rotate to change the angle of attack at 1° interval. The supporting system can maintain the model stationary in the wind tunnel and force the model to vibrate in vertical and torsional direction. The shaker in the system simply consists of the link mechanics, the motor (SPEEDDYNE, SD-400-11A) at the ground and the timing belt. The rotation of the motor was transferred to the link mechanics forming the vertical and torsional displacement of the model by the timing belt, which connected the parallel axis of the link mechanics and the motor without slipping. The maximum vibration frequency of the supporting system was 2.7Hz, while the maximum double amplitude of vibration in vertical and torsional direction was 50mm and 5° , respectively.



(a)



(b)

Fig. 2-16 Apparatus for forced vibration tests

2.4.3 Aerodynamic force tests on the stationary model

In the aerodynamic force experiment, three aerodynamic forces working on the stationary model were measured by the load cells. The angle of attack (α) was defined as nose-up positive. The three aerodynamic force coefficients (lift: C_{Fy} , drag: C_{Fx} , and pitching moment: C_M), Strouhal number St , and fluctuating lift force coefficient C_{Fy}' are defined on the structural axis as follows:

$$C_{Fy} = \frac{F_y}{\frac{1}{2} \rho U^2 B l} \quad \text{Eq. 2-18}$$

$$C_{F_x} = \frac{F_x}{\frac{1}{2}\rho U^2 D l} \quad \text{Eq. 2-19}$$

$$C_M = \frac{F_M}{\frac{1}{2}\rho U^2 B^2 l} \quad \text{Eq. 2-20}$$

$$C'_{F_y} = \frac{F'_y(t)_{std}}{\frac{1}{2}\rho U^2 B l} \quad \text{Eq. 2-21}$$

where F_y (upward direction is positive), F_x (streamwise direction is positive), and F_M (nose-up direction is positive) are the mean values of lift force (N), drag force (N), and pitching moment (N·m) defined on the structural axis (Fig. 2-17); l is the span length, ρ is the air density (kg/m^3), U is the approaching wind velocity (m/s), $F_y(t)$ is the fluctuating lift force time series, $F'_y(t)$ is the lift force component fluctuating in the frequency of f_{st} (f_{st} is the dominant frequency (Hz) of the Kármán-vortex shedding), $F'_y(t)_{std}$ is the standard deviation of $F'_y(t)$. f_{st} was identified from the fluctuating lift force $F_y(t)$, and $F'_y(t)$ was calculated by applying a bandpass filter with a center frequency of f_{st} to the fluctuating lift force $F_y(t)$. Based on the quasi-steady theory, galloping occurs when the lift slope ($dC_{F_y}/d\alpha$) is negative, that is, the well-known Den Hartog criterion (Den Hartog, 1985). Furthermore, the Kármán vortex shedding intensity, which indicates the strength of Kármán vortex shedding, is defined by the fluctuating lift force coefficients C'_{F_y} . The drag coefficient C_{F_x} is sensitive to the Kármán vortex shedding intensity. Strong vortex shedding is accompanied by a strong roll-up of the separating shear layers at the near wake and negative base pressure of a large absolute value, which leads to a large C_{F_x} (Bearman and Trueman, 1972; Matsumoto et al., 2006; Dong et al., 2017).

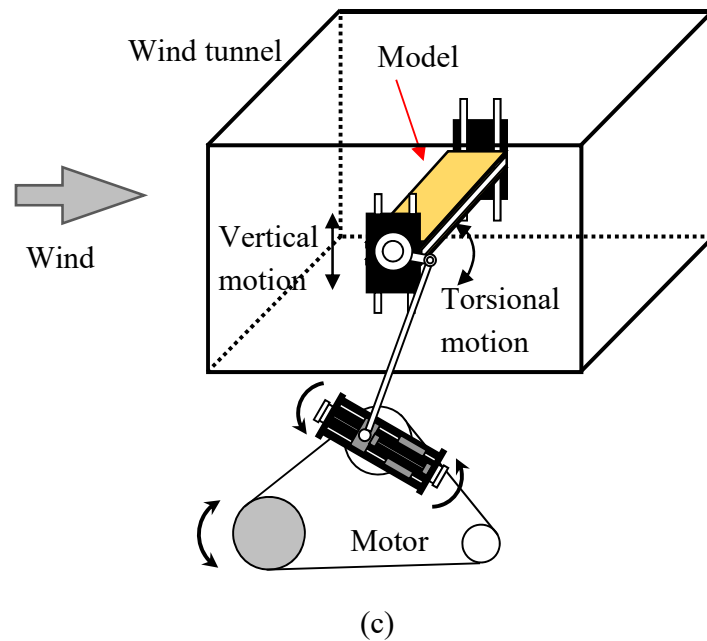


Fig. 2-16 Continued

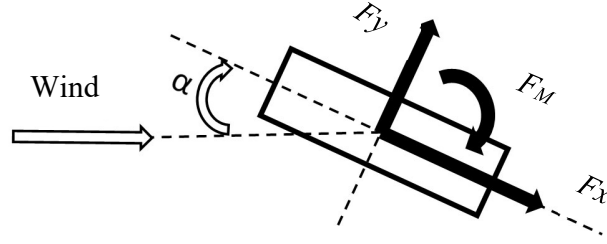


Fig. 2-17 Definitions of aerodynamic forces.

2.4.4 Forced vibration tests

The self-excited aerodynamic forces working on an oscillating bluff body were formulated by the aerodynamic derivatives H_i^* , A_i^* ($i = 1\sim 4$) as follows, according to Scanlan and Tomko (1971):

$$L_{se} = \frac{1}{2} \rho (2b) U^2 \left\{ kH_1^* \frac{\dot{\eta}}{U} + kH_2^* \frac{b\dot{\varphi}}{U} + k^2 H_3^* \varphi + k^2 H_4^* \frac{\eta}{b} \right\} \quad \text{Eq. 2-22}$$

$$M_{se} = \frac{1}{2} \rho (2b^2) U^2 \left\{ kA_1^* \frac{\dot{\eta}}{U} + kA_2^* \frac{b\dot{\varphi}}{U} + k^2 A_3^* \varphi + k^2 A_4^* \frac{\eta}{b} \right\} \quad \text{Eq. 2-23}$$

where L_{se} is the self-excited lift force per unit span (N/m) (downward direction is positive), M_{se} is the self-excited pitching moment per unit span (N·m/m) (nose-up direction is positive), η is the vertical displacement (m) (downward direction is positive), φ is the torsional displacement ($^\circ$) (nose-up direction is positive), (\cdot) indicates the time differentiation, b is the half-length of the body width (m), k is the reduced frequency ($b\omega/U$), and ω is the angular frequency (rad/s).

Aerodynamic derivatives are used in practice to analyze galloping, torsional flutter, and coupled flutter. The coupled flutter, where the contribution of the coupling effect between torsional and vertical vibration is dominant, is mainly characterized by A_2^* , A_1^* , and H_3^* (Matsumoto, 1996; Chen and Kareem, 2006; Yang et al., 2007; Ge et al., 2016). Galloping is mainly characterized by positive H_1^* , whereas the torsional flutter is mainly characterized by positive A_2^* (Scanlan and Tomko, 1971; Matsumoto, 1996). The effects of side-surface openings on the galloping and torsional flutter were discussed based on the aerodynamic damping in vertical direction H_1^* and the aerodynamic damping in torsional direction A_2^* , which were identified from the vertical/torsional 1DOF forced vibration tests, respectively. Aerodynamic self-excited forces were measured by load cells rigidly connected to the model under vertical or torsional 1DOF forced vibration; the displacement of the model was simultaneously recorded using laser gages (Keyence, IL-300). The aerodynamic derivatives were then calculated based on the displacement and aerodynamic self-excited force time series.

Actually, the force measured by the load cell consists of the inertial force and the aerodynamic force. In order to take off the inertial force, the inertial force working on the oscillating model was measured through the same forced vibration tests without wind. The digital system phase lag between the force and displacement was calculated by putting an additional mass to the model.

The measurement and calculation of the aerodynamic force and aerodynamic derivatives are explained as follows.

Firstly, because the inertial force has no phase lag to the displacement when the displacement is expressed as $dis = dis_0 \exp(i\omega t)$, the inertial force working on the oscillating body without wind is:

$$F = F_0 \exp(i(\omega t - \Delta)) \quad \text{Eq. 2-24}$$

where F_0 is the amplitude of inertial force, Δ is the digital phase lag between the displacement and the system. Because the inertial force is small, when calculating the inertial force and phase lag, an additional mass usually is put at the leading edge of the model to increase the measured force and minimize the error.

When it is under the wind, the measured force F is:

$$F = F_t \exp(i(\omega t - \Psi_t)) = \{F_a \exp(i(\omega t - \Psi_a)) + F_0 \exp(i(\omega t))\} \exp(i(-\Delta)) \quad \text{Eq. 2-25}$$

where F_t is the amplitude of the measured force under wind; Ψ_t is the phase lag between the displacement and the measured force F ; F_a is the amplitude of the aerodynamic force working on the model under wind; Ψ_a is the phase lag between the displacement and the aerodynamic force.

If the model is under vertical 1DOF sinusoidal vibration, the displacement, the unsteady lift force and the pitching moment are in the following form:

$$\eta(t) = \eta_0 \sin \omega t \quad \text{Eq. 2-26}$$

$$L_{se} = L_{\eta 0} \sin(\omega t - \Psi_{L\eta}) \quad \text{Eq. 2-27}$$

$$M_{se} = M_{\eta 0} \sin(\omega t - \Psi_{M\eta}) \quad \text{Eq. 2-28}$$

where η_0 is the displacement amplitude; $\Psi_{L\eta}$ is the phase lag between unsteady lift and vertical displacement; $L_{\eta 0}$ is the amplitude of the lift working on the vertical 1DOF sinusoidal vibration model per unit (downward direction is positive); $M_{\eta 0}$ is the amplitude of the pitching moment working on the vertical 1DOF sinusoidal vibration model per unit (nose-up direction is positive); $\Psi_{M\eta}$ is the phase lag between the pitching moment and displacement.

For the vertical 1DOF vibration, the unsteady lift force working on the model is:

$$L_{se} = \frac{1}{2} \rho (2b) U^2 \left\{ k H_1^* \frac{\dot{\eta}}{U} + k^2 H_4^* \frac{\eta}{b} \right\} \quad \text{Eq. 2-29}$$

By summarizing Eq. 2-26 and Eq. 2-29, the flutter derivatives can be obtained based on the following formulas:

$$H_1^* = - \frac{L_{\eta 0} \sin \Psi_{L\eta}}{\rho b^2 \omega^2 \eta_0} \quad \text{Eq. 2-30}$$

$$H_4^* = \frac{L_{\eta 0} \cos \Psi_{L\eta}}{\rho b^2 \omega^2 \eta_0} \quad \text{Eq. 2-31}$$

$$A_1^* = - \frac{M_{\eta 0} \sin \Psi_{M\eta}}{\rho b^3 \omega^2 \eta_0} \quad \text{Eq. 2-32}$$

$$A_4^* = \frac{M_{\eta_0} \cos \Psi_{L\eta}}{\rho b^3 \omega^2 \eta_0} \quad \text{Eq. 2-33}$$

If the model is under torsional 1DOF sinusoidal vibration, the torsional displacement, unsteady lift force and unsteady pitching moment are:

$$\varphi(t) = \varphi_0 \sin \omega t \quad \text{Eq. 2-34}$$

$$L_{se} = L_{\varphi_0} \sin(\omega t - \Psi_{L\varphi}) \quad \text{Eq. 2-35}$$

$$M_{se} = M_{\varphi_0} \sin(\omega t - \Psi_{M\varphi}) \quad \text{Eq. 2-36}$$

where φ_0 is the torsional displacement amplitude; $\Psi_{L\varphi}$ is the phase lag between unsteady lift and torsional displacement; L_{φ_0} is the amplitude of the lift working on the torsional 1DOF sinusoidal vibration model per unit (downward direction is positive); M_{φ_0} is the amplitude of the pitching moment working on the torsional 1DOF sinusoidal vibration model per unit (nose-up direction is positive); $\Psi_{M\varphi}$ is the phase lag between the pitching moment and the torsional displacement.

The aerodynamic derivatives identified from the force working on the torsional 1DOF oscillating model are:

$$H_2^* = -\frac{L_{\varphi_0} \sin \Psi_{L\varphi}}{\rho b^3 \omega^2 \varphi_0} \quad \text{Eq. 2-37}$$

$$H_4^* = \frac{L_{\varphi_0} \cos \Psi_{L\varphi}}{\rho b^2 \omega^2 \varphi_0} \quad \text{Eq. 2-38}$$

$$A_1^* = -\frac{M_{\varphi_0} \sin \Psi_{M\varphi}}{\rho b^3 \omega^2 \varphi_0} \quad \text{Eq. 2-39}$$

$$A_4^* = \frac{M_{\varphi_0} \cos \Psi_{L\varphi}}{\rho b^3 \omega^2 \varphi_0} \quad \text{Eq. 2-40}$$

2.4.5 Free vibration tests

The free vibration tests were applied to measure directly the aerodynamic response in the wind tunnel. The model was horizontally supported in the wind tunnel by two arms connecting to the two endplates of the model (Fig. 2-18). Four coil springs were utilized to support each arm outside the wind tunnel. The supporting system can rotate to change the angle of attack at 1° interval. The supporting system can realize the vertical one-degree of freedom (1DOF), torsional 1DOF, and the vertical and torsional 2DOF free vibration tests. The horizontal and vertical displacement can be restrained by the piano wire in the horizontal and the vertical direction respectively, while the torsional displacement can be restrained by rigidly connecting the axis of the model and the bar supported by the springs (Fig. 2-18). Because the coupling effects between the vertical and torsional direction was out of the interest of the current research, only vertical 1DOF and torsional 1DOF free vibration tests were carried out. The model displacement was measured by the laser gages (Keyence, IL-300). The digital data from the laser gages was then transferred to the A/D adapter. The sampling frequency is 1000Hz.

The Scruton numbers for the vertical and torsional directions are defined as follows, respectively:

$$S_{c\eta} = \frac{2m\delta_{\eta}}{\rho D^2} \quad \text{Eq. 2-41}$$

$$S_{c\varphi} = \frac{2I\delta_{\varphi}}{\rho D^4} \quad \text{Eq. 2-42}$$

where m is the mass per unit (kg/m), I is the moment of inertia per unit (kg·m), δ_{η} and δ_{φ} are the vertical and torsional structural damping quantified by logarithmic decrement, and ρ is the air density (kg/m³).

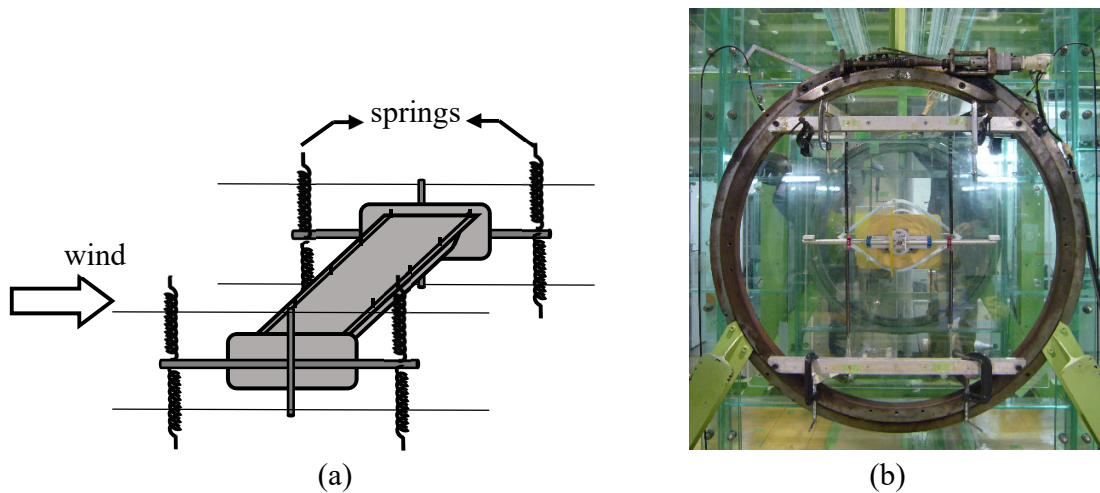


Fig. 2-18 Free vibration test supporting system.

2.4.6 Wind velocity measurement

The hot-wire anemometry of Constant temperature anemometry (CTA) type was utilized in current research. The basic mechanism of the hot-wire anemometry is that the electrical resistance of a metal conductor is a function of its temperature. The metal conductor is heated by the electrical current and inserted into the flow under investigation. The transfer of heat from the metal conductor to the flow increases with increasing velocity in the neighborhood of the element. The resistance is kept constant in CTA, which is achieved by using a variable-current feedback loop which ensures that the cooling effect of the flow is compensated and the resistance of the sensitive metal conductor remains constant. The compensating current or voltage is then used as a measure of the flow velocity in the immediate neighborhood of the sensor.

In the current research, the 'X' type probe (0242R-T5) was used for the measurement of wind velocity. The 'X' type probe is capable of simultaneously resolving two orthogonal velocity components. Each probe consisted of two thin cylindrical sensors that were at right angles to each other and at 45° to the probe axis. The hot wires were operated by two Kanomax model 1011 CTA modules and the voltage signals linearized by two Kanomax model 1013 linearizers.

2.5 Conclusion remarks

This chapter provides a general background about the aerodynamic instabilities, i.e., vortex-induced vibration, torsional flutter, and galloping. Firstly, the characteristics and the exciting mechanism related to those aerodynamic instabilities are illustrated. The focus is then put on the lessons related to the stabilization against the galloping. Two important factors to evaluate and control the galloping performance, i.e., the critical wind velocity and the aerodynamic damping, are addressed. The roles of the side ratio, vortex shedding and turbulence on the galloping are illustrated, indicating that the interference between the shear layer and afterbody is the core in stabilizing the galloping instability. Finally, the wind tunnel tests utilized in current research and the analysis method are outlined.

Reference

- Andrienne, T., 2012. Experimental and Numerical Investigations of the Aeroelastic Stability of Bluff Structures. University of Liege.
- Bearman, P., Trueman, D. (1972), “An Investigation of the Flow around Rectangular Cylinders”, *Aeronautical Quarterly*, **23**(3), 229-237.
- Bearman, P.W., Gartshore, I.S., Maull, D.J., Parkinson, G. V., 1987. Experiments on flow-induced vibration of a square-section cylinder. *J. Fluids Struct.* 1, 19–34. [https://doi.org/10.1016/S0889-9746\(87\)90158-7](https://doi.org/10.1016/S0889-9746(87)90158-7)
- Billah, K.Y., Scanlan, R.H., 1991. Resonance, Tacoma Narrows bridge failure, and undergraduate physics textbooks. *Am. J. Phys.* 59, 118–124.
- Bokaian, A.R., Geoola, F., 1984. Hydroelastic instabilities of square cylinders. *J. Sound Vib.* 92, 117–141.
- Chen, X., Kareem, A., 2006. Revisiting Multimode Coupled Bridge Flutter: Some New Insights. *J. Eng. Mech.* 132, 1115–1123.
- Chauhan, M.K., Dutta, S., More, B.S., Gandhi, B.K., 2018. Experimental investigation of flow over a square cylinder with an attached splitter plate at intermediate reynolds number. *J. Fluids Struct.* 76, 319–335. <https://doi.org/10.1016/j.jfluidstructs.2017.10.012>
- Corless, R.M., Parkinson, G. V., 1988. A model of the combined effects of vortex-induced oscillation and galloping. *J. Fluids Struct.* 203–220.
- Corless, R.M., Parkinson, G. V., 1993. Mathematical modelling of the combined effects of vortex-induced vibration and galloping. Part 2. *J. Fluid Struct.* 7, 825–848.
- Dabiri, D., 2007. Cross-Correlation Digital Particle Image Velocimetry – A Review.
- Den Hartog, J.P., 1985. *Mechanical Vibrations*, Dover Publication, New York, NY, USA.
- Dong, H., Cao, S., Ge, Y., 2017. Large-eddy simulation of stably stratified flow past a rectangular cylinder in a channel of finite depth. *J. Wind Eng. Ind. Aerodyn.* 170, 214–225.

- Gao, G., Zhu, L., 2016. Measurement and verification of unsteady galloping force on a rectangular 2:1 cylinder. *J. Wind Eng. Ind. Aerodyn.* 157, 76–94. <https://doi.org/10.1016/j.jweia.2016.08.004>
- Gao, G., Zhu, L., 2017. Nonlinear mathematical model of unsteady galloping force on a rectangular 2:1 cylinder. *J. Fluids Struct.* 70, 47–71. <https://doi.org/10.1016/j.jfluidstructs.2017.01.013>
- Ge Y., Liu Z., Yang Y., 2016. Energy conversion mechanism of aerodynamic flutter of a box girder. *Proceedings of the First International Symposium on Flutter and its Application*. Tokyo, Japan.
- Hillier, R., Cherry, N.J., 1981. The effects of stream turbulence on separation bubbles. *J. Wind Eng. Ind. Aerodyn.* 8, 49–58.
- Horitsu, T., 2007. Role of Kármán vortex on aerodynamic performance of bluff body. *Doctoral Thesis*. Kyoto University.
- Hu, G., Tse, K.T., Kwok, K.C.S., 2016. Aerodynamic mechanisms of galloping of an inclined square cylinder. *J. Wind Eng. Ind. Aerodyn.* 148, 6–17. <https://doi.org/10.1016/j.jweia.2015.10.011>
- Kiya, M., Nozawa, T., 1987. Turbulence structure in the leading-edge separation zone of a blunt circular cylinder. *Trans. JSME Ser. B.* 53, 1183–1189.
- Komatsu, S., Kobayashi, H., 1980. Vortex-induced oscillation of bluff cylinders. *J. Wind Eng. Ind. Aerodyn.* 6, 335–362.
- Kwok, K.C.S., Melbourne, W.H., 1977. The effects of freestream turbulence on a galloping square tower. *Proceedings of the 6th Australasian Hydraulics and Fluid Mechanics Conference*, Adelaide, Australia.
- Kwok, K.C.S., Melbourne, W.H., 1980. Freestream turbulence effects on galloping. *J. Eng. Mech. Div.* 106, 273–288.
- Laneville, A., Parkinson, G., 1971. Effects of turbulence on galloping of bluff cylinders. In *Proceedings 3rd International Conference on Wind Effects on Buildings and Structures*, Tokyo, Japan.
- Matsumoto, M., Shiraishi, N., Kitazawa, M., Knisely, C., Shirato, H., Kim, Y., Tsujii, M., 1990. Aerodynamic behavior of inclined circular cylinders-cable aerodynamics. *J. Wind Eng. Ind. Aerodyn.* 33, 63–72.
- Matsumoto, M., 1996. Aerodynamic damping of prisms. *J. Wind Eng. Ind. Aerodyn.* 59, 159–175.
- Matsumoto, M., Daito, Y., Yoshizumi, F., Ichikawa, Y., Yabutani, T., 1997. Torsional flutter of bluff bodies. *J. Wind Eng. Ind. Aerodyn.* 69–71, 871–882.
- Matsumoto, M., Yagi, T., Shigemura, Y., Tsushima, D., 2001. Vortex-induced cable vibration of cable-stayed bridges at high reduced wind velocity. *J. Wind Eng. Ind. Aerodyn.* 89, 633–647.

- Matsumoto, M., Yagi, T., Lee, J., Hori, K., Kawashima, Y., 2006. Karman Vortex Effect on the Aerodynamic Forces to Rectangular Cylinders. Press. Vessel. Pip. Div. Conf. ASME 307–316. <https://doi.org/10.1115/PVP2006-ICPVT-11-93783>
- Matsumoto, M., Yagi, T., Tamaki, H., Tsubota, T., 2008. Vortex-induced vibration and its effect on torsional flutter instability in the case of $B/D = 4$ rectangular cylinder. J. Wind Eng. Ind. Aerodyn. 96(6–7), 971–983.
- Matsumoto, M., Yagi, T., Hatsuda, H., Shima, T., Tanaka, M., Naito, H., 2010. Dry galloping characteristics and its mechanism of inclined/yawed cables. J. Wind Eng. Ind. Aerodyn. 98, 317–327.
- Massai, T., 2016. On the Interaction between vortex-induced vibrations and galloping in rectangular cylinders of low side ratio. Dr.-Ing. Thesis, Technische Universität Braunschweig, Braunschweig, Germany.
- Mannini, C., Marra, A.M., Bartoli, G., 2014. VIV-galloping instability of rectangular cylinders: Review and new experiments. J. Wind Eng. Ind. Aerodyn. 132, 109–124. <https://doi.org/10.1016/j.jweia.2014.06.021>
- Mannini, C., Marra, A.M., Massai, T., Bartoli, G., 2016. Interference of vortex-induced vibration and transverse galloping for a rectangular cylinder. J. Fluids Struct. 66, 403–423. <https://doi.org/10.1016/j.jfluidstructs.2016.08.002>
- Mannini, C., Massai, T., Marra, A.M., 2018a. Unsteady galloping of a rectangular cylinder in turbulent flow. J. Wind Eng. Ind. Aerodyn. 173, 210–226. <https://doi.org/10.1016/j.jweia.2017.11.010>
- Mannini, C., Massai, T., Marra, A.M., 2018b. Modeling the interference of vortex-induced vibration and galloping for a slender rectangular prism. J. Sound Vib. 419, 493–509. <https://doi.org/10.1016/j.jsv.2017.12.016>
- Massai, T., 2016. On the Interaction between vortex-induced vibrations and galloping in rectangular cylinders of low side ratio. Dr.-Ing. Thesis, Technische Universität Braunschweig, Braunschweig, Germany.
- Mizota, T., Okajima, A., 1981. Experimental studies of time mean flows around rectangular prisms. Proc. Japan Soc. Civ. Eng. 312, 39-47(in Japanese).
- Nakaguchi, H., Hashimoto, K., Muto, S., 1968. An experimental study on aerodynamic drag of rectangular cylinders. Trans. Japan. Soc. Aero. Space. Sci. 16, 1–5 (in Japanese).
- Nakamura, Y., Nakashima, M., 1986. Vortex excitation of prisms with elongated rectangular, H and \downarrow cross-sections. J. Fluids Struct. 163, 149–169.
- Nakamura, Y., Hirata, K., Urabe, T., 1991. Galloping of rectangular cylinders in the presence of a splitter plate. J. Fluids Struct. 5(5), 521–549.
- Nakamura, Y., Hirata, K., 1994. The aerodynamic mechanism of galloping. Trans. Jpn. Soc. Aeronaut. Space Sci. 36, 257–269.
- Nakamura, Y., Mizota, T., 1975. Unsteady lifts and wakes of oscillating rectangular prisms. J. Eng. Mechanics Div. 101, 855–871.

- Nakamura, Y., Tomonari, Y., 1977. Galloping of rectangular prisms in a smooth and in a turbulent flow. *J. Sound Vib.* 52, 233–241. [https://doi.org/10.1016/0022-460X\(77\)90642-3](https://doi.org/10.1016/0022-460X(77)90642-3)
- Naudascher, E., Weske, J.R., Fey, B., 1981. Exploratory study on damping of galloping vibrations. *J. Wind Eng. Ind. Aerodyn.* 8, 211–222.
- Naudascher, E., Wang, Y., 1993. Flow-induced vibrations of prismatic bodies and grids of prisms. *J. Fluids Struct.* 7, 341–373.
- Novak, M., 1972. Galloping oscillation of prismatic structures. *J. Eng. Mech. Div.* 98, 27–46.
- Novak, M., Davenport Alan G., 1970. Aeroelastic Instability of Prisms in Turbulent Flow. *J. Eng. Mech. Div.* 96, 17–39.
- Nguyen, D.T., Hargreaves, D.M., Owen, J.S., 2018. Vortex-induced vibration of a 5:1 rectangular cylinder: A comparison of wind tunnel sectional model tests and computational simulations. *J. Wind Eng. Ind. Aerodyn.* 175, 1–16.
- Obasaju, E.D., 1983. Forced-vibration study of the aeroelastic instability of a square-section cylinder near vortex resonance. *J. Wind Eng. Ind. Aerodyn.* 12, 313–327.
- Okajima, A., 1983. Flow around a rectangular cylinder with a section of various width/height ratios. *J. Wind Eng. (JAWE)* 17, 1–19. (in Japanese)
- Otsuki, Y., Washizu, K., Tomizawa, H., Ohya, A., 1974. A note on the aeroelastic instability of a prismatic bar with square section. *J. Sound Vib.* 34, 233–248.
- Otsuki Y., Fujii K., Washizu K., Ohya A., 1978. Wind tunnel experiments on aerodynamic forces and pressure distributions of rectangular cylinders in a uniform flow. *Proceedings of 5th symposium on Wind Effects on Structures*, 169–176.
- Parkinson, G. V., Brooks, N.P.H., 1961. On the Aeroelastic Instability of Bluff Cylinders. *J. Appl. Mech.* 28, 252–258.
- Parkinson, G. V., Smith, J.D., 1964. The square prism as an aeroelastic non-linear oscillator. *Quart. Jonrn. Mech. Appl. Math.* 17(2), 225–239.
- Parkinson, G. V., Sullivan, P.P., 1979. Galloping response of towers. *J. Wind Eng. Ind. Aerodyn.* 4, 253–260.
- Parkinson, G. V., Wawzonek, M.A., 1981. Some considerations of combined effects of galloping and vortex resonance. *J. Wind Eng. Ind. Aerodyn.* 8, 135–143.
- Parkinson, G. V., 1989. Phenomena and modelling of flow-induced vibrations of bluff bodies. *Prog. Aerosp. Sci.* 26, 169–224.
- Sakamoto H., Haniu H., Kobayashi Y., 1989. Fluctuating force acting on rectangular cylinders in uniform flow, *Trans. of JSME Ser. B.*, Tokyo, 55(516), 2310–2317.
- Scanlan, R. H., Tomko, J., 1971. Air foil and bridge deck flutter derivatives. *J. Eng. Mech.* 97(6), 1717–1937.
- Simiu E. and Scanlan R. H., 1996. *Wind Effect on Structures: Fundamentals and Applications to Design*. New York: John Wiley & Sons Inc.

- Shiraishi, N. and Matsumoto M., 1983. On classification of vortex-induced oscillation and its application for bridge structures. *Journal of Wind Engineering and Industrial Aerodynamics* 14(1): 419-430.
- Shimada, K., Meng, Y., 1998. Applicability of modified k-e model on the estimation of aerodynamic properties of rectangular cylinders with various elongated cross sections. *J. Struct. Constr. Eng.* 514, 73–80. (in Japanese)
- Shirakashi, M., Wakiya, S., Hasegawa, A., 1986. Effect of the secondary flow on Karman vortex shedding from a yawed cylinder. *JSME Int. J. Ser. B* 29, 1124–1128.
- Takeuchi, T., Matsumoto, M., 1992. Aerodynamic response characteristics of rectangular cylinders in tandem arrangement. *J. Wind Eng. Ind. Aerodyn.* 41, 565–575. [https://doi.org/10.1016/0167-6105\(92\)90466-N](https://doi.org/10.1016/0167-6105(92)90466-N)
- Tamura, T., Ito, Y., 1996. Aerodynamic characteristics and flow structures around a rectangular cylinder with a section of various depth/breadth ratios. *J. of Struct. Constr. Eng. (Trans. of AIJ)* 486, 153-162.
- Washizu, K., Ohya, A., Otsuki, Y., Fujii, K., 1978. Aeroelastic instability of rectangular cylinders in a heaving mode. *J. Sound Vib.* 59, 195–210.
- Wu, T., Kareem, A., 2012. An overview of vortex-induced vibration (VIV) of bridge decks. *Front. Archit. Civ. Eng.* 6, 335–347.
- Yagi, T., Shinjo, K., Narita, S., Nakase, T., Shirato, H., 2013. Interferences of vortex sheddings in galloping instability of rectangular cylinders. *Journal of Structural Engineering. A (JSCE)*. **59A**, 552–561 (in Japanese).
- Yang, Y., Ge, Y., Xiang, H., 2007. Investigation on flutter mechanism of long-span bridges with 2d-3DOF method. *Wind Struct. An Int. J.* 10, 421–435.

3 Aerodynamic performance of single box girders with side-surface openings

3.1 Introduction

This chapter presents the experimental investigation on the aerodynamic performance of the single box girders with side-surface openings. Two butterfly web girders with side ratios B/D $B/D= 3.24$ and 5 , where B is the girder width and D is the depth, are evaluated through a series of wind tunnel tests. By covering the side-surface openings of the butterfly web girders, two conventional box girders serve as the control group. The aerodynamic performance of a conventional box girder can generally be characterized as that of a rectangular cylinder of the same B/D ratio. Therefore, as explained in section 2.2, a $B/D = 3.24$ box girder may show the motion-induced vortex vibration, the galloping instability at a certain angle of attack, and torsional flutter, whereas at $B/D= 5$, the box girder may show the motion-induced vortex vibration and torsional flutter. However, the flow can get through the side-surface openings into the inner space and then into the wake of the box girder, potentially affecting the flow field around the body. According to past researches (Koutmos et. al., 2004; Huang et al., 2010 and 2017), the jet flow from the rear surface of the square cylinder can disturb the flow entrainment in the near wake or shoot far downstream, affecting the time-averaged flow around the body. These effects on the flow field related to the rear jet flow, which is similar to the outflow from the downstream side-surface openings, indicate the potentially complicated disturbances that the side-surface openings may bring to the unsteady flow and the time-averaged flow. Therefore, it is difficult to assume the effects of side-surface openings on aerodynamic performance. Furthermore, the Kármán-vortex shedding is confirmed to be suppressed owing to the side-surface openings by controlling the fluctuating lift force coefficient of a square cylinder (Nakato, 2016). According to section 2.3.4, the suppression of the Kármán-vortex shedding may result in more galloping instability. Therefore, it is of most concern to understand the effects of side-surface openings on the galloping instability. In summary, it is necessary to investigate the effects of side-surface openings on these aerodynamic phenomena, i.e., motion-vortex induced vibration, galloping, and torsional flutter, through a series of wind tunnel tests.

In this chapter, the details of the wind tunnel tests conducted on the models are illustrated at first. Then the effects of the side-surface openings on the aerodynamic performance of the $B/D = 3.24$ box girder are evaluated, including the vortex-induced vibration, the torsional flutter, and the galloping. The wind velocity vectors in the wake and inner space of the $B/D = 3.24$ models are described to explain the reason for the effects of the side-surface openings on the galloping instability. As the strong dependence of the torsional flutter on the side ratio, the effects of the side-surface openings on the torsional flutter and vortex-induced vibration are further evaluated by a $B/D = 5$ butterfly web girder.

3.2 Wind tunnel test details

A series of wind tunnel tests was carried out for two butterfly web girders: one is with a side ratio of 3.24 and the other one is with a side ratio of 5. The wind tunnel tests include free vibration tests, aerodynamic force tests, forced vibration tests. These wind tunnel tests aimed to evaluate the role of the side-surface openings on the aerodynamic performance. The details of the wind tunnel tests are addressed as follows.

3.2.1 Model details

Two butterfly web girder sectional models were adopted in this research, one with a 1:80 geometrical scale and a B/D ratio of 3.24, and the other with a 1:100 geometrical scale and a B/D ratio of 5. The cross sections and side-surface openings of each model are shown in Fig. 3-1 and Fig. 3-2, respectively. The width (B) and depth (D) of the model with a B/D ratio of 3.24 were 161.9 mm and 50 mm, respectively, and those of the $B/D = 5$ model were 300 mm and 60 mm, respectively. The Opening-area Ratio is defined by the ratio between the opening area and half the total area of the front/rear surface. The Opening-area Ratio is 30% for the $B/D = 3.24$ model and 33% for the $B/D = 5$ model. For the convenience of discussion, a butterfly web girder is defined as an open girder, and a conventional box girder of the same shape as the butterfly web girder is defined as a closed girder. A conventional box girder can be realized by covering the side-surface openings of a butterfly web girder with an acrylic plate. To understand this better, open girders with $B/D = 3.24$ and 5 are shown in Fig. 3-3 (a)-(b), respectively, and closed girders with $B/D = 3.24$ and 5 are shown in Fig. 3-3 (c)-(d), respectively. Additionally, as shown in Fig. 3-4, at a certain angle of attack (α) due to the mean wind, the model has an equivalent length (B') and depth (D').

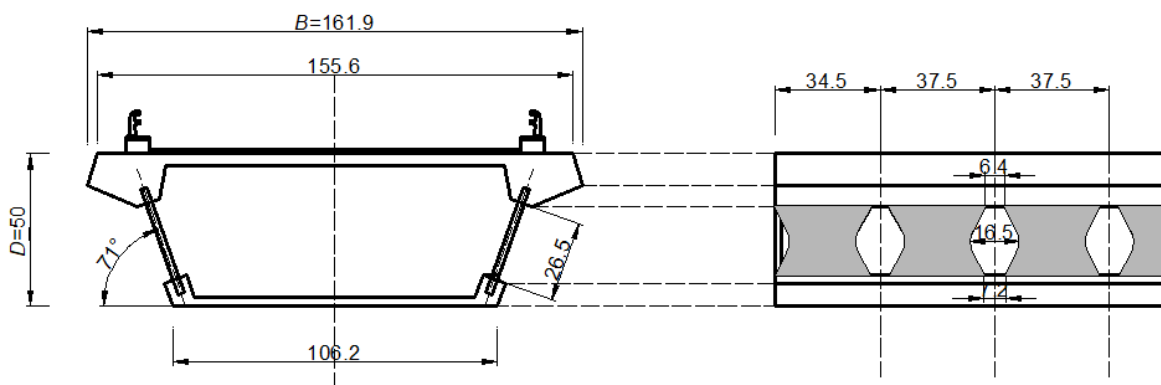


Fig. 3-1 Section of the $B/D = 3.24$ side ratio model and side-surface opening detail (unit: mm).

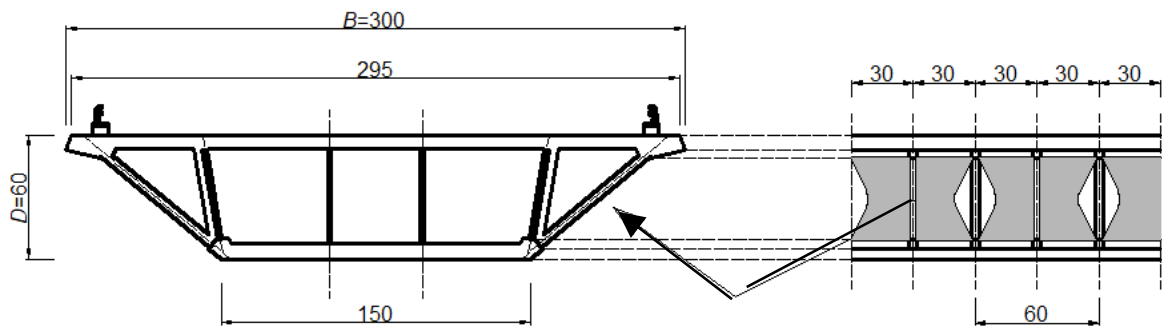
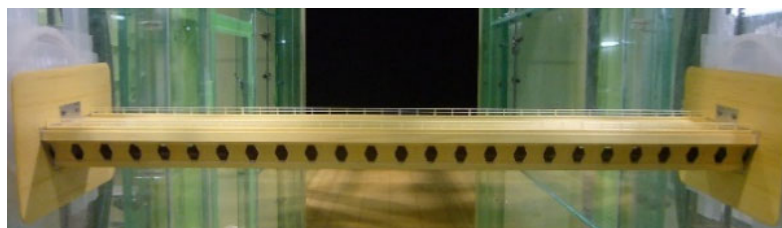


Fig. 3-2 Section of the $B/D = 5$ model and side-surface opening detail (unit: mm).



(a)



(b)



(c)



(d)

Fig. 3-3 Models used in the experiment: (a) open girder ($B/D = 3.24$); (b) open girder ($B/D = 5$); (c) closed girder ($B/D = 3.24$, side-surface openings covered); (d) closed girder ($B/D = 5$, side-surface openings covered).

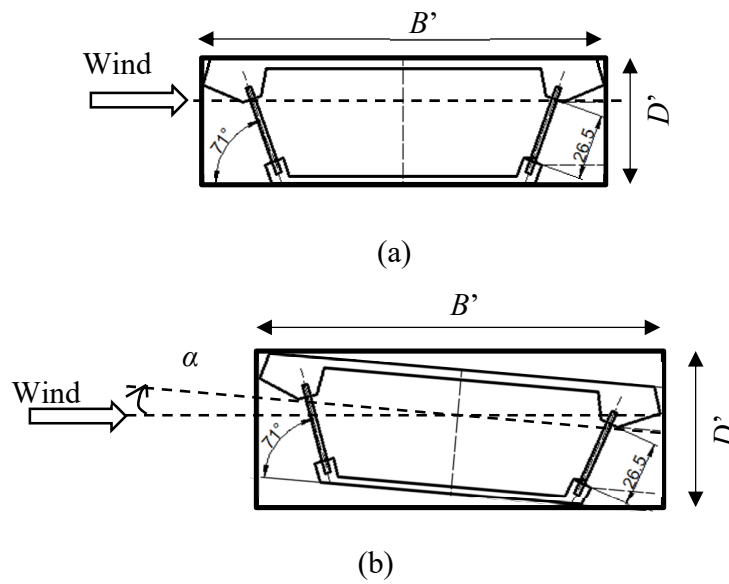


Fig. 3-4 Equivalent size of the model. (a) shows the case at $\alpha = 0^\circ$. (b) shows the case at $\alpha = +3^\circ$. α is the angle of attack due to mean wind.

3.2.2 Free vibration tests

As explained in section 3.1, both the $B/D = 5$ and $B/D = 3.24$ models must show the torsional flutter. The $B/D = 3.24$ model may show galloping at a certain angle of attack. A vertical one degree of freedom (1DOF) free vibration test was conducted for the $B/D = 3.24$ model, and vertical 1DOF and torsional 1DOF free vibration tests were conducted for the $B/D = 5$ model. Supported by eight coil springs, the displacement of the girder in smooth flow was measured at $\alpha = 0^\circ$, -3° , and $+3^\circ$. Low values were assigned to the mass and damping of the system to facilitate observation of the effects of the side-surface openings on the aerodynamic properties (Table 3-1, Table 3-2 and Table 3-3).

Table 3-1 Characteristic parameters for the model (side ratio $B/D = 3.24$) used in free vibration experiments; the model has one vertical degree of freedom (1DOF) and the experiment is in smooth flow.

Case name	Angle of attack	m (kg/m)	f (Hz)	δ_η	Sc_η
Closed girder	-3°	2.40	4.56	0.0028	4.5
	0°	2.40	4.57	0.0027	4.4
	$+3^\circ$	2.40	4.55	0.0026	4.2
Open girder	-3°	2.36	4.60	0.0028	4.5
	0°	2.36	4.52	0.0029	4.5
	$+3^\circ$	2.36	4.60	0.0029	4.5

Table 3-2 Characteristic parameters for the model ($B/D = 5$) used in free vibration experiments (torsional 1DOF, smooth flow).

Case name	Angle of attack	I (kg·m)	f (Hz)	δ_φ	Sc_φ
Closed girder	-3°	4.64×10^{-2}	6.41	0.0069	43
	0°	4.65×10^{-2}	6.41	0.0056	35
	$+3^\circ$	4.63×10^{-2}	6.41	0.0063	39
Open girder	-3°	4.63×10^{-2}	6.45	0.0068	42
	0°	4.64×10^{-2}	6.42	0.0057	36
	$+3^\circ$	4.56×10^{-2}	6.45	0.0073	45

Table 3-3 Characteristic parameters for the model ($B/D = 5$) used in free vibration experiments (vertical 1DOF, smooth flow).

Case name	Angle of attack	m (kg/m)	f (Hz)	δ_η	Sc_η
Closed girder	-3°	6.48	2.23	0.0027	8.5
	0°	6.49	2.23	0.0028	8.6
	$+3^\circ$	6.47	2.23	0.0027	8.5
Open girder	-3°	6.40	2.25	0.0027	8.4
	0°	6.40	2.25	0.0027	8.4
	$+3^\circ$	6.40	2.25	0.0027	8.4

3.2.3 Aerodynamic force tests on stationary girder

The aerodynamic forces were measured through the load cell rigidly connected to the model in the smooth flow. The aerodynamic forces were measured at $\alpha = -10^\circ \sim 10^\circ$, where α is the angle of attack to mean wind and is positive in nose-up direction (Fig. 2-17). The lift (C_{Fy}) and drag (C_{Fx}) force coefficients, fluctuating lift force coefficient (C_{Fy}') and Strouhal number (St) were measured. The tests were carried out in the smooth flow and the approaching wind velocity was 6m/s.

3.2.4 Forced vibration tests

The vertical and torsional 1DOF forced vibration tests were conducted for the $B/D = 3.24$ model at $\alpha = 0^\circ$ and $+3^\circ$, and the torsional 1DOF vibration tests were conducted for the $B/D = 5$ model at $\alpha = 0^\circ$ and $+3^\circ$. To improve the accuracy of the flutter derivatives, the amplitude of the forced vibration cannot be too small to obtain large aerodynamic self-excited forces. Therefore, the vertical amplitude and frequency were set to 10mm and 2Hz, respectively, and the torsional amplitude and frequency were set to 2° and 2.6Hz, respectively.

3.3 Aerodynamic performance of a butterfly web girder with side ratio $B/D = 3.24$

3.3.1 Aerodynamic forces

The lift (C_{Fy}), drag (C_{Fx}), and pitching moment (C_M) coefficients are presented in the structural axis in Fig. 3-5 (a), (b), and (c), respectively. These coefficients showed the same trend in the closed and open girders. However, the absolute values of the coefficients of the open girder were smaller than those of the closed girder for each angle of attack. These results indicate that the side-surface openings can reduce the lift, drag, and pitching moment. According to Fig. 3-5 (a), the closed girder showed a negative gradient in the lift coefficient (C_{Fy}) at $1^\circ \leq \alpha \leq 4^\circ$, whereas the open girder had a negative slope at $2^\circ \leq \alpha \leq 4^\circ$. Because a negative gradient of the lift force indicates galloping instability, both the closed and open girders might show galloping instability at $\alpha = +3^\circ$. This is because, with the change of α from 0° to $+3^\circ$, the equivalent side ratio B'/D' decreased from 3.24 to 2.6. Meanwhile, the flow pattern around the girder changed from a reattachment type to a detachment type, which makes the model prone to galloping instability at $\alpha = +3^\circ$. Therefore, the discussion on the side-surface opening effects focuses mainly on the results of the free vibration and forced vibration tests at $\alpha = +3^\circ$.

The Kármán vortex generates a large drag force coefficient and increases the curvature of a substantially separated flow (Bearman and Trueman, 1972; Matsumoto et al., 2006). Consequently, the smaller drag force coefficient of the open girder indicates the suppression of Kármán vortex shedding. As presented in Table 3-4, the Strouhal number of the closed girder and open girder was almost the same, indicating that the Strouhal number was not affected by the side-surface openings with an opening-area ratio 30%. Meanwhile, the fluctuating lift force coefficients of the open girder were smaller than those of the closed girder (Fig. 3-6), confirming that Kármán vortex shedding was suppressed owing to the side-surface openings.

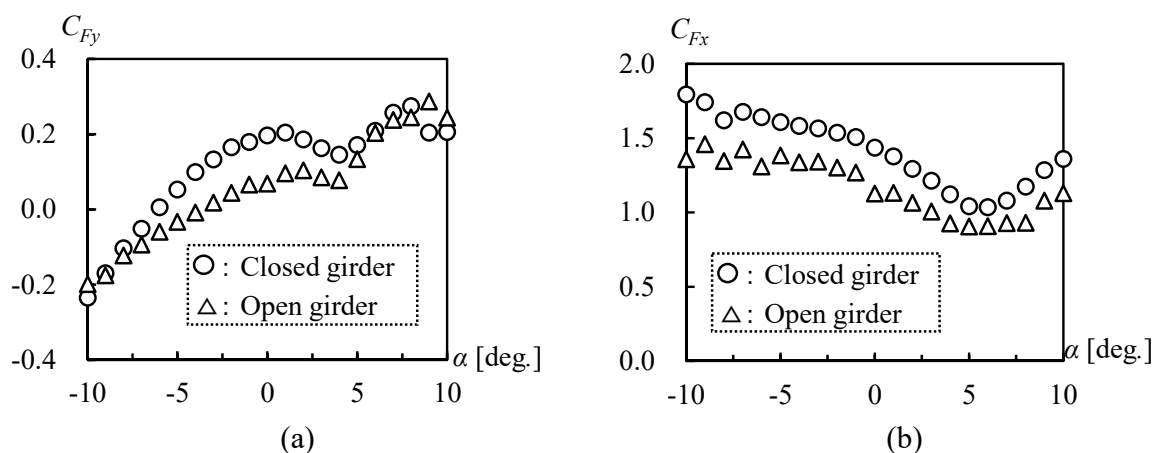


Fig. 3-5 Aerodynamic force coefficients ($B/D = 3.24$ model, $U = 6$ m/s, smooth flow) for (a) lift force C_{Fy} ; (b) drag force C_{Fx} ; (c) pitching moment C_M .

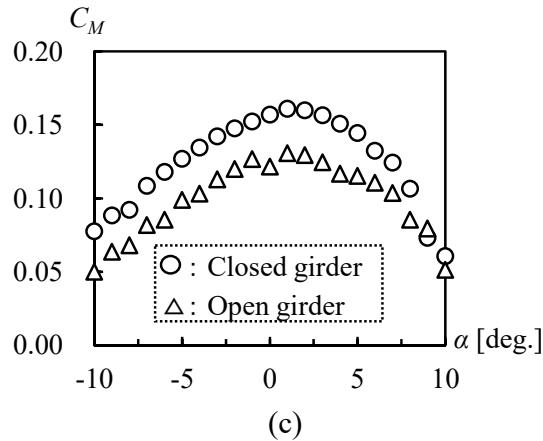


Fig. 3-5 Continued

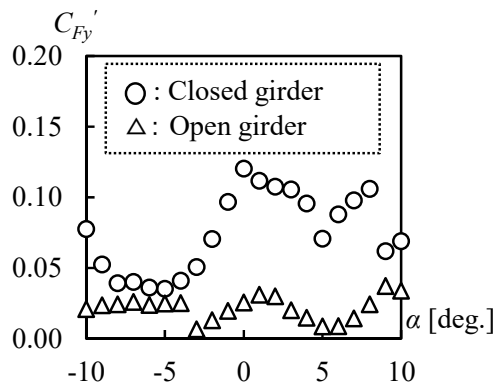


Fig. 3-6 Fluctuating lift force coefficient C_{Fy}' ($B/D = 3.24$ model, $U = 6$ m/s, smooth flow).

Table 3-4 Strouhal number identified from fluctuating lift force ($B/D = 3.24$ model, $U = 6$ m/s, smooth flow, $\alpha = 0^\circ$).

	Closed girder	Open girder
Strouhal number	0.167	0.164

3.3.2 Vertical 1DOF aerodynamic performance

The vertical aerodynamic responses of the closed and open girders at $\alpha = +3^\circ$ are shown in Fig. 3-7. For convenient comparison of the free vibration and forced vibration test results, the double magnitude of the forced vibration is also included in the figure. U is the horizontal velocity of wind approaching the wind tunnel. The Scruton number was set to a small value for easier observation of the aerodynamic response (see Table 3-1). The symbol of two points connected by the vertical line indicates “limit cycle oscillation”. For the closed girder, vortex-induced vibration with the largest reduced double amplitude (0.42) occurred at a reduced wind velocity range ($4 < Ur < 6$) and galloping occurred at $Ur > 47$ (Fig. 3-7). The maximum reduced double amplitude of the

vortex-induced vibration was 0.24, and galloping did not occur at $Ur < 70$ for the open girder (Fig. 3-7). Regarding vortex-induced vibration, the $1/St$ values for the closed and open girders were 5.78 ($St = 0.173$) and 5.99 ($St = 0.167$), respectively, which are slightly larger than $1.67B/D (= 5.41)$. Thus, the reduced critical wind velocity of the Kármán vortex vibration ($1/St$) was slightly larger than that of the motion-induced vortex vibration. Therefore, it is concluded that the vortex-induced vibration of the $B/D = 3.24$ model was of the motion-induced type.

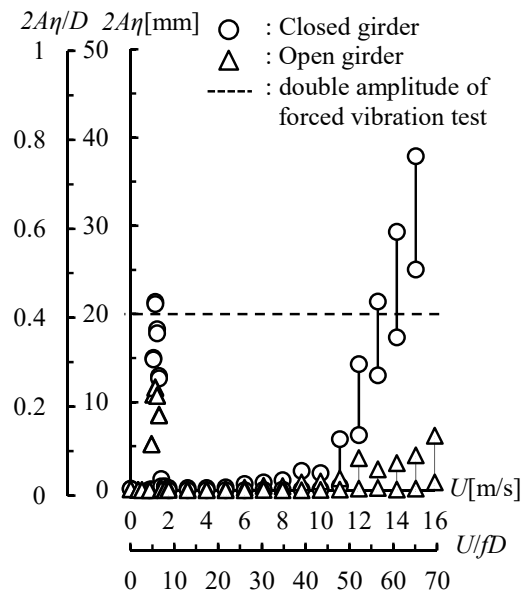


Fig. 3-7 Aerodynamic response of the $B/D = 3.24$ model ($B'/D' = 2.6$, vertical one degree of freedom (1DOF), $\alpha = +3^\circ$, smooth flow).

To discuss the effects of side-surface openings on the critical wind velocity of galloping and aerodynamic damping further, the aerodynamic derivative H_1^* values of the closed and open girders at $\alpha = +3^\circ$ are shown in Fig. 3-8. The reduced critical wind velocity of galloping was approximately $Ur = 60$ for the closed girder and approximately $Ur = 80$ for the open girder. These results demonstrate that galloping occurred in the open girder within the higher wind velocity range. The double magnitude of the vertical response of the closed girder reached 20 mm (the double amplitude of the forced vibration) at approximately $Ur = 60$ (Fig. 3-7), which was close to the reduced critical wind velocity of galloping ($Ur = 60$) observed in Fig. 3-8. Therefore, the critical wind velocity of galloping determined from the free vibration tests corresponded very well to that from the forced vibration tests, considering the aerodynamic damping corresponding to a double amplitude of 20 mm. The H_1^* values for the closed girder obtained from the forced vibration test results were larger than those for the open girder in the high wind velocity range. These results indicate that the open girder was more stable than the closed girder at high wind velocities.

Therefore, the side-surface openings can mitigate the motion-induced vortex vibration and stabilize the galloping. However, despite the suppression of Kármán vortex shedding,

demonstrated by the fluctuating lift force coefficient, the open girder still showed better galloping stability than the closed girder. To further discuss the effects of side-surface openings, the flow field around and within the bridge deck will be investigated in the next section.

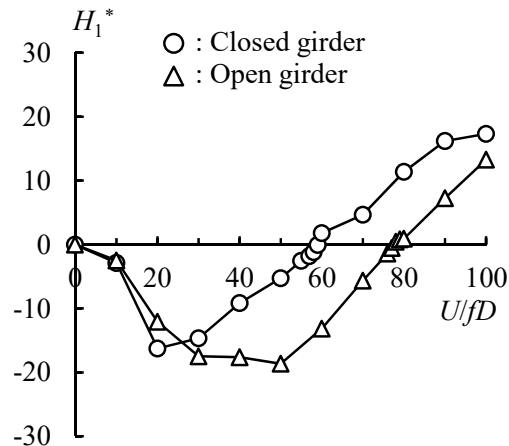


Fig. 3-8 Aerodynamic derivative H_1^* of the $B/D = 3.24$ model ($B'/D' = 2.6$, vertical 1DOF, $\alpha = +3^\circ$, $f = 2.0$ Hz, $2A\eta = 20$ mm, smooth flow).

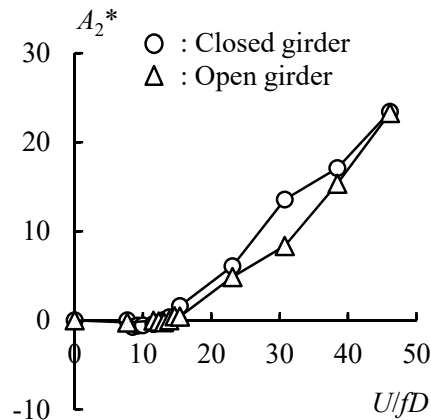


Fig. 3-9 Aerodynamic derivative A_2^* of the $B/D = 3.24$ model ($B'/D' = 2.6$, torsional 1DOF, $\alpha = +3^\circ$, $f = 2.6$ Hz, $2A\phi = 4^\circ$, smooth flow).

3.3.3 Torsional 1DOF aerodynamic performance

The same mechanism is responsible for motion-induced vortex vibration in both the vertical and torsional directions. Thus, for the torsional direction, only the effects of side-surface openings on flutter instability are discussed, based on the forced vibration result. Fig. 3-9 and Fig. 3-10 show A_2^* of the closed and open girder at $\alpha = +3^\circ$ and 0° . With the change in α from $+3^\circ$ to 0° , A_2^* was shown in the order that the equivalent side ratio B'/D' increases from 2.6 to 3.24. According to Fig. 3-9, at $\alpha = +3^\circ$, A_2^* of the closed girder has a positive value at $Ur > 12$, whereas that of the

open girder is positive at $Ur > 14$. The A_2^* value of the closed girder is almost the same as that of the open girder. According to Fig. 3-10, at $\alpha = 0^\circ$, A_2^* of the closed girder also showed almost the same value as that of the open girder. By comparing Fig. 3-9 and Fig. 3-10, with the change in α from $+3^\circ$ to 0° , A_2^* of the closed/open girder obviously decreased. The decrease in A_2^* is related to the increase in the equivalent side ratio B'/D' from 2.6 to 3.24. This will be discussed later by comparing these results with the results of the $B/D = 5$ model. In summary, the side-surface openings do not have obvious effects on the critical wind velocity of the torsional flutter and aerodynamic damping in the torsional direction.

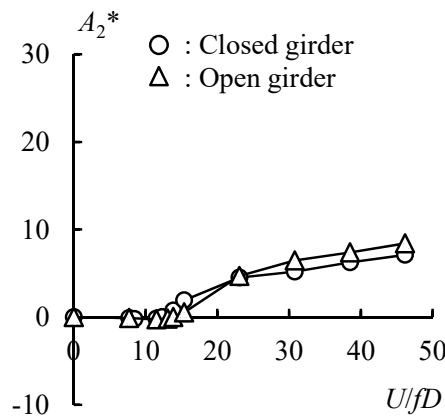


Fig. 3-10 Aerodynamic derivative A_2^* of the $B/D = 3.24$ model ($B'/D' = 3.24$, torsional 1DOF, $\alpha = 0^\circ$, $f = 2.6$ Hz, $2A\phi = 4^\circ$, smooth flow).

3.4 Flow field characteristics in the wake and inner space of the $B/D = 3.24$ girder

As discussed in the previous section, the side-surface openings contributed to the suppression of Kármán vortex shedding. As explained in section 2.3.4, the suppression of Kármán-vortex shedding can lead to galloping instability (Yagi, et. al., 2013; Nakamura et al., 1991 and 1994; Horitsu, 2007; Matsumoto et al., 1990, 2001, 2008, 2010). However, side-surface openings can still stabilize the galloping. To clarify the mechanism of the side-surface opening effects on aerodynamic performance, wind velocity measurements in the wake and inner space of the $B/D = 3.24$ model were conducted.

3.4.1 Wind velocity measurement around the girder

The wind velocity distributions in the wake of the $B/D = 3.24$ girders with and without side-surface openings were measured using an 'X' hot-wire anemometer; the wind velocity within the butterfly web girder was also measured. The measurement was performed with a sampling frequency of 1000Hz. An 'X' hot-wire anemometer provided the X - and Y -direction components of wind velocity. The measurement points and parameter definitions are shown in Fig. 3-11, where the origin of the coordinates is the center of the span and girder section, X/B and Y/D are non-

dimensional coordinates in the main flow and vertical direction, respectively, and Z is the center distance in the span-wise direction. Because the center of the opening at the middle span coincides with the span center of the model (Fig. 3-3 (a)), the wind velocity distribution in the wake and inner space of the open girder was measured in the vertical plane (X - Y plane) at the span center ($Z = 0$). Meanwhile, the wind velocity distribution in the wake of the closed girder was also measured in the vertical plane (X - Y plane) at the span center ($Z = 0$). Because the center of the opening coincides with the span center, for both the closed girder and open girder, the mean wind velocity distribution in the wake was measured in the vertical plane (X - Y plane) at the span center of the model ($Z = 0$) (Fig. 3-11). By comparing the mean wind velocity vectors in the wakes of the closed and open girders, the effects of side-surface openings on the time-averaged streamline were examined.

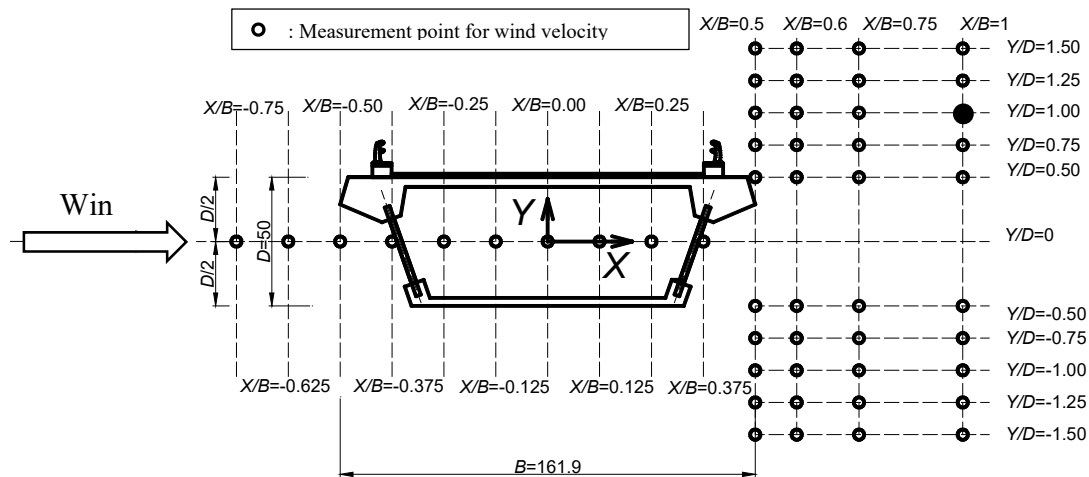


Fig. 3-11 Measurement points ($B/D = 3.24$ model) in the X - Y plane (unit: mm).

3.4.2 Time-averaged flow in the girder wake and side-surface openings

Fig. 3-12 shows the distributions of mean wind velocity vectors in the wakes of the closed and open girders along the Y -direction at $X/B = 0.50, 0.60, 0.75,$ and 1.00 . The approaching wind velocity vector of 6 m/s is also included in the plot, which has the same scale as the mean wind velocity vectors in the wake. The mean wind velocity vectors in the wake of the closed girder were generally different in magnitude and/or direction from those of the open girder. More specifically, the vectors of the closed girder at $|Y/D| \geq 0.5$ and $0.5 \leq X/B \leq 1$ exhibited larger angles between the vector and the X -direction than those at the opening center of the open girder. This indicates that the side-surface openings reduced the curvature of the time-averaged streamline in the wake.

The curvature of the time-averaged streamline in the wake was reduced by the side-surface openings. The curvature of the time-averaged streamline in the wake of the rectangular cylinder was reduced by increasing the side ratio (Nakaguchi, 1968). The side-surface openings likely

reduced the curvature of the time-averaged streamline in the wake in a similar way to the reduction in curvature due to the increase in side ratio. As illustrated in section 2.3.3, by increasing the side ratio, it enhances the reattachment of the time-averaged flow field on the side surface (Nakaguchi, 1968). Therefore, the small curvature of the time-averaged streamline in the wake due to the side-surface openings indicates that they equivalently increase the side ratio and enhance the reattachment of the separated shear layer on the model side surface. Owing to the reattachment of the time-averaged shear layer on the surface, the critical wind velocity of the galloping can be increased (Bearman and Tureman, 1972; Mizota and Okajima, 1981; Kwok and Melbourne, 1977; Nakamura et al., 1991). Consequently, by enhancing the reattachment of the separated shear layer on the side surface for the $B/D = 3.24$ model at $\alpha = +3^\circ$, the side-surface opening stabilized the galloping.

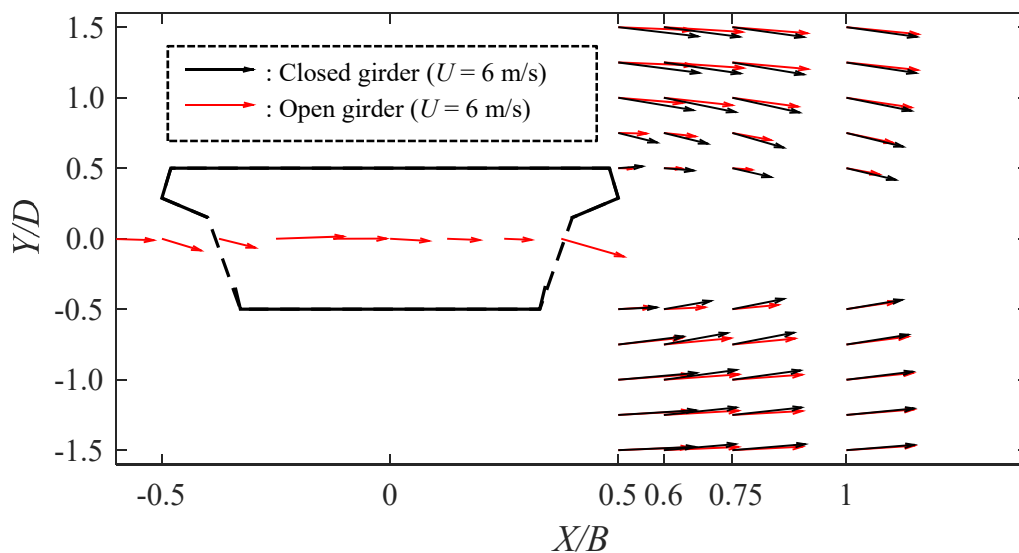


Fig. 3-12 Mean wind velocity vector distribution in the wake of the $B/D = 3.24$ model ($\alpha = 0^\circ$, $U = 6$ m/s, smooth flow). The black arrow represents the wind velocity vector of the closed girder. The red arrow represents the wind velocity vector of the open girder.

As shown in Fig. 3-12, at high wind velocities, the flow reaches the inner space of the girder and bursts out from the downstream-side-surface opening. Because the flow from the downstream opening can disturb the fluid entrainment in the wake and the formation of the reversed flow (Bearman and Trueman, 1972; Laneville and Yong, 1983; Deniz and Staubli 1997), the smaller curvature of the time-averaged streamline around an open girder may be related to the outflow from downstream openings.

With internal distance, the side-surface openings are discretely distributed along the span-wise direction. Therefore, the outflow from the side-surface openings may cause the flow field around the girder to change along the span-wise direction, exhibiting three-dimensional characteristics.

This is consistent with the low correlation of the fluctuating wind velocity in the wake of a stationary and oscillating square cylinder with side-surface openings observed in the previous studies (Nakato, 2016). Because the reduction in the correlation of wind velocity may lead to a decrease in the correlation of forces working on the model along the span, the three-dimensional effects of the flow field may be another reason for the stabilization of vibration owing to the side-surface openings.

In summary, potentially affected by the outflow from the side-surface opening in the wake, the time-averaged flow field around the girder is changed owing to the side-surface openings.

3.5 Aerodynamic performance of a butterfly web girder with side ratio $B/D = 5$

As discussed previously, the galloping instability and motion-induced vortex vibration of the $B/D = 3.24$ model were stabilized by the side-surface openings. However, the side-surface openings exhibited no significant effects on torsional flutter instability in the $B/D = 3.24$ model. Therefore, the effects of side-surface openings on the aerodynamic performance of the slenderer girder ($B/D = 5$) are discussed in this section. The aerodynamic force of the stationary $B/D = 5$ model was not observed to fluctuate in a frequency of vortex shedding owing to the flow field of the reattachment type. Because of the flow pattern of the reattachment type, the $B/D = 5$ model should experience torsional flutter instability rather than galloping instability. Therefore, vertical 1DOF and torsional 1DOF free vibration tests, and torsional 1DOF forced vibration tests are conducted for the $B/D = 5$ model. The results of the torsional 1DOF free vibration tests and forced vibration tests are shown in the order that the equivalent side ratio of the $B/D = 5$ model increased from $B'/D' = 4.1$ to $B'/D' = 5$ with the change of α from $+3^\circ$ to 0° .

A previous study (Matsumoto et al. 2006) demonstrated that the reduced critical wind velocity of the Kármán vortex vibration ($1/St$) was slightly larger than that of the motion-induced vortex vibration (vertical direction $1.67B/D$ and torsional direction $2/3 \times 1.67B/D$) for a $B/D = 5$ rectangular cylinder. In such a case, the vortex-induced vibration is of the motion-induced type. The vortex-induced vibration of the $B/D = 5$ model, which is a rectangular cylinder-like structure, is therefore of the motion-induced type.

3.5.1 Torsional 1DOF aerodynamic performance

The results of the torsional 1DOF free and forced vibration tests at $\alpha = +3^\circ$ are shown in Fig. 3-13 and Fig. 3-14, respectively. The $B/D = 5$ model at $\alpha = +3^\circ$ has an equivalent side ratio of $B'/D' = 4.1$. The horizontal axis U in Fig. 3-13 is the approaching wind velocity in the wind tunnel. The Scruton number was set to a small value for the 1DOF torsional free vibration system (Table 3-2). The symbol of two points connected by the vertical line indicates “limit cycle oscillation”. As shown in Fig. 3-13, the vortex-induced vibration for both the closed and open girder occurred at approximately $Ur = 5$, which is close to $2/3 \times 1.67B/D$ (Eq. (2)), confirming that the vortex-induced vibration is of the motion-induced type. The largest double amplitude of the torsional

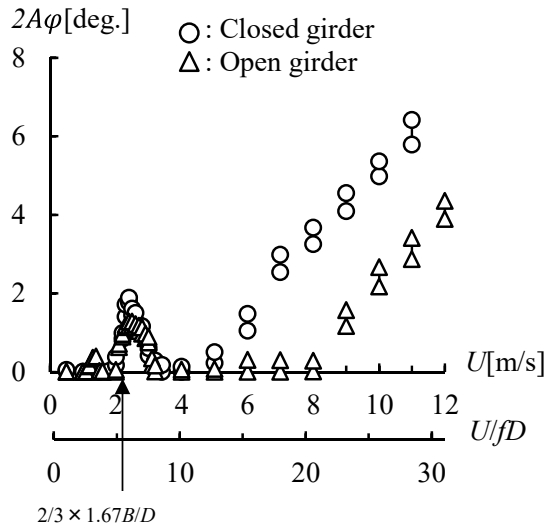


Fig. 3-13 Aerodynamic response of the $B/D = 5$ model ($B^*/D' = 4.1$, torsional 1DOF, $\alpha = +3^\circ$, smooth flow).

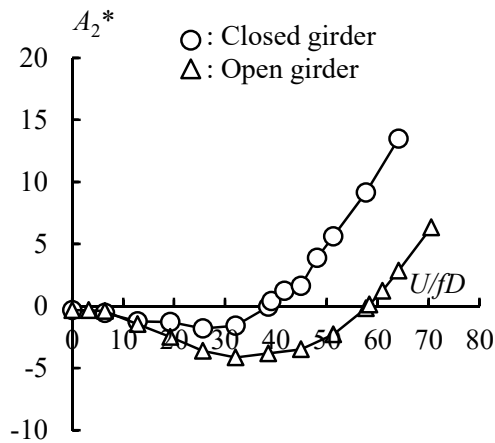


Fig. 3-14 Aerodynamic derivative A_2^* of the $B/D = 5$ model ($B^*/D' = 4.1$, torsional 1DOF, $\alpha = +3^\circ$, $f = 2.6$ Hz, $2A\phi = 4^\circ$, smooth flow).

motion-induced vortex vibration for the closed girder was 2.1° , and that of the open girder was 1.7° . The reduced critical wind velocity of torsional flutter was 10 for the closed girder and 20 for the open girder. According to Fig. 3-14, based on A_2^* , torsional flutter instability was evident in the closed girder at $Ur > 40$ and in the open girder at $Ur > 60$. However, according to Fig. 3-13, the double amplitude of the vibration reached 4° at $Ur = 23$ in the closed girder, which was the double amplitude of the forced vibration, and this value ($Ur = 23$) was far smaller than that ($Ur = 40$) of the forced vibration (Fig. 3-14). In the open girder, the cross point of the double amplitude of the vibration and 4° occurred at $Ur = 32$ (Fig. 3-13), which was far smaller than that ($Ur = 60$) observed in the forced vibration test (Fig. 3-14). This result indicates that at $\alpha = +3^\circ$, the results of the free vibration and forced vibration tests did not correspond well. However, the results of these

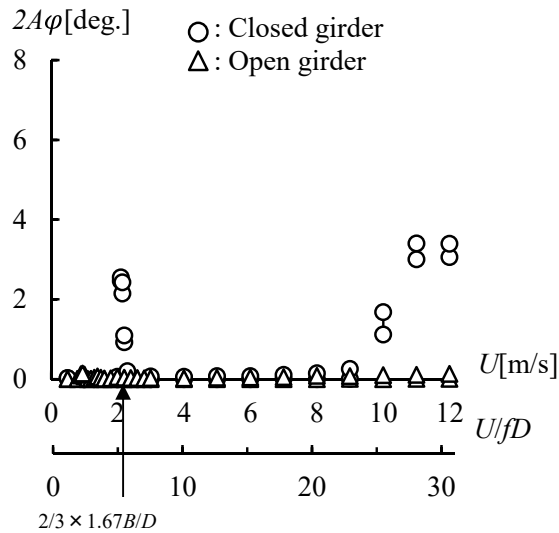


Fig. 3-15 Aerodynamic response of the $B/D = 5$ model ($B'/D' = 5$, torsional 1DOF, $\alpha = 0^\circ$, smooth flow).

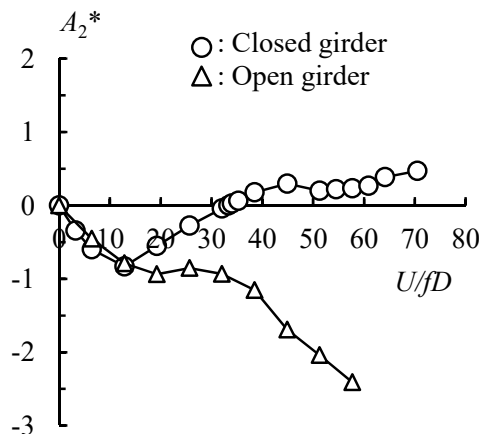


Fig. 3-16 Aerodynamic derivative A_2^* of the $B/D = 5$ model ($B'/D' = 5$, torsional 1DOF, $\alpha = 0^\circ$, $f = 2.6$ Hz, $2A\phi = 4^\circ$, smooth flow).

tests still demonstrate qualitatively that the side-surface openings can stabilize the motion-induced vortex vibration and torsional flutter.

The torsional vibration responses and aerodynamic derivative A_2^* of the closed and open girders at $\alpha = 0^\circ$ are shown in Fig. 3-15 and Fig. 3-16. The $B/D = 5$ model at $\alpha = 0^\circ$ has an equivalent side ratio of $B'/D' = 5$. According to Fig. 3-15, the vortex-induced vibration for both the closed and open girder occurred at approximately $Ur = 5$, which is close to $2/3 \times 1.67B/D$ (Eq. (2)). This also confirmed that the vortex-induced vibration is of the motion-induced type. The double amplitude of the torsional motion-induced vortex vibration for the closed girder at $\alpha = 0^\circ$ was 2.4° , and that for the open girder was almost 0° (Fig. 3-15). These results confirmed that the side-surface openings diminished the torsional motion-induced vortex vibration. Additionally, the closed girder

exhibited torsional flutter instability at $Ur > 23$ and the open girder did not show torsional flutter instability until $Ur = 32$. Thus, the torsional flutter was mitigated by the side-surface openings. This finding was further confirmed by the aerodynamic derivative A_2^* (Fig. 3-16), whose positive value indicates aerodynamic instability. The closed girder showed torsional flutter instability at $Ur > 32$ and the open girder did not show torsional flutter until $Ur = 60$ (Fig. 3-16). Moreover, as shown in Fig. 3-15, the double amplitude of torsional vibration of the closed girder was less than 4° until $Ur = 32$, which is the double amplitude of the forced vibration. Because the double amplitude of the aerodynamic response at $Ur = 32$ was close to 4° (Fig. 3-15), the critical wind velocity of torsional flutter in the free vibration test was close to that of forced vibration ($Ur = 32$) considering the aerodynamic damping corresponding to a double amplitude of 4° (Fig. 3-16). Therefore, the reduced critical wind velocity of torsional flutter in the free vibration test corresponds well with that of the forced vibration test.

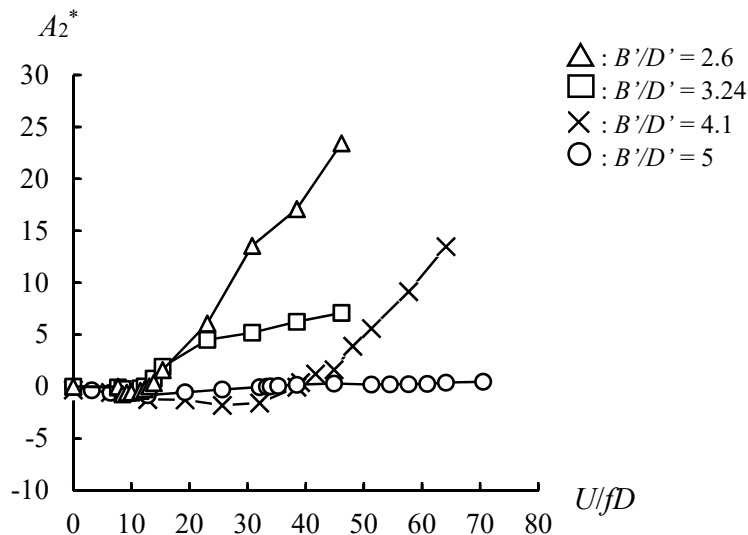


Fig. 3-17 Relationship between A_2^* of closed girder and equivalent side ratio B'/D' .

Comparing Fig. 3-9, Fig. 3-10, Fig. 3-14 and Fig. 3-16 shows that the side-surface openings had no effects on the torsional flutter for the $B/D = 3.24$ model at $\alpha = +3^\circ$ and 0° , but increased the reduced critical wind velocity of the torsional flutter from $Ur = 60$ to $Ur = 80$ for the $B/D = 5$ model at $\alpha = +3^\circ$, and totally mitigated the torsional flutter for the $B/D = 5$ model at $\alpha = 0^\circ$. In terms of this difference in the effects of the side-surface openings on torsional flutter between these two models, the model configuration may play an important role. As mentioned before, the opening area ratio is 15.5% for the $B/D = 3.24$ model and 16.7% for the $B/D = 5$ model. Therefore, rather than the opening area ratio, the equivalent side ratio B'/D' of the model probably plays the main role. By comparing Fig. 3-9, Fig. 3-10, Fig. 3-14 and Fig. 3-16, the torsional flutter of the model with equivalent side ratio $B'/D' = 2.6$ and 3.24 was characterized by the relatively large A_2^* ,

while the torsional flutter of the model with equivalent side ratio $B'/D' = 4.1$ and 5 was characterized by the relatively small A_2^* . Therefore, A_2^* of the closed girder gradually decreased with the increase in equivalent side ratio from $B'/D' = 2.6$ to $B'/D' = 5$ (Fig. 3-17). Meanwhile, as shown in Fig. 3-18, A_2^* decreased with the increase in side ratio from 3 to 10 for the rectangular cylinder. Similar to decrease in A_2^* with the increase in side ratio for the rectangular cylinder, A_2^* of these two models decreased owing to the increase in equivalent side ratio B'/D' . Furthermore, the torsional flutter of the rectangular cylinder gradually switches from the wind velocity-restricted type to the divergent type with an increase in side ratio from 2 to 10 , because the flow pattern gradually changes from the intermittent reattachment type to the steady reattachment type (Matsumoto et al., 1997). Possibly because of the change in flow pattern with the side ratio, the side-surface openings did not have effects on the torsional flutter characterized by the comparatively large A_2^* , but stabilized that characterized by the comparatively small A_2^* .

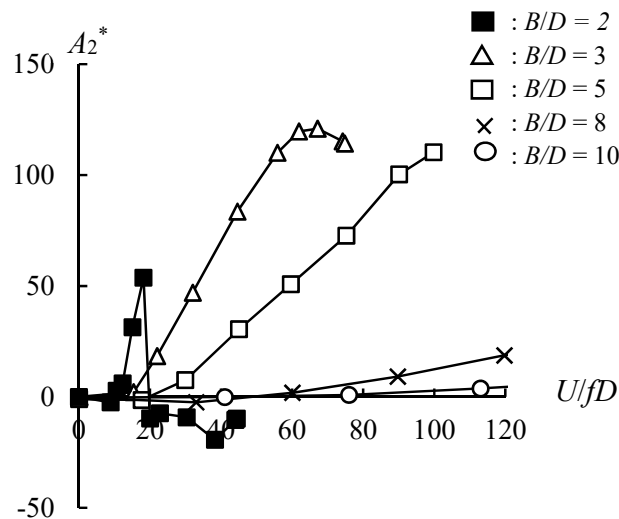


Fig. 3-18 A_2^* of the rectangular cylinder with different side ratios (Matsumoto 1996).

3.5.2 Vertical 1DOF aerodynamic performance

The vertical 1DOF aerodynamic performances of the closed and open girders at $\alpha = 0^\circ$ are summarized in Fig. 3-19. The mass and damping of the system were minimized as much as possible to more clearly observe the responses of the closed and open girders (Table 3-3). The largest reduced double amplitude of the motion-induced vortex vibration of the closed girder was approximately 0.23 , whereas that of the open girder was almost 0 . Consequently, the side-surface openings mitigated the motion-induced vortex vibration for the $B/D = 5$ model. Neither the closed nor the open girder exhibited galloping instability. However, the closed girder showed a larger amplitude than the open girder at high wind velocities, indicating that side-surface openings can limit the amplitude of the vertical vibration at high wind velocities.

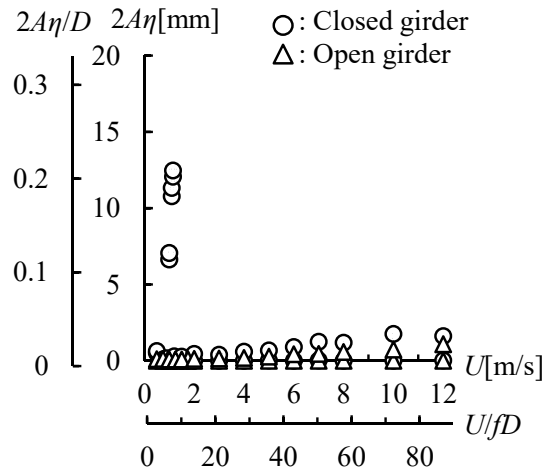


Fig. 3-19 Aerodynamic response of the $B/D = 5$ model ($B'/D' = 5$, vertical 1DOF, $\alpha = 0^\circ$, smooth flow).

3.6 Conclusion remarks

The proposition of this chapter was to study the effects of side-surface openings on the aerodynamic performance of box girders. Two butterfly web girders with side ratio $B/D = 3.24$ and 5, where B is the girder width and D is the girder depth, were examined through a series of wind tunnel tests, i.e., free vibration tests, aerodynamic force tests and forced vibration tests. By covering the openings of these two butterfly web girders, two conventional box girders were also examined through the aforementioned wind tunnel tests. The $B/D = 3.24$ butterfly web girder showed the motion-induced vortex vibration, the galloping instability, and the torsional flutter. While the $B/D = 5$ butterfly web girder showed the motion-induced vortex vibration and the torsional flutter. The effects of side-surface openings on these phenomena were illustrated by comparing the results of the butterfly web girders with those of the conventional box girders. Additionally, the distribution of the wind velocity vectors in the wake of the $B/D = 3.24$ butterfly web girder was studied to explain the influence of the openings on the near wake flow and further interpret the potential reason for the effects of openings on the galloping. The conclusions are summarized as follows:

- The side-surface openings had no effects on the critical wind velocity of motion-induced vortex vibration but stabilized it in both the heaving and torsional directions by reducing the vibration amplitude.
- The torsional flutter of $B/D = 3.24$ and $B/D = 5$ girders was different regarding the mechanism, as indicated by the decrease of the aerodynamic damping (A_2^*) at high wind velocities with their equivalent side ratio B'/D' , where B' is the equivalent girder width and D' is the equivalent girder depth due to the angle of attack. Subsequently, the side-surface

openings had no effects on the torsional flutter of the $B/D = 3.24$ butterfly web girder but significantly stabilized the torsional flutter of the $B/D = 5$ butterfly web girder by increasing its critical wind velocity and reducing the vibration amplitude and the aerodynamic damping (A_2^*).

- Owing to the openings on the side surface, the flow got through the inner space of the box girder into the wake, promoting the separated flow from the leading edge to approach the trailing edge. Even though such a change in the flow field caused by the openings had no effects on the Strouhal number, the side-surface openings significantly suppressed the Kármán-vortex shedding as confirmed by the reduction in the drag force coefficients (C_{Fx}) and fluctuating lift force coefficients (C_{Fy}'). Furthermore, the side-surface openings stabilized the galloping, by increasing the critical wind velocity and reducing the vibration amplitude and the aerodynamic damping (H_1^*). This is probably because the side-surface openings enhanced the reattachment of the separated flow on the side surface.

In summary, even though the stabilization against the torsional flutter owing to the side-surface openings showed the side-ratio dependency, the side-surface openings significantly stabilized the vortex-induced vibration and galloping instability. However, these conclusions were limited to the single box girder. Another concern is raised regarding the effects of the side-surface openings on the aerodynamic performance of the box girder when it is accompanied by another girder, owing to that this aerodynamic performance is sometimes more unstable. This question will be addressed in Chapter 4. Furthermore, the $B/D = 3.24$ butterfly web girder is with Opening-area Ratio of 30%, the ratio of the area of the opening to the half front-surface area, while Opening-area Ratio of the $B/D = 5$ butterfly web girder is 33%. Therefore, the conclusions were limited to the Opening-area Ratio of about 30%. More investigations related to the relationship between the opening size and galloping instability are under the requirement. This question will be addressed more detailed in Chapter 5.

Reference

- Bearman, P., Trueman, D., 1972. An Investigation of the Flow around Rectangular Cylinders. *Aeronautical Quarterly*. 23(3), 229-237.
- Deniz, S., Staubli, T., 1997. Oscillating rectangular and octagonal profiles: Interaction of leading- and trailing-edge vortex formation. *J. Fluids Struct.* 11, 3–31.
- Huang, R.F., Lin, B.H., Yen, S.C., 2010. Time-averaged topological flow patterns and their influence on vortex shedding of a square cylinder in crossflow at incidence. *J. Fluids Struct.* 26, 406–429. <https://doi.org/10.1016/j.jfluidstructs.2010.01.003>

Huang, R.F., Hsu, C.M., Chen, Y.T., 2017. Modulating flow and aerodynamic characteristics of a square cylinder in crossflow using a rear jet injection. *Phys. Fluids* 29, 015103-1–15. <https://doi.org/10.1063/1.4972982>

Horitsu, T., 2007. Role of Kármán vortex on aerodynamic performance of bluff body. Doctoral Thesis. Kyoto University.

Koutmos, P., Papailiou, D., Bakroziis, A., 2004. Experimental and computational study of square cylinder wakes with two-dimensional injection into the base flow region. *Eur. J. Mech. B/Fluids*. 23, 353–365. <https://doi.org/10.1016/j.euromechflu.2003.09.004>

Kwok, K.C.S., Melbourne, W.H., 1977. The effects of freestream turbulence on a galloping square tower. *Proceedings of the 6th Australasian Hydraulics and Fluid Mechanics Conference*. Adelaide, Australia.

Laneville, A., Yong L.Y., 1983. Mean flow patterns around two-dimensional rectangular cylinders and their interpretation. *J. Wind Eng. Ind. Aerodyn.* 14, 387–398.

Matsumoto, M., Shiraishi, N., Kitazawa, M., Knisely, C., Shirato, H., Kim, Y., Tsujii, M., 1990. Aerodynamic behavior of inclined circular cylinders-cable aerodynamics. *J. Wind Eng. Ind. Aerodyn.* 33, 63–72.

Matsumoto, M., 1996. Aerodynamic damping of prisms. *J. Wind Eng. Ind. Aerodyn.* 59, 159–175.

Matsumoto, M., Daito, Y., Yoshizumi, F., Ichikawa, Y., Yabutani, T., 1997. Torsional flutter of bluff bodies. *J. Wind Eng. Ind. Aerodyn.* 69–71, 871–882.

Matsumoto, M., Yagi, T., Shigemura, Y., Tsushima, D., 2001. Vortex-induced cable vibration of cable-stayed bridges at high reduced wind velocity. *J. Wind Eng. Ind. Aerodyn.* 89, 633–647.

Matsumoto, M., Yagi, T., Hatsuda, H., Shima, T., Tanaka, M., Naito, H., 2010. Dry galloping characteristics and its mechanism of inclined/yawed cables. *J. Wind Eng. Ind. Aerodyn.* 98, 317–327.

Matsumoto, M., Yagi T., Lee, J.H., Hori, K., Kawashima, Y., 2006. Kármán vortex effect on the aerodynamic forces to rectangular cylinders. *ASME Pressure Vessels and Piping/ICPVT-11 Conference*. Vancouver, BC, Canada.

Matsumoto, M., Hashimoto, M., Yagi, T., Nakase, T., Maeta, K., 2008. Steady galloping/unsteady galloping and vortex-induced vibration of bluff bodies associated with mitigation of Kármán vortex. *Proceeding of 6th International Colloquium on Bluff Body Aerodynamics and Applications*. Milan, Italy.

Mizota, T., Okajima, A., 1981. Experimental studies of time mean flows around rectangular prisms. *Proc. Japan Soc. Civ. Eng.* 312, 39-47(in Japanese).

Nakaguchi, H., Hashimoto, K., Muto, S., 1968. An experimental study on aerodynamic drag of rectangular cylinders. *Trans. Japan. Soc. Aero. Space. Sci.* 16, 1–5 (in Japanese).

Nakamura, Y., Hirata, K., Urabe, T., 1991. Galloping of rectangular cylinders in the presence of a splitter plate. *J. Fluids Struct.* 5(5), 521–549.

Nakamura, Y., Hirata, K., 1994. The aerodynamic mechanism of galloping. *Trans. Jpn. Soc. Aeronaut. Space Sci.* 36, 257–269.

Nakato, S., 2016. Correlation of fluctuating velocity in the wake of an oscillating square cylinder with openings or appendages. *Proceeding of First International Symposium on Flutter and its Application (ISFA2016)*, Tokyo, Japan.

Yagi, T., Shinjo, K., Narita, S., Nakase, T., Shirato, H., 2013. Interferences of vortex sheddings in galloping instability of rectangular cylinders. *Journal of Structural Engineering. A (JSCE)*, 59A, 552–561 (in Japanese).

4 Aerodynamic performance of parallel box girders with side-surface openings.

4.1 Introduction

The principal target of this chapter is to investigate the aerodynamic performance of the box girder with side-surface openings in the tandem arrangement. As explained in section 1.1, to accommodate the increase of traffic, the bridge is sometimes added to the existing one, resulting in some more unstable aerodynamic phenomena of the bluff bodies in the tandem arrangement. When two girders are in tandem, the vortex-induced vibration of each girder is significantly affected by the other one (Okajima et al. 1990b; Takeuchi et al. 1992; Kimura et al. 2008; Meng et al. 2011; Park and Kim 2017a). The galloping of downstream girder is stabilized by the turbulent wake flow of the upstream girder, while the upstream girder is sometimes more unstable in the galloping owing to the downstream girder (Takeuchi et al. 1992; Honda et al. 1993). Furthermore, as explained in section 3.4, by introducing the side-surface openings, the approaching flow can get through the inner space of the box girder changing the time-averaged flow around the model. When the two girders are at the tandem arrangement, the side-surface openings of each girder not only affect the flow field around the girder itself but also potentially affect the girder next to it. Therefore, this chapter aims to deal with the effects of the side-surface openings on the aerodynamic performance of two box girders in the tandem arrangement. To accomplish the goal, the $B/D = 3.25$ butterfly web girder (Fig. 3-1), which shows good performance in the vortex-induced vibration and galloping, is duplicated (Fig. 4-1) and both the two girders are applied in a series of wind tunnel tests.

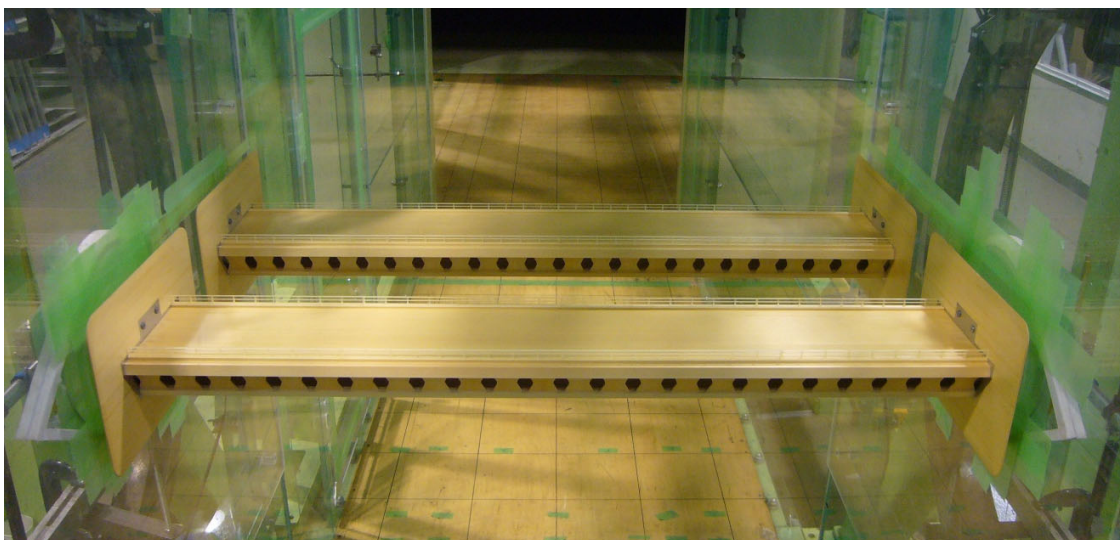


Fig. 4-1 Duplicated $B/D = 3.24$ butterfly web girders in the wind tunnel.

In this chapter, the details of the wind tunnel are outlined at first. Following that, the effects of the side-surface openings on the aerodynamic forces of the stationary girders in the tandem arrangement are illustrated. Then the aerodynamic performance of the upstream girder and downstream girder are investigated respectively, regarding the aerodynamic response and aerodynamic damping. The aerodynamic performance of the upstream girder is evaluated by rigidly supporting the other girder at the downstream side. The role of the downstream closed girder on the aerodynamic performance of the upstream girder is investigated at first. Then the aerodynamic performance of the upstream girder is illustrated when introduce the side-surface openings to the downstream girder. The effects of the side-surface openings of the upstream girder on the aerodynamic performance of the upstream girder are evaluated. On the other hand, the aerodynamic performance of the downstream girder is investigated by rigidly supporting the other girder at the upstream side. The effects of the upstream closed girder on the aerodynamic performance of the downstream girder are explained at first. Then the effects of side-surface openings of two girders on the aerodynamic performance of the downstream girder are illustrated.

4.2 Details of wind tunnel tests

The relationship between the side-surface openings of both two girders in the tandem arrangement and the aerodynamic interference was investigated through a series of wind tunnel tests, i.e. aerodynamic force tests, spring-supported free vibration tests (vertical one-degree-of-freedom (1DOF)), and forced vibration tests (vertical 1DOF). The aerodynamic interference between two rectangular cylinder-like bluff bodies depends on the **supporting condition** of the two girders and the **center distance** between the two girders (Okajima et al. 1990a and b; Honda et al. 1993; Takeuchi et al. 1992; Kimura et al. 2008; Meng et al. 2011; Kim et al. 2013; Seo et al. 2013; Argentini et al. 2015; Park et al. 2017a and b). Some knowledge relevant is addressed to define the condition of the wind tunnel tests at first. Then the details of the wind tunnel tests are outlined.

4.2.1 Background

The aerodynamic performance of a bluff body is significantly affected by the existing of the other bluff body owing to their aerodynamic interference. The aerodynamic interference strongly depends on the center distance between two bluff bodies and the supporting conditions. Some important conclusions are illustrated as follows.

The center distance is important for the aerodynamic interference between two bluff bodies. As shown in Fig. 4-2, both the Strouhal number identified from the wake of two adjacent box girders and the maximum vibration amplitude of two box girders change obviously with their center distance (Park et al., 2017). According to Sakamoto (1987), in a similar way as the aforementioned variation of Strouhal number, the Strouhal number of both the upstream and downstream square cylinders shows the same magnitude, decreasing with the center distance to a certain value and then increasing (Fig. 4-6). The reasons for the same Strouhal number of the upstream and

downstream cylinders are explained as follows: the two adjacent square cylinders behave like one body, connecting by the vortex from the upstream cylinder at small $S/D < 3$, where S is the gap distance and D is the width of the square cylinder; while St of the downstream cylinder is the same as that of the upstream girder owing that the arrival of the vortex from the upstream cylinder triggering the vortex shedding from the downstream cylinder at $10 > S/D > 3$. In another word, the same Strouhal number of the upstream and downstream girders is caused by the synchronization in the vortex shedding from upstream and downstream girders. Consequently, as shown in Fig. 4-2 (b), the amplitude of vortex-induced vibration of both box girders in tandem arrangement increases with the center distance to a certain value and then decreases. As shown in Fig. 4-4, the vertical aerodynamic response of the downstream $B/D = 3$ rectangular cylinder, which has a similar configuration of the $B/D = 3.24$ butterfly web girder applied in this chapter, shows the maximum amplitude of vibration at a center distance of about $2B$ (Okajima et al., 1990a). Because the purpose of this chapter is to investigate the effects of side-surface openings on the aforementioned aerodynamic interference rather than the effects of the center distance, a center distance of two times the girder width ($2B$) was applied in the current research.

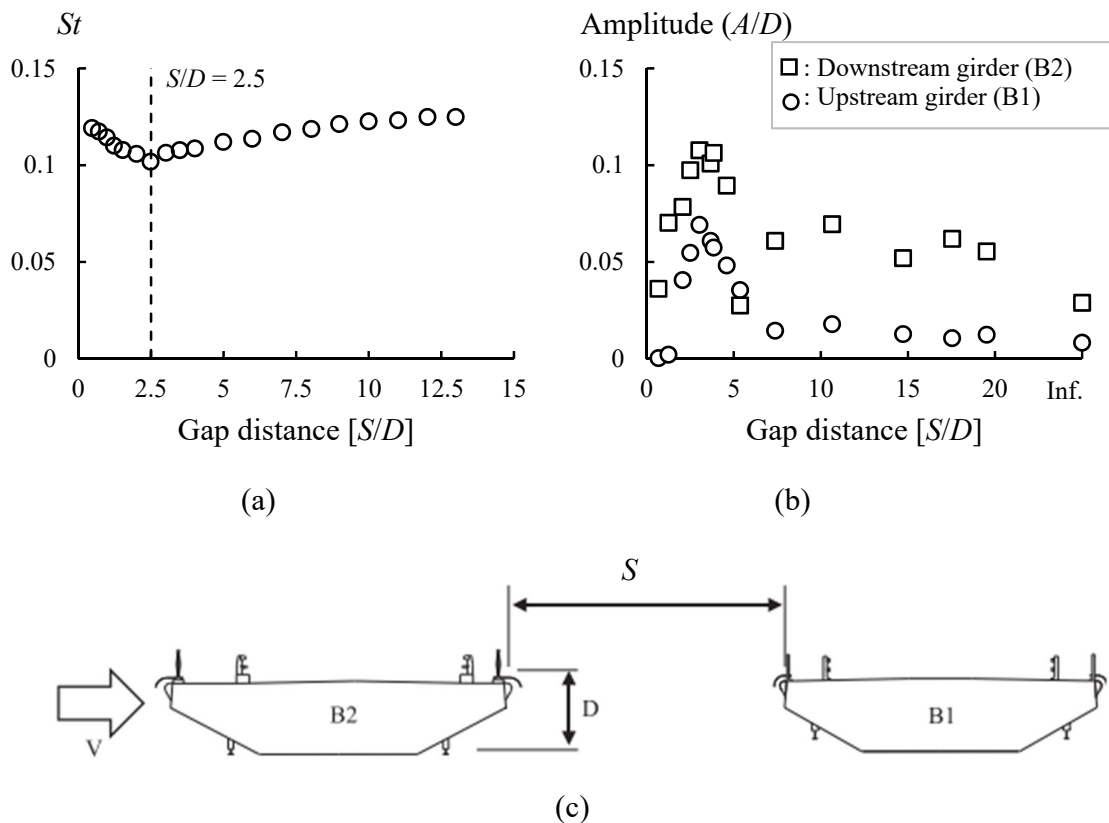


Fig. 4-2 (a) Variation of Strouhal number with center distance; (b) Variation of maximum amplitude of vortex-induced vibration with center distance (c) Disposition of two girders. (Park et al., 2017a)

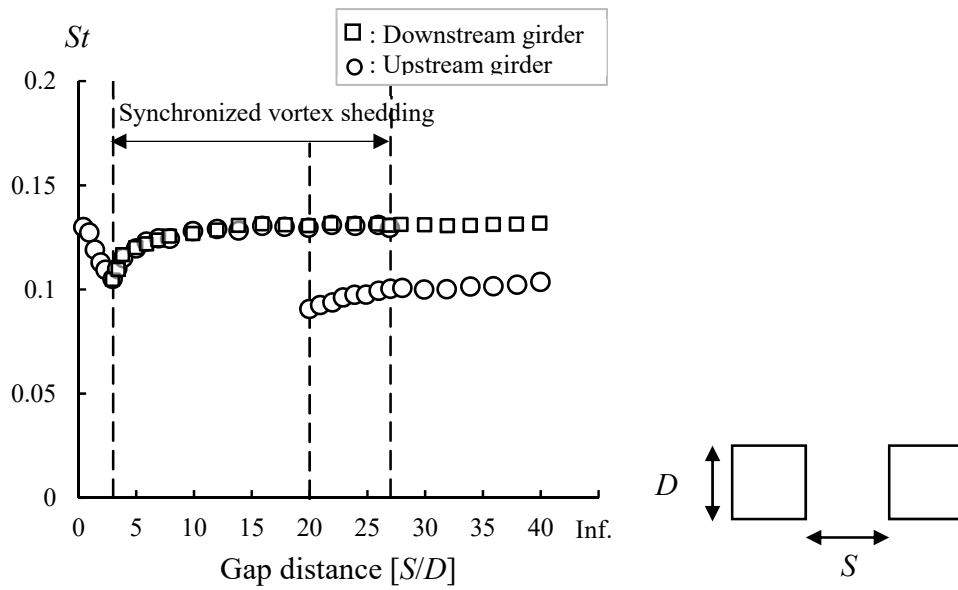


Fig. 4-3 Variation of Strouhal number St with spacing ratio S/D . (Sakamoto et al, 1987)

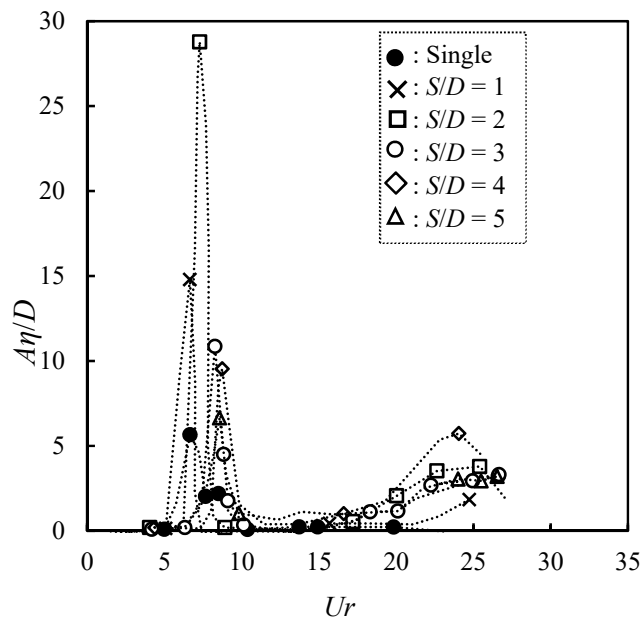
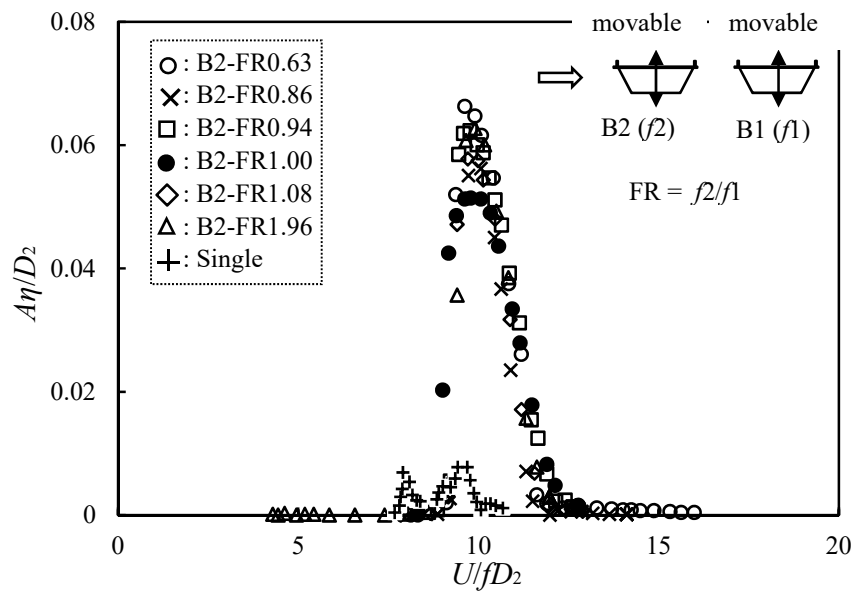


Fig. 4-4 Aerodynamic response of the downstream $B/D = 3$ rectangular cylinder. (Okajima et al., 1990a)

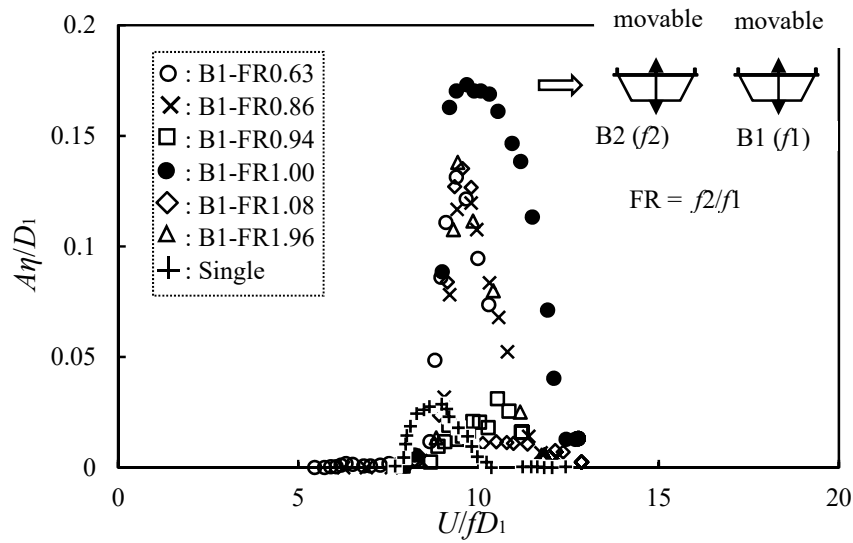
The free vibration tests are widely utilized to evaluate the aerodynamic performance of the girder by directly monitoring the response time series and the vibration amplitude. When investigating the aerodynamic interference between two girders, it involves another important issue, i.e. the supporting condition for two girders. It is suggested by several pieces of research

(Kimura et al., 2007; Honda et al., 1993) that both two girders should be elastically supported to accurately study their interference effects of the parallel bridges. However, a close investigation on the supporting condition of two girders shows that the vibration of the upstream girder is barely affected by the supporting condition of the downstream girder (Fig. 4-5 (a)) (Park et al., 2017). Meanwhile, the aerodynamic response of the downstream girder achieves the maximum only when the two girders have a similar frequency (Fig. 4-5 (b)). When two girders are both elastically supported, the dependence of the aerodynamic response of the downstream girder on the frequency ratio between two girders is because that the vortex shedding from a vibrating body is in the frequency of the natural system. Meanwhile, by rigidly supporting the upstream girder, the downstream girder shows an obviously amplified the wind-velocity-restricted vibration (Fig. 4-5 (c)). Therefore, in this research, to simplify the condition, the supporting condition for the free vibration tests is that one girder was rigidly supported to measure the aerodynamic response of the other girder.

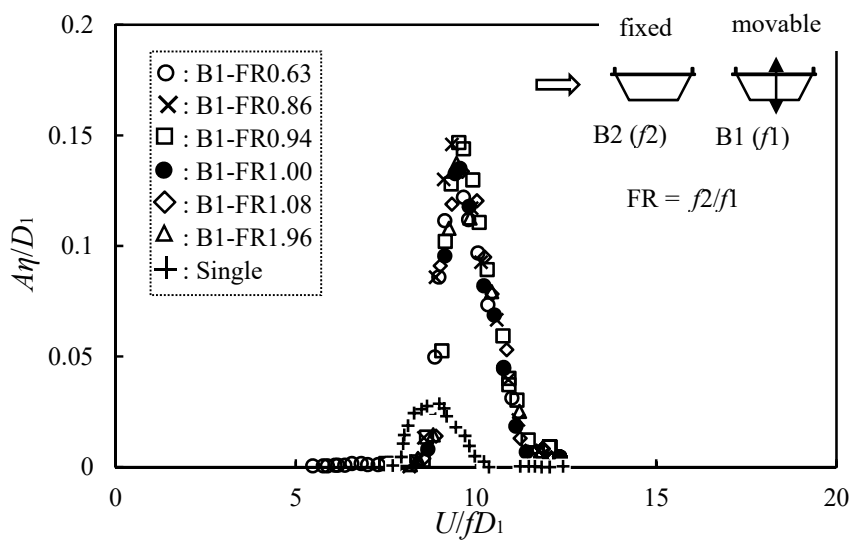


(a)

Fig. 4-5 Aerodynamic response: (a) upstream girder; (b) downstream girder with an elastically supported upstream girder; (c) downstream girder with a rigidly supported upstream girder. D_2 is the body height of the upstream girder. D_1 is the body height of the downstream girder. FR is the frequency ratio of upstream girder frequency to the downstream girder frequency. (Park and Kim, 2017b)



(b)



(c)

Fig. 4-5 Continued

4.2.2 Spring-supported free vibration test

Supported by 8 coil springs, the vertical 1DOF displacement of the girder in the smooth flow was measured by laser gages. For the set-up of the girders in tandem, when one girder was under measurement, the other one was rigidly supported (Fig. 4-6). The angle of attack (α) of the vertical 1DOF free vibration tests was 0° and $+3^\circ$ (Fig. 4-7). The cases for the upstream girder and downstream girder were listed in Table 4-1 and Table 4-2 respectively. The mass and damping of the system were kept the same as those of the single girder (Table 3-1) and assigned low values to

observe the effects of side-surface openings on the aerodynamic response more obviously (Table 4-1 and Table 4-2).

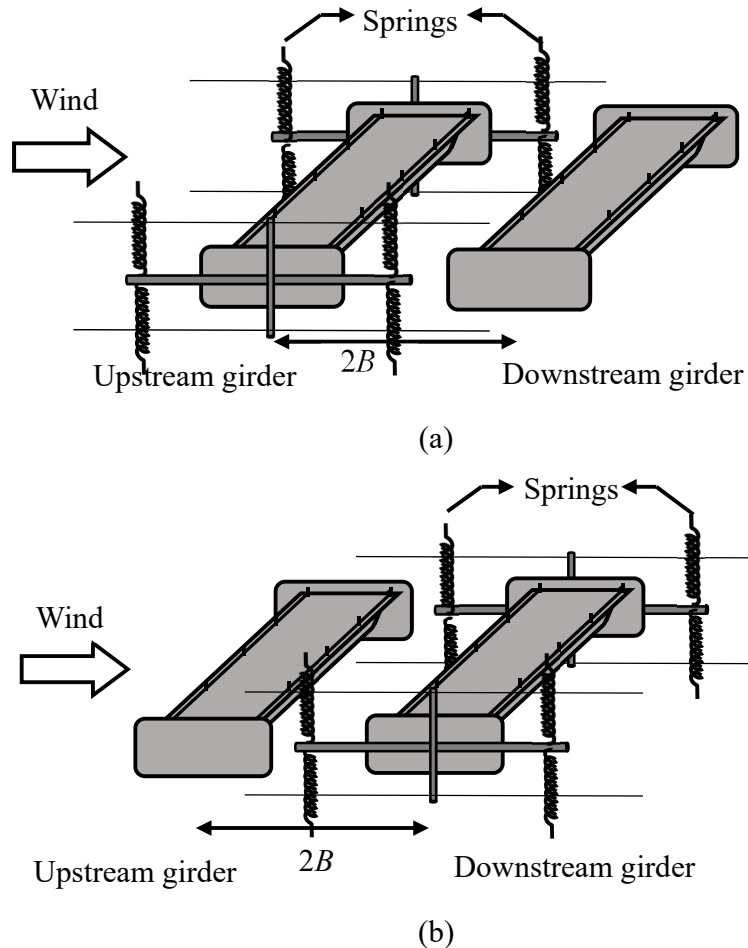


Fig. 4-6 Free vibration system for: (a) upstream girder; (b) downstream girder.

4.2.3 Aerodynamic force test on the stationary girder and forced vibration tests

The aerodynamic forces working on the stationary upstream girder were measured by the load cells and the downstream girder was rigidly supported at the downstream (Fig. 4-7). While the aerodynamic forces working on the stationary downstream girder were measured by rigidly supporting the other girder at the upstream side. The angle of attack (α) was 0° and $+3^\circ$ for all the aerodynamic force tests on the stationary girder. The tests were carried out in the smooth flow, and the approaching wind velocity was 6m/s.

The aerodynamic self-excited forces were measured by load cells rigidly connected to the model under the vertical 1DOF forced vibration in a smooth flow. When one girder was under measurement, the other model was rigidly supported at the downstream side or upstream side in the wind tunnel (Fig. 4-7). To improve the accuracy of the flutter derivatives, the vertical amplitude

and frequency were set to 10 mm and 2 Hz to get relatively large aerodynamic self-excited forces. The vertical 1DOF forced vibration tests for both the single girder and two girders in tandem were at $\alpha = 0^\circ$ and $+3^\circ$.

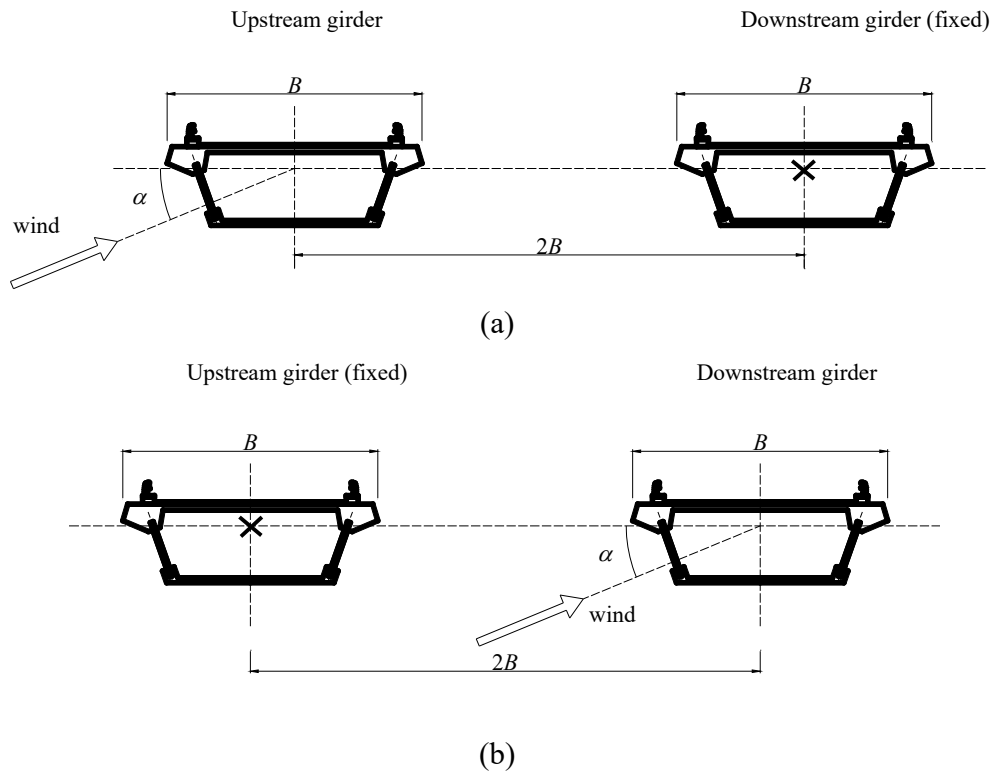


Fig. 4-7 Disposition of two girders in the wind tunnel: (a) the upstream girder is under measurement with a fixed girder at the downstream side; (b) the downstream girder is under measurement with a fixed girder at the upstream side.

Table 4-1 Characteristic parameters for the upstream girder used in free vibration experiments (vertical 1DOF, smooth flow).

Upstream girder	Downstream girder (fixed)	α ($^\circ$)	m (kg/m)	f (Hz)	δ_η	Sc_η
Closed girder	Closed girder	0°	2.40	4.57	0.0027	4.3
Closed girder	Open girder		2.36	4.61	0.0027	4.2
Open girder	Closed girder		2.40	4.57	0.0027	4.4
Open girder	Open girder		2.36	4.61	0.0027	4.3
Closed girder	Closed girder	$+3^\circ$	2.40	4.57	0.0027	4.4
Closed girder	Open girder		2.36	4.61	0.0027	4.2
Open girder	Closed girder		2.40	4.57	0.0027	4.3
Open girder	Open girder		2.36	4.61	0.0027	4.3

Table 4-2 Characteristic parameters for the downstream girder used in free vibration experiments (vertical 1DOF, smooth flow).

Upstream girder (fixed)	Downstream girder	α ($^\circ$)	m (kg/m)	f (Hz)	δ_η	Sc_η
Closed girder	Closed girder	0 $^\circ$	2.40	4.57	0.0027	4.4
Closed girder	Open girder		2.36	4.61	0.0029	4.5
Open girder	Closed girder		2.40	4.57	0.0027	4.4
Open girder	Open girder		2.36	4.61	0.0027	4.4
Closed girder	Closed girder	+3 $^\circ$	2.40	4.57	0.0027	4.3
Closed girder	Open girder		2.36	4.61	0.0027	4.4
Open girder	Closed girder		2.40	4.57	0.0026	4.3
Open girder	Open girder		2.36	4.61	0.0028	4.4

4.3 Aerodynamic force of stationary girders in tandem arrangement

In this section, firstly the aerodynamic forces of the fixed upstream girder are investigated in terms of the effects of the side-surface openings of both the upstream girder and downstream girder. Additionally, the aerodynamic forces of the upstream girder are compared with those of the single girder to explain the aerodynamic interference. Secondly, the effects of the side-surface openings of both two girders in the tandem arrangement on the aerodynamic forces of the downstream girder are illustrated. Meanwhile, the aerodynamic interference is discussed by comparing the aerodynamic forces of the downstream girder and those of the single girder.

4.3.1 Aerodynamic force of upstream girder

The aerodynamic forces of the upstream girder are discussed in this section. Table 4-3 and Table 4-4 show the aerodynamic force coefficients and Strouhal number of the upstream girders at $\alpha = 0^\circ$, respectively.

The relationship between the side-surface openings (of both the upstream and downstream girder) and the aerodynamic forces of the upstream girder is discussed at first. According to Table 4-3, when the fixed downstream girder changed from the closed girder to the open girder, C_{Fx} , C_{Fy} and C_{Fy}' of the upstream closed/open girder did not change at $\alpha = 0^\circ$. Therefore, C_{Fx} , C_{Fy} and C_{Fy}' of the upstream girder were barely affected by the side-surface openings of the downstream girder. The upstream closed girder and the upstream open girder showed almost the same magnitude of C_{Fx} (Table 4-3). However, C_{Fy} of the upstream closed girder was about 1.5~1.6 times as much as C_{Fy} of the upstream open girder (Table 4-3). The small C_{Fy} of the upstream open girder indicates that the time-averaged flow around the upstream open girder was changed owing to its side-surface openings. Even though C_{Fy}' was small for all the upstream girders (Table 4-3), C_{Fy}' of the upstream closed girder was about 4~5 times as much as C_{Fy}' of the upstream open girder. The small C_{Fy}' of the upstream open girder indicates that the vortex shedding from the upstream open girder was

suppressed owing to its side-surface openings. Consequently, the side-surface openings of the upstream girder likely changed the time-averaged flow field and suppressed the vortex shedding irrespective of the downstream girder type (closed girder or open girder).

Table 4-3 Aerodynamic force coefficients of the upstream girder ($\alpha = 0^\circ$, $U = 6\text{m/s}$)

Upstream girder	Downstream girder	C_{Fx}	C_{Fy}	C_{Fy}'
Closed girder	Closed girder	1.060	0.336	0.034
Closed girder	Open girder	1.160	0.362	0.038
Open girder	Closed girder	1.056	0.224	0.008
Open girder	Open girder	1.075	0.226	0.009

Table 4-4 Strouhal number of the upstream girder ($\alpha = 0^\circ$, $U = 6\text{m/s}$)

Upstream girder	Downstream girder	Strouhal number	$1/St$
Closed girder	Closed girder	0.129	7.77
Closed girder	Open girder	0.130	7.71
Open girder	Closed girder	0.142	7.03
Open girder	Open girder	0.147	6.80

Table 4-5 Aerodynamic force coefficients of the single girder ($\alpha = 0^\circ$, $U = 6\text{m/s}$)

Single girder	C_{Fx}	C_{Fy}	C_{Fy}'
Closed girder	1.436	0.196	0.120
Open girder	1.128	0.069	0.026

Table 4-6 Strouhal number of the single girder ($\alpha = 0^\circ$, $U = 6\text{m/s}$)

Single girder	Strouhal number	$1/St$
Closed girder	0.165	6.07
Open girder	0.164	6.10

The effects of the downstream girder on the aerodynamic forces of the upstream girder are discussed secondly. The aerodynamic forces working on the single girder at $\alpha = 0^\circ$ in Fig. 3-5 and Fig. 3-6 are summarized in Table 4-5 and the Strouhal number of the single girder in Table 3-4 is shown again in Table 4-6 for the convenience of comparison. By comparing Table 4-5 and Table 4-3, the upstream closed/open girder showed smaller C_{Fx} and larger C_{Fy} than those of the single closed/open girder at $\alpha = 0^\circ$, correspondingly. The difference between the aerodynamic forces of the upstream girders and those of the single girder indicates that the time-averaged flow around the upstream girder was also changed owing to the downstream girder. C_{Fy}' of the upstream closed/open girder was about 30% of C_{Fy}' of the single closed/open girder correspondingly (Table 4-5 and Table 4-3). The smaller C_{Fy}' of the upstream girder indicates that the vortex shedding from

the upstream girder was also suppressed owing to the downstream girder. Therefore, the downstream girder also changed the time-averaged flow field around the upstream girder and suppressed the vortex shedding from the upstream girder.

The vortex-shedding frequency of the upstream girder is discussed thirdly. According to Table 4-4, the upstream closed girder showed almost the same Strouhal number, which is slightly smaller than that of the upstream open girder at $\alpha = 0^\circ$, irrespective of whether the downstream girder has side-surface openings or not. Subsequently, the side-surface openings of both the upstream girder and downstream girder barely affected the vortex shedding frequency from the upstream girder. Furthermore, by comparing Table 4-6 and Table 4-4, Strouhal number of the upstream girder was slightly smaller than that of the single girder. This is because that the vortex-shedding frequency from the upstream girder was reduced owing to the downstream girder, which blocked the vortex formation in the wake of the upstream girder and led to a longer distance of the vortex formation (Gerrard 1966; Bearman and Trueman 1972; Sakamoto et al. 1987). Consequently, the downstream girder reduced the vortex-shedding frequency of the upstream girder, while the side-surface openings of both the upstream and downstream girders did not affect the vortex-shedding frequency.

In summary, the side-surface openings of the downstream girder did not affect the aerodynamic forces of the upstream girder. However, the downstream girder and the side-surface openings of the upstream girder both changed the time-averaged flow around the upstream girder and suppressed vortex shedding from the upstream girder. The downstream girder may block the flow entrainment in the near wake of the upstream girder, directly suppressing the vortex shedding and subsequently changing the time-averaged flow field around the upstream girder. The blockage may also reduce the frequency of the vortex shedding from the upstream girder. On the other hand, the effects of the side-surface openings should come from the reduced bluffness, which is directly caused by the flow getting through the inner space of the box girder and enhances the reattachment of the separated flow on the side surface.

4.3.2 Aerodynamic force of downstream girder

The aerodynamic forces of the downstream girder are discussed in this section. Table 4-7 and Table 4-8 show the aerodynamic force coefficients and Strouhal number of the downstream girder at $\alpha = 0^\circ$, respectively.

The relationship between the side-surface openings (of both the upstream and downstream girder) and the aerodynamic forces of the downstream girder is discussed at first. According to Table 4-7, in the wake of the closed girder, C_{Fx} , C_{Fy} and C_{Fy}' of the closed girder was almost the same with those of the open girder. In the wake of the open girder, C_{Fx} , C_{Fy} and C_{Fy}' of the closed girder were also almost the same with those of the open girder. Therefore the side-surface openings of the downstream girder barely affected the time-averaged flow around the downstream girder and vortex shedding from the downstream girder. On the other hand, the time-averaged flow around the downstream girder and the vortex shedding from the downstream girder were affected

by the turbulent flow from the upstream girder. C_{Fx} , absolute C_{Fy} and C_{Fy}' of the downstream girder were reduced, when the upstream girder changed from closed girder to open girder (e.g., C_{Fx} of the downstream closed girder was reduced by 25%, when the upstream girder changed from closed girder to open girder). Therefore, the time-averaged flow around the downstream girder and the vortex shedding from the downstream girder were affected by the turbulent flow of the upstream girder. Consequently, rather than the side-surface opening of the downstream girder, the side-surface openings of the upstream girder affected the flow field around the downstream girder.

Table 4-7 Aerodynamic force coefficients of the downstream girder ($\alpha = 0^\circ$, $U = 6\text{m/s}$)

Upstream girder	Downstream girder	C_{Fx}	C_{Fy}	C_{Fy}'
Closed girder	Closed girder	0.476	-0.162	0.355
Closed girder	Open girder	0.447	-0.184	0.295
Open girder	Closed girder	0.359	-0.136	0.233
Open girder	Open girder	0.337	-0.154	0.252

Table 4-8 Strouhal number of the downstream girder ($\alpha = 0^\circ$, $U = 6\text{m/s}$)

Upstream girder	Downstream girder	Strouhal number	$1/St$
Closed girder	Closed girder	0.131	7.65
Closed girder	Open girder	0.129	7.76
Open girder	Closed girder	0.146	6.83
Open girder	Open girder	0.148	6.78

The effects of the upstream girder on the aerodynamic forces of the downstream girder are discussed secondly. Comparing Table 4-7 with Table 4-5, C_{Fx} of the downstream closed/open girder was smaller than those of the single closed/open girder at $\alpha = 0^\circ$. Meanwhile, the lift force of the downstream girder was downward direction, while the single girder showed an upward lift force. The time-averaged flow around the downstream girder was further proofed to be changed owing to the vortex shedding from the upstream girder. Furthermore, by comparing Table 4-7 and Table 4-5, C_{Fy}' of the downstream girder was obviously larger than that of the single girder. This indicates that the shear-layer instability of the downstream girder was obviously strengthened by the vortex shedding from the upstream girder. Accordingly, the turbulent flow from the upstream girder changed the time-averaged flow around the downstream girder and strengthen the shear-layer instability of the downstream girder.

The vortex-shedding frequency of the downstream girder was discussed thirdly. According to Table 4-8, the closed girder and open girder in the wake of the closed girder showed almost the same Strouhal number, while the closed girder and open girder in the wake of the open girder showed almost the same Strouhal number at $\alpha = 0^\circ$. The Strouhal number of the girders in the wake of the closed girder was slightly smaller than that of the girders in the wake of the open

girder. By comparing Table 4-4 and Table 4-8, Strouhal number of the downstream and upstream girder were almost the same for the same arrangement. By comparing Table 4-6 and Table 4-8, Strouhal number of the downstream girder was slightly smaller than that of the single girder. According to Sakamoto (1987), the same vortex-shedding frequency of the downstream girder and upstream girder is related to the synchronization between the vortex shedding from the upstream girder and the vortex formation of the downstream girder.

In summary, the time-averaged flow around the downstream girder was obviously affected by the vortex shedding from the upstream girder. The shear-layer instability of the downstream girder was strengthened owing to the periodic turbulent flow from the upstream girder. The synchronization between the vortex shedding from the upstream girder and the vortex formation of the downstream girder led to the same Strouhal number of the upstream girder and downstream girder. The side-surface openings of the downstream girder barely not affected the time-averaged flow field of and vortex shedding from the downstream girder. On the other hand, the side-surface openings of the upstream girder slightly affected the flow field around the downstream girder.

4.4 Aerodynamic performance of the upstream girder

When a girder is rigidly supported at the downstream, the flow field around the stationary upstream girder seems to be affected by the side-surface openings of the upstream rather than those of the downstream girder. In this section, the effects of the stationary downstream closed girder on the aerodynamic performance of the upstream girder is discussed by comparing the results of the upstream girder with the results of the single girder at first. Then the effects of the side-surface openings (of both the upstream girder and downstream girder) on the aerodynamic instability of the upstream girder are discussed.

4.4.1 Effects of fixed downstream girder

The effects of the downstream girder on the aerodynamic performance of the upstream girder are discussed in this section. The comparison between the aerodynamic response of the upstream girder and single girder is shown in Fig. 4-8, and the comparison between the aerodynamic derivative H_1^* of the upstream girder and single girder is shown in Fig. 4-9.

According to Fig. 4-8 (a), the motion-induced vortex vibration of the upstream closed girder showed almost the same magnitude with that of the single closed girder. Meanwhile the upstream open girder and the single open girder also showed the same amplitude Fig. 4-8 (b). Therefore, with a center distance of $2B$, the motion-induced vortex vibration of the upstream girder was not affected by the downstream girder. According to Fig. 4-8, another noticeable result is that the critical wind velocity of galloping (U_{rc0}) of the upstream girder was smaller than that of the single girder. According to Fig. 4-8 (a), U_{rc0} ($= 25$) of the upstream closed girder was smaller than that ($U_{rc0} = 47$) of the single closed girder. According to Fig. 4-8 (b), the upstream open girder showed galloping from about $U_{rc0} = 40$, whereas the single open girder did not show galloping until $U_r =$

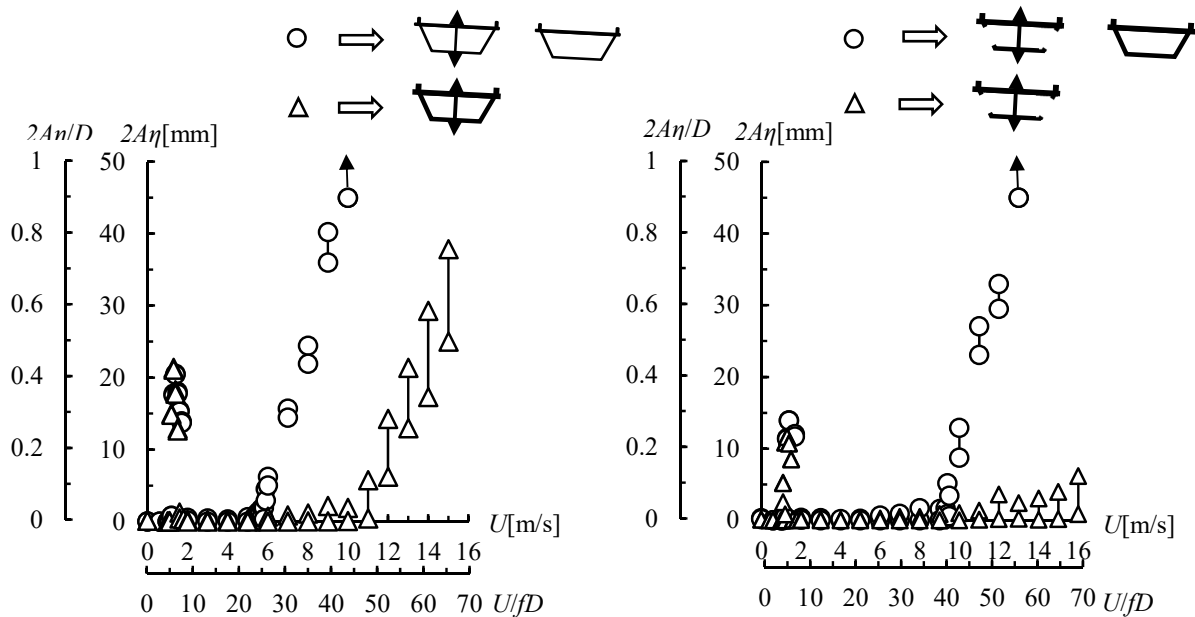


Fig. 4-8 (a) Comparison between the aerodynamic response of the upstream closed girder and the single closed girder; (b) comparison between the aerodynamic response of the upstream open girder and the single open girder. (Vertical one-degree of freedom [1DOF], $\alpha = 3^\circ$, smooth flow)

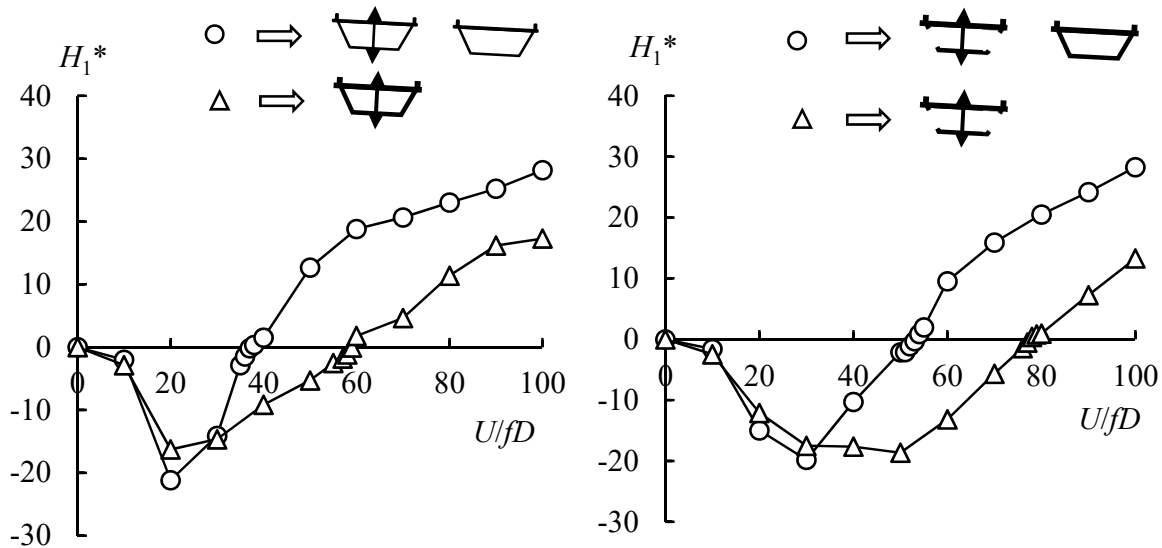


Fig. 4-9 (a) Comparison between the aerodynamic derivative H_1^* of the upstream closed girder and the single closed girder; (b) comparison between the aerodynamic derivative H_1^* of the upstream open girder and the single open girder. (Vertical 1DOF, $\alpha = 3^\circ$, $f = 2.0$ Hz, $2A\eta = 20$ mm, smooth flow)

70. Therefore, the downstream closed girder made the upstream girder more galloping unstable. This conclusion can be supported by a comparison between H_1^* of the upstream girder and single girder (Fig. 4-9). The upstream closed girder has smaller U_{rc_for} (= 40) than U_{rc_for} (= 60) of the single closed girder (Fig. 4-9 (a)). U_{rc_for} (= 52 and 56) of the upstream open girder was smaller than U_{rc_for} (= 80) of the single open girder (Fig. 4-9 (b)). According to past researches (Matsumoto et al. 2008b; Yagi et al. 2013), the galloping of the upstream girder was more unstable owing to the suppression of the vortex shedding, which is indicated by the small fluctuating lift coefficients of the upstream girder (Table 4-3) owing to the blockage of the downstream girder.

In summary, the existing of the fixed downstream closed girder did not affect the motion-induced vortex vibration of the upstream girder but made the upstream girder more unstable in the galloping.

4.4.2 Effects of side-surface openings

The relationship between the side-surface openings of both the upstream and downstream girders and the motion-induced vortex vibration of the upstream girder is discussed based on the aerodynamic response (at $U < 2.4\text{m/s}$ or $U_r < 10.4$) at $\alpha = 0^\circ$ (Fig. 4-10). According to Fig. 4-10 (a) and (b), for the upstream closed girder, the largest reduced double amplitude of the motion-induced vortex vibration ($2A\eta(\text{max})/D$) was 0.40 irrespective of the downstream girder type (closed girder or open girder). According to Fig. 4-10 (c) and (d), $2A\eta(\text{max})/D$ of the upstream open girder was 0.24 irrespective of the downstream girder type. Subsequently, $2A\eta(\text{max})/D$ (= 0.40) of the upstream closed girder was about 1.7 times as much as $2A\eta(\text{max})/D$ (= 0.24) of the upstream open girder. Therefore, introducing the side-surface openings to the downstream closed girder, the motion-induced vortex vibration of the upstream girder was not affected. However, irrespective of the downstream girder's type, the side-surface openings mitigated the motion-induced vortex vibration of the upstream girder by reducing the largest amplitude by 45%.

The effects of the side-surface openings on the galloping instability are further discussed based on the aerodynamic response (Fig. 4-11) and H_1^* (Fig. 4-12) at $\alpha = +3^\circ$. In Fig. 4-11, one noticeable result is that the galloping instability of the upstream girder was barely affected when the side-surface openings was introduced to the downstream closed girder. According to Fig. 4-11 (a) and (b), when the downstream girder changed from closed girder to open girder, the upstream closed girder showed almost the same amplitude of vibration for each wind velocity. The upstream closed girder showed galloping from the reduced critical wind velocity (U_{rc0}) of 25, irrespective of the type of the downstream girder (closed girder or open girder). By comparing Fig. 4-11 (c) and (d), the upstream open girder showed galloping from $U_{rc0} = 40$ with a closed girder at the downstream, and from $U_{rc0} = 50$ with an open girder at the downstream. Despite the difference between U_{rc0} of these two cases (Fig. 4-11 (c) and (d)), the upstream open girder for these two cases achieved a reduced double amplitude larger than 45 at $U_{rc0} = 55$. Therefore, the galloping instability of the upstream girder was barely affected when the side-surface openings were introduced to the downstream closed girder. This conclusion can be also summarized by H_1^* of the upstream girder

(Fig. 4-12). When the downstream girder changed from closed girder to open girder, H_1^* of the upstream closed girder was almost the same (Fig. 4-12 (a) and (b)). According to Fig. 4-12 (c) and (d), the same conclusion can be summarized for H_1^* of the upstream open girder. In summary, the side-surface openings of the downstream girder did not affect the galloping instability of the upstream girder.

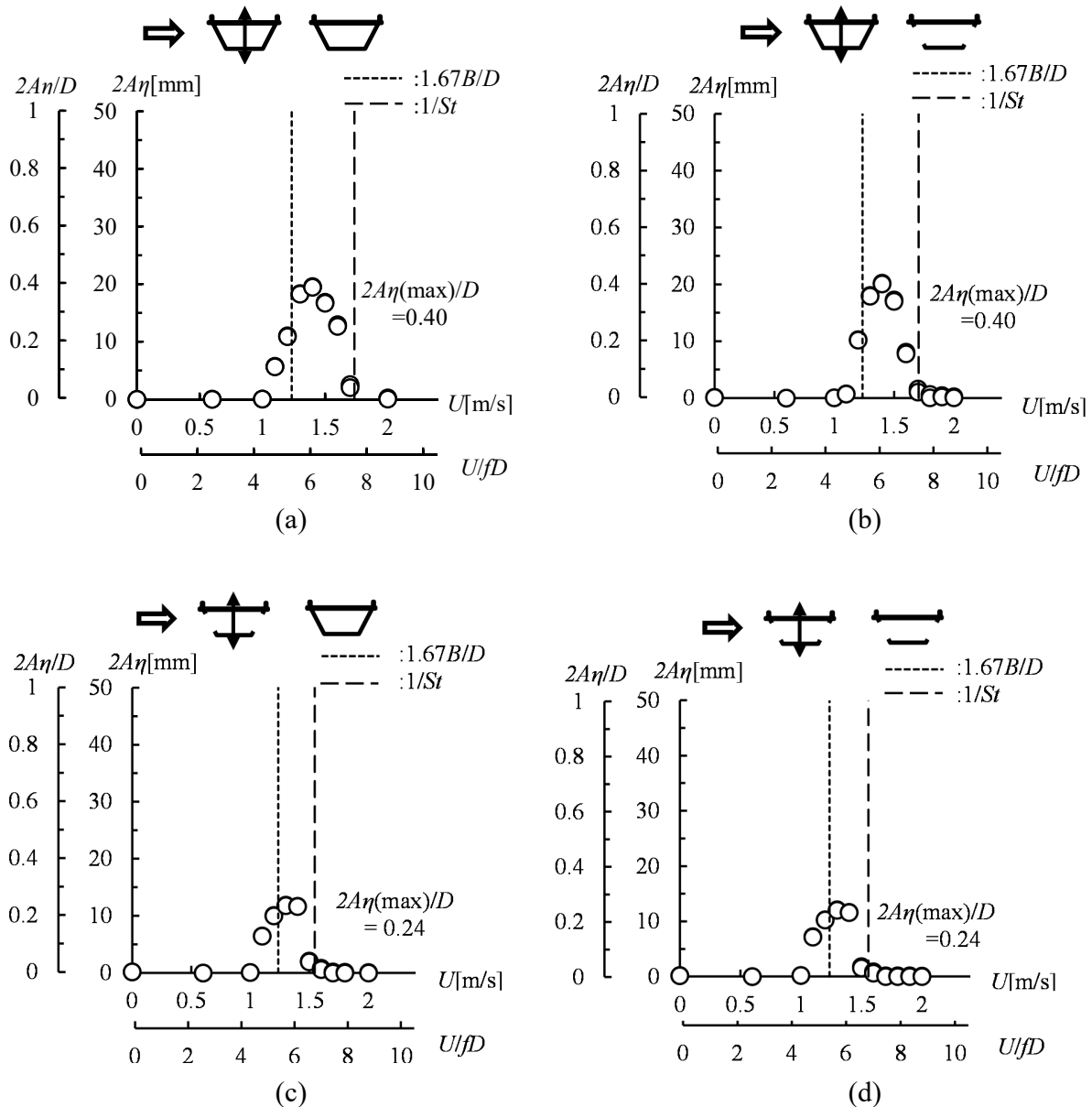


Fig. 4-10 Vortex-induced vibration for (vertical 1DOF, $\alpha = 0^\circ$, smooth flow) (a) upstream closed girder with a fixed downstream closed girder; (b) upstream closed girder with a fixed downstream open girder; (c) upstream open girder with a fixed downstream closed girder; (d) upstream open girder with a fixed downstream open girder.

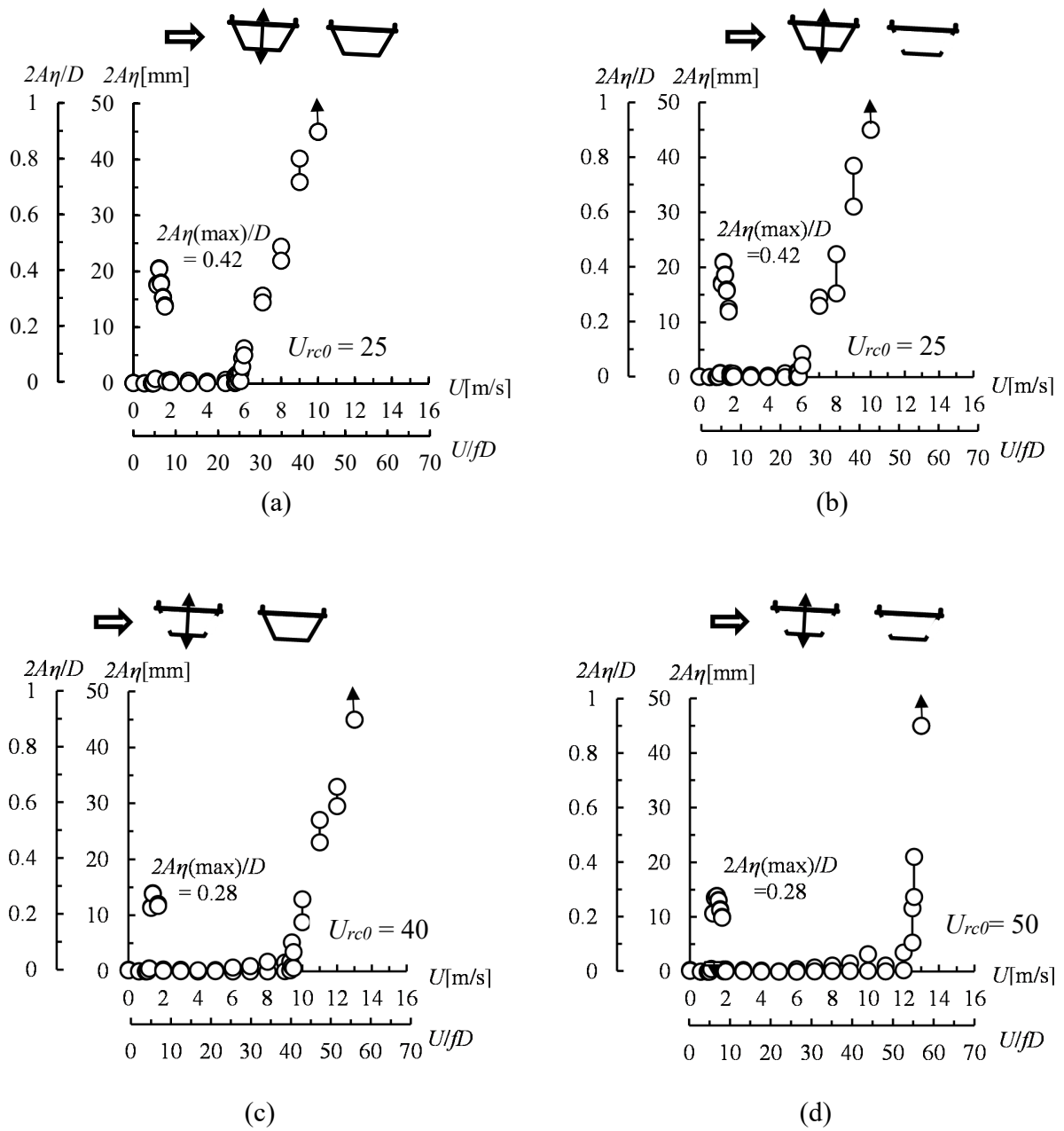


Fig. 4-11 Aerodynamic response for (vertical 1DOF, $\alpha = +3^\circ$, smooth flow): (a) upstream closed girder with a fixed downstream closed girder; (b) upstream closed girder with a fixed downstream open girder; (c) upstream open girder with a fixed downstream closed girder; (d) upstream open girder with a fixed downstream open girder.

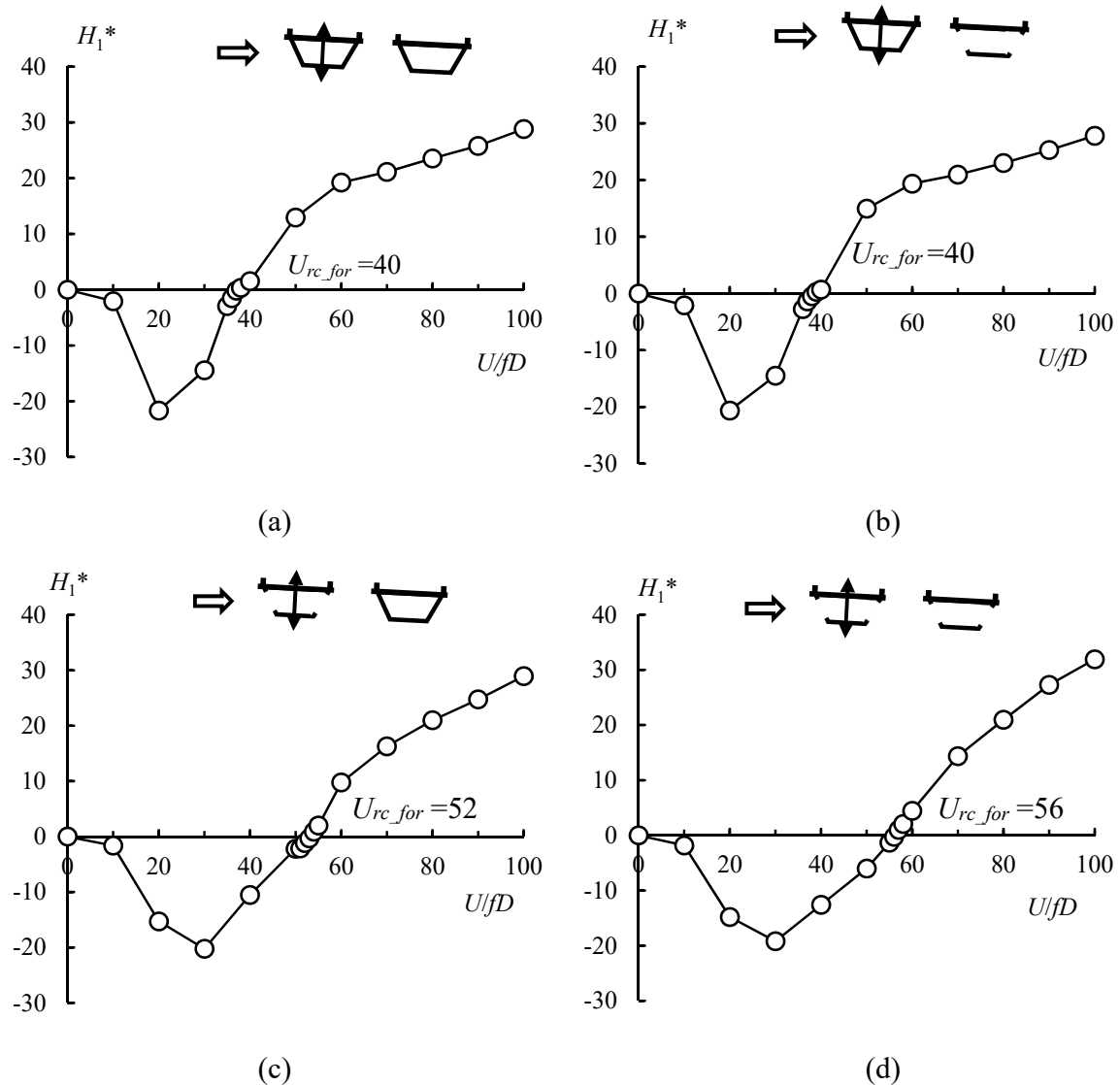


Fig. 4-12 Aerodynamic derivative H_1^* for (vertical 1DOF, $\alpha = 3^\circ$, $f = 2.0$ Hz, $2A\eta = 20$ mm, smooth flow): (a) upstream closed girder with a fixed downstream closed girder; (b) upstream closed girder with a fixed downstream open girder; (c) upstream open girder with a fixed downstream closed girder; (d) upstream open girder with a fixed downstream open girder.

According to Fig. 4-11 and Fig. 4-12, another noticeable result is that the side-surface openings of upstream girders can stabilize the galloping instability of the upstream girder by increasing the reduced critical wind velocity. By comparing Fig. 4-11 (a) and (c), with a fixed closed girder at the downstream side, the upstream closed girder showed a smaller reduced critical wind velocity of galloping ($U_{rc0} = 25$) than $U_{rc0} (= 40)$ of the upstream open girder. By comparing Fig. 4-11 (b) and (d), with a fixed open girder at the downstream side, $U_{rc0} (= 25)$ of the upstream closed girder was smaller than $U_{rc0} (50)$ of the upstream open girder. Furthermore, according to Fig. 4-12, H_1^* of the upstream closed girder turned positive at $U_{rc_for} = 40$, which was smaller than $U_{rc_for} (52/56)$

of the upstream open girder. Consequently, the side-surface openings of the upstream girder can stabilize the galloping instability of the upstream girder by increasing the reduced critical wind velocity. In summary, introducing the side-surface openings to the downstream closed girder did not affect the aerodynamic performance of the upstream girder. However, introducing the side-surface openings to the upstream closed girder stabilized it against the motion-induced vortex vibration and galloping.

4.5 Aerodynamic performance of the downstream girder

When a girder was rigidly supported at the upstream side, the flow field around the stationary downstream girder seems to be more related to the side-surface openings of the upstream girder rather than the side-surface openings of the downstream girder. In this section, the effects of the turbulence flow from the upstream closed girder on the aerodynamic performance of the downstream girder are discussed by comparing the results of the downstream girder with the results of the single girder at first. Then the effects of the side-surface openings of both the upstream girder and downstream girder on the aerodynamic instability of the downstream girder are discussed.

4.5.1 Effects of fixed upstream girder

The effects of turbulent flow from the upstream closed girder on the aerodynamic performance of the downstream girder are discussed in this section. The comparison between the aerodynamic response of the downstream girder and single girder is shown in Fig. 4-13, and the comparison between the aerodynamic derivative H_1^* of the downstream girder and single girder is shown in Fig. 4-14.

According to Fig. 4-13 and Fig. 4-14, one noticeable characteristic is that the galloping instability of the downstream girder was stabilized by the turbulent flow from the upstream closed girder. As shown in Fig. 4-13 (a), the downstream closed girders did not show galloping instability at $\alpha = +3^\circ$, whereas the single closed girder showed galloping at $Ur > 47$. Furthermore, as shown in Fig. 4-14 (a), the downstream closed girder did not show galloping while the single closed girder showed galloping at $Ur > 60$. The downstream open girder did not galloping while the single open girder showed galloping at $Ur > 80$ (Fig. 4-14 (b)). Therefore, the turbulent flow from the upstream closed girder stabilized the galloping of the downstream girder. This is because the turbulent flow from the upstream girder caused the intermittent reattachment of the shear layer on the side surface of the downstream girder (Takeuchi et al. 1992; Lee 1975).

According to Fig. 4-13, another noticeable characteristics is that the vortex-induced vibration of the downstream girder showed larger amplitude than that of the single girder. For the convenience of discussion, this matter is further discussed based on the Fig. 4-15, which only compares the vortex-induced vibration of the downstream girder and the single girder. The largest reduced double amplitude of the vortex-induced vibration ($2A\eta(\max)/D = 0.75$) of the downstream closed girder was larger than $2A\eta(\max)/D (= 0.40)$ of the single closed girder (Fig. 4-15 (a)).

$2A\eta(\max)/D$ ($=0.59$) of the downstream open girder was larger than $2A\eta(\max)/D$ ($= 0.22$) of the single open girder (Fig. 4-15 (b)). Therefore, owing to the upstream closed girder, the amplitude of the vortex-induced vibration of the downstream girder was amplified almost 2 times. According to Fig. 4-15, the reduced critical wind velocity of the vortex-induced vibration of the downstream girder was about 6, which is larger than that of the single girder (about 4). This difference may be caused by the increase of $1/St$ of the downstream girder from that of the single girder (Table 4-6 and Table 4-8). Furthermore, $1/St$ of the upstream girder and downstream girder in the same arrangement were almost the same (Table 4-4 and Table 4-8). The amplification in the vortex-induced vibration may be related to the synchronization between the vortex shedding from the upstream girder and the vortex formation of the downstream girder (Sakamoto et al. 1987; Meng et al. 2011; Argentini et al. 2015; Park et al. 2017a). As discussed before, the fluctuating lift force coefficients of the downstream girder were obviously larger than those of the single girder (Table 4-5 and Table 4-7). Therefore, the vortex-induced vibration of the downstream girder can be regarded as a ‘forced vibration’ or ‘resonance buffeting’ due to the periodic turbulent flow from the upstream girder (Takeuchi et al. 1992; Argentini et al. 2015).

In summary, the stationary upstream closed girder stabilized the galloping of the downstream girder and amplified the amplitude of the vortex-induced vibration of the downstream girder about 2 times. The vortex-induced vibration of the downstream girder was regarded as a ‘forced vibration’ or ‘resonance buffeting’ due to the periodic turbulent flow from the upstream girder.

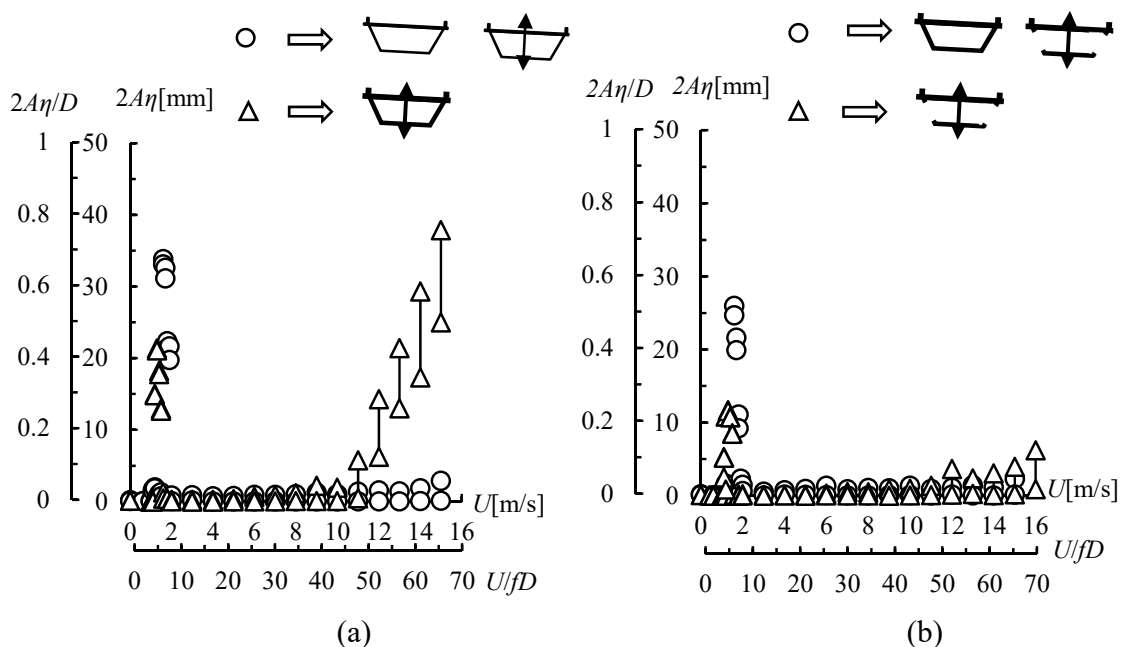


Fig. 4-13 (a) Comparison between the aerodynamic response of the downstream closed girder and single closed girder; (b) comparison between the aerodynamic response of the downstream open girder and single open girder. (Vertical 1DOF, $\alpha = 3^\circ$, smooth flow)

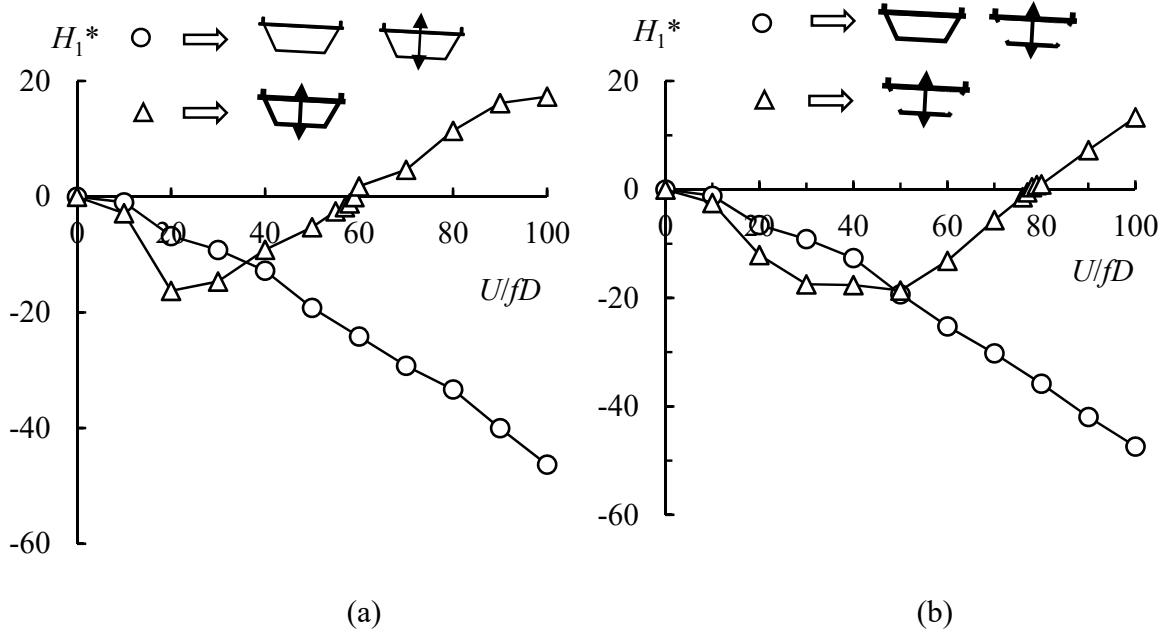


Fig. 4-14 (a) Comparison between the aerodynamic derivative H_1^* of the upstream closed girder and the single closed girder; (b) comparison between the aerodynamic derivative H_1^* of the upstream open girder and the single open girder. (Vertical 1DOF, $\alpha = 3^\circ$, $f = 2.0$ Hz, $2A\eta = 20$ mm, smooth flow)

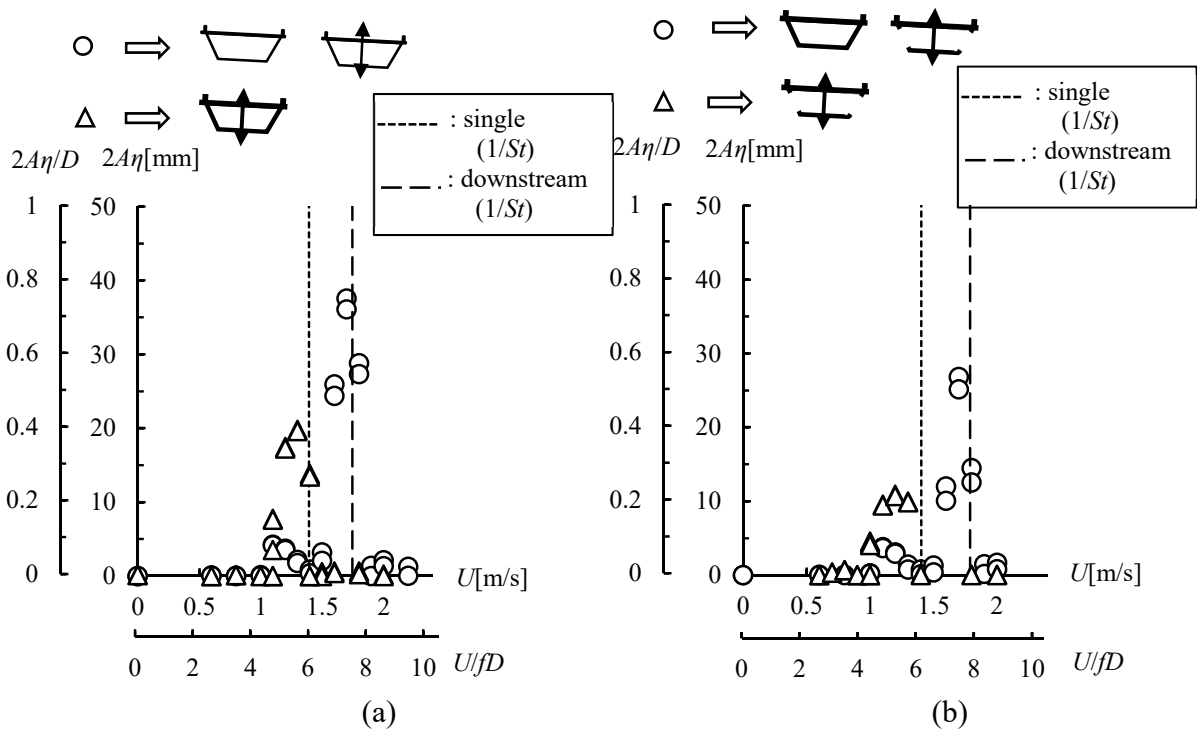


Fig. 4-15 (a) Comparison between the vortex-induced vibration of the downstream closed girder and single closed girder; (b) comparison between the vortex-induced vibration of the downstream open girder and single open girder. (Vertical 1DOF, $\alpha = 0^\circ$, smooth flow)

4.5.2 Effects of side-surface openings

The effects of the side-surface openings on the vortex-induced vibration of the downstream girder are discussed based on the aerodynamic response (at $U < 2.4\text{m/s}$ or $U_r < 10.4$) at $\alpha = 0^\circ$ (Fig. 4-16). According to Fig. 4-16, the most noticeable result is that the vortex-induced vibration of the downstream girder is more affected by the side-surface openings of the downstream girder itself rather than the side-surface openings of the upstream girder. As shown in Fig. 4-16 (a) and (c), for the downstream closed girder, the largest reduced double amplitude of the vortex-induced vibration ($2A\eta(\text{max})/D$) was about 0.75, independence of the upstream girder type (closed girder or open girder). As shown in Fig. 4-16 (b) and (d), when the upstream girder changed from the closed girder to open girder, the difference between $2A\eta(\text{max})/D$ ($= 0.54$ and 0.59) of the downstream open girder was minor. Furthermore, $2A\eta(\text{max})/D$ (about 0.75) of the downstream closed girder was about 1.3 times as much as $2A\eta(\text{max})/D$ ($= 0.54/0.59$) of the downstream open girder (Fig. 4-16). Therefore, introducing the side-surface openings to the upstream closed girder did not affect the vortex-induced vibration of the downstream girder. The side-surface openings of downstream girders can mitigate the vortex-induced vibration of itself by reducing the largest amplitude by about 21%, irrespective of the type of the upstream girder.

According to Fig. 4-17, at $\alpha = +3^\circ$, the downstream girders only showed the vortex-induced vibration, while the galloping did not occur. According to Fig. 4-18, H_1^* showed a continually negative magnitude at $U_r < 100$, indicating that the downstream girder did not show galloping instability. Meanwhile, all the cases showed the almost same H_1^* at high wind velocity, indicating that the side-surface openings of both the upstream girder and downstream girder did not affect the aerodynamic damping of the downstream girder at high wind velocity range.

In summary, the side-surface openings of the upstream girder did not affect the vortex-induced vibration of the downstream girder. However, the side-surface openings of the downstream girder stabilized the vortex-induced vibration of the downstream girder by reducing the largest amplitude by about 21%.

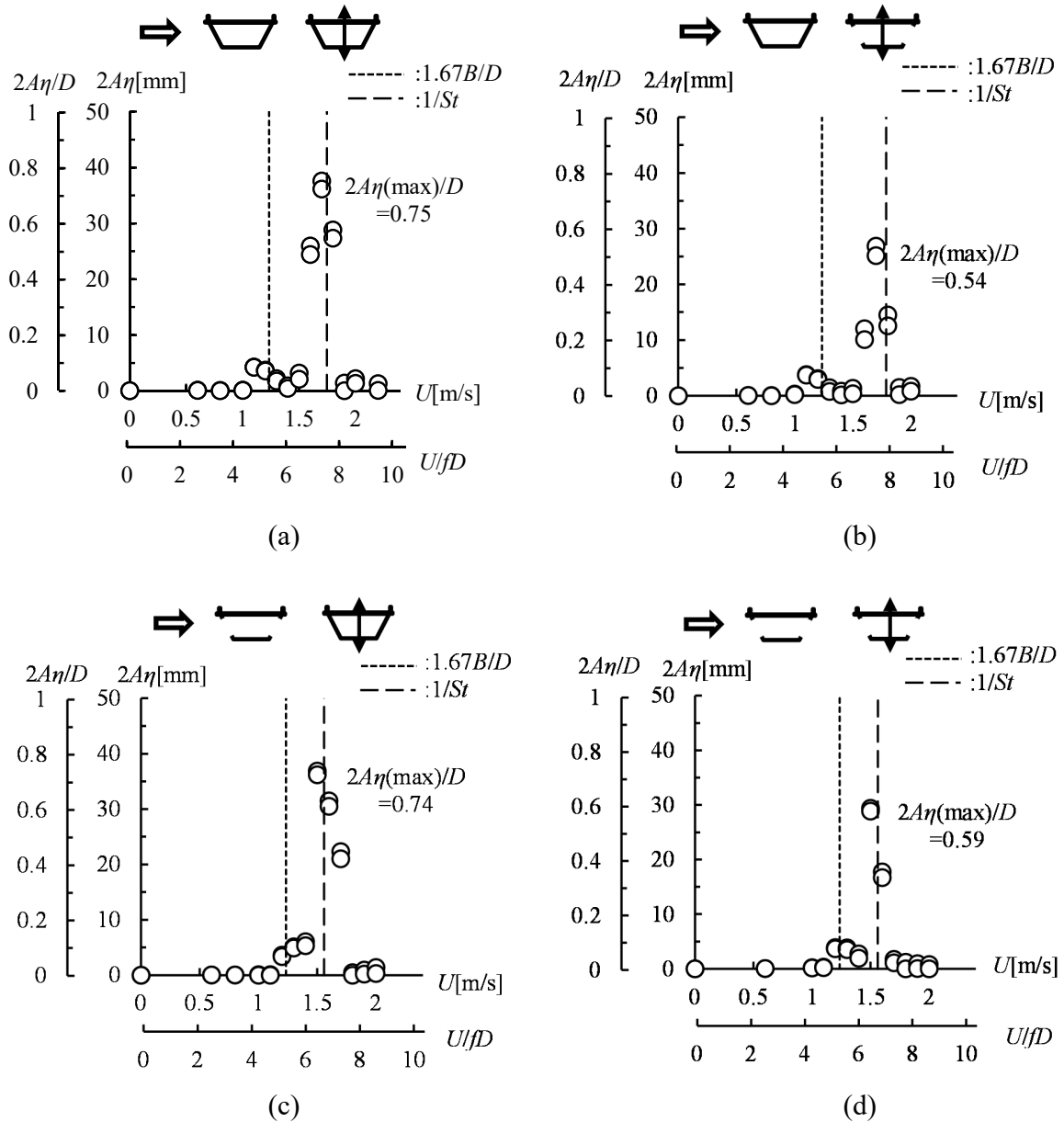


Fig. 4-16 Vortex-induced vibration for (vertical 1DOF, $\alpha = 0^\circ$, smooth flow): (a) downstream closed girder with a fixed upstream closed girder; (b) downstream closed girder with a fixed upstream open girder; (c) downstream open girder with a fixed upstream closed girder; (d) downstream open girder with a fixed upstream open girder.

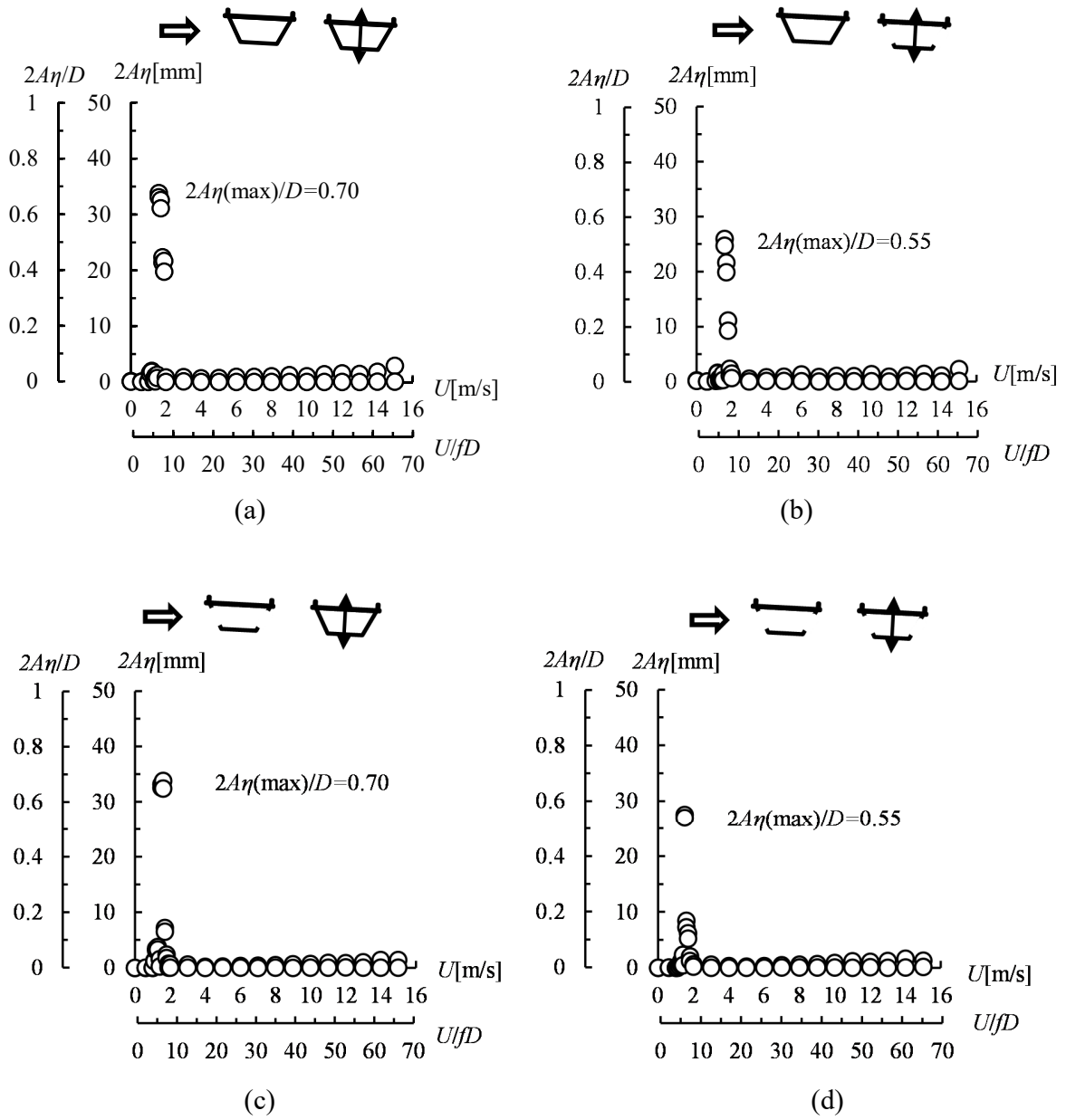


Fig. 4-17 Aerodynamic response for (vertical 1DOF, $\alpha = +3^\circ$, smooth flow): (a) downstream closed girder with a fixed upstream closed girder; (b) downstream closed girder with a fixed upstream open girder; (c) downstream open girder with a fixed upstream closed girder; (d) downstream open girder with a fixed upstream open girder.

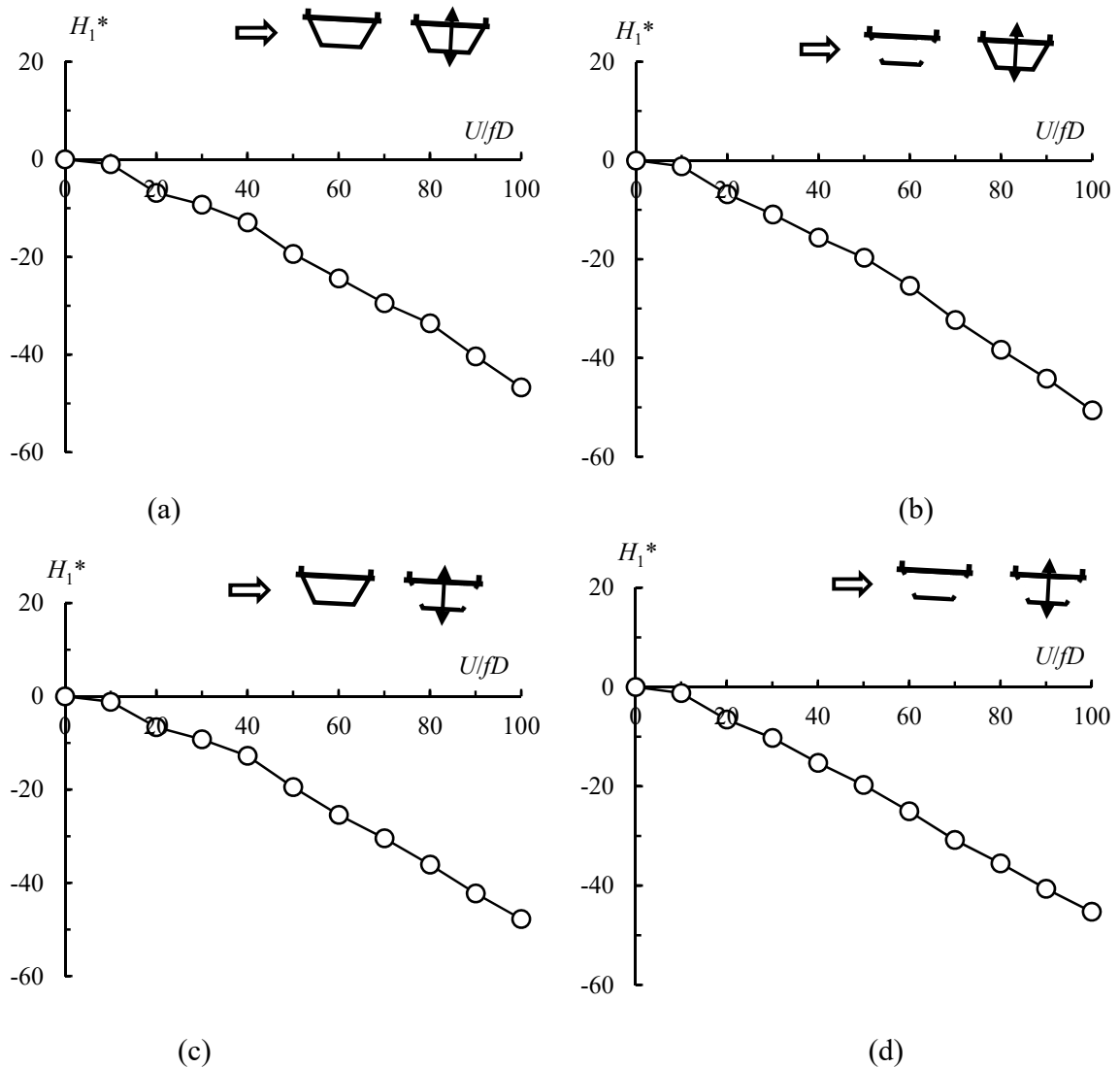


Fig. 4-18 Aerodynamic derivative H_1^* for (vertical 1DOF, $\alpha = 3^\circ$, $f = 2.0\text{Hz}$, $2A\eta = 20\text{mm}$, smooth flow): (a) downstream closed girder with a fixed upstream closed girder; (b) downstream open girder with a fixed upstream closed girder; (c) downstream closed girder with a fixed upstream open girder; (d) downstream open girder with a fixed upstream open girder.

4.6 Conclusion remarks

The proposition of this chapter was to study the effects of side-surface openings on the aerodynamic interference between two box girders in the tandem arrangement. A series of wind tunnel tests, i.e., aerodynamic force tests, vertical 1DOF free vibration tests, vertical 1DOF forced vibration tests, was carried out for two butterfly web girders with a side ratio B/D of 3.24 arranged in tandem. For simplicity, either of the two girders was fixed to the wind tunnel wall, and the other girder was investigated with regard to aerodynamic damping and vibration responses. The center

distance between two girders was twice the girder width. The following conclusions have been summarized:

- Owing to the blockage of the flow entrainment in the wake of the upstream girder, the downstream girder suppressed the vortex shedding from the upstream girder by controlling the fluctuating lift force coefficient (C_{Fy}') and reduced Strouhal number of the upstream girder. Furthermore, the lift force coefficients (C_{Fy}) were also amplified owing to the downstream girder, indicating the strong impact of the downstream girder on the time-averaged flow around the upstream girder. Meanwhile, introducing side-surface openings to the downstream girder did not affect the aerodynamic forces coefficients (drag force C_{Fx} , C_{Fy} , C_{Fy}') of the upstream girder. Introducing the side-surface openings to the upstream girder did not affect the Strouhal number of the upstream girder but minimized C_{Fy} , indicating that the upstream-girder openings significantly changed the time-averaged flow around the upstream girder.
- The aerodynamic force coefficients (C_{Fx} , C_{Fy} and C_{Fy}') of the downstream girder were significantly affected by the vortex shedding from the upstream girder. The synchronization between the vortex shedding from the upstream girder and the vortex formation of the downstream girder led to the same Strouhal number of the upstream and downstream girders. Introducing the openings to the downstream girder did not affect the aerodynamic force coefficients (C_{Fx} , C_{Fy} and C_{Fy}') of the downstream girder, while the aerodynamic force coefficients (C_{Fx} , C_{Fy} and C_{Fy}') of the downstream girder were slightly affected by introducing the openings to the upstream girder.
- The fixed downstream closed girder did not affect the motion-induced vortex vibration of the upstream girder but made it more unstable in the galloping by minimizing the critical wind velocity and amplifying the vibration amplitude and aerodynamic damping (H_1^*). Introducing the side-surface openings to the downstream closed girder did not affect the aerodynamic performance of the upstream girder, regarding the vibration amplitude and aerodynamic damping (H_1^*). The side-surface openings of the upstream girder stabilized its motion-induced vortex vibration. The side-surface openings of the upstream girder also stabilized its galloping by increasing the critical wind velocity and minimizing the vibration amplitude and aerodynamic damping (H_1^*).
- The periodic turbulent flow from the fixed upstream girder slightly increased the critical wind velocity of the vortex-induced vibration of the downstream girder owing to the decrease of the Strouhal number, which is caused by the synchronization between the vortex shedding from the upstream girder and the vortex formation of the downstream girder. The turbulent flow from the upstream girder also amplified the vortex-induced

vibration of the downstream girder in amplitude. Meanwhile, the turbulent flow from the upstream girder totally stabilized the downstream girder against the galloping. The side-surface openings of the fixed upstream girder did not affect the aerodynamic response of the downstream girder. While the side-surface openings of the downstream girder stabilized the vortex-induced vibration of the downstream girder in vibration amplitude.

The box girder was more unstable in the galloping when it was accompanied by the other girder in the wake, while the box girder was more unstable in the vortex-induced vibration when it was in the wake of the other girder. These aerodynamic instabilities can be stabilized by the side-surface openings.

Reference

- Argentini, T., Rocchi, D., Zasso, A., 2015. Aerodynamic interference and vortex-induced vibrations on parallel bridges: The Ewijk bridge during different stages of refurbishment. *J. Wind Eng. Ind. Aerodyn.* 147, 276–282. <https://doi.org/10.1016/j.jweia.2015.07.012>
- Bearman, P., Trueman, D., 1972. An Investigation of the Flow around Rectangular Cylinders. *Aeronautical Quarterly.* 23(3), 229-237. <https://doi.org/10.1017/S0001925900006119>
- Gerrard, J.H., 1966. The mechanics of the formation region of vortices behind bluff bodies. *J. Fluid Mech.* 25, 401–413. <https://doi.org/10.1017/S0022112066001721>
- Honda, A., Shiraishi, N., Motoyama S., Fuse, Y., Sumi, K., Sasaki, N., 1990. Aerodynamic stability of Kansai International Airport Access Bridge. *J. Wind Eng. Ind. Aerodyn.* 33, 369-376. [https://doi.org/10.1016/0167-6105\(93\)90047-R](https://doi.org/10.1016/0167-6105(93)90047-R).
- Kimura, K., Shima, K., Sano, K., Kubo, Y., Kato, K., Ukon, H., 2008. Effects of separation distance on wind-induced response of parallel box girders. *J. Wind Eng. Ind. Aerodyn.* 96, 954–962. <https://doi.org/10.1016/j.jweia.2007.06.021>
- Kim, S.-J., Kim, H.-K., Calmer, R., Park, J., Kim, G.S., Lee, D.K., 2013. Operational field monitoring of interactive vortex-induced vibrations between two parallel cable-stayed bridges. *J. Wind Eng. Ind. Aerodyn.* 123, 143–154.
- Lee, B.E., 1975. The effect of the turbulence on the surface pressure field of a square cylinder. *J. Fluid Mech.* 69, 263–382. <https://doi.org/10.1017/S0022112075001437>
- Matsumoto, M., Hashimoto, M., Yagi, T., Nakase, T., Maeta, K., 2008. Steady Galloping / Unsteady Galloping and Vortex-Induced Vibration of Bluff Bodies Associated With Mitigation of Karman Vortex Shedding. *Proc., 6th Int. Colloq. Bluff Bodies Aerodyn. & Appl.* 20–24. Milan, Italy.
- Meng, X.L., Zhu, L.D., Guo, Z.S., 2011. Aerodynamic interference effects and mitigation measures on vortex induced vibrations of two adjacent parallel bridges. *Front. Archit. Civ. Eng. China.* 5(4), 510–517. <https://doi.org/10.1007/s11709-011-0129-3>

Okajima, A., Kiwata T., 1990a. “Aerodynamic characteristics of two rectangular cylinders in a tandem arrangement.” *Kozo Kogaku Ronbunshu. (J. Structural Eng. A)*, 36, 849-857 (in Japanese).

Okajima, A., Abe, A., and Kiwata, T., 1990b. “Aeroelastic instability of two rectangular cylinders in a tandem arrangement.” *Kozo Kogaku Ronbunshu. (J. Structural Eng. A)*, 36, 859-864 (in Japanese).

Park, J., Kim, S., Kim, H.K., 2017a. Effect of gap distance on vortex-induced vibration in two parallel cable-stayed bridges. *J. Wind Eng. Ind. Aerodyn.* 162, 35–44. <https://doi.org/10.1016/j.jweia.2017.01.004>

Park, J., Kim, H.K., 2017b. Effect of the relative differences in the natural frequencies of parallel cable-stayed bridges during interactive vortex-induced vibration. *J. Wind Eng. Ind. Aerodyn.* 171, 330–341. <https://doi.org/10.1016/j.jweia.2017.10.010>

Seo, J. W., Kim, H. K., Park, J., Kim, K. T., and Kim, G. N., 2013. Interference effect on vortex-induced vibration in parallel twin cable-stayed bridge. *J. Wind Eng. Ind. Aerodyn.* 116, 7-20. <https://doi.org/10.1016/j.jweia.2013.01.014>

Sakamoto, H., Hainu, H., Obata, Y., 1987. Fluctuating forces acting on two square prisms in a tandem arrangement. *J. Wind Eng. Ind. Aerodyn.* 26, 85–103. [https://doi.org/10.1016/0167-6105\(87\)90037-7](https://doi.org/10.1016/0167-6105(87)90037-7)

Sohankar, A., 2008. Large eddy simulation of flow past rectangular-section cylinders: Side ratio effects. *J. Wind Eng. Ind. Aerodyn.* 96, 640–655.

Takeuchi, T., Matsumoto, M., 1992. Aerodynamic response characteristics of rectangular cylinders in tandem arrangement. *J. Wind Eng. Ind. Aerodyn.* 41, 565–575. [https://doi.org/10.1016/0167-6105\(92\)90466-N](https://doi.org/10.1016/0167-6105(92)90466-N)

Yagi, T., Shinjo, K., Narita, S., Nakase, T., Shirato, H., 2013. Interferences of vortex sheddings in galloping instability of rectangular cylinders. *Journal of Structural Engineering. A (JSCE)*. 59A, 552–561 (in Japanese).

5 Effects of side-surface openings on galloping instability of rectangular cylinder

5.1 Introduction

This chapter presents a more profound understanding of the mechanism related to the stabilization against the galloping instability owing to the side-surface openings. As illustrated in section 3.3.2, the side-surface openings make the box girder more stable in the galloping vibration. Nonetheless, it still lacks general conclusions regarding the relationship between the size of the openings and the galloping instability, e.g., vibration amplitude, critical wind velocity of galloping, aerodynamic damping and etc. Another question remains regarding what the mechanism is for the mitigation effects of the openings on the galloping. To answer these questions, the $B/D = 3.24$ butterfly web girder is simplified as the $B/D = 2$ rectangular cylinder for the experimental investigation.

The vortex shedding can stabilize the galloping until the reduced wind velocity characterized as the reciprocal of Strouhal number (Parkinson and Brooks, 1961; Parkinson, 1989; Novak, 1972; Massai, 2016; Mannini, et al., 2014). With the increase of turbulence intensity, for the low mass-damping system, the critical wind velocity of galloping increases accompanied by the decrease of Strouhal number (2018). Meanwhile, with the increase of the side ratio from 2 to 2.8, the onset of galloping increases also accompanied by the decrease of Strouhal number as explained in section 2.3.3. However, the side-surface openings do not affect the Strouhal number, but obviously stabilize the galloping by increasing the critical wind velocity for the $B/D = 3.24$ butterfly web girder. This chapter intends to investigate firstly what is the effects of the opening size are on the relationship between Strouhal number and critical wind velocity of galloping, which is core in stabilizing the galloping.

According to the quasi-steady theory, the force acting on an oscillating body can be expressed as the force acting on the stationary body, which is subject to the relative wind velocity (sum vector of the approaching wind velocity and the instantaneous vibration velocity). For the forced vibration, of which the variables are reduced to amplitude and frequency compared with the free vibration tests, the aerodynamic damping is asymptotic to the linear quasi-steady aerodynamic damping (Nakamura and Mizota, 1975; Obasaju, 1983; Washizu et al., 1978; Yagi et al., 2013). Because the flow can get through the inner space of the model, one question under concern is whether the quasi-steady theory is valid in predicting the asymptotic behavior of the aerodynamic damping of the rectangular cylinder with openings at high wind velocities. Furthermore, what is the relationship between the size of the openings and the aerodynamic damping at high wind velocities?

The turbulence flow, the vortex shedding, and the afterbody, defined as the portion of the body downstream of the separation point or the entire cross-section, all play an important role in galloping instability, as explained in section 2.3. Meanwhile, these factors all affect the galloping

instability by changing the reattachment of the shear layer on the side surface. For example, the higher turbulence promotes the reattachment of the shear layer on the side surface indicating a strong interference between the shear layer and the afterbody, subsequently stabilizing the galloping. This provides an important clue for the stabilization mechanism against galloping owing to side-surface openings. This chapter also intends to investigate what the effects of openings are on the time-averaged flow field, which qualitatively indicates the interference strength between the separated flow and the side surface.

In this chapter, firstly, the details of the wind tunnel tests are outlined, including the model details and case list. Secondly, the relationship between the size of the openings and the aerodynamic performance, i.e. the amplitude of the vortex-induced vibration, the critical wind velocity of galloping and the aerodynamic damping, are evaluated. It is assumed that an effective change in the side ratio owing to the change in the opening size leads to the change in the onset of galloping. This assumption is falsified by evaluating the change of aerodynamic force coefficient and Strouhal number with the opening size. Thirdly, the flow field around the model in the vertical plane is monitored through the PIV method along with the flow field in the inner space and the wake of the model in the horizontal plane. Additionally, the wind velocity through the inner space of the model into the wake is measured by the hotwire. The change in the flow field in the vertical plane owing to the change in the opening size is qualitatively explained based on the change in the flow field in the inner space and wake of the model in the horizontal plane. The change in the time-averaged flow in the vertical plane with the opening size qualitatively explains the change of the aerodynamic damping with the opening size and falsifies the assumption that the side openings effectively changed the side ratio stabilizing the galloping.

5.2 Set-up of wind tunnel tests

In order to investigate the relationship between the size of the openings and the aerodynamic performance, vertical one-degree-of-freedom (1DOF) free vibration tests, vertical 1DOF forced vibration tests and aerodynamic force tests are carried out. The model details and case list are explained at first. Then the details of the free vibration tests, aerodynamic force tests and forced vibration tests are explained.

5.2.1 The detail of the model and case list

The main body of the model for wind tunnel tests is shown in Fig. 5-1 (a). The model has a length (l) of 900mm. As shown in Fig. 5-1 (b), the model was with a side ratio B/D of 2, where the width (B) and the depth (D) were 140 mm and 70 mm, respectively. The rectangular cylinder with a side ratio of 2 should show galloping and motion-induced vortex vibration. Owing to an open space with a height (D_0) of 35mm in the center of the model (Fig. 5-1 (b)), the flow can get through the inner space of the model. The height (D_0) of the open inner space was set as half of the model depth to reflect the real condition for the bridge section (Fig. 3-1). Here, the concept of the effective

side ratio B'/D' , where B' is the effective body width and D' is the effective body depth, is introduced for the convenience of further discussion.

According to Fig. 5-2, the discretely distributed openings were realized by attaching the plastic plates to the front/rear surface in a constant interval. The size of the openings is decided based on two parameters, i.e., Opening-area Ratio (OR) and Repeating Element-size Ratio (RER). OR and RER are defined as follows (Fig. 5-2):

$$OR = S_1/(S_1 + S_2) = l_1/(l_1 + l_2) \quad \text{Eq. 5-1}$$

$$RER = (l_1 + l_2)/D_0 \quad \text{Eq. 5-2}$$

where l_1 and l_2 are the widths of the opening and plastic plate, respectively; D_0 is the height of the openings. OR represents the ratio between the area of the total openings and the front-surface area of the inner space. For a certain OR , RER represents the ratio of the width of a repeating element (consisting of one plate and one opening) to the inner-space height. The model with openings of different OR and RER was listed in Table 5-1. Case 1 represents the rectangular cylinder without openings, Case 10 represents the case that the inner space is totally opened without any cover. Cases 2-5 represent the rectangular cylinder with different OR for $RER = 1.07$, while Cases 6-9 represent the rectangular cylinder with different OR for $RER = 2.14$.

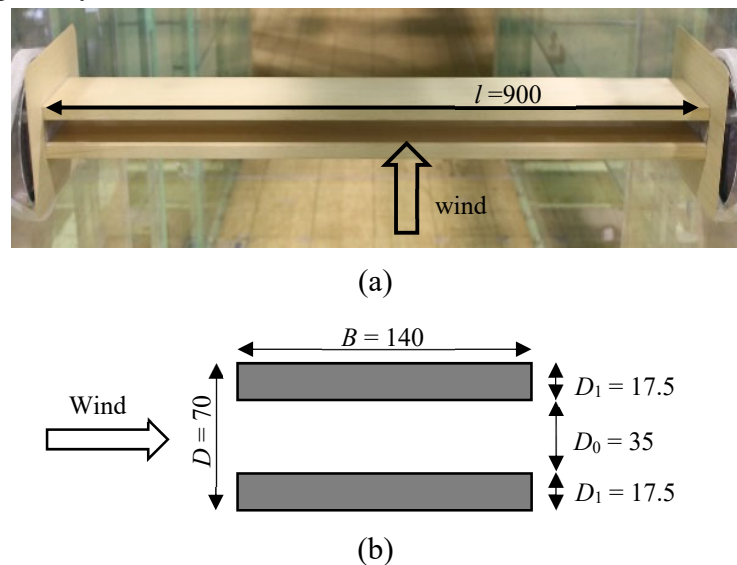


Fig. 5-1 Model information: (a) main body; (b) model section (unit: mm).

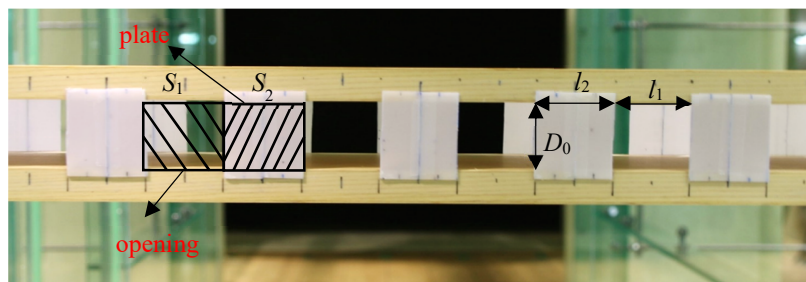
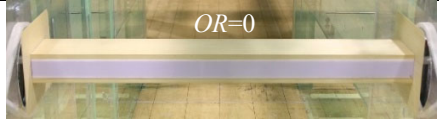
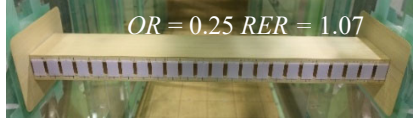

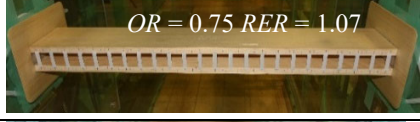
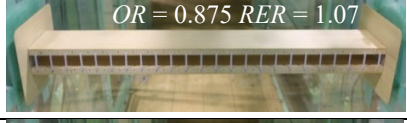

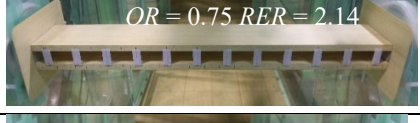
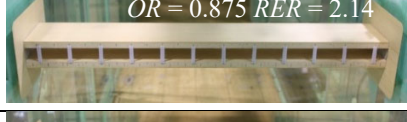


Fig. 5-2 Detail of side-surface openings

Table 5-1 Case lists of wind tunnel tests

Case name	Opening-area Ratio (<i>OR</i>)	Repeating Element-size Ratio (<i>RER</i>)	Configuration
Case 1	0		 <i>OR</i> =0
Case 2	0.25	1.07	 <i>OR</i> = 0.25 <i>RER</i> = 1.07
Case 3	0.50		 <i>OR</i> = 0.5 <i>RER</i> = 1.07
Case 4	0.75		 <i>OR</i> = 0.75 <i>RER</i> = 1.07
Case 5	0.875		 <i>OR</i> = 0.875 <i>RER</i> = 1.07
Case 6	0.25		2.14
Case 7	0.50	 <i>OR</i> = 0.5 <i>RER</i> = 2.14	
Case 8	0.75	 <i>OR</i> = 0.75 <i>RER</i> = 2.14	
Case 9	0.875	 <i>OR</i> = 0.875 <i>RER</i> = 2.14	
Case 10	1		

5.2.2 Free vibration test

The $B/D = 2$ rectangular cylinder should show the vortex-induced vibration and the galloping. To investigate the effects of the different-sized openings on the vortex-induced vibration and the galloping, the vertical one-degree-of-freedom (1DOF) free vibration tests were conducted. The model was supported by 8 springs and the displacement was measured by four laser gages at $\alpha =$

0° in the smooth flow. The current research mainly focuses on the aerodynamic response for the low mass-damping system. The galloping for the low mass-damping system is referred to as ‘full interaction between vortex-induced vibration and galloping’ (Gao and Zhu, 2016; Mannini et al., 2014), which starts from the resonance wind velocity characterized by the reciprocal of the Strouhal number. The mass and damping were minimized for the convenience of the discussion on the effects of the different sized openings on the relationship between the critical wind velocity of galloping and Strouhal number. Furthermore, the mass and damping of the system were also minimized as possible to facilitate observation of the aerodynamic response and were kept the same for all the cases for the convenience of comparison (Table 5-2).

Table 5-2 Characteristic parameters for free vibration tests of different cases (vertical one degree of freedom 1DOF, smooth flow)

Case name	OR	RER	m (kg/m)	f (Hz)	δ_η ($2A_\eta = 5\text{mm}$)	$Sc\eta$
Case 1	0		3.26	4.52	0.0030	3.4
Case 2	0.25	1.07	3.25	4.53	0.0027	3.0
Case 6		2.14	3.25	4.53	0.0031	3.5
Case 4	0.75	1.07	3.31	4.49	0.0026	3.0
Case 8		2.14	3.31	4.49	0.0021	2.4
Case 10	1		3.27	4.51	0.0025	2.8

5.2.3 Aerodynamic force test on stationary girder

The aerodynamic forces were measured through the load cell rigidly connected to the model in the smooth flow. Because the model section is symmetry to its centerline, the aerodynamic forces were measured at $\alpha = -2^\circ \sim 10^\circ$, where α is the angle of attack to mean wind and is positive in nose-up direction (Fig. 2-17). The lift (C_{Fy}) and drag (C_{Fx}) force coefficients, fluctuating lift force coefficient (C_{Fy}) and Strouhal number (St) were measured. The tests were carried out in the smooth flow, and the approaching wind velocity is 6m/s. For the rectangular cylinder with openings, the real area of the front/rear surface does not include the area of the openings. Therefore, the ‘real’ drag force coefficient C_{Fxr} (Eq. 5-3) was calculated based on the real area of the rear surface as follows:

$$C_{Fxr} = \frac{F_x}{\frac{1}{2}\rho U^2 D l} \times \frac{2}{2 - OR} \quad \text{Eq. 5-3}$$

5.2.4 Forced vibration test

To investigate the relationship between the opening size and the linear unsteady aerodynamic damping, the vertical 1DOF forced vibration tests were carried out for the models. The self-excited lift force was measured by the load cells rigidly connected to the model under the vertical 1DOF sinusoidal oscillation at $\alpha = 0^\circ$ in the smooth flow; the displacement of the model was simultaneously recorded using laser gages. The aerodynamic derivatives were then calculated based on the self-excited lift force and displacement. The linear unsteady aerodynamic damping in the vertical direction is characterized by the identified aerodynamic derivative H_1^* , the positive value of which indicates the instability in the vertical direction (Scanlan and Tomko, 1971; Matsumoto, 1996). The effects of the openings on the galloping were discussed by comparing the aerodynamic damping H_1^* of the rectangular cylinder with different sized openings. To obtain large enough self-excited force, the vertical amplitude and frequency were set to 5 mm and 2.6 Hz, respectively. Furthermore, the inertial forces were set to a small value by minimizing the mass, and the inertial forces were removed to obtain the accurate aerodynamic self-excited force.

5.3 Opening size and galloping instability

In this section, the relationship between the aerodynamic performance and the size of the side-surface openings is illustrated. As mentioned in 5.2.1, the size of the openings was described by two parameters, Opening-area Ratio (*OR*) and Repeating Element-size Ratio (*RER*). Firstly, based on the vertical 1DOF aerodynamic response, the effects of *OR* and *RER* on the vortex-induced vibration and galloping vibration, i.e. the vibration amplitude and the onset wind velocity, are evaluated. Secondly, the effects of *OR* and *RER* on the aerodynamic damping are evaluated. Additionally, the asymptotic behavior of the linear unsteady aerodynamic damping to the linear quasi-steady aerodynamic damping is investigated to validate the quasi-steady theory for the rectangular cylinder with side-surface openings. Thirdly, the effects of the openings on the relationship between the critical wind velocity of galloping and Strouhal number are discussed. Based on the comparison between the change of aerodynamic force coefficient with the opening size and the change of the aerodynamic force coefficient with the side ratio, the assumption on the effective increase in the side ratio of the model owing to the increase of openings size is validated.

5.3.1 Vertical 1DOF aerodynamic response

The vertical 1DOF aerodynamic responses of the rectangular cylinder with different-sized openings are summarized in Fig. 5-3. $2A\eta/D$ is the non-dimensional double amplitude of the displacement, $A\eta$ being the amplitude of displacement (D the model depth). As explained before, U/fD is the reduced wind velocity, where U is the approaching wind velocity and f is the natural frequency of the system. Fig. 5-3 (a)-(d) shows the change of aerodynamic response with the increase of *OR* ($=0, 0.25, 0.75$ and 1) for *RER* = 1.07. Additionally, Fig. 5-3 (e)-(f) shows the results for the cases of *OR* = 0.25 and 0.75 for *RER* = 2.14. For the convenience to identify the

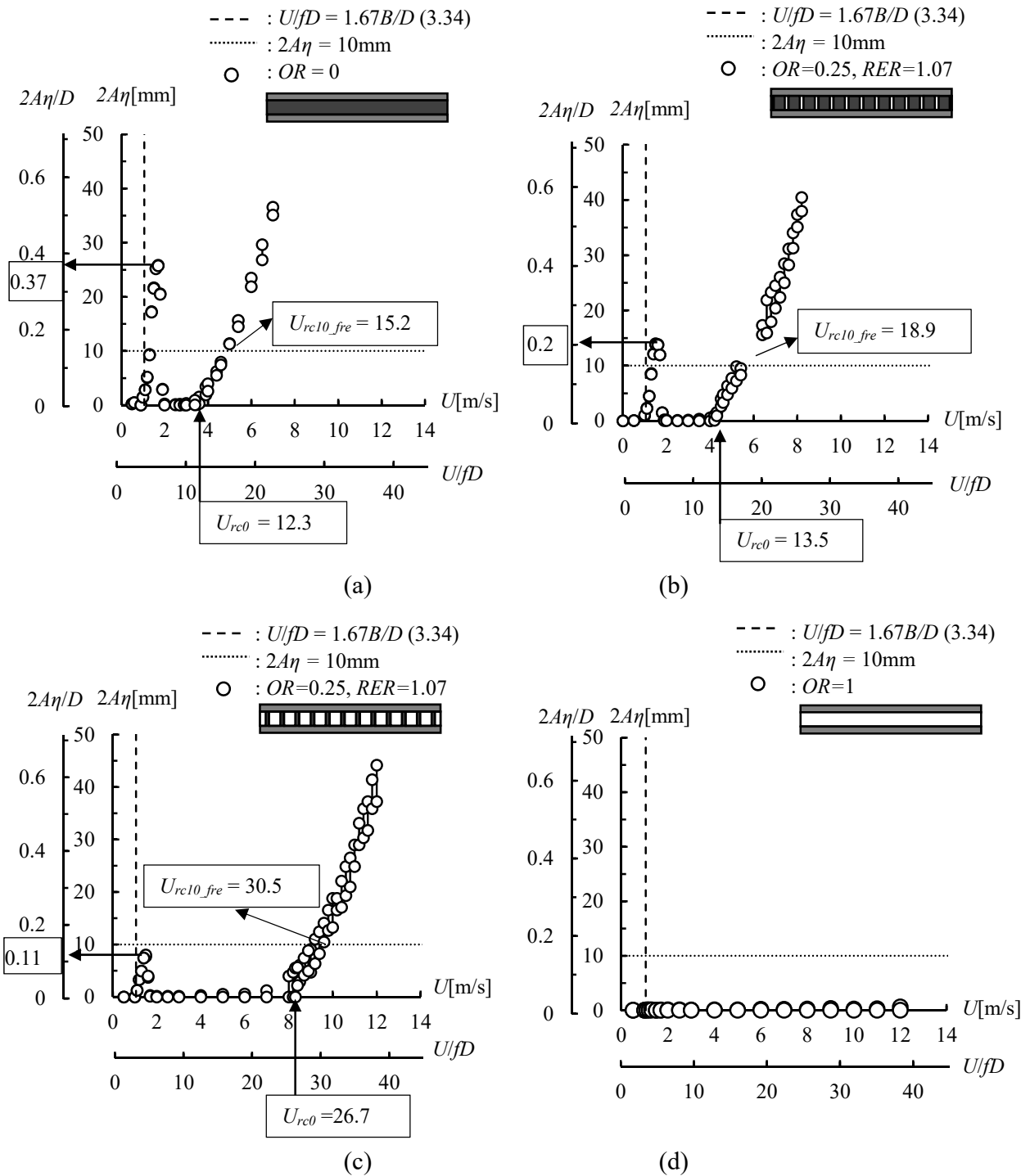


Fig. 5-3 Aerodynamic response of: (a) Case 1 ($OR=0$); (b) Case 2 ($OR=0.25, RER=1.07$); (c) Case 4 ($OR=0.75, RER=1.07$); (d) Case 10 ($OR=1$); (e) Case 6 ($OR=0.25, RER=2.14$); (f) Case 6 ($OR=0.75, RER=2.14$). (Vertical one degree of freedom (1DOF), $\alpha = 0^\circ$, smooth flow). U_{rc0} is the critical wind velocity of galloping corresponding to $2A\eta$ of 0mm. U_{rc10_fre} represents the wind velocity corresponding to $2A\eta$ of 10mm. f is the frequency of the system.

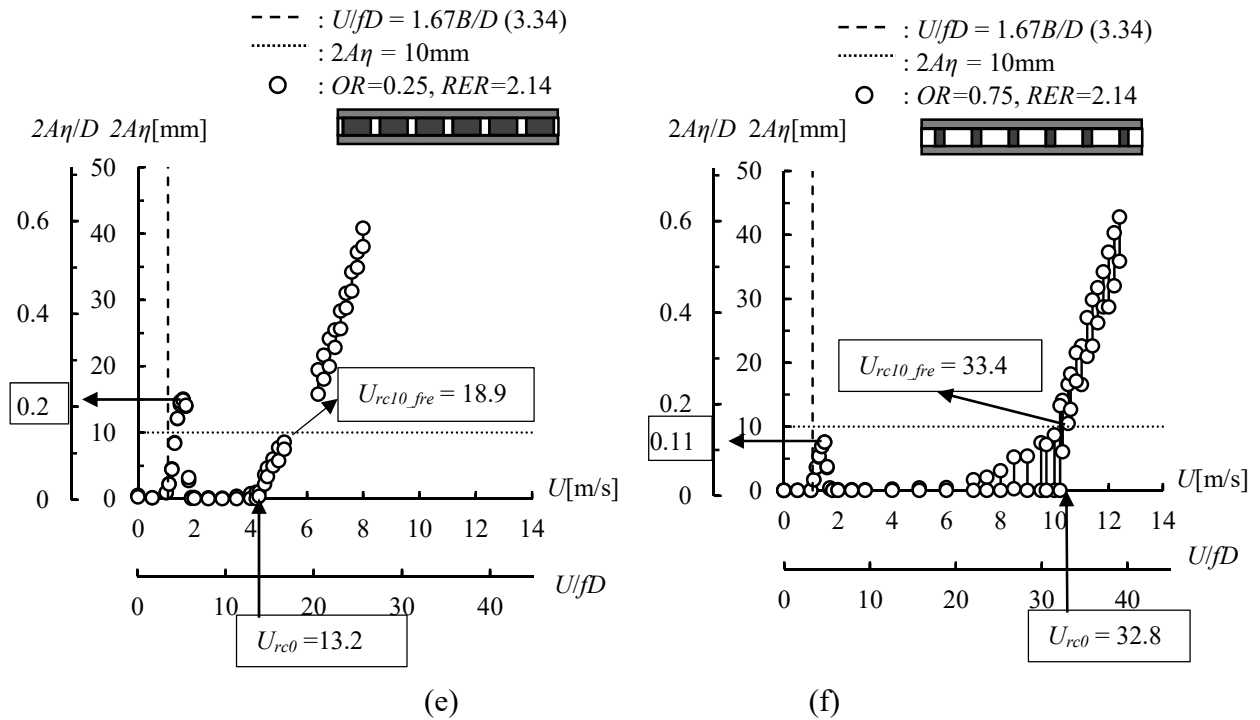


Fig. 5-3 Continued

cases, the front view of each case is included in the legend for each figure. According to Fig. 5-3, two phenomena, i.e., the vortex-induced vibration and galloping, were observed for all the cases except the case 10 ($OR = 1$) (Fig. 5-3 (e)), which did not show vibration at $U_r < 44$. The relationship between the size of the openings and those two phenomena are discussed separately.

Vortex-induced vibration

According to Fig. 5-3, one noticeable result is that for Case 1 ($OR = 0$), Case 2 ($OR = 0.25$, $RER = 1.07$), Case 4 ($OR = 0.75$, $RER = 1.07$), Case 6 ($OR = 0.25$, $RER = 2.14$), and Case 8 ($OR = 0.75$, $RER = 2.14$), the reduced critical wind velocity of vortex-induced vibration were constant ($U_r = 3.2$), which is close to the value of $1.67B/D$ (3.34). According to past research (Matsumoto et al. 2008), the vortex-induced vibration is roughly divided into two types: the Kármán-vortex and motion-induced types. Because the motion-induced vortex vibration occurs at $U_r = 1.67B/D$ (Matsumoto et al. 2008), the vortex-induced vibration for the current models (Cases 1, 2, 4, 6 and 8) is of the motion-induced type. The motion-induced vortex vibration is caused by the resonance between the system and the vortex convection along the surface. The velocity of the vortex convection along the surface is about 60% of the approaching wind velocity U (Kiya and Nozawa 1987). Because B is the same for all the cases, the same critical wind velocity of vortex-induced vibration for all the cases indicates that the openings did not affect the velocity of vortex

convection along the surface. Therefore, the critical wind velocity of the motion-induced vortex vibration was not affected by the openings.

According to Fig. 5-3 (a)-(d), another noticeable result is that for $RER = 1.07$, the largest reduced double amplitude of the motion-induced vortex vibration ($2A\eta(\max)/D$) gradually decreased from 0.37 to 0 with an increase of OR from 0 to 1. Meanwhile, by comparing Fig. 5-3 (b) and (e), for $OR = 0.25$, $2A\eta(\max)/D$ was almost the same (0.2) for $RER = 1.07$ and 2.14. By comparing Fig. 5-3 (c) and (f), for $OR = 0.75$, $2A\eta(\max)/D$ was almost the same (0.11) for $RER = 1.07$ and 2.14. Therefore, the amplitude of motion-induced vortex vibration was gradually minimized by increasing OR , while RER has no significant effects on the amplitude of the motion-induced vortex vibration.

In summary, the openings had no effects on the critical wind velocity of the motion-induced vortex vibration. RER had no significant effects on the amplitude of the motion-induced vortex vibration, while the amplitude of the motion-induced vortex vibration decreased with the increase of OR .

Galloping Instability

By comparing Fig. 5-3 (a)-(d), the effect of increasing OR was a progressive decrease of vibration amplitude at a certain wind velocity. Meanwhile, the reduced critical wind velocity (U_{rc0}) of galloping increased with OR ($U_{rc0} = 12.3$ for $OR = 0$; $U_{rc0} = 13.5$ for $OR = 0.25$; $U_{rc0} = 26.7$ for $OR = 0.75$) and galloping did not occur to Case10 ($OR = 1$). Additionally, for $OR = 0.25$ (Fig. 5-3 (b) and (e)), U_{rc0} was almost the same ($U_{rc0} = 13.5$) for $RER = 1.07$ and 2.14; whereas, for $OR = 0.75$ (Fig. 5-3 (c) and (f)), U_{rc0} was slightly different ($U_{rc0} = 26.7$ for $RER = 1.07$; $U_{rc0} = 32.8$ for $RER = 2.14$) for different RER . The reduced wind velocity (U_{rc10_fre}) corresponding to the stable double amplitude of $2A\eta = 10$ mm is marked by the cross point between the aerodynamic response and $2A\eta = 10$ (dot line) in the figure. By comparing Fig. 5-3 (b) and (e), for $OR = 0.25$, $2A\eta$ approached 10 mm at around $U_{rc10_fre} = 18.9$ for both $RER = 1.07$ and 2.14. By comparing Fig. 5-3 (c) and (f), for $OR = 0.75$, $2A\eta$ approached 10 mm at $U_{rc10_fre} = 30.5$ for $RER = 1.07$ and at $U_{rc10_fre} = 33.4$ for $RER = 2.14$. Therefore, RER slightly affected the onset of galloping for the case of large OR (i.e., 0.75), whereas had no significant effects on that for small OR (i.e., 0.25). Once the galloping occurred, RER barely had effects on the aerodynamic response. OR played an important role in stabilizing the galloping owing to that the amplitude of galloping response decreased and the critical wind velocity of galloping increased obviously with the increase of OR .

5.3.2 Aerodynamic force characteristics

The aerodynamic response confirmed that the Opening-area Ratio (OR) played an important role in stabilizing the motion-induced vortex vibration and galloping. The relationship between the size of the openings and the galloping was further discussed based on the linear unsteady aerodynamic damping identified from the forced vibration tests and the linear quasi-steady

aerodynamic damping calculated based on the lift force coefficient. As explained in section 2.3.2, at high wind velocities, the linear unsteady aerodynamic damping approaches the linear quasi-steady aerodynamic damping (Nakamura and Mizota, 1975; Obasaju, 1983; Washizu et al., 1978; Yagi et al., 2013). According to the quasi-steady theory, the instantaneous aerodynamic forces acting on the oscillating cylinder equal to those of the stationary cylinder subject to the relative velocity $U_{rel} = (U^2 + \dot{\eta}^2)^{1/2}$, resulting from the relative angle of attack α_0 ($\alpha_0 = \arctan(\dot{\eta}/U)$, $\dot{\eta}$ is the vertical cylinder velocity). $\dot{\eta}$ is positive in the downward direction, while α_0 is positive in the nose-up direction. Therefore, based on the linear quasi-steady theory, the lift force L_{qs} (downward direction is positive) working on the oscillating body is:

$$L_{qs} = -\frac{1}{2}\rho U^2 B \frac{dC_{Fy}}{d\alpha} \frac{\dot{\eta}}{U} \quad \text{Eq. 2-14}$$

where η is the vertical 1DOF sinusoidal displacement (downward direction is positive). The galloping would occur at a certain wind velocity when $dC_{Fy}/d\alpha$ is negative. Furthermore, the self-excited lift force (downward direction is positive) working on the model under vertical 1DOF sinusoidal displacement is expressed as:

$$L_{se} = \frac{1}{2}\rho(2b)U^2 \left\{ kH_1^* \frac{\dot{\eta}}{U} + k^2 H_4^* \frac{\eta}{b} \right\} \quad \text{Eq. 2-29}$$

To compare with the aerodynamic damping H_1^* identified from the forced vibration tests, the H_1^* based on linear quasi-steady theory is calculated as:

$$H_1^* = -\frac{1}{k} \frac{dC_{Fy}}{d\alpha} \quad \text{Eq. 5-4}$$

The effects of *OR* and *RER* on galloping instability are discussed based on the aerodynamic damping as follows.

Opening-area Ratio (OR) and galloping instability

The distribution of lift force coefficients (C_{Fy}) against the angle of attack (α) for different Opening-area Ratio (*OR*) is shown in Fig. 5-4 and Fig. 5-5. Fig. 5-4 shows the cases of *RER* = 1.07, while Fig. 5-5 shows cases of *RER* = 2.14. Because the models were symmetry to the central lines, the distribution of C_{Fy} (defined on the structural axis) against α was zero-point antisymmetric. Therefore, C_{Fy} was shown only at $-2^\circ \leq \alpha \leq 10^\circ$. According to Fig. 5-4, with the increase of *OR* from 0 to 0.875, the angle of attack (α) range, where the lift slope $dC_{Fy}/d\alpha$ showed negative value, decreased ($-8^\circ \leq \alpha \leq 8^\circ$ for *OR* = 0; $-7^\circ \leq \alpha \leq 7^\circ$ for *OR* = 0.25; $-4^\circ \leq \alpha \leq 4^\circ$ for *OR* = 0.5; $-3^\circ \leq \alpha \leq 3^\circ$ for *OR* = 0.75; $-2^\circ \leq \alpha \leq 2^\circ$ for *OR* = 0.875). Meanwhile, $dC_{Fy}/d\alpha$ of Case 10 (*OR* = 1) was positive at $-10^\circ \leq \alpha \leq 10^\circ$. As shown in Fig. 5-5, the α range, where $dC_{Fy}/d\alpha$ was negative, also decreased with the increase of *OR* for *RER* = 2.14. Because the negative lift slope $dC_{Fy}/d\alpha$ indicates the galloping instability, with the increase of *OR*, the galloping would occur at a relatively smaller α range. Furthermore, $-dC_{Fy}/d\alpha$ at $\alpha = 0^\circ$ calculated based on C_{Fy} in Fig. 5-4 and Fig. 5-5 are summarized in Fig. 5-6. According to Fig. 5-6, $-dC_{Fy}/d\alpha$ increased from 2.4 to 13.9 with the

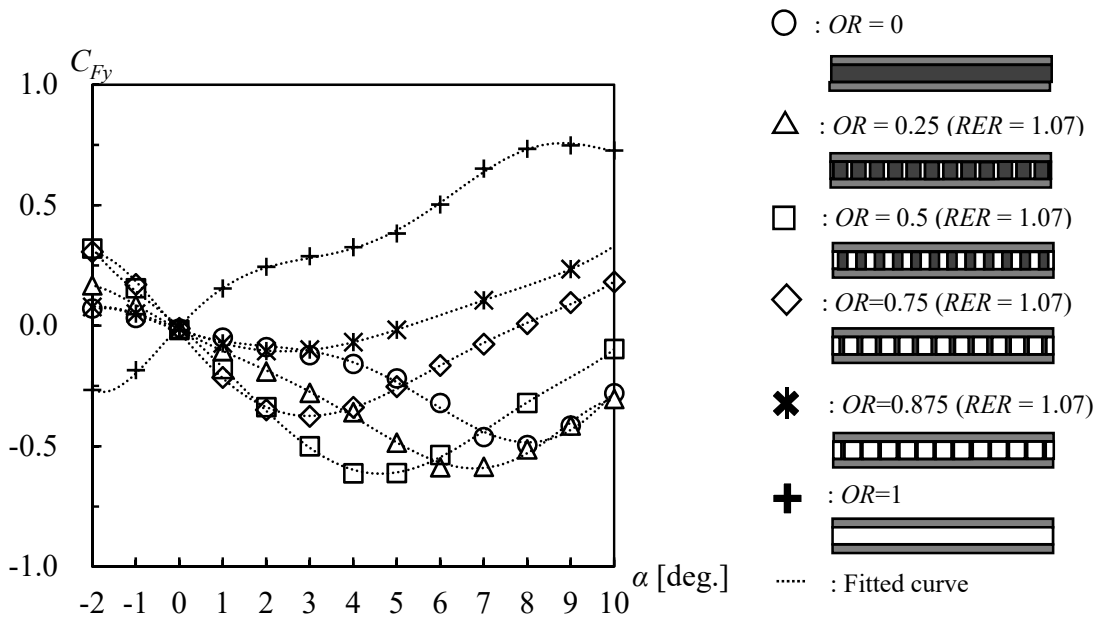


Fig. 5-4 Change of lift force coefficients with OR ($OR = 0, 0.25, 0.5, 0.75, 0.875$ and 1) for $RER = 1.07$ ($U = 6\text{m/s}$, smooth flow).

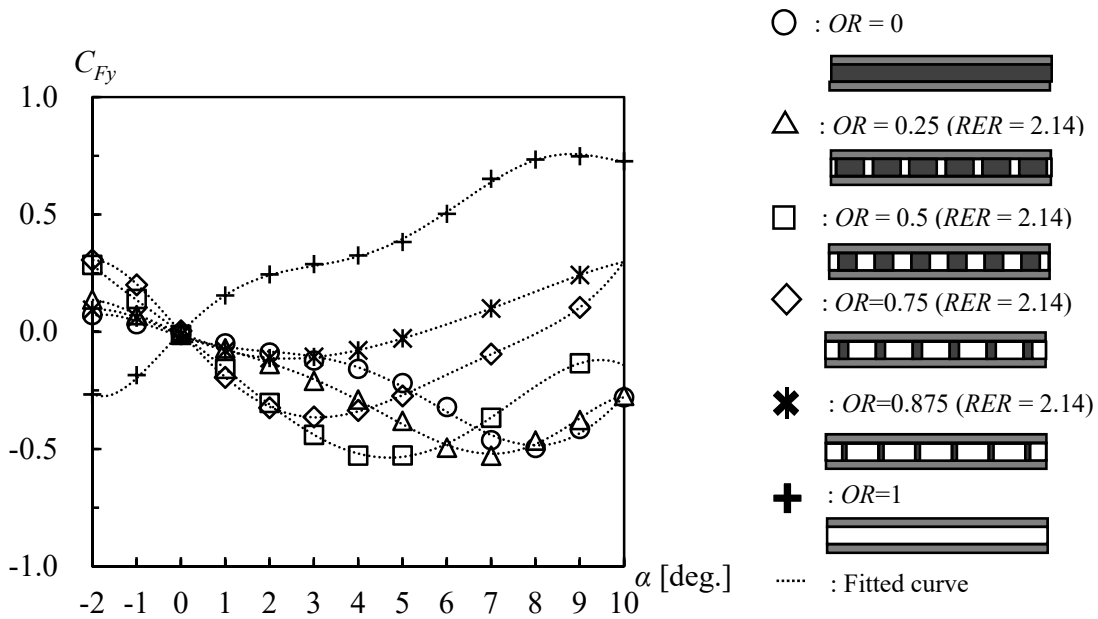


Fig. 5-5 Change of lift force coefficients with OR ($OR = 0, 0.25, 0.5, 0.75, 0.875$ and 1) for $RER = 2.14$ ($U = 6\text{m/s}$, smooth flow).

increase of OR from 0 to 0.75 and decreased from 13.9 to 5.8 with the increase of OR from 0.75 to 0.875. The relationship between $-dC_{Fy}/d\alpha$ and OR will be discussed later based on the time-averaged flow field. Furthermore, $-dC_{Fy}/d\alpha$ of the same OR was almost the same for $RER = 1.07$ and 2.14. Therefore, OR played an important role in determining the aerodynamic damping

characterized by $-dC_{Fy}/d\alpha$, whereas RER had no significant effects on the aerodynamic damping. In summary, with the increase of OR from 0 to 0.875, the galloping would occur at a relatively smaller α range and the galloping should not occur for $OR = 1$. Furthermore, the aerodynamic damping ($-dC_{Fy}/d\alpha$) increased with the increase of OR from 0 to 0.75 and then decreased with the increase of OR from 0.75 to 0.875.

To further discuss the effects of the openings on the aerodynamic damping, H_1^* for different OR is shown in Fig. 5-7 and Fig. 5-8. Fig. 5-7 includes the cases of $RER = 1.07$, while Fig. 5-8 includes the cases of $RER = 2.14$. Additionally, Fig. 5-7 and Fig. 5-8 include H_1^* identified from the forced vibration tests and calculated based on the linear quasi-steady theory. According to Fig. 5-7 and Fig. 5-8, for both $RER = 1.07$ and $RER = 2.14$, the reduced critical wind velocity of galloping, which is characterized by the change of H_1^* from the negative to the positive, gradually increased with the increase of OR from 0 to 0.875, and Case 10 ($OR = 1$) did not show galloping. Furthermore, even though there are some discrepancies between H_1^* identified from the forced vibration tests and H_1^* calculated based on the linear quasi-steady theory at low wind velocities, the former one gradually approached the latter one at high wind velocities. Therefore, at the high wind velocity range, the linear quasi-steady theory can predict the linear unsteady aerodynamic damping for the rectangular cylinder with openings. Meanwhile, at high wind velocities (about $Ur > 40$), H_1^* gradually increased with the increase of OR from 0, achieving the maximum at $OR = 0.75$, and then decreased with OR from 0.75 to 1.

In summary, the angle of attack (α) range, where the galloping would occur, decreased with the increase of OR . The critical wind velocity of galloping increased with the increase of OR from 0 to 0.875, while Case 10 ($OR = 1$) did not show galloping. The linear unsteady aerodynamic damping was asymptotic to the linear quasi-steady aerodynamic damping. At high wind velocities, the aerodynamic damping (H_1^*) increased with OR from 0 to 0.75, achieving its maximum value for $OR = 0.75$, and then decreased with OR from 0.75 to 1. These results confirmed that OR played an important role in the galloping instability.

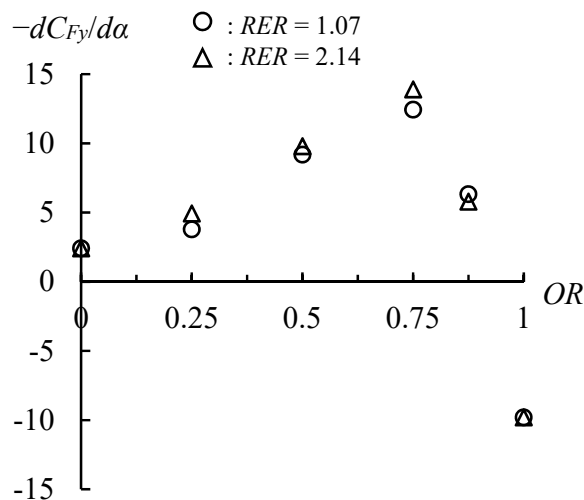


Fig. 5-6 Lift slope at angle of attack $\alpha = 0^\circ$. ($U = 6\text{m/s}$, smooth flow)

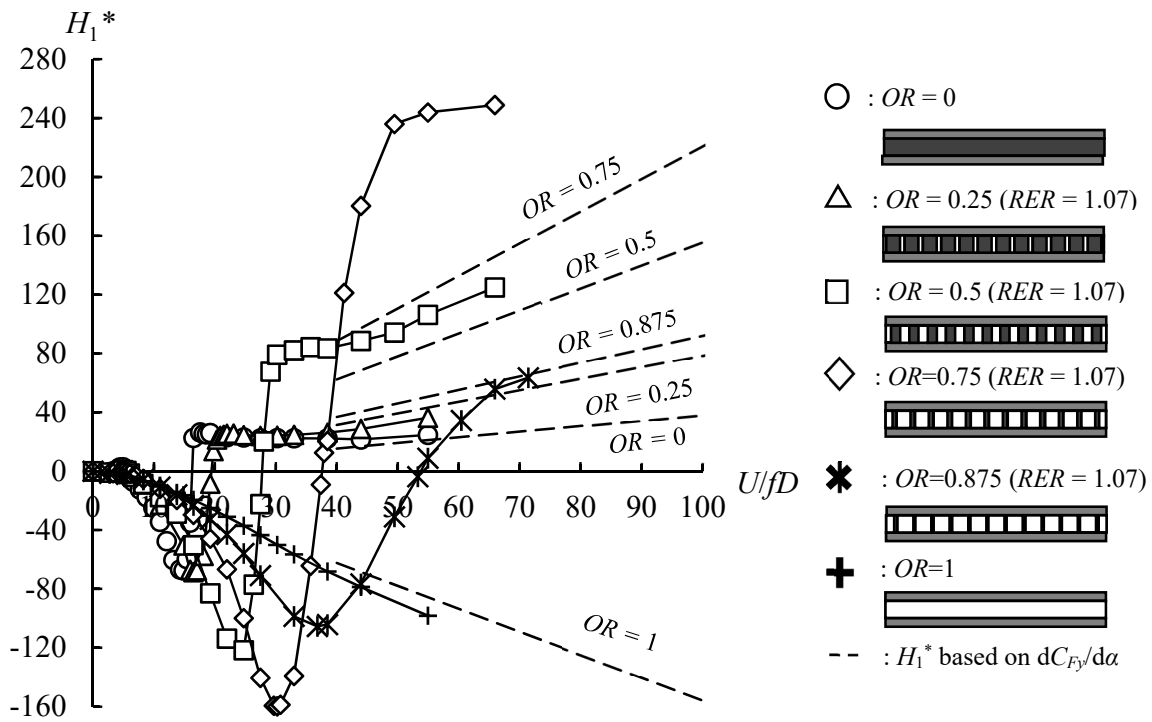


Fig. 5-7 Change of H_1^* with OR ($OR = 0, 0.25, 0.5, 0.75, 0.875$ and 1) for $RER = 1.07$ (smooth flow, $\alpha = 0^\circ, f = 2.6\text{Hz}, 2A_\eta = 10\text{mm}$).

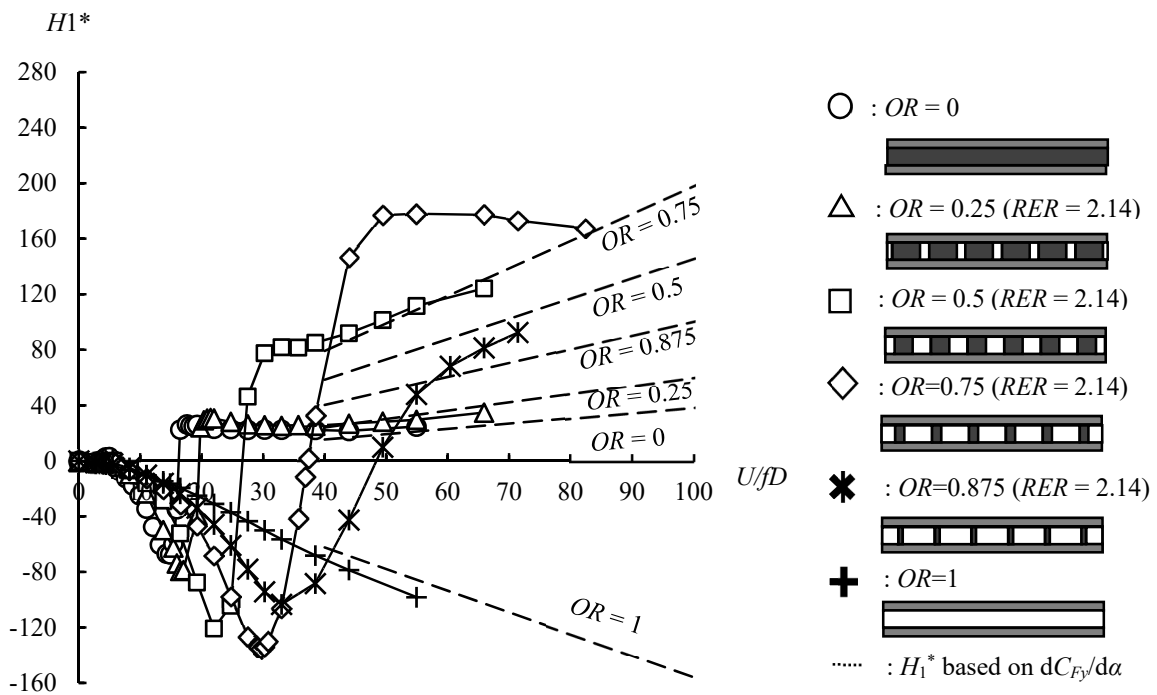


Fig. 5-8 Change of H_1^* with OR ($OR = 0, 0.25, 0.5, 0.75, 0.875$ and 1) for $RER = 2.14$ (smooth flow, $\alpha = 0^\circ, f = 2.6\text{Hz}, 2A_\eta = 10\text{mm}$).

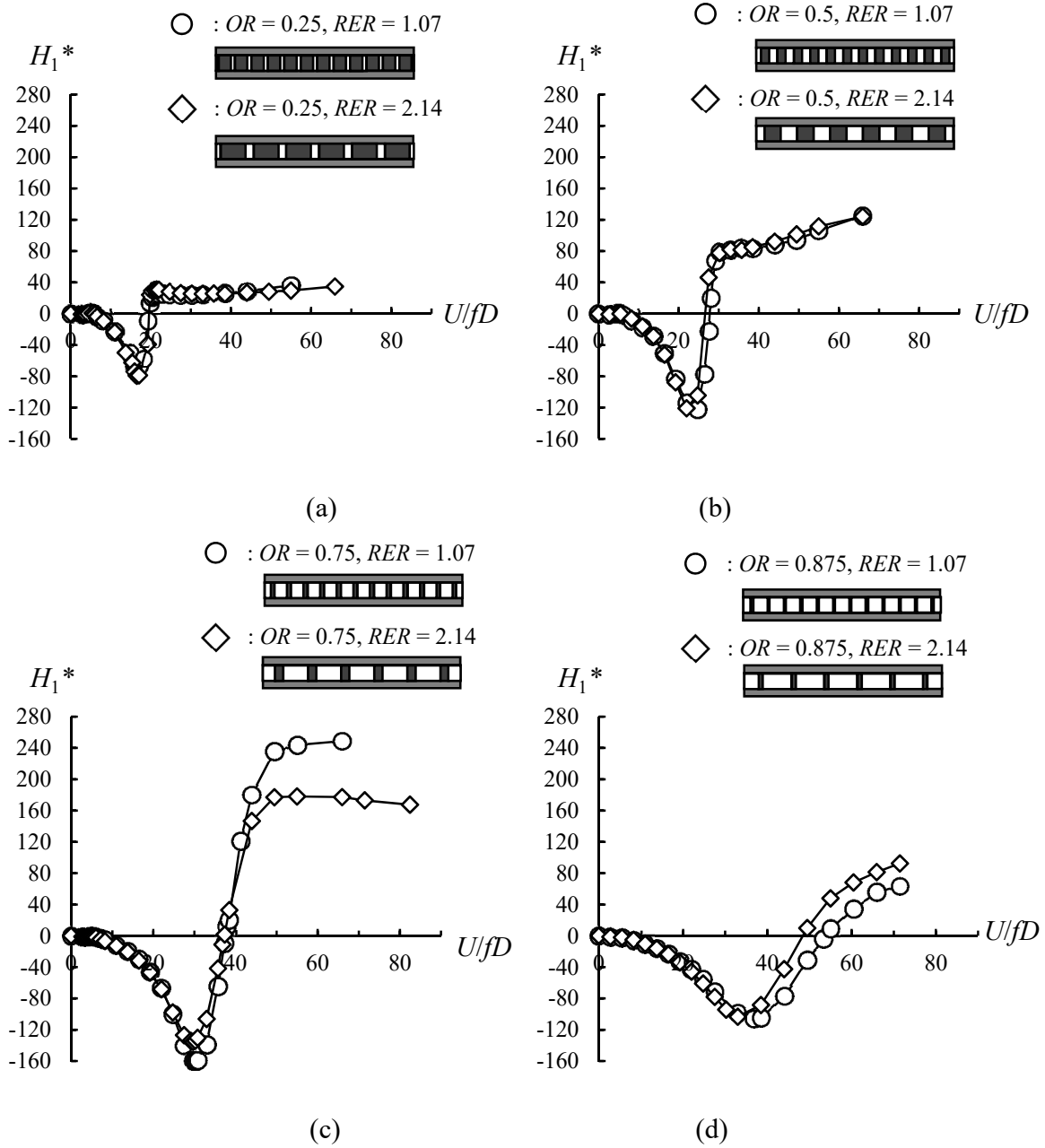


Fig. 5-9 Comparison between H_1^* of cases of $RER = 1.07$ and 2.14 for (a) $OR = 0.25$; (b) $OR = 0.5$; (c) $OR = 0.75$; (d) $OR = 0.875$ (smooth flow, $\alpha = 0^\circ$, $f = 2.6\text{Hz}$, $2A_\eta = 10\text{mm}$).

Repeating Element-size Ratio (RER) and galloping instability

To discuss the relationship between Repeating Element-size Ratio (RER) and the galloping instability, for each OR , H_1^* of different RER ($RER = 1.07$ and 2.14) is compared in Fig. 5-9. According to Fig. 5-9 (a) and (b), for small OR ($OR = 0.25$ or 0.5), H_1^* showed almost the same value at each wind velocity for $RER = 1.07$ and 2.14 . As shown in Fig. 5-9 (c) and (d), for large OR ($OR = 0.75$ or 0.875), H_1^* showed slightly different value for the different RER at high reduced

wind velocities. Therefore, the effects of REr on the aerodynamic damping are insignificant. Additionally, the relationship between aerodynamic damping and $OR \times REr$, the value of which is l_1/D_0 , is included in Appendix C, also confirming that the aerodynamic damping was not affected by the absolute opening size (l_1). Because OR played a more important role in the galloping instability of the rectangular cylinders with side-surface openings, only the effects of OR on the galloping instability (critical wind velocity and aerodynamic damping) was further discussed.

5.3.3 Critical wind velocity of galloping and Strouhal number

The mechanism related to the increase of critical wind velocity of galloping with OR was further discussed in this subsection. As proved before, with the increase of OR , the vibration amplitude at a certain wind velocity decreased and the critical wind velocity of galloping increased. Meanwhile, according to past researches (Otsuki et al., 1974; Nakamura and Mizota, 1975; Luo and Bearman, 1990; Mannini et al., 2014, 2016), the vortex shedding can stabilize the galloping until $Ur = 1/St$ (St is Strouhal number). Therefore, the relationship between St and OR is shown in Fig. 5-10 (a). To calculate St , the frequency of vortex shedding was identified from the fluctuating lift force. St was almost the same for $OR = 0$ and 0.25 and then decreased with the increase of OR from 0.25 to 0.875 (Fig. 5-10). For $OR = 1$, the frequency of vortex shedding cannot be identified from the lift force. Fig. 5-10 (b) shows the relationship between the critical wind velocity of galloping and OR . The reduced critical wind velocity (U_{rc0}) of galloping from the free vibration tests were almost the same with $1/St$. This confirms that the vortex shedding stabilized the galloping until $Ur = 1/St$. Furthermore, U_{rc0_fre} and $1/St$ increased simultaneously with the increase of OR , indicating that the increase of the critical wind velocity of galloping (U_{rc0}) with OR is controlled by the increase of $1/St$. To better understand this, St of the rectangular cylinder with different side ratios is shown in Fig. 5-11 (Nakaguchi et al., 1968; Tamura and Ito, 1995; Shimada and Meng, 1998; Sakamoto et al. 1989; Okajima, 1983; Washizu et al. 1978; Matsumoto et al. 2006). St of different OR is also included as a comparison in Fig. 5-11. The model of Case 1 ($OR = 0$) was the rectangular cylinder with a side ratio of 2, and St of Case 1 ($OR = 0$) was 0.082, which was the same with St (0.075~0.089) of the $B/D = 2$ rectangular cylinder from the past researches. Furthermore, St of the rectangular cylinder decreased with the increase of side ratio from 2 to about 2.8. The decrease of St with B/D from 2 to 2.8 is in a similar way as the decrease of St with OR from 0/0.25 to 0.875. Subsequently, the side ratio of the model effectively increased from 2 to about 2.8 owing to the increase of OR from 0 to 0.875. Meanwhile, the vortex shedding frequency cannot be identified from the lift force for $OR = 1$, indicating the fluctuating lift force coefficient is extremely small for $OR = 1$. The model of Case 10 ($OR = 1$) likely had a side ratio larger than 2.8, with the side ratio of which the rectangular cylinder shows a small fluctuating lift coefficient. Here, the rectangular cylinder with side-surface openings is assumed to have an effective side ratio B'/D' , where B' is the effective body width and D' is the effective body depth. Therefore, the increase of OR had effects on increasing the effective side ratio B'/D' and subsequently increased the critical wind velocity of galloping.

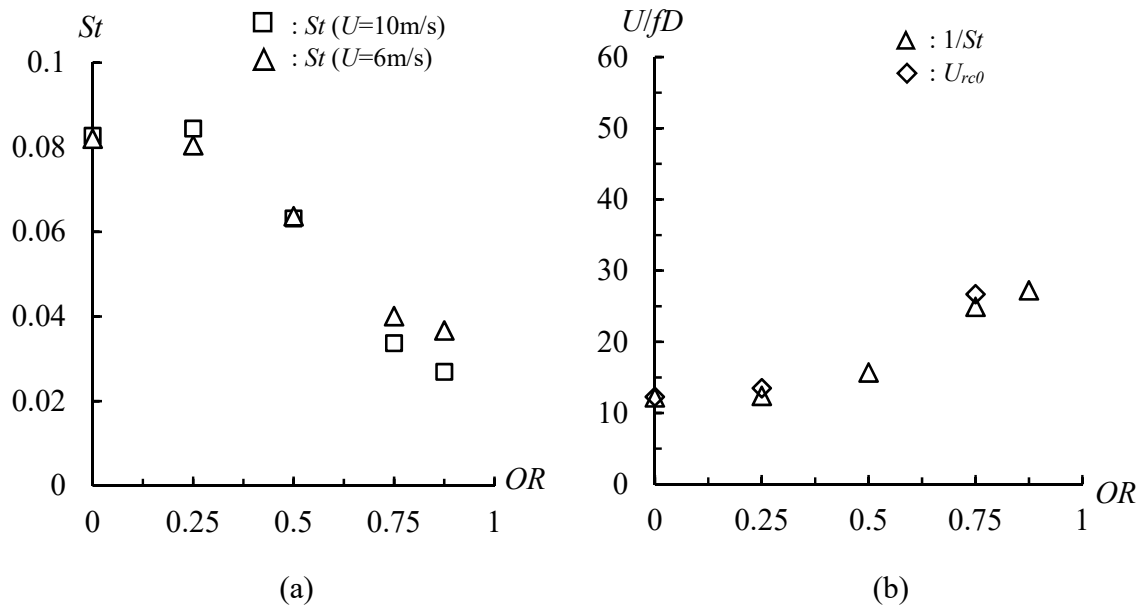


Fig. 5-10 (a) Change of Strouhal number (St) with OR ($RER = 1.07$, $U = 6\text{m/s}$, smooth flow). (b) Change of reduced critical wind velocity of galloping with OR ($RER = 1.07$, smooth flow). U_{rc0} is the reduced critical wind velocity of galloping corresponding to $2A\eta$ of 0mm (decided from free vibration tests).

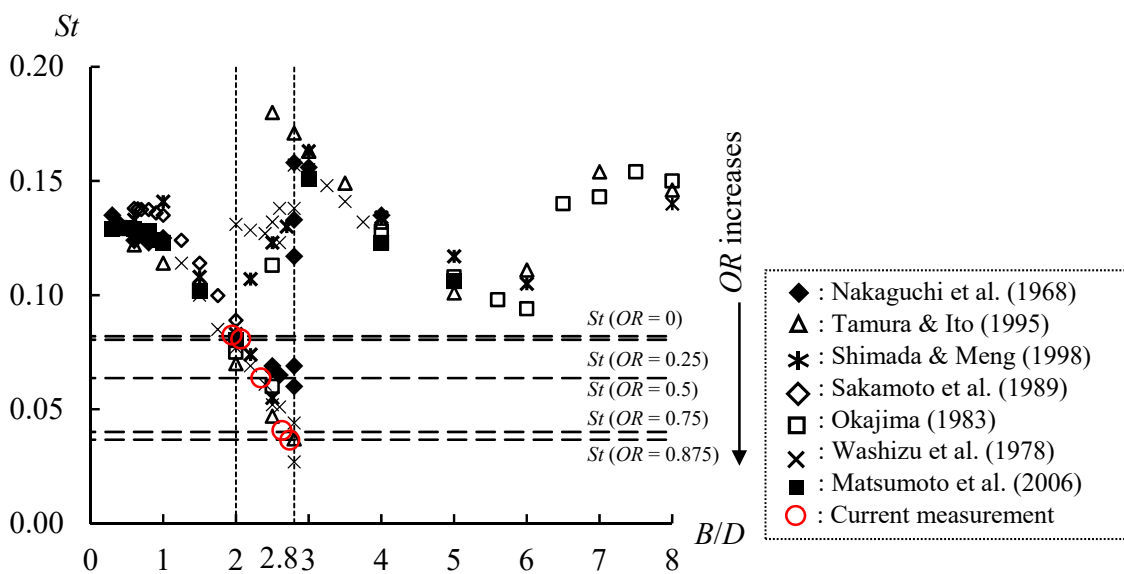
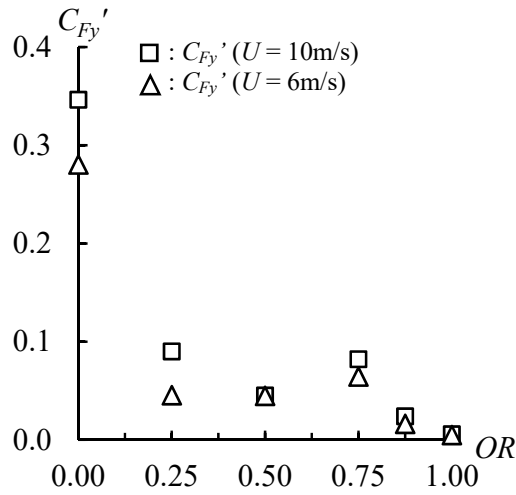
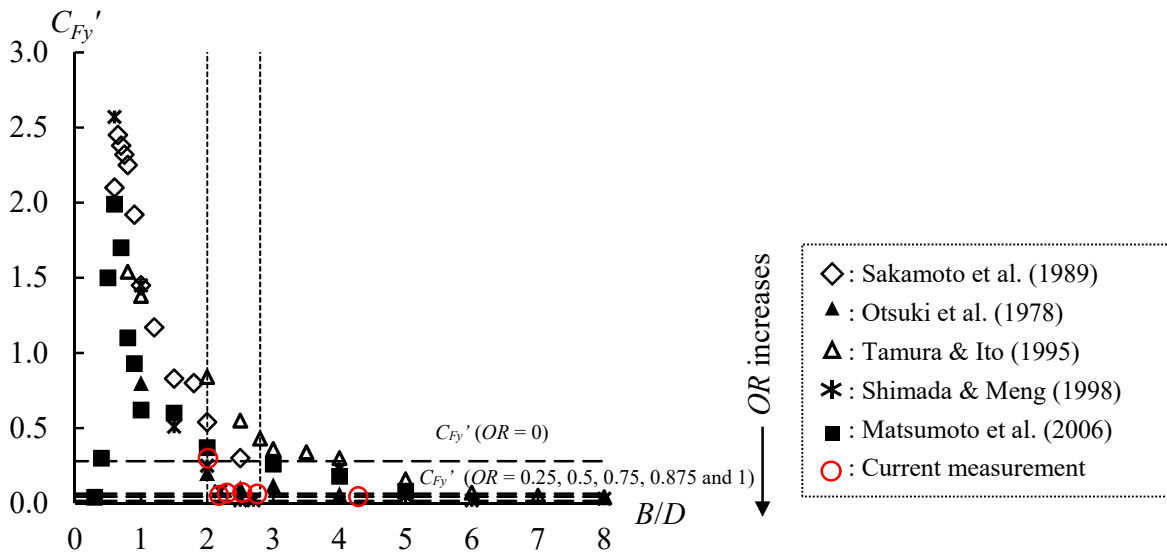


Fig. 5-11 Change of Strouhal number with side ratio B/D .



(a)



(b)

Fig. 5-12 Change of fluctuating lift force coefficients: (a) with OR ($RER = 1.07$, $U = 6\text{m/s}$, smooth flow); (b) with side ratio B/D .

To further validate the assumption of the increase of the effective side ratio B'/D' owing to the increase of OR , the relationship between aerodynamic force coefficients ($C_{Fy'}$, C_{Fx} and C_{Fxr}) and OR , and the relationship between those ($C_{Fy'}$ and C_{Fx}) and side ratio B/D are comparatively investigated. The change of fluctuating lift force coefficient $C_{Fy'}$ with OR is shown in Fig. 5-12 (a), and is compared with the change of $C_{Fy'}$ with side ratio from past researches in Fig. 5-12 (b). As shown in Fig. 5-12, $C_{Fy'}$ of Case 1 ($OR = 0$) was about 0.28, which agrees with $C_{Fy'}$ (0.2~0.84) of the $B/D = 2$ rectangular cylinder from the past researches (Sakamoto et al., 1989; Otsuki et al., 1978; Tamura and Ito, 1995; Shimada and Meng, 1998; Matsumoto et al. 2006). $C_{Fy'}$ drastically

decreased to < 0.1 with the increase of OR from 0 to 0.25 and then kept less than 0.1 for OR from 0.25 to 1 (Fig. 5-12 (a)). Meanwhile, according to Fig. 5-12 (b), C_{Fy}' gradually decreased to almost 0 with the increase of B/D from 2 to > 5 . This also indicates that the effective side ratio increased owing to the increase of OR . Because C_{Fy}' was almost 0 for Case 10 ($OR = 1$), the openings of $OR = 1$ made the model an effective side ratio larger than 2.8. The drag force coefficient C_{Fx} , which was calculated based on the total front/rear surface (Eq. (4)), is shown in Fig. 5-13 (a), while the drag force coefficient C_{Fxr} , which was calculated based on the real front/rear surface (Eq. (7)), is shown in Fig. 5-13 (b). The latter one is compared with the change of C_{Fx} with B/D from past researches. According to Fig. 5-13 (a) and (b), the drag force coefficients C_{Fx} or C_{Fxr} of Case 1 ($OR = 0$) was about 1.6, which was almost the same with C_{Fx} (1.43~1.6) of the $B/D = 2$ rectangular cylinder from the past researches (Fig. 5-13 (c)). C_{Fx} gradually decreased from 1.6 to about 0.5 with the increase of OR from 0 to 1 (Fig. 5-13 (a)). C_{Fxr} kept almost the same value of 1.6 for $0 \leq OR < 0.5$ and decreased from 1.6 to 1.25 with the increase of OR from 0.5 to 0.875 (Fig. 5-13 (b)). According to Fig. 5-13 (c), C_{Fx} decreased from about 1.6 to 1.2 with the increase of B/D from 2 to 2.8. Therefore, the effective side ratio of the model with openings increased from 2 to about 2.8 with the increase of OR from 0 to 0.875. Because C_{Fxr} of Case 10 ($OR = 1$) was 1.1, which was almost the same with C_{Fx} (1.05~1.18) of the rectangular cylinder with a side ratio of about 4, the model of $OR = 1$ had an effective side ratio larger than 3 (about 4). To summarize, the effective side ratio of the model increased from 2 to about 2.8 owing to the increase of OR from 0 to 0.875, while for $OR = 1$, the model had an effective side ratio larger than 3.

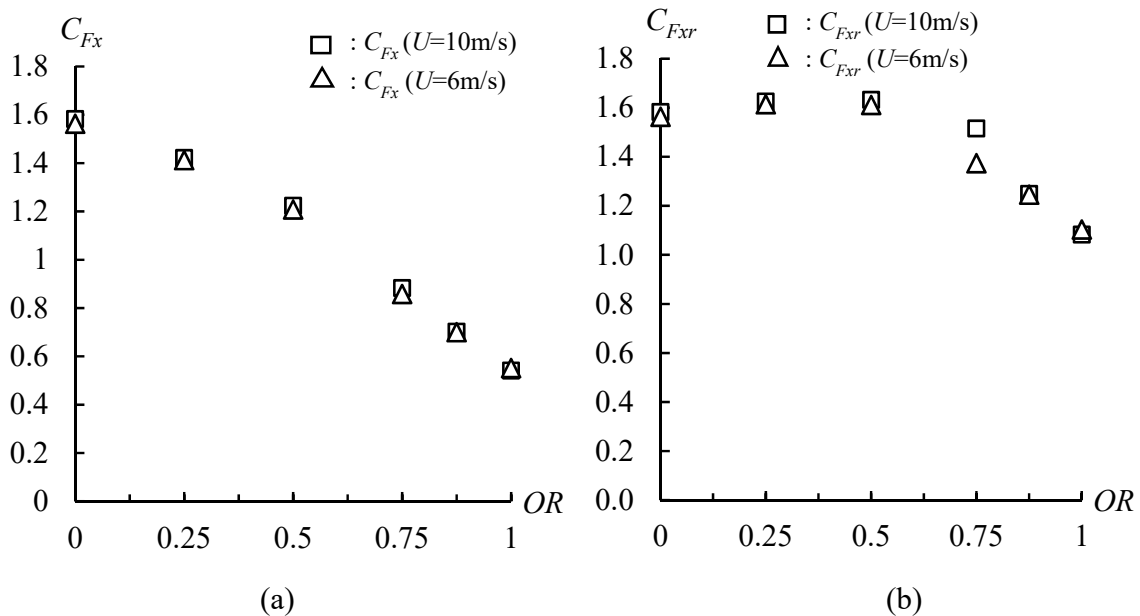


Fig. 5-13 (a) Change of drag force coefficient C_{Fx} with OR ($RER = 1.07$, $U = 6\text{m/s}$, smooth flow); (b) change of drag force coefficient C_{Fxr} with OR ($RER = 1.07$, $U = 6\text{m/s}$, smooth flow); (c) change of C_{Fx} with side ratio B/D . (C_{Fx} was calculated based on the total front/rear surface, while C_{Fxr} was calculated based on the real area of the front/rear surface).

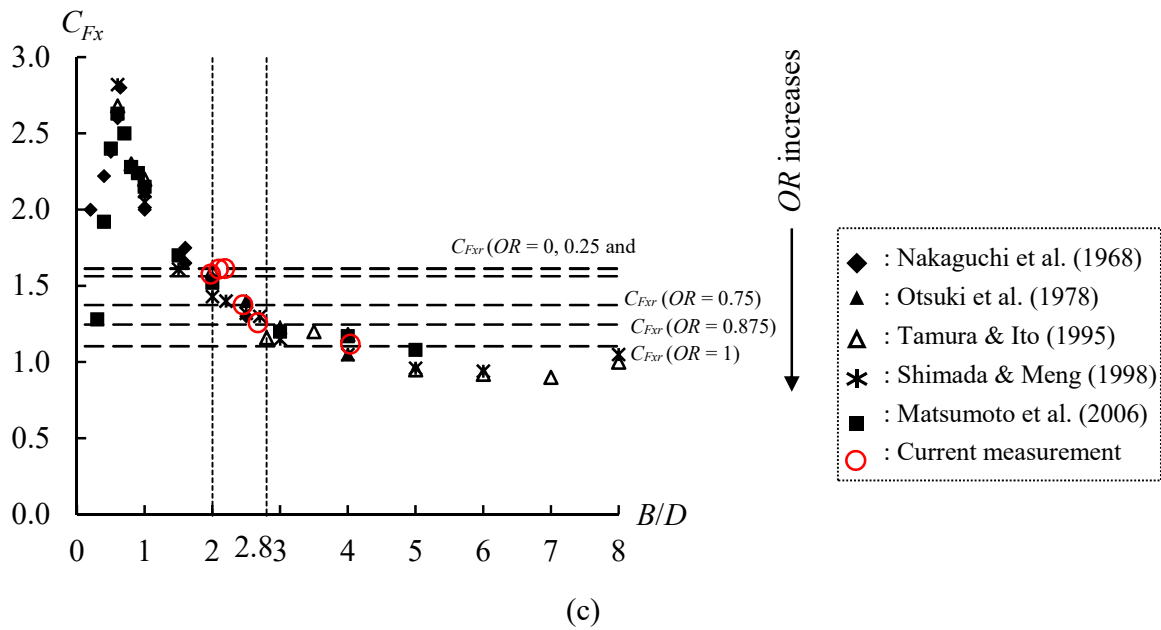


Fig. 4-13 Continued

According to past researches (Parkinson and Wawzonek, 1981; Smith, 1960; Parkinson and Brooks, 1961; Hirata K., 1993; Nakamura and Hirata, 1994), with the increase of the side ratio B/D from 0.67 to about 3, the amplitude of galloping vibration at a certain wind velocity gradually decreased, and the critical wind velocity of galloping increased. The rectangular cylinder with $B/D > 3$ did not show the galloping. Meanwhile, as mentioned before, the effective side ratio of the rectangular cylinder with side-surface openings increased owing to the increase of OR . Therefore, the critical wind velocity of galloping and $1/St$ increased with the increase of OR from 0 to 0.875, because that the effective side ratio increased from 2 to about 2.8 with the increase of OR from 0 to 0.875. Because Case 10 ($OR = 1$) had an effective side ratio larger than 3, Case 10 did not show galloping. According to past researches (Laneville and Parkinson, 1971; Laneville, 1973; Nakamura and Tomonari, 1977; Kwok and Melbourne, 1980; Nakamura et al., 1991 and 1994; Hirata, 1993), the increase in the critical wind velocity of galloping with the side ratio is related to the promotion of the reattachment of the shear layer to the upside/downside surface of the model. Therefore, the relationship between the time-averaged flow and OR will be investigated further to discuss how openings of different OR affect the reattachment of the shear layer to the side surface of the model. Meanwhile, because the linear quasi-steady aerodynamic damping is related to the time-averaged flow field, the change of aerodynamic damping with OR will be explained based on the change of time-averaged flow with OR .

5.4 Flow field around rectangular cylinder with side-surface openings

In this section, the flow field around the rectangular cylinder with side-surface openings is investigated. Firstly, the set-up for the flow visualization tests is outlined. Secondly, the flow field

in the inner space and wake of the model is investigated in the horizontal plane, regarding the flow rate of the through-body flow and the distribution of the wind velocity in span-wise direction and stream-wise direction. Thirdly, the relationship between the time-averaged flow around the model in the vertical plane and the Opening-area Ratio (OR) is illustrated and further explained based on the flow rate of the through-body flow. Meanwhile, the relationship between the time-averaged flow and OR is qualitatively compared with the relationship between the time-averaged flow and the side ratio to validate the assumption that the side ratio is effectively increased owing to the increase of OR . Lastly the relationship the relationship between the time-averaged flow in vertical plane and OR is utilized to interpret the effects of openings on the aerodynamic damping and the critical wind velocity of galloping, explaining the mechanism related to the stabilization against the galloping owing to the side-surface openings.

5.4.1 PIV measurement

The Particle-Image Velocimetry (PIV) tests were carried out to monitor the separated flow around the model in the vertical plane and the flow through the inner space of the model into the wake in the horizontal plane at angle of attack $\alpha = 0^\circ$. Through the PIV analysis, the instantaneous wind-velocity vectors were calculated.

Model for PIV measurement

A transparent acrylic model was applied to monitor the flow field around and in the model, as shown in Fig. 5-14. The section of the model was the same as the section of the wooden model for the free-vibration tests (Fig. 5-1 (b)). As shown in Fig. 5-14, for the flow visualization tests in the vertical plane, the upside surface of the model and the downside surface of the inner space of the girder were wrapped with black paper to avoid the reflection of the laser. Meanwhile, the surface of the plate for making the openings was wrapped by the black paper. For the flow visualization tests in the horizontal plane, the black paper on the upside surface of the model was taken off for the camera to monitor the flow field in the inner space from the upside.

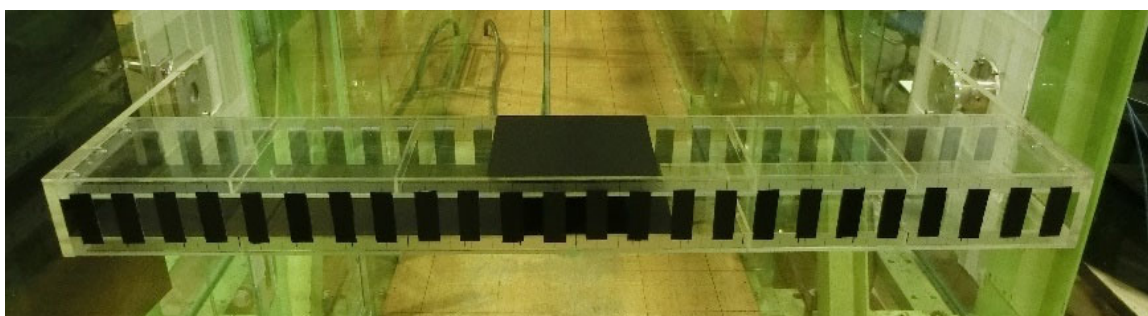


Fig. 5-14 Model for flow visualization tests

Set-up for PIV measurement

The set-up for the flow visualization tests in the X - Y plane (vertical plane) is shown in Fig. 5-15, and that in the X - Z plane (horizontal plane) is shown in Fig. 5-16. The coordination was in the right-hand system: the approaching wind direction was defined as the positive X direction, the upside vertical direction was defined as the positive Y direction, and the span-wise direction was defined as the Z direction. The flow was seeded with $0.3\sim 1\mu\text{m}$ droplets of glycol (glycol) provided by the smoke generator (KANOMAX, MOEL 8384) and illuminated by the thin laser sheet provided by the continuous laser (KATO KOKEN, PIV laser LB2000). The PIV high-speed camera (KATO KOKEN, k8-USB) with a maximum spatial resolution of 2592×2048 pixels was located perpendicular to the laser sheet to acquire sequential images of the illuminated flow field. The approaching wind velocity was $U = 1.5\text{m/s}$ ($Re = 2.8\times 10^4$). The images were captured at 300fps for 14s with a shutter speed of $1/500\text{s}$. The shutter speed of the camera was $1/300\text{s}$ to avoid the particle image streaking. As shown in Fig. 5-15, for the tests in the X - Y plane, the laser was put at the downstream side and the camera was set outside the wind tunnel pointing at the Z direction. The flow field around the closed section and open section were both monitored (Fig. 5-17). The closed section was at the center of the plate (Fig. 5-17 (a)), while the open section was at the center of the opening (Fig. 5-17 (b)). Because the flow around the model in the X - Y plane is symmetry to the horizontal centerline of the section, only the flow field over the upside surface and in the wake of the model was monitored. According to Fig. 5-16, for the tests in the X - Z plane, the laser sheet was set in the X - Z plane through the section center and the camera was put on the upside transparent wall of the wind tunnel perpendicular to the laser sheet. For the inner space, the laser was put outside of the wind tunnel pointing at Z direction, and the camera center was set at the span center of the leading edge. For the wake part, the laser was set downstream side of the model, and the camera center was at the span center of the trailing edge. The particle images were processed by

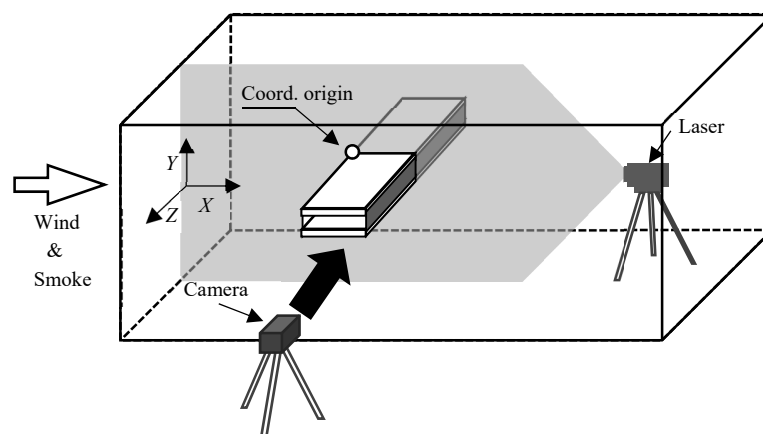
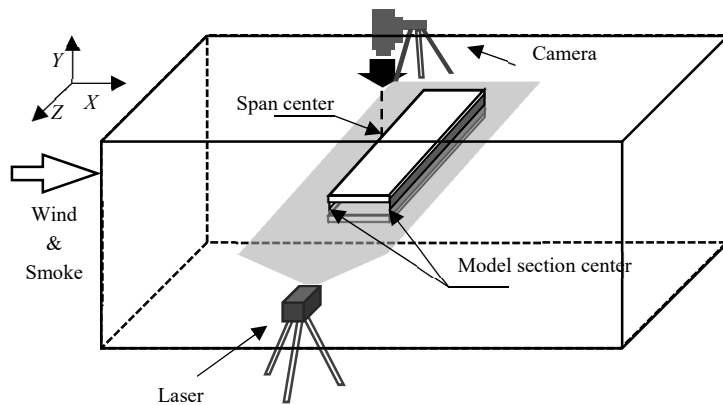
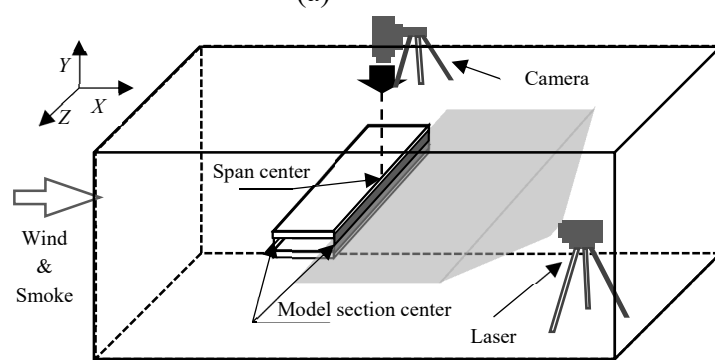


Fig. 5-15 Set-up for the flow visualization test the X - Y plane. The X -direction is the approaching wind velocity. Y -direction is the vertical direction. Z -direction is the span-wise direction. The origin of coordinate is at the span center and upside leading edge.

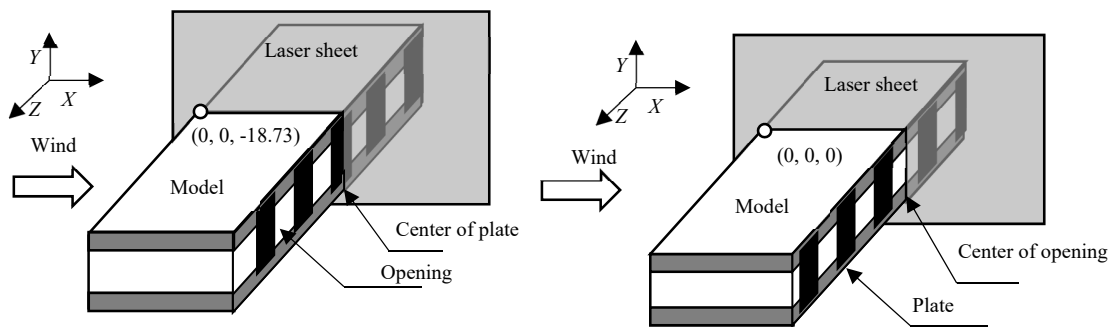


(a)



(b)

Fig. 5-16 Set-up for the flow visualization test in X - Z plane for (a) the inner space of model; (b) the wake of the model. The laser sheet is set in the X - Z plane through the center of the model section.



(a)

(b)

Fig. 5-17 Measurement position (X - Y plane) for: (a) closed section ($z = 0\text{mm}$); (b) open section ($z = 18.73\text{mm}$).

using the 2-dimensional fluid analysis software (FlowNizer 2D v1.12). Based on the sequential particle image, the cross-correlation method was utilized to extract instantaneous vector fields. The interrogation window was 15×15 pixels² with a 75% overlap. The instantaneous vector fields

were ensemble-averaged to obtain the spatial distributions of the mean wind velocity vector and the time-averaged streamline.

In addition to the wind-velocity vectors calculated by the PIV measurement, the wind velocity of the flow getting through the openings was also measured by the ‘X’-type hotwire. The measurement points are shown in Fig. 5-18, distributing at the near front, the inner space and the near wake of the model. The measurement was along the horizontal centerline of the model ($Y = -37.5 \text{ mm}$).

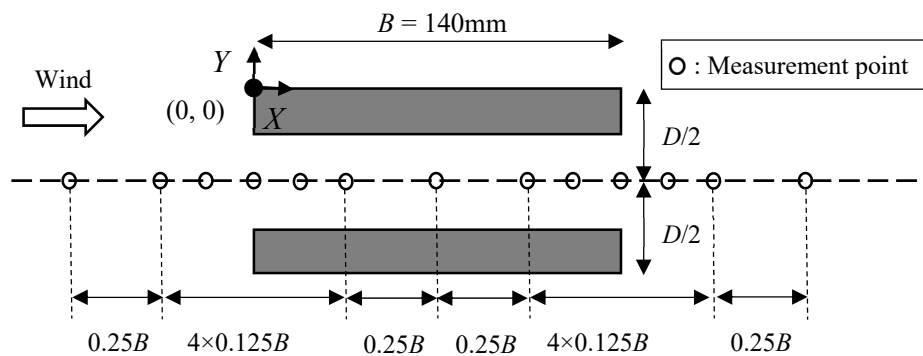


Fig. 5-18 Distribution of the measurement points for the wind velocity of the flow getting through the inner space of the rectangular cylinder.

5.4.2 Through-body flow in X - Z plane

This subsection presents the investigation on the effects of side-surface openings on the distribution of the wind velocity in the inner space and wake in the horizontal plane. Firstly, the wind velocity measured by the hotwire and PIV tests is compared to validate the results. Secondly, the change in the flow rate through the inner space of the model into the wake with Opening-area Ratio (OR) is investigated. Thirdly, the distribution of the wind velocity in the inner space of the model is discussed. Fourthly, the change of the outflow from the downstream openings into the wake with OR is described to illustrate the potential disturbance of the outflow to the flow entrainment in the wake.

The wind velocity U_1 of the flow through the openings into the wake was measured by both the hotwire (approaching wind velocity $U = 6\text{m/s}$) and PIV tests ($U = 1.5\text{m/s}$) to validate both two results. The contour map of the non-dimensional X -direction wind velocity U_{1X}/U (U_{1X} is the measured X -direction wind velocity) in the X - Z plane is shown in Fig. 5-19. For Case 1 ($OR = 0$), only the wake part was measured. According to Fig. 5-19, the flow got through the upstream openings into the inner space of the model and then got out from downstream openings into the wake. Fig. 5-20 shows the wind velocity measured by the hotwire and the PIV tests in the X - Y plane and the X - Z plane along X direction ($Z = 0 \text{ mm}$ and $Y = -D/2$ (-35mm)). According to Fig. 5-20, in the inner space of the model ($0 \text{ mm} < X < 140 \text{ mm}$), the wind velocity measured from PIV tests and hot wire were almost the same at each point, indicating that the results of the two methods

agreed well with each other in the inner space. In the wake ($140 \text{ mm} < X < 210 \text{ mm}$), the wind velocity U_{1X} measured by PIV tests was slightly smaller than U_{1X} measured by the hotwire for small OR ($OR = 0.25, 0.5$) owing to the technical problem. For large OR ($OR = 0.75, 0.875$ and 1), the wind velocity U_{1X} from the two methods was almost the same. Therefore, the PIV results can qualitatively explain the change of flow field with OR .

According to Fig. 5-19 and Fig. 5-20, one noticeable characteristic is that the overall wind velocity U_{1X}/U of the flow through the inner space into the wake in the X - Z plane increased with OR , indicating that the flow rate through the inner space increased. According to Fig. 5-20, U_{1X}/U almost equals to 1 at $X = 0\text{mm}$ and 140mm for $OR = 0.25\sim 1$, confirming that the wind velocity U_{1X} at the upstream openings ($X = 0\text{mm}$) and downstream openings ($X = 140\text{mm}$) is not affected by OR . Therefore, the flow passed through the upstream and downstream openings with the approaching wind velocity of U . The flow rate Q through the total front surface area S_{fro} ($S_{\text{fro}} = D \times l$) of the model separated into two parts: the flow rate Q_1 through the total opening area S_{op} ($S_{\text{op}} = nS_1$, S_1 is single opening area, n is the number of the openings), and the flow rate Q_2 into the separated flow (Fig. 5-21). Owing to the increase of S_{op} , the flow rate Q_1 through the total openings increased with OR (Table 5-3). Because the flow rate Q through the total front surface of the model was a constant (about $0.378\text{m}^3/\text{s}$), the flow rate Q_2 ($Q_2 = Q - Q_1$) decreased with OR (Table 5-3).

According to Fig. 5-19, another noticeable characteristic of the flow field is that owing to the discretely distributed openings, the time-averaged wind velocity of the flow behind the plate was generally smaller than that behind the openings in both the inner space and the wake. Meanwhile, the difference between the wind velocity of the flow behind the openings and behind the plate was very obvious at $X = 0 \text{ mm}$, and the difference gradually decreased from $X = 0 \text{ mm}$ to $X = 140 \text{ mm}$ for $0.25 \leq OR \leq 0.75$. According to Fig. 5-20, in the inner space, the wind velocity gradually decreased from $X = 0\text{mm}$ to $X = 140\text{mm}$ for $0.25 \leq OR \leq 0.75$, indicating that the flow strongly diffused from the upstream openings into the inner space. For $0.875 \leq OR \leq 1$, the wind velocity was almost the same with the approaching wind velocity U along X direction at $0\text{mm} < X < 140 \text{ mm}$ (Fig. 5-20). Therefore, for $0.875 \leq OR \leq 1$, the flow went through the inner space directly into the wake without obvious diffusion. Even though the flow field in the inner space of the model changed both along Z direction and X direction, the flow in the inner space of the model was limited to a narrow space of a constant height in Y direction (between upside and downside inner surface), and the model was symmetry to the horizontal centerline of the section. Therefore, it is assumed that the flow field in the inner space did not obviously contribute to aerodynamic performance. This assumption is supported by the fact that for the rectangular cylinder with side-surface openings the quasi-steady theory is valid, because this fact indicates that the lift force working on the model is mainly decided by pressure distribution on the upside and downside surfaces of the rectangular cylinder rather than the pressure on the surfaces in the inner space of the rectangular cylinder with openings.

According to Fig. 5-19, the wind velocity of the outflow from the downstream openings was relatively larger than that behind the plate at the near wake (about $140 \text{ mm} < X < 210 \text{ mm}$). For

small OR ($OR = 0.25$ and 0.5), the outflow turned uniform along the Z -direction from about $X = 160$ mm \sim 180 mm, and the wind velocity at $X > 160$ mm was small ($U_{1X}/U < 0.4$) (Fig. 5-19 and Fig. 5-20). Therefore, the outflow from downstream openings was into a short distance in the wake ($X < 160$ mm), and then soon dispersed into the wake for small OR ($OR = 0.25$ and 0.5). For large OR ($OR = 0.75$ and 0.875), the outflow from the downstream openings into the wake turned uniform from $X = 230$ mm \sim 260 mm, and the wind velocity was relatively larger at $X > 230$ mm ($U_{1X}/U > 0.4$) than that for small OR (Fig. 5-19 and Fig. 5-20). Therefore, for large OR ($OR = 0.75$ and 0.875) the outflow from the downstream openings shot a far downstream distance ($X < 210$ mm) and penetrated the wake with a uniform high wind velocity ($U_{1X}/U > 0.4$). Furthermore, according to past researches (Laneville and Yong, 1983; Koutmos et al., 2004; Huang et al., 2017), the outflow from the downstream openings may disturb the flow entrainment in the wake, affecting the flow field around the model in the X - Y plane. Because the wind velocity of the outflow from the discretely-distributed openings varied along Z direction (Fig. 5-19), the interaction between the outflow and flow entrainment in the wake may also vary along the Z direction. Therefore, the flow field in the X - Y plane is probably affected by the outflow from the downstream openings into the wake.

In summary, because of the openings, the flow got through the inner space of the model into the wake. Owing to the constant height of the model inner space, the contribution of the flow in the inner space is assumed to be minor. However, with the increase of OR , the flow rate through the total area of openings increased potentially affecting the flow field around the model in the vertical plane. Furthermore, with the increase of OR , the outflow from the downstream openings gradually shot a further distance into the wake and the flow field in the wake varied along the span-wise direction, also potentially affecting the flow field around the model in the vertical plane.

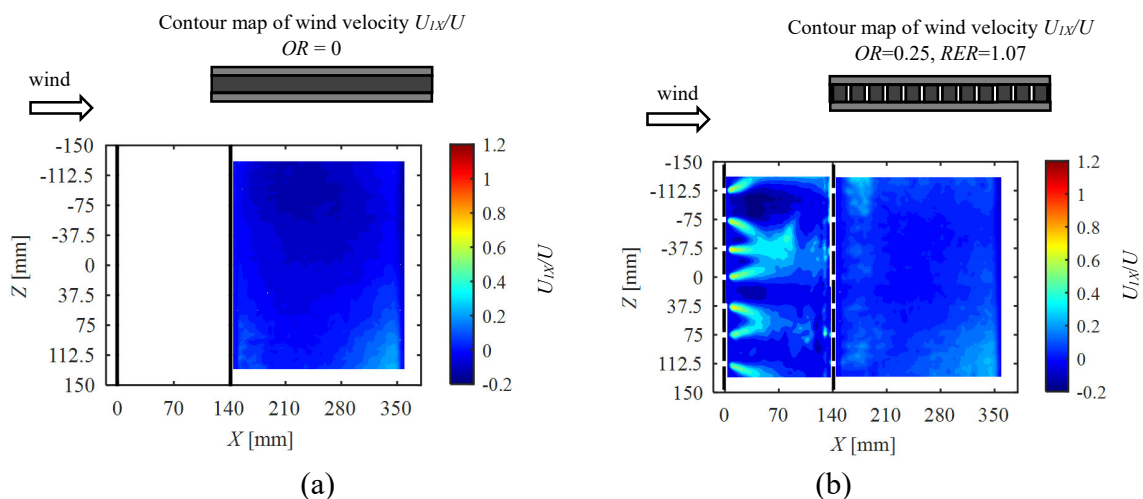


Fig. 5-19 Contour map of non-dimensional X -direction wind velocity (U_{1X}/U) in X - Z plane of: (a) Case 1 ($OR = 0$); (b) Case 2 ($OR = 0.25$, $RER = 1.07$); (c) Case 3 ($OR = 0.50$, $RER = 1.07$); (d) Case 4 ($OR = 0.75$, $RER = 1.07$); (e) Case 5 ($OR = 0.875$, $RER = 1.07$), (f) Case 10 ($OR = 1$) ($U = 1.5$ m/s, smooth flow).

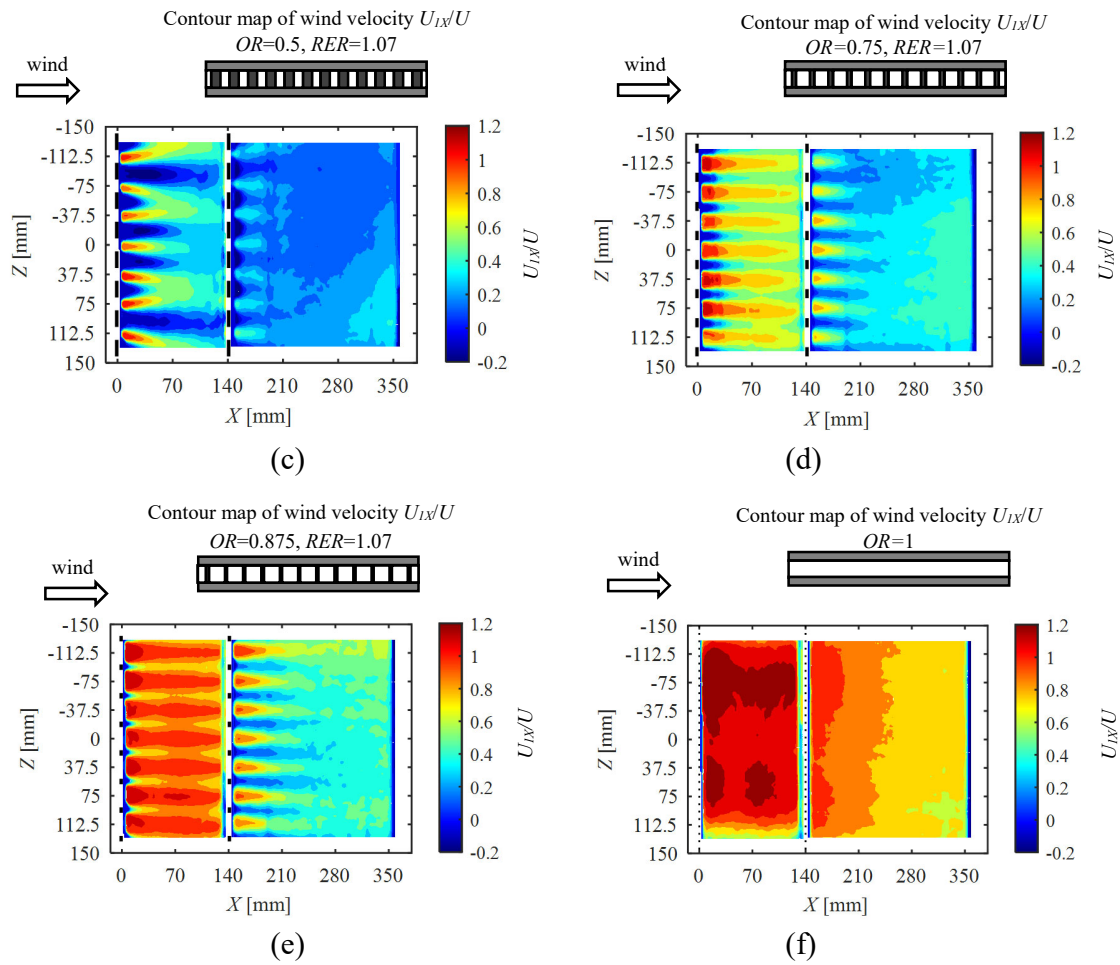
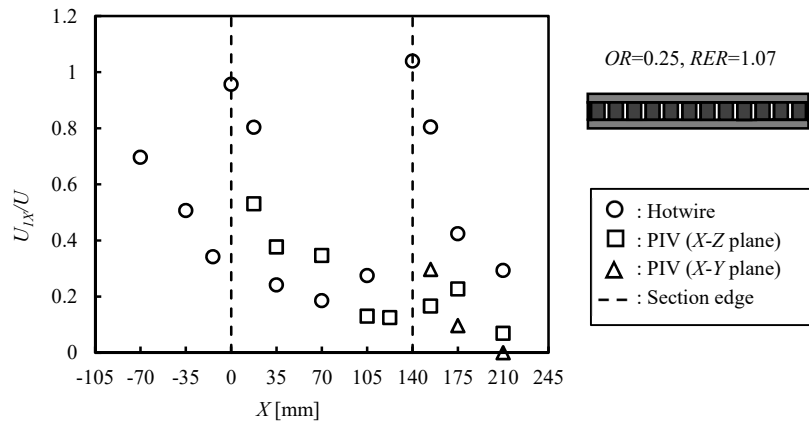
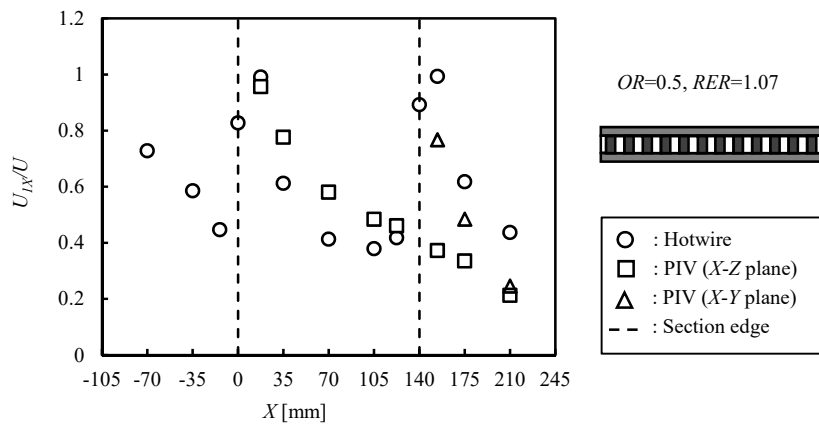


Fig. 5-19 Continued

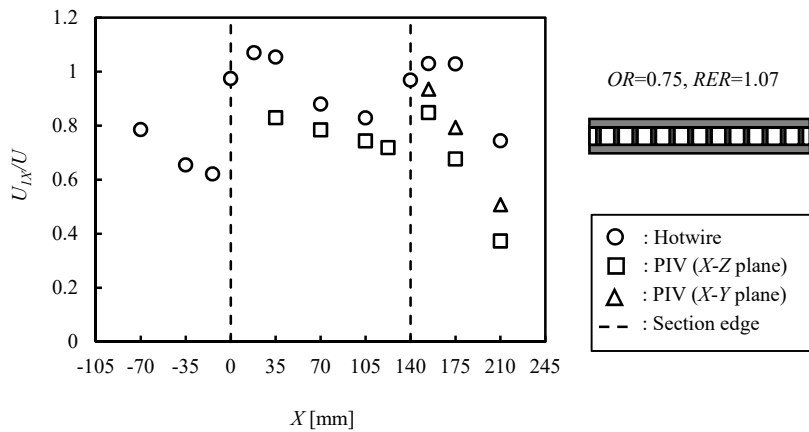


(a)

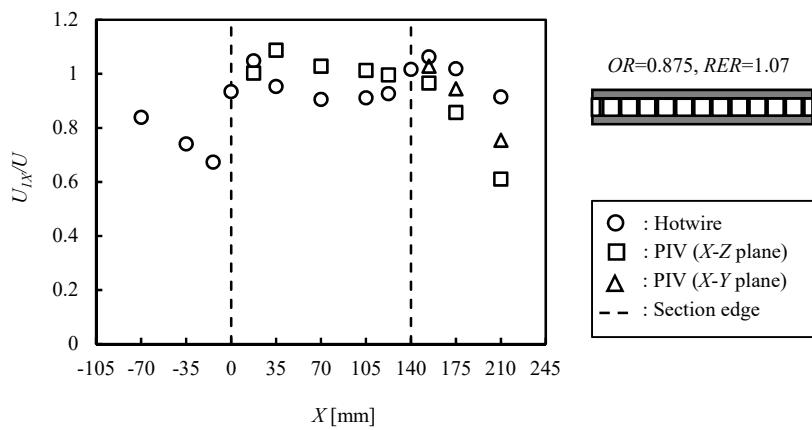
Fig. 5-20 Non-dimensional X -direction wind velocity (U_{1X}/U) of the flow through the model of: (a) Case 2 ($OR = 0.25, RER = 1.07$); (b) Case 3 ($OR = 0.50, RER = 1.07$); (c) Case 4 ($OR = 0.75, RER = 1.07$); (d) Case 5 ($OR = 0.875, RER = 1.07$); (e) Case 10 ($OR = 1$) (PIV tests: $U = 1.5\text{m/s}$, smooth flow; wind velocity measurement: $U = 6\text{m/s}$, smooth flow).



(b)



(c)



(d)

Fig. 5-20 Continued.

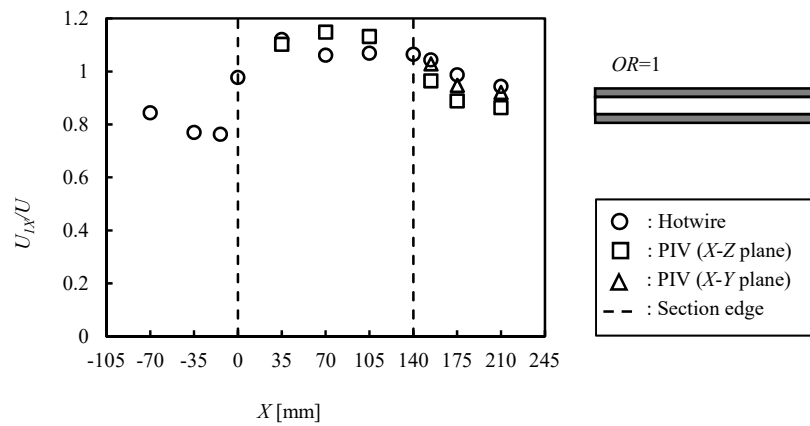


Fig. 5-20 Continued.

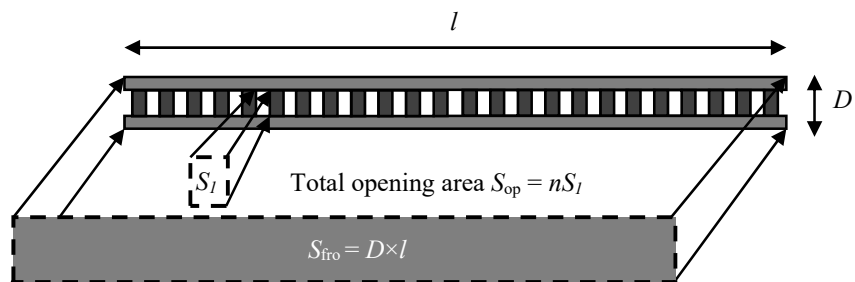
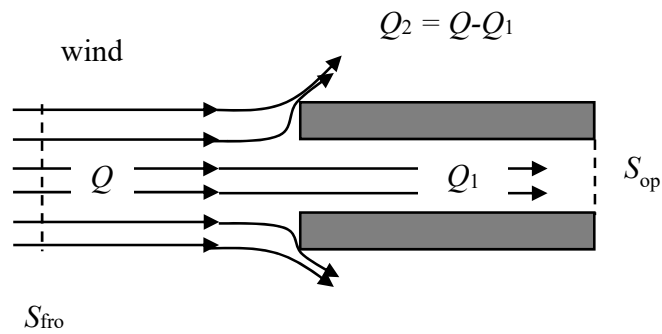


Fig. 5-21 (a) Side view (span-wise direction) of the flow rate Q through the total front surface S_{fro} of the model, the flow rate Q_1 through the total opening area S_{op} and the flow rate Q_2 into the separated flow. (b) Sketch for S_{fro} and S_{op} (n is 24 for $RER = 1.07$; $S_l = D_0^2 \times OR \times RER$).

Table 5-3 Flow rate Q_1 through the total opening area ($REr = 1.07$, $n = 24$, $U = 6\text{m/s}$; $Q = 0.378\text{m}^3/\text{s}$)

OR	Total opening area S_{op} (unit: m^2)	Flow rate Q_1 (unit: m^3/s) ($Q_1 = S_{op} \times U$)	Flow rate Q_2 (unit: m^3/s) ($Q_2 = Q - Q_1$)
0	0	0.000	0.378
0.25	3.277×10^{-4}	0.047	0.331
0.5	6.554×10^{-4}	0.094	0.284
0.75	9.831×10^{-4}	0.142	0.236
0.875	1.147×10^{-4}	0.165	0.213
1	1.311×10^{-4}	0.189	0.189

5.4.3 Separated flow in X - Y plane

This subsection presents the explanation for the stabilization against the galloping owing to the side-surface openings based on the relationship between the time-averaged separated flow in the X - Y plane and the Opening-area Ratio (OR). Firstly, the relationship between the time-averaged separated flow around the model in the X - Y plane and OR is described. This relationship is assumed to be affected by the flow rate of the through-body flow. Additionally, the relationship between the time-averaged separated flow and OR is qualitatively compared with the relationship between the time-averaged separated flow and side ratio to validate the assumption that increasing OR resulted in the increase of the effective side ratio B'/D' . Secondly, the effects of side-surface openings on the critical wind velocity of galloping and aerodynamic damping (H_1^*) are further discussed based on the time-averaged separated flow in the X - Y plane.

Time-averaged streamline and Opening-area Ratio

The time-averaged streamline in the X - Y plane around the closed section and the open section for different OR is shown in Fig. 5-22. Fig. 5-22 (a) shows the time-averaged streamline around the $B/D = 2$ rectangular cylinder ($OR = 0$). By comparing Fig. 5-22 (b) and (c) or comparing Fig. 5-22 (d) and (e), the time-averaged streamline around the closed section and the open section for small OR ($OR = 0.25$ and 0.5) were almost the same. This may be related to that the wind velocity of the outflow from the downstream openings into the wake was small for small OR ($OR = 0.25$, 0.5), the interaction between the outflow and the flow entrainment in the wake was minor (Fig. 5-20). However, by comparing Fig. 5-22 (f) and (g) or comparing Fig. 5-22 (h) and (i), the time-

averaged streamline around the trailing edge of the closed section was slightly different from that around the trailing edge of the open section for large OR ($OR = 0.75$ and 0.875). Because the wind velocity of the outflow into the wake was relatively large for large OR ($OR = 0.75$ and 0.875), the interaction between the outflow and the flow entrainment in the wake became stronger (Fig. 5-20). Possibly, owing to the interaction between the outflow and flow entrainment was not uniform in the wake along the Z direction, the time-averaged streamline around trailing edge of the closed section was slightly different from that around trailing edge of the open section for large OR ($OR = 0.75, 0.875$). Therefore, even though the openings discretely distributed along the span-wise direction, the time-averaged separated flow slightly changed along the span-wise direction around the trailing edge only for large OR ($OR = 0.75$ and 0.875). Furthermore, the time-averaged separated flow gradually approached the side surface with the increase of OR from 0 to 0.875, starting to reattach to the side surface for $OR = 0.875$ (Fig. 5-22(a), (b), (d), (f), (h)). For $OR = 1$, the time-averaged separated flow totally reattached to the side surface forming a separation bubble (Fig. 5-22 (j)). Because the streamline is the contour line of the stream function, the difference of which is the flow rate (White, 2011), the time-averaged separated flow gradually approached the side surface with OR owing to the decrease of the flow rate Q_2 from the total front surface into the separated flow with OR .

According to past researches (Nakaguchi et al., 1968; Mizota and Okajima, 1981; Laneville and Yong, 1983; Nakagawa et al., 1999; Sohankar, 2008), the time-averaged separated flow gradually approached the side surface with the increase of B/D from 2 to 2.8, finally reattaching to the trailing edge and forming a separation bubble for $B/D = 2.8$. With a further increase of B/D from 2.8, the reattachment point gradually moved upstream. Because that the time-averaged separated flow approached the side surface of the model with the increase of OR from 0 to 0.875 and with the increase of B/D from 2 to about 2.8 in a similar way, the effective side ratio B'/D' of the rectangular cylinder with openings increased from 2 to about 2.8 owing to the increase of OR from 0 to 0.875. The time-averaged separated flow around the model of Case 10 ($OR = 1$) was the total reattachment type, confirming that the model of Case 10 had an effective side ratio B'/D' larger than 2.8. More generally, because the openings reduced windward-surface area S_{fro} resulting in the decrease in the flow rate Q_2 , the effective depth D' of the model was reduced while the effective length B' equaled to the model length B . Therefore, based on the time-averaged separated flow in the X - Y plane, the side ratio of the model effectively increased owing to the increase of OR .

In summary, even though the openings discretely distributed along the Z direction, the time-averaged separated flow in the X - Y plane was almost the same along Z direction. Furthermore, with the increase of OR , the side-surface openings promoted the time-averaged separated flow to approach the side surface owing to the increase in the flow rate through the area of the total openings, resulting in an increase in the effective side ratio.

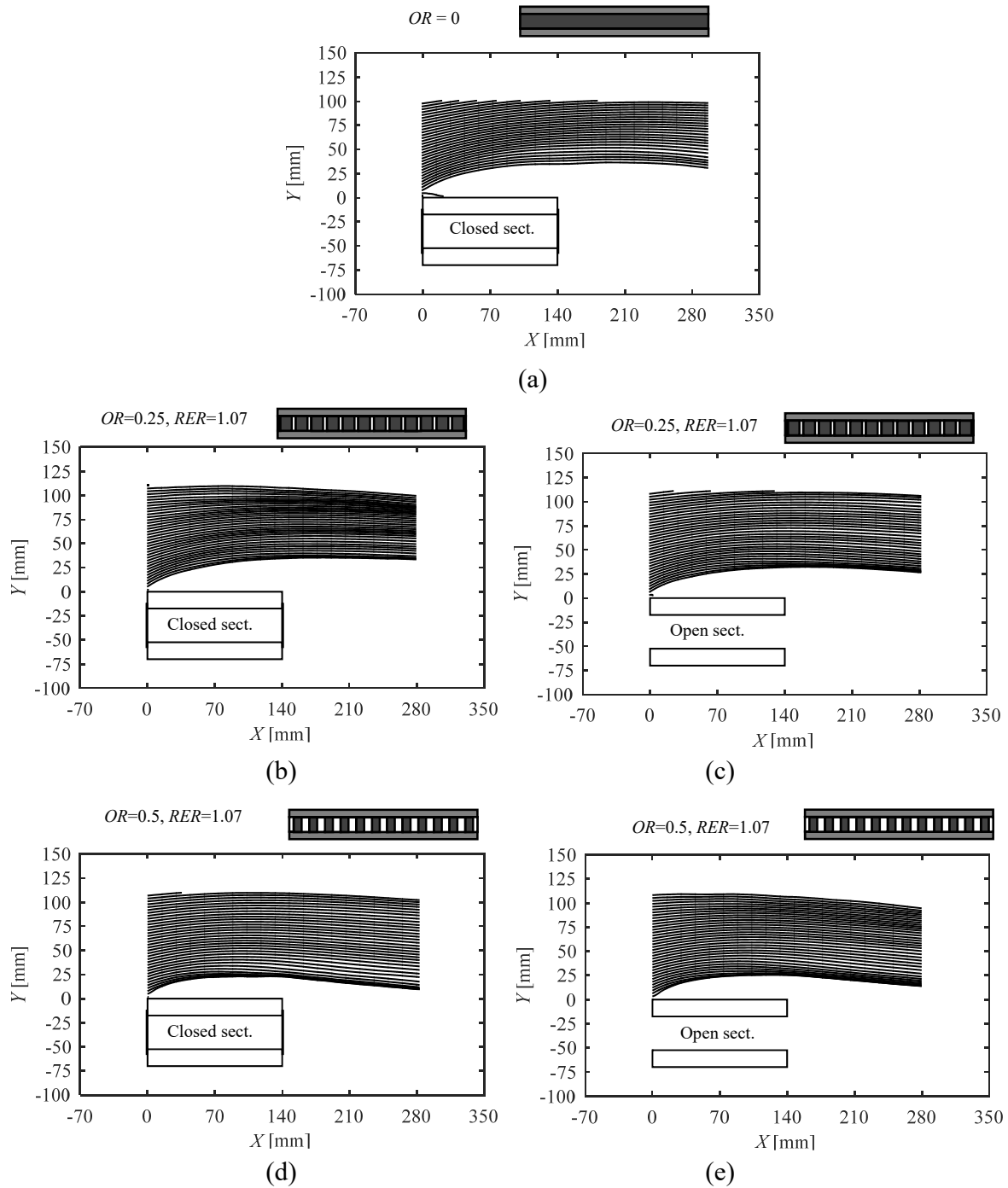


Fig. 5-22 Time-averaged streamline in X - Y plane around: (a) section of Case 1 ($OR = 0$); (b) closed section of Case 2 ($OR = 0.25, RER = 1.07$); (c) open section of Case 2; (d) closed section of Case 3 ($OR = 0.50, RER = 1.07$); (e) open section of Case 3; (f) closed section of Case 4 ($OR = 0.75, RER = 1.07$); (g) open section of Case 4; (h) closed section of Case 5 ($OR = 0.875, RER = 1.07$); (i) open section of Case 5; (j) section of Case 10 ($OR = 1$) ($U = 1.5\text{m/s}$, smooth flow).

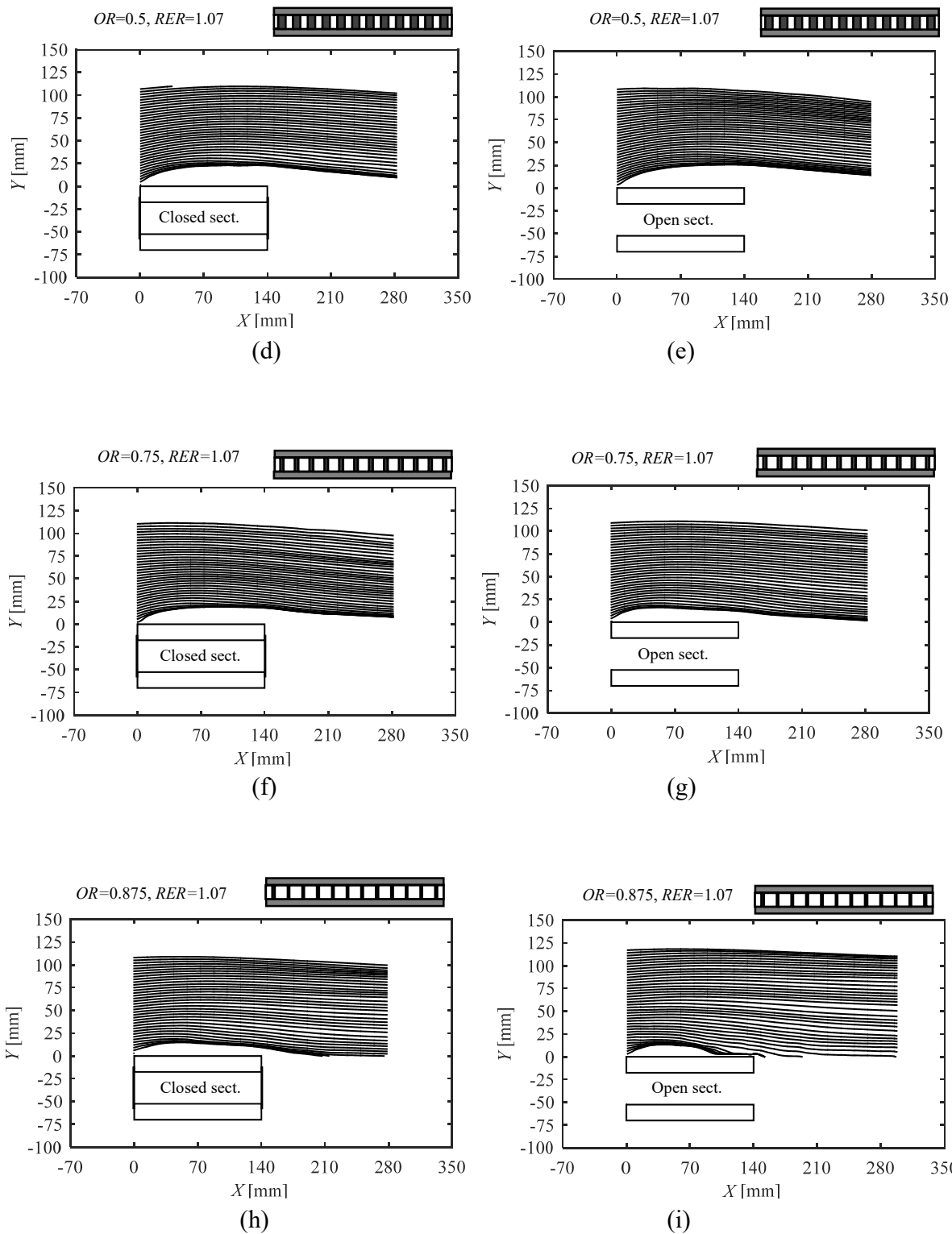


Fig. 5-22 Continued

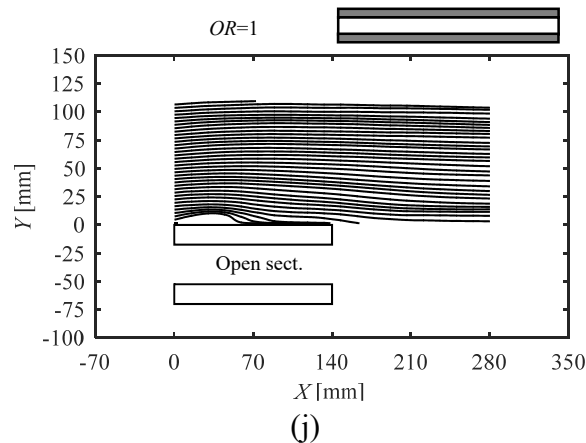


Fig. 5-22 Continued

Effects of side-surface openings on galloping

As explained before, the time-averaged separated flow in the X - Y plane gradually approached the side surface and finally reattached on the side surface with the increase of OR . Firstly, the effects of the side-surface openings on the critical wind velocity were further explained in this subsection. Secondly, the linear quasi-steady aerodynamic damping H_1^* is characterized by $-dC_{Fy}/(d\alpha)$, which is closely related to the time-averaged separated flow in the X - Y plane. Therefore, the relationship between the lift slope $-dC_{Fy}/d\alpha$ and OR was discussed based on the time-averaged separated flow to explain the change of aerodynamic damping with OR . Before that, the relationship between the lift force coefficient (C_{Fy}) and angle of attack (α) was explained.

The time-averaged separated flow gradually approached the side surface with the increase of OR from 0 to 0.875 and totally reattached for $OR = 1$, indicating an increasing interference between the separated flow and the model afterbody with OR . According to past researches (Gerrard, 1966; Nakaguchi et al., 1968; Laneville and Yong, 1983; Bearman and Trueman, 1987), an increasing interference between the separated flow and the afterbody, which is caused by the increase of B/D from 2 to 2.8, leads to the decrease in the drag force coefficient (C_{Fx}), fluctuating lift force coefficient (C_{Fy}') and Strouhal number (St). Meanwhile, because of the increasing interference between the separated flow and afterbody with OR , C_{Fxr} , C_{Fy}' and St also decreased with the increase of OR from 0 to 0.875. For $OR = 1$, the small C_{Fxr} and the small C_{Fy}' can be explained by the strong interference between the separated flow and the afterbody as indicated by the flow field of the reattachment type. Furthermore, according to past researches (Parkinson and Wawzonek, 1981; Laneville and Parkinson, 1971; Laneville, 1973; Nakamura and Tomonari, 1977; Kwok and Melbourne, 1980; Nakamura et al., 1991 and 1994; Hirata, 1993), the promotion of the interference between the separated flow and the afterbody, which is accompanied by the time-averaged separated flow approaches to the side surface, can cause the increase in the critical wind velocity of galloping and the decrease in the vibration amplitude. The interference between the separated

flow and the afterbody was strengthened owing to the increase of OR from 0 to 0.875, and subsequently the critical wind velocity of galloping increased with OR from 0 to 0.875. While for $OR = 1$, with the increase of OR , the galloping was totally stabilized owing to the reattachment-type flow field. Therefore, the time-averaged separated flow gradually approached the side surface, indicating a stronger interference between the separated flow and the trailing edge, and subsequently caused the increase in the critical wind velocity of galloping.

The lift force coefficient (C_{Fy}) is associated with the time-averaged flow separating from the leading edge (Kwok and Melbourne, 1980; Hu et. al., 2016; Melbourne, 1979). Because the models were symmetry to the axis for all the cases, the discussion between the time-averaged separated flow and C_{Fy} was limited to at $\alpha \geq 0^\circ$. C_{Fy} of the rectangular cylinder was 0 at $\alpha = 0^\circ$. When α is slightly larger than 0° (nose-up direction), the rectangular cylinder with the time-averaged separated flow of detached type, started to show the negative lift force (downward direction) because that the upside shear layer got far from the model leading to the pressure recovery at the upside surface and the downside shear layer approached the model (Nakamura et al., 1991; Mizota and Okajima, 1981). With the increase of α , accompanied by that the downside shear layer gradually approached the trailing edge, the absolute value of the C_{Fy} (negative) increased, achieving the maximum when the downside shear layer started to reattach to the side surface at $\alpha = \alpha_{max1}$. At $\alpha > \alpha_{max1}$, the separated flow totally reattached to the downside surface. Because the reattachment can cause pressure recovery on the surface (Mizota and Okajima, 1981; Hu et. al., 2016; Guissart et al., 2019), the pressure recovery on the downside surface reduced the absolute value of C_{Fy} . Therefore, with the further increase of α ($> \alpha_{max1}$) the absolute value of C_{Fy} (negative) started to decrease owing to that the reattachment point on the downside surface moved to the upstream side. By introducing the side-surface openings, the time-averaged separated flow approached the model surface at $\alpha = 0^\circ$, resulting in the early reattachment of the downside shear layer to the side surface at α_{max2} ($\alpha_{max1} > \alpha_{max2}$), where the absolute value of C_{Fy} (negative) achieved the maximum. Additionally, the more the time-averaged separated flow approached the side surface, the smaller the angle of attack α_{max} would be. Therefore, because that the time-averaged separated flow gradually approached the side surface with the increase of OR from 0 to 0.875 at $\alpha = 0^\circ$, the angle of attack α_{max} decreased with OR as shown in Fig. 5-4. If the time-averaged separated flow is of the reattachment type at $\alpha = 0^\circ$, at $\alpha > 0^\circ$ the reattachment point on the downside surface should move upstream, while the reattachment point on the upside surface should move downstream, resulting in an upward lift force. Therefore, for $OR = 1$, the C_{Fy} continuously increased with α from 0° to 10° and $dC_{Fy}/(d\alpha)$ kept positive at $-10^\circ < \alpha < 10^\circ$.

At high wind velocities, the relative angle of attack α_0 between the body vibration velocity and the approaching wind velocity is small, and the aerodynamic damping can be predicted by the linear quasi-steady aerodynamic damping characterized by the lift slope $-dC_{Fy}/d\alpha$. According to Fig. 5-6 and Fig. 5-22, the increase of the absolute value of lift slope $|-dC_{Fy}/d\alpha|_{\alpha=0^\circ}$ (the subscript indicates at $\alpha = 0^\circ$) with the increase of OR from 0 to 0.75 was accompanied by approaching of the time-averaged separated flow to the side surface at $\alpha = 0^\circ$. Therefore, the more the time-

averaged separated flow approached the side surface at $\alpha = 0^\circ$, the larger the pressure difference between the upside and downside surfaces at a small α ($\alpha > 0^\circ$) would be. For $OR = 0.875$, when the time-averaged separated flow started to reattach to the side surface at $\alpha = 0^\circ$, the separated flow reattached to the downside surface more at even a small α ($\alpha > 0^\circ$), resulting in the decrease in the absolute value of C_{Fy} . Therefore, $|-dC_{Fy}/d\alpha|_{\alpha=0^\circ}$ started to decrease with the increase of OR from 0.75 to 0.875.

In summary, at high wind velocities, the aerodynamic damping increased with the increase of OR from 0 to 0.75 when the time-averaged separated flow gradually approached the side surface and started to decrease with OR above 0.875 when the time-averaged separated flow started to reattach on the side surface. Despite of this complicated relationship between the aerodynamic damping and OR , the interference between the separated flow and the afterbody increased, as indicated by the approaching of the time-averaged separated flow to the side surface with the increase of OR , resulting in the increase in the critical wind velocity of galloping with OR . While the galloping was stabilized for $OR = 1$ owing to the reattachment-type flow.

5.5 Conclusion Remarks

The proposition of this chapter is to study the mechanism related to the stabilization against the galloping owing to the side-surface openings. The box girder was simplified as the rectangular cylinder with a side ratio B/D of 2, where B is the girder width and D is the girder depth. A series of wind tunnel tests, i.e., aerodynamic force tests, vertical 1DOF free vibration tests, vertical 1DOF forced vibration tests, wind velocity measurement and PIV tests, was carried out for the rectangular cylinder with discretely distributed side-surface openings. The opening size was defined by two parameters: Opening-area Ratio (OR) was the ratio between the total opening area and half the front surface area of the model; Repeating Element-size Ratio (RER) was the ratio between the length of a repeating element (defined as a group of a plate and an opening) and half the model depth. The following conclusions can be summarized:

- The critical wind velocity of the motion-induced vortex vibration was not affected by the openings, indicating that the vortex-convection velocity from the leading edge along the side surface is not affected by the side-surface openings. RER had no effects on the amplitude of the motion-induced vortex vibration, while the amplitude decreased with the increase of OR .
- The galloping response was slightly affected by RER for large OR ($OR = 0.75$) but not affected by RER for small OR ($OR = 0.25$). However, with the increase of OR , the amplitude of galloping vibration significantly decreased. Furthermore, because the reduced critical wind velocity of galloping is controlled by the reciprocal of Strouhal number, the decrease in the Strouhal number owing to the increase of OR resulted in the increase of the critical wind velocity of galloping.

- The lift force coefficients (C_{Fy}) and lift slope ($dC_{Fy}/d\alpha$) were not affected by RER , but significantly affected by OR . More specifically, the angle of attack α range, where the negative lift slope ($dC_{Fy}/d\alpha < 0$) showed, gradually decreased with the increase of OR . Therefore, with the increase of OR , the side-surface openings reduced the angle of attack α range, where the galloping may occur. Furthermore, the aerodynamic damping (H_1^*) was slightly affected by RER for large OR ($OR = 0.75$ and $OR = 0.875$) but not affected by RER for small OR ($OR = 0.25$ and $OR = 0.5$). At high reduced wind velocities, the aerodynamic damping (H_1^*) identified from the forced vibration tests was asymptotic to the curve of H_1^* predicted by the linear quasi-steady theory, which is characterized by negative lift slope ($-dC_{Fy}/d\alpha$). This indicates the validation of the linear quasi-steady theory for the rectangular cylinder with side-surface openings. Furthermore, the aerodynamic damping (H_1^* and $-dC_{Fy}/d\alpha$) increased with the growth of OR from 0 to 0.75, achieving the maximum at $OR = 0.75$, because the time-averaged separated flow gradually approached the trailing edge of the model with OR . With further increase of OR , the aerodynamic damping (H_1^* and $-dC_{Fy}/d\alpha$) started to decrease at $OR = 0.875$, owing to that the time-averaged separated flow started to reattach on the side surface. For $OR = 1$, the aerodynamic damping (H_1^* and $-dC_{Fy}/d\alpha$) showed negative value owing to the total reattachment of the time-averaged separated flow on the side surface.
- Even though the openings discretely distributed along the span-wise direction, the time-averaged separated flow in the vertical plane around the rectangular cylinder was almost the same at the opening center and the plate center (Gap between the plates is the opening). Furthermore, because the flow got through the openings with the approaching wind velocity for all the cases, the flow rate through the total openings increased significantly with the increase in the area of total openings, which is nondimensionalized as OR . Meanwhile, owing to the increase of flow rate through the openings, the time-averaged separated flow gradually approached the side surface with the increase of OR . Therefore, rather than RER , OR played an important role in the aerodynamic performance of the rectangular cylinder with side-surface openings.
- With the increase of OR , the side-surface openings promoted the time-averaged separated flow to approach the side surface and effectively increased the side ratio. The effective increase of side ratio owing to the increase of OR was also validated by that Strouhal number (St), drag force coefficient (C_{Fxr}) and fluctuating lift force coefficient (C_{Fy}') changed with OR in a similar way as the change of those coefficients with the side ratio. The approaching of the time-averaged separated flow to the side surface indicated an increasing interference between the separated flow and side surface, resulting in the

increase of the critical wind velocity of galloping with the increase of OR from 0 to 0.875. While the galloping was stabilized for $OR = 1$ owing to the total reattachment-type flow.

Even though at high wind velocities, the relationship between the aerodynamic damping and opening size was complicated, increasing OR effectively increased the side ratio by promoting the separated flow to reattach to the side surface, resulting in better galloping stability. Therefore, applying the openings is a promising method to manipulate the flow field around the rectangular cylinder-like bluff bodies to benefit the aerodynamic performance.

Reference

- Bearman, P.W., Trueman, D.M., 1972. An Investigation of the Flow around Rectangular Cylinders. *Aeronaut. Q.* 23, 229–237. <https://doi.org/10.1017/s0001925900006119>
- Frank M. White, 2011. *Fluid Mechanics*, Seventh Ed. The McGraw-Hill Companies, Inc., New York.
- Gao, G., Zhu, L., 2016. Measurement and verification of unsteady galloping force on a rectangular 2:1 cylinder. *J. Wind Eng. Ind. Aerodyn.* 157, 76–94. <https://doi.org/10.1016/j.jweia.2016.08.004>
- Gerrard, J.H., 1966. The mechanics of the formation region of vortices behind bluff bodies. *J. Fluid Mech.* 25, 401–413. <https://doi.org/10.1017/S0022112066001721>
- Guissart, A., Andrienne, T., Dimitriadis, G., Terrapon, V.E., 2019. Numerical and experimental study of the flow around a 4:1 rectangular cylinder at moderate Reynolds number. *J. Wind Eng. Ind. Aerodyn.* 189, 289–303.
- Hirata, K., 1993. Mechanism of galloping. Ph.D. thesis, University of Kyushu, Kyushu, Japan. <https://DOI.org/10.11501/3071379>
- Hu, G., Tse, K.T., Kwok, K.C.S., 2016. Aerodynamic mechanisms of galloping of an inclined square cylinder. *J. Wind Eng. Ind. Aerodyn.* 148, 6–17. <https://doi.org/10.1016/j.jweia.2015.10.011>
- Huang, R.F., Hsu, C.M., Chen, Y.T., 2017. Modulating flow and aerodynamic characteristics of a square cylinder in crossflow using a rear jet injection. *Phys. Fluids.* 29, 015103-1–15. <https://doi.org/10.1063/1.4972982>
- Kiya, M., Nozawa, T., 1987. Turbulence structure in the leading-edge separation zone of a blunt circular cylinder. *Trans. JSME Ser. B.* 53, 1183–1189.
- Koutmos, P., Papailiou, D., Bakroziis, A., 2004. Experimental and computational study of square cylinder wakes with two-dimensional injection into the base flow region. *Eur. J. Mech. B/Fluids.* 23, 353–365. <https://doi.org/10.1016/j.euromechflu.2003.09.004>
- Kwok, K.C.S., Melbourne, W.H., 1980. Freestream turbulence effects on galloping. *J. Eng. Mech. Div.* 106, 273–288.

Laneville, A., Parkinson, G., 1971. Effects of turbulence on galloping of bluff cylinders. In Proceedings 3rd International Conference on Wind Effects on Buildings and Structures, Tokyo, Japan.

Laneville, A., 1973. Effects of turbulence on wind induced vibrations of bluff cylinders. Ph.D. thesis, the University of British Columbia, Vancouver, BC, Canada.

Laneville, A., LüZhi Yong, 1983. Mean flow patterns around two-dimensional rectangular cylinders and their interpretation. *J. Wind Eng. Ind. Aerodyn.* 14, 387–398. [https://doi.org/10.1016/0167-6105\(83\)90040-5](https://doi.org/10.1016/0167-6105(83)90040-5)

Luo, S.C., Bearman, P.W., 1990. Predictions of fluctuating lift on a transversely oscillating square-section cylinder. *J. Fluids Struct.* 4, 219–228. [https://doi.org/10.1016/0889-9746\(90\)90086-K](https://doi.org/10.1016/0889-9746(90)90086-K)

Matsumoto, M. 1996. Aerodynamic damping of prism. *J. Wind Eng. Ind. Aerodyn.* 59, 159–175.

Matsumoto, M., Yagi, T., Lee, J., Hori, K., Kawashima, Y., 2006. Kármán Vortex Effect on the Aerodynamic Forces to Rectangular Cylinders. Press. Vessel. Pip. Div. Conf. ASME., Vancouver, BC, Canada. <https://doi.org/10.1115/PVP2006-ICPVT-11-93783>

Matsumoto, M., Yagi, T., Tamaki, H., Tsubota, T., 2008. Vortex-induced vibration and its effect on torsional flutter instability in the case of $B/D = 4$ rectangular cylinder. *J. Wind Eng. Ind. Aerodyn.* 96(6–7), 971–983. <https://doi.org/10.1016/j.jweia.2007.06.023>

Mannini, C., Marra, A.M., Bartoli, G., 2014. VIV-galloping instability of rectangular cylinders: Review and new experiments. *J. Wind Eng. Ind. Aerodyn.* 132, 109–124. <https://doi.org/10.1016/j.jweia.2014.06.021>

Mannini, C., Marra, A.M., Massai, T., Bartoli, G., 2016. Interference of vortex-induced vibration and transverse galloping for a rectangular cylinder. *J. Fluids Struct.* 66, 403–423. <https://doi.org/10.1016/j.jfluidstructs.2016.08.002>

Massai, T., 2016. On the Interaction between vortex-induced vibrations and galloping in rectangular cylinders of low side ratio. Dr.-Ing. Thesis, Technische Universität Braunschweig, Braunschweig, Germany.

Mizota, T., Okajima, A., 1981. Experimental studies of time mean flows around rectangular prisms. *Proc. Jpn. Soc. Civ. Eng.* 312, 39–47 (in Japanese). https://doi.org/10.2208/jscej1969.1981.312_39

Nakamura, Y., Mizota, T., 1975. Unsteady lifts and wakes of oscillating rectangular prisms. *J. Eng. Mechanics Div.* 101, 855–871.

Nakamura, Y., Tomonari, Y., 1977. Galloping of rectangular prisms in a smooth and in a turbulent flow. *J. Sound Vib.* 52, 233–241. [https://doi.org/10.1016/0022-460X\(77\)90642-3](https://doi.org/10.1016/0022-460X(77)90642-3)

Nakamura, Y., Hirata, K., Urabe, T., 1991. Galloping of rectangular cylinders in the presence of a splitter plate. *J. Fluids Struct.* 5, 521–549. [https://doi.org/10.1016/S0889-9746\(05\)80004-0](https://doi.org/10.1016/S0889-9746(05)80004-0)

Nakamura, Y., Hirata, K., 1994. The aerodynamic mechanism of galloping. *Trans. Jpn. Soc. Aeronaut. Space Sci.* 36, 257–269.

- Nakagawa, S., Nitta, K., Senda, M., 1999. An experimental study on unsteady turbulent near wake of a rectangular cylinder in channel flow. *Exp. Fluids* 27, 284–294.
- Nakaguchi, H., Hashimoto, K., Muto, S., 1968. An experimental study on aerodynamic drag of rectangular cylinders. *J. Japan Soc. Aeronaut. Space Sci.* 16, 1–5 (in Japanese).
- Novak, M., 1972. Galloping oscillation of prismatic structures. *J. Eng. Mech. Div.* 98, 27–46.
- Obasaju, E.D., 1983. Forced-vibration study of the aeroelastic instability of a square-section cylinder near vortex resonance. *J. Wind Eng. Ind. Aerodyn.* 12, 313–327.
- Okajima, A., 1983. Flow around a rectangular cylinder with a section of various width/height ratios. *J. Wind Eng. (JAWE)* 17, 1–19. (in Japanese)
- Otsuki, Y., Washizu, K., Tomizawa, H., Ohya, A., 1974. A note on the aeroelastic instability of a prismatic bar with square section. *J. Sound Vib.* 34, 233–248.
- Otsuki Y., Fujii K., Washizu K., Ohya A., 1978. Wind tunnel experiments on aerodynamic forces and pressure distributions of rectangular cylinders in a uniform flow. *Proceedings of 5th symposium on Wind Effects on Structures*, 169-176.
- Parkinson, G. V., Brooks, N.P.H., 1961. On the Aeroelastic Instability of Bluff Cylinders. *J. Appl. Mech.* 28, 252–258.
- Parkinson, G. V, Wawzonek, M.A., 1981. Some considerations of combined effects of galloping and vortex resonance. *J. Wind Eng. Ind. Aerodyn.* 8, 135-143.
- Parkinson, G. V., 1989. Phenomena and modelling of flow-induced vibrations of bluff bodies. *Prog. Aerosp. Sci.* 26, 169–224.
- Sakamoto H., Haniu H., Kobayashi Y., 1989. Fluctuating force acting on rectangular cylinders in uniform flow, *Trans. of JSME Ser. B., Tokyo*, 55(516), 2310-2317.
- Scanlan, R. H., Tomko, J., 1971. Air foil and bridge deck flutter derivatives. *J. Eng. Mech.* 97(6), 1717–1937.
- Shimada, K., Meng, Y., 1998. Applicability of modified k-ε model on the estimation of aerodynamic properties of rectangular cylinders with various elongated cross sections. *J. Struct. Constr. Engrg., Tokyo* 514, 73–80.
- Smith, J.D., 1960. An Experimental Study of the Aeroelastic Instability of Rectangular Cylinders. Master's thesis, University of British Columbia, Vancouver, BC, Canada.
- Sohankar, A., 2008. Large eddy simulation of flow past rectangular-section cylinders: Side ratio effects. *J. Wind Eng. Ind. Aerodyn.* 96, 640–655. <https://doi.org/10.1016/j.jweia.2008.02.009>
- Tamura, T., Ito, Y., 1995. Aerodynamic characteristics and flow structures around a rectangular cylinder with a section of various depth/breadth ratios. *J. of Struct. Constr. Eng. (Trans. of AIJ)* 486, 153-162.
- Wang, J., Yagi, T., Ushioda, J., Nagamoto, N., Uchibori, H., Shirato, H., 2017. Aerodynamic Performance of Box Girder with Side-surface openings. *Proc., 9th Asia-Pacific Conf. Wind Eng., Auckland, New Zealand.*
- Washizu, K., Ohya, A., Otsuki, Y., Fujii, K., 1978. Aeroelastic instability of rectangular cylinders in a heaving mode. *J. Sound Vib.* 59, 195–210.

Yagi, T., Shinjo, K., Narita, S., Nakase, T., Shirato, H., 2013. Interferences of vortex sheddings in galloping instability of rectangular cylinders. *J. of Struct. Eng. A (JSCE)*. 59A, 552–561 (in Japanese).

6 Conclusion and the future topic

6.1 Conclusion

This research aimed to assess the feasibility of the method to stabilize the box girder against the aerodynamic instabilities by discretely setting the openings on the side surface. The side-surface openings, which are shaped by the gaps between the webs on the side surface of the butterfly web girder, are a design to achieve a good balance between the lightness and the structural performance for the box girder, benefiting the expansion of the span length. However, the sensitivity of the flexible bridge to the natural wind arises the concern regarding the effects of the side-surface openings on the aerodynamic performance of the box girder, the ignorance of which may lead to the catastrophic vibration. Furthermore, when the bridge is accompanied by another adjacent bridge, the aerodynamic performance of the bridge would be even more unstable. This raises another concern regarding the aerodynamic performance of the box girder with side-surface openings in the tandem arrangement. Among all the aerodynamic instabilities, the focus of this research is the galloping owing to its potentially destructive effects on the bridge. In this context, the study sought to answer two questions:

1. How is the aerodynamic performance of the box girder with the side-surface openings in a single stand-alone situation and in the tandem arrangement?
2. What is the mechanism related to the effects of side-surface openings on the galloping instability?

In order to answer the **first question**, two single butterfly web girders with different side ratios B/D , where B is the body width and D is the body height, were examined through a series of wind tunnel tests, i.e., free vibration tests, forced vibration tests, aerodynamic force tests, and wind velocity measurement tests. By covering the openings of these two butterfly web girders, two conventional box girders were also examined through the aforementioned wind tunnel tests. The $B/D = 3.24$ conventional box girder was characterized by the vortex-induced vibration, the torsional flutter, and the galloping, while $B/D = 5$ conventional box girder was characterized by the vortex-induced vibration and the torsional flutter. Whether introducing the side-surface opening to the conventional box girder can stabilize these aerodynamic phenomena was investigated. Furthermore, the $B/D = 3.24$ butterfly web girder was duplicated to investigate the aerodynamic performance of the box girders with side-surface openings in the tandem arrangement through a series of wind tunnel tests, i.e., free vibration tests, forced vibration tests and aerodynamic force tests. Either of two girders was rigidly supported in the wind tunnel, while the other girder was investigated at upstream or downstream side with a center distance of twice the girder width B . The main **achievements** regarding the first question are summarized below:

- For the single stand-alone girder, the side-surface openings had no effects on the critical wind velocity of the motion-induced vortex vibration but stabilized the motion-induced vortex vibration in both the vertical and torsional directions. The torsional flutter of $B/D = 3.24$ and $B/D = 5$ girders was different regarding the mechanism, as indicated by the decrease of the aerodynamic damping at high wind velocities with the increase of their equivalent side ratio B'/D' , where B' is the equivalent girder width and D' is the equivalent girder depth due to the angle of attack. Subsequently, the side-surface openings had no effects on the torsional flutter of the $B/D = 3.24$ butterfly web girder but significantly stabilized the torsional flutter of the $B/D = 5$ butterfly web girder by increasing its critical wind velocity. Meanwhile, as indicated by the time-averaged wind velocity vector in the near wake and within the girder, the flow got through the inner space of the box girder into the wake, promoting the separated flow from the leading edge to approach the trailing edge. Even though such a change in the flow field caused by the openings had no effects on the Strouhal number, the side-surface openings significantly suppressed the Kármán-vortex shedding. Furthermore, potentially owing to the enhanced reattachment of the separated flow on the side surface, the side-surface openings stabilized the galloping by increasing its critical wind velocity and minimizing the vibration amplitude and aerodynamic damping.
- For two girders in the tandem arrangement, the fixed downstream box girder did not affect the motion-induced vortex vibration of the upstream girder but made the upstream girder more unstable in the galloping. The upstream girder was more unstable in the galloping owing to the suppression of the Kármán-vortex shedding from the upstream girder caused by the downstream girder. Introducing the side-surface openings to the downstream box girder did not affect the aerodynamic performance of the upstream girder, regarding the vibration amplitude and aerodynamic damping. The side-surface openings of the upstream girder stabilized its motion-induced vortex vibration and galloping. The periodic turbulent flow from the fixed upstream box girder slightly increased the critical wind velocity of the vortex-induced vibration of the downstream girder owing to the decrease of the Strouhal number, which is caused by the synchronization between the vortex shedding from the upstream girder and the vortex formation of the downstream girder. The turbulent flow from the upstream box girder also amplified the vortex-induced vibration of the downstream girder and totally stabilized the downstream girder against the galloping. The side-surface openings of the fixed upstream girder did not affect the aerodynamic response of the downstream girder. While the side-surface openings of the downstream girder stabilized the vortex-induced vibration of the downstream girder.

In order to answer the **second question**, the $B/D = 3.24$ butterfly web girder with a side ratio of 3.24 was simplified as the rectangular cylinder with a side ratio of 2. A series of wind tunnel tests, free vibration tests, forced vibration tests, aerodynamic force tests, wind velocity measurement

tests and PIV tests, was carried out for the rectangular cylinder with different sized side-surface openings. The opening size was nondimensionalized by two parameters: Opening-area Ratio (OR) is the ratio between the area of the total openings and half the front-surface area; Repeating Element-size Ratio (RER) is the ratio between the width of a repeating element (consisting of one plate and one opening) to the inner-space height. The mechanism related to the stabilization against the galloping is firstly explained based on the general relationship between the different sized side-surface openings and the galloping, regarding the aerodynamic response and aerodynamic damping. This mechanism is further interpreted based on the flow visualization results. The main **achievements** regarding the second question are summarized below:

- Introducing the openings to the side surface of the rectangular cylinder did not affect the onset of the motion-induced vortex vibration. RER had no effects on the amplitude of the motion-induced vortex vibration, while the amplitude decreased with the increase of OR .
- The galloping instability was significantly affected by the Opening-area Ratio (OR) rather than the Repeating Element-size Ratio (RER). Firstly, because the reduced critical wind velocity of galloping is controlled by the reciprocal of Strouhal number, the decrease in the Strouhal number owing to the increase in OR resulted in the increase in the critical wind velocity of galloping. Secondly, with the increase of OR , the angle of attack α range, where the negative lift slope ($dC_{Fy}/d\alpha < 0$, C_{Fy} is the lift force coefficient and α is the angle of attack) showed, gradually decreased. Therefore, with the increase of OR , the side-surface openings reduced the angle of attack range, where the galloping may occur. Thirdly, at high reduced wind velocities, the quasi-steady theory was valid for the rectangular cylinder with side-surface openings, because that its unsteady linear aerodynamic damping identified from the forced vibration tests was asymptotic to the aerodynamic damping predicted by the linear quasi-steady theory. Therefore, even introducing the openings to the rectangular cylinder, the linear unsteady aerodynamic damping can be characterized by the lift slope ($dC_{Fy}/d\alpha < 0$). Meanwhile, the aerodynamic damping increased with the increase of OR from 0 to 0.75 owing to the approaching of the time-averaged separated flow to the side surface, achieving the maximum for $OR = 0.75$. With a further increase of OR from 0.875, the aerodynamic damping started to decrease when the time-averaged separated flow started to reattach on the side surface. Fourthly, even though the openings discretely distributed along the span-wise direction, the time-averaged separated flow in the vertical plane around the rectangular cylinder did not change along the span-wise direction. Owing to that the flow rate through the total openings increased with OR , the time-averaged separate flow gradually approached the side surface with the increase of OR . Therefore, with the increase of OR , the side-surface openings promoted the time-averaged separated flow to approach the side surface and effectively increased the side ratio. The effective increase in the side ratio owing to the increase in OR was supported by the fact that Strouhal

number and aerodynamic force coefficients varied with OR in a similar way as the change of those coefficients with side ratio. Consequently, even though at high reduced wind velocities, the aerodynamic damping showed a complicated relationship with OR , the side-surface openings significantly stabilized the galloping by increasing the critical wind velocity and reducing the vibration amplitude. This is because that the side-surface openings promoted the reattachment of the separated flow on the side surface and strengthened the interference between the shear layer and side surface.

The side-surface openings were confirmed to stabilize the box girder against the different aerodynamic instabilities, i.e. the vortex-induced vibration, the galloping, and the torsional flutter. When the girders were in the tandem arrangement, the side-surface openings still stabilized the box girder against the vortex-induced vibration and galloping. These findings show that introducing the side-surface openings is a promising method to design the strong-and-light box girder with good aerodynamic performance. Furthermore, the side-surface openings were proved to stabilize the rectangular cylinder against the galloping by promoting the reattachment of the separated flow on the side surface. This finding highly coincides with past researches related to the effects of the side ratio and the turbulent flow on the galloping: the increase in the side ratio or the turbulence intensity can also stabilize the galloping by promoting the reattachment of the separated flow on the side surface. Therefore, the implication of the side-surface openings is not just limited to the box girder but also more general rectangular cylinder-like bluff bodies, i.e. high-rise buildings.

6.2 Future topics

This research confirms the feasibility of the method to stabilize the box girder against the aerodynamic instabilities by introducing the side-surface openings and provides an explanation for the mechanism related to the stabilization against the galloping owing to the side-surface openings. However, some questions still remain regarding the mechanism related to the effects of side-surface openings on the vortex-induced vibration and torsional flutter.

Firstly, the onset of the motion-induced vortex vibration was not affected by the side-surface openings. While the increase in OR significantly reduced the amplitude of motion-induced vortex vibration. Because the vortex-induced vibration is an unsteady aerodynamic phenomenon, these stabilization effects need further investigation on the effects of the side-surface openings on the pressure field around the oscillating body at the wind velocity range of the motion-induced vortex vibration.

Secondly, the stabilization against the torsional flutter owing to the side-surface openings depended on the side ratio. This is thought to be caused by that the mechanism of the torsional flutter depends on the side ratio. A more careful examination of the effects of the side-surface openings on the flow field and pressure field around the torsional-vibrating body with different

side ratios should be carried out to reach an explanation for the stabilization against the torsional flutter owing to the side-surface openings.

Appendix

Appendix A

Extensive results for the single butterfly web girder

Aerodynamic force coefficient for $B/D = 3.24$ butterfly web girder ($U = 10\text{m/s}$).

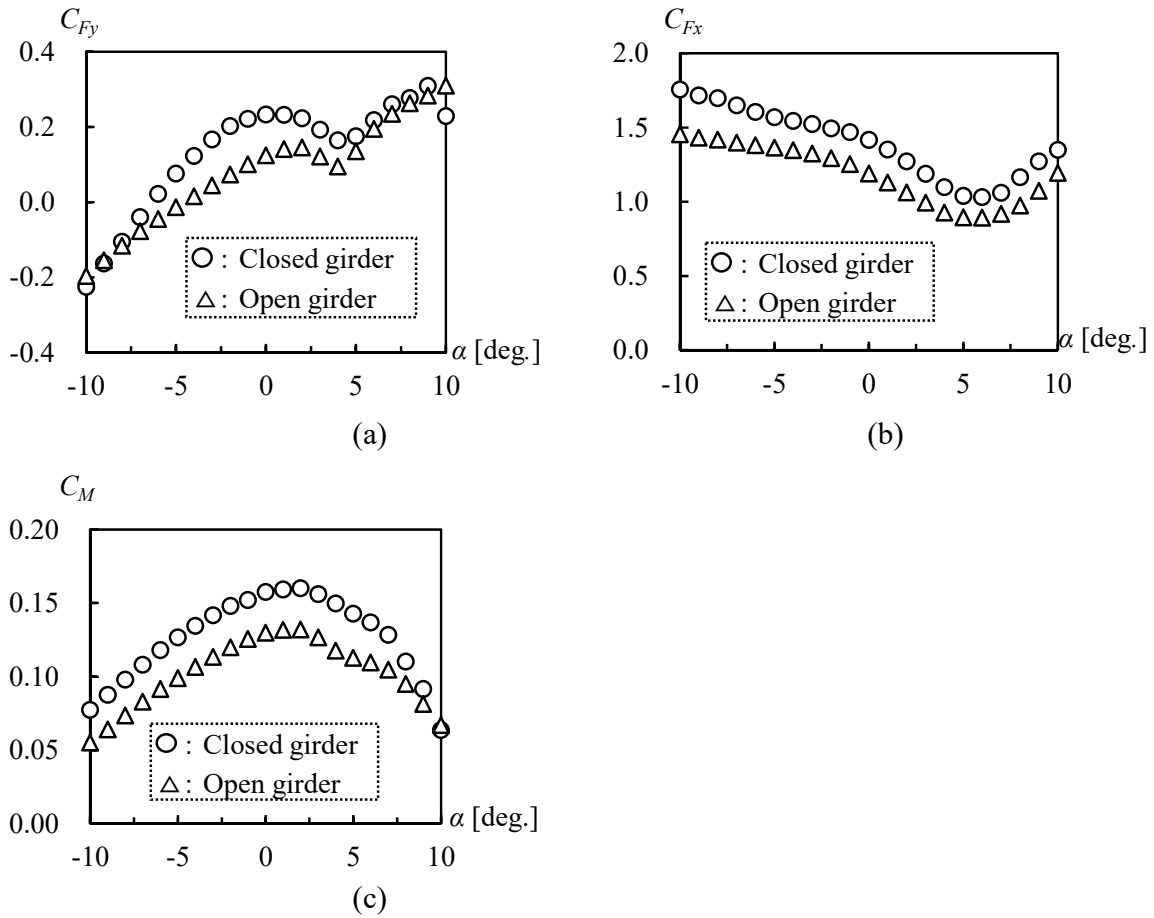


Fig. A 1 Aerodynamic force coefficients ($B/D = 3.24$ model, $U = 10\text{ m/s}$, smooth flow) for (a) lift force C_{Fy} ; (b) drag force C_{Fx} ; (c) pitching moment C_M .

Aerodynamic response for $B/D = 3.25$ butterfly web girder at $\alpha = 0^\circ$ and $\alpha = -3^\circ$

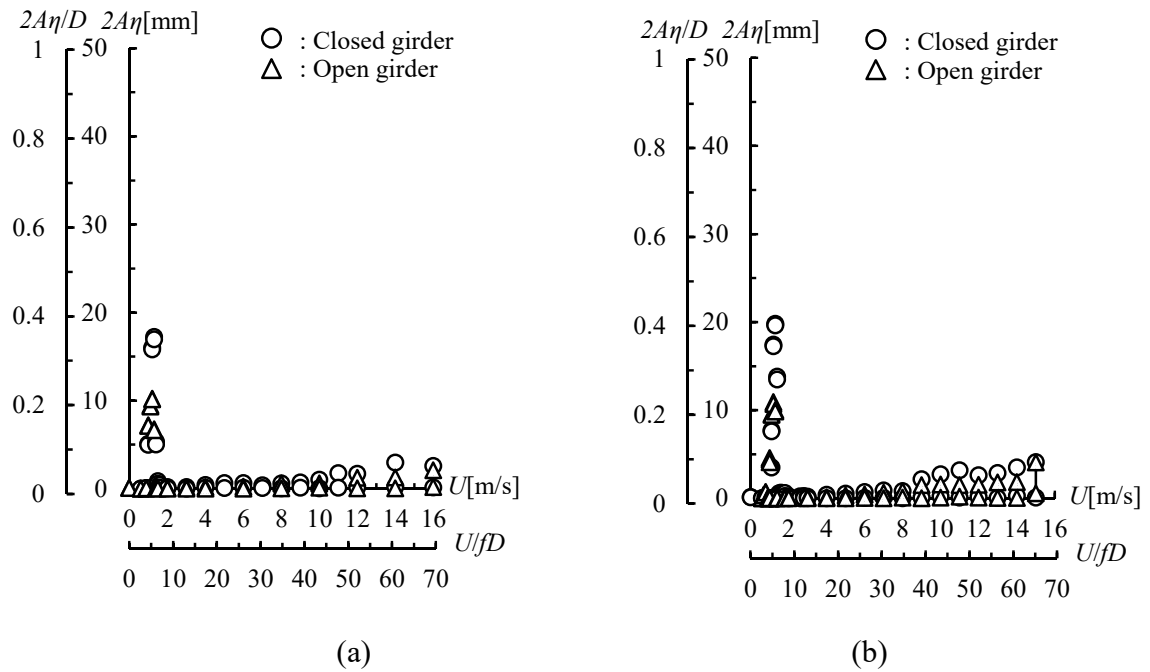


Fig. A 2 Aerodynamic response of the $B/D = 3.25$ model (vertical 1DOF, smooth flow): (a) at $\alpha = -3^\circ$; (b) at $\alpha = 0^\circ$.

Flutter derivatives of the $B/D = 3.24$ butterfly web girder at $\alpha = +3^\circ$.

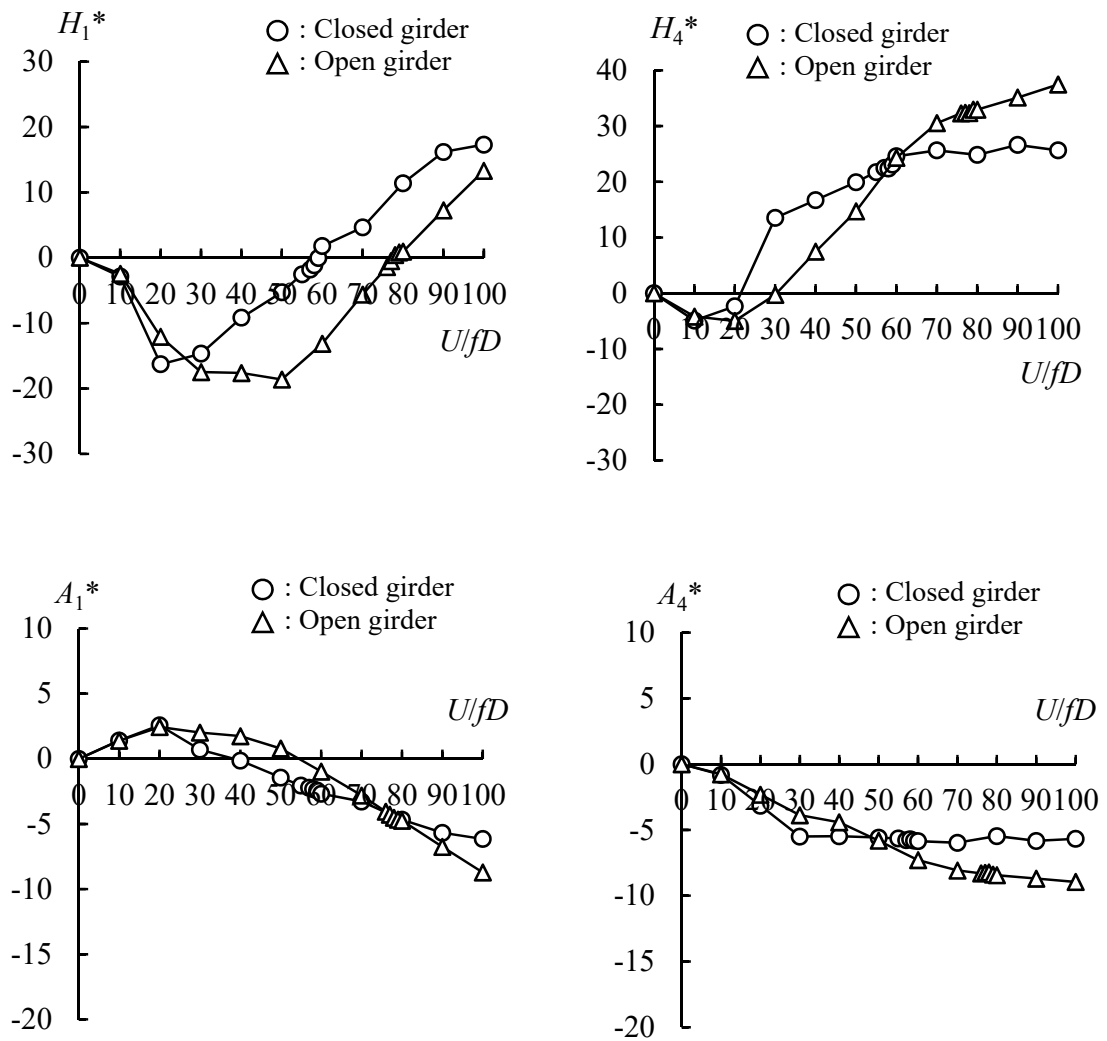


Fig. A 3 Flutter derivatives ($B/D = 3.24$, vertical 1DOF, $\alpha = +3^\circ$, $f = 2.0$ Hz, $2A\eta = 20$ mm, smooth flow).

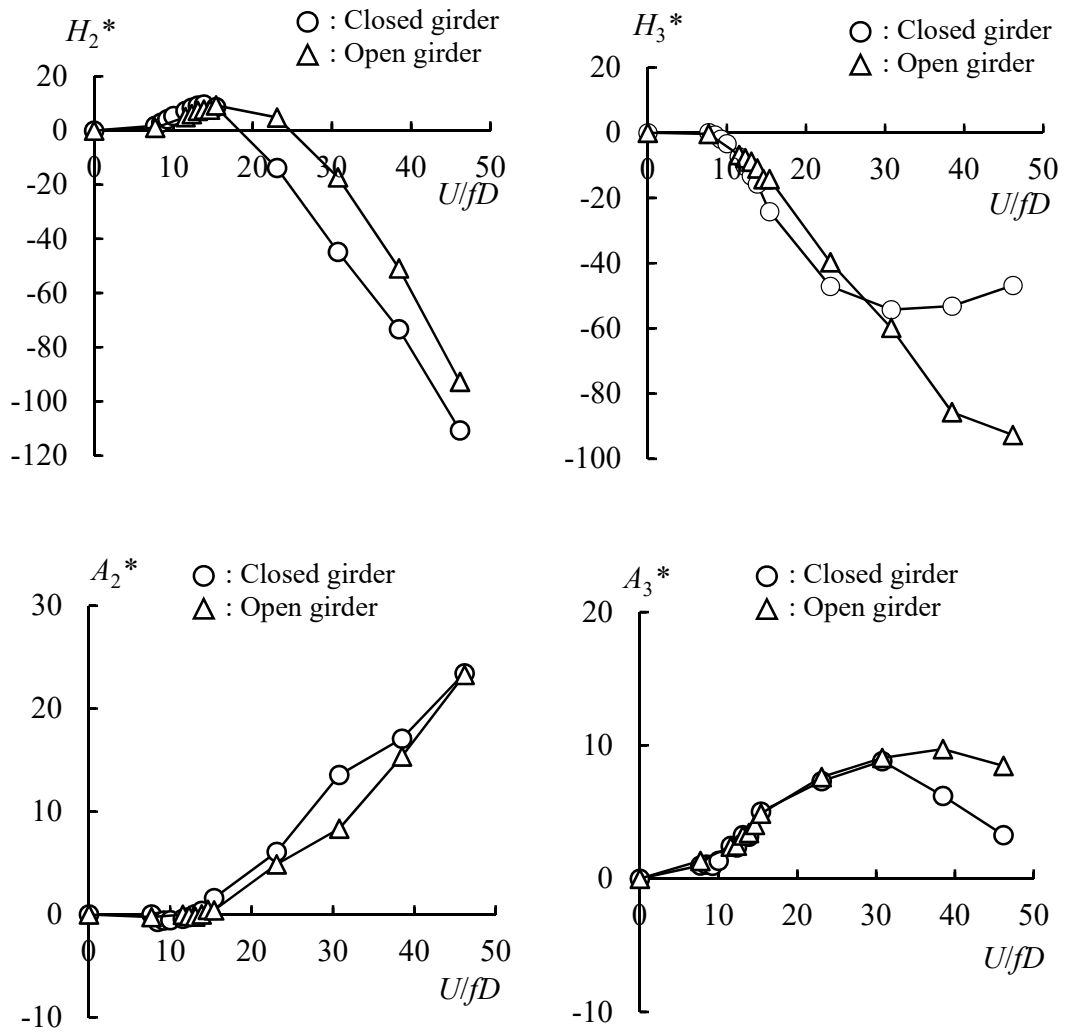


Fig. A 4 Flutter derivatives ($B/D = 3.24$, torsional 1DOF, $\alpha = +3^\circ$, $f = 2.6$ Hz, $2A\varphi = 4^\circ$, smooth flow).

Flutter derivatives of the $B/D = 3.24$ butterfly web girder at $\alpha = 0^\circ$.

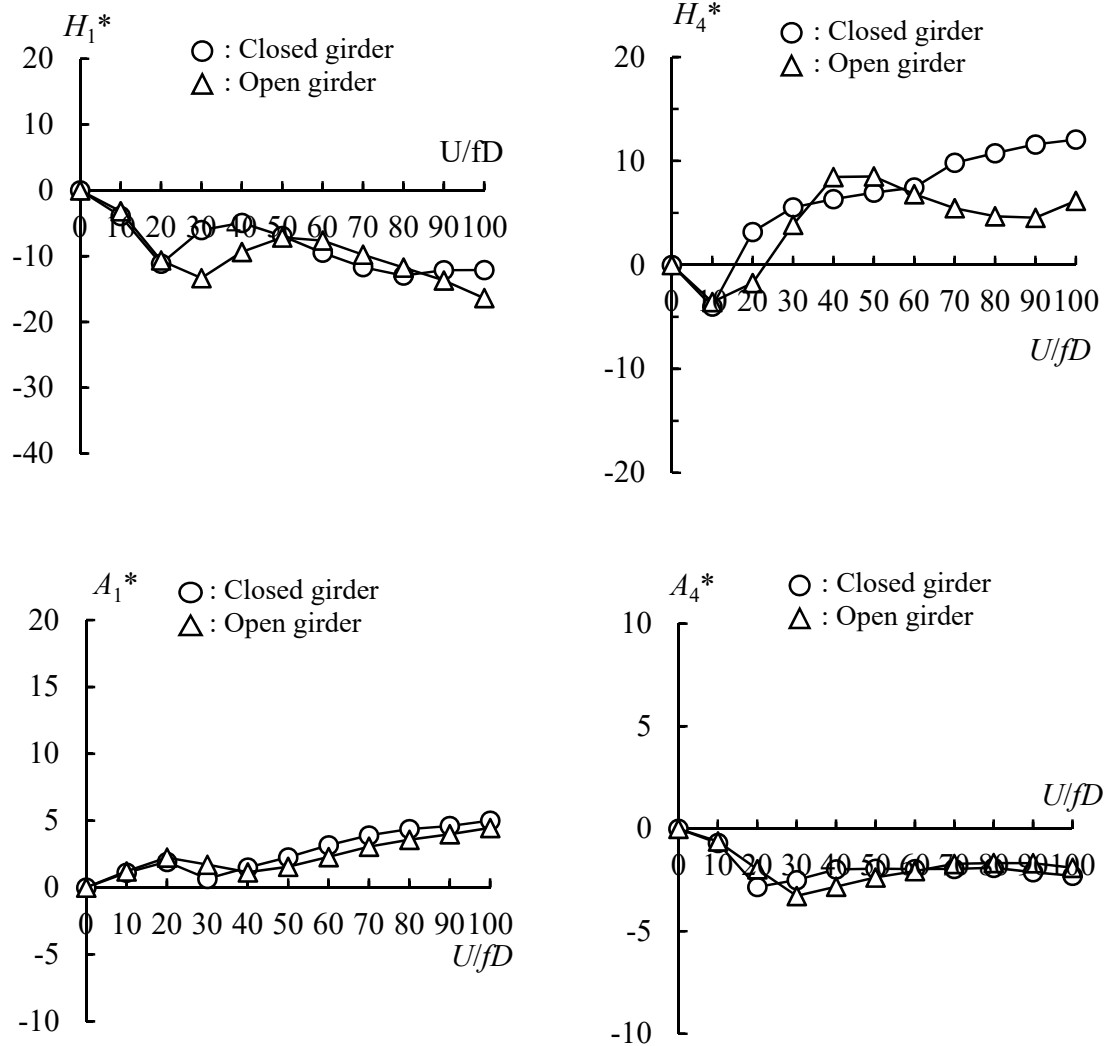


Fig. A 5 Flutter derivatives ($B/D = 3.24$, vertical 1DOF, $\alpha = 0^\circ$, $f = 2.0$ Hz, $2A\eta = 20$ mm, smooth flow).

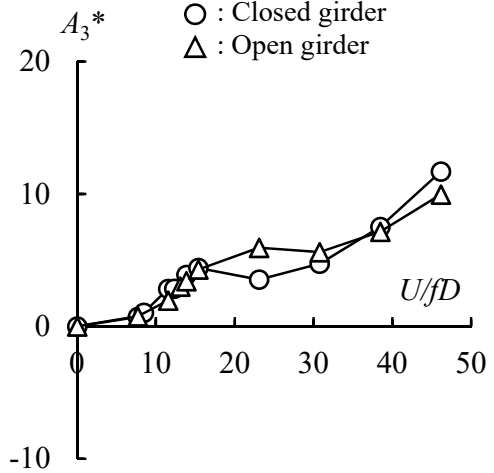
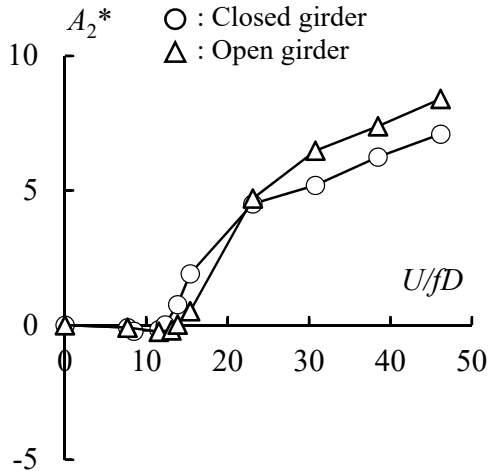
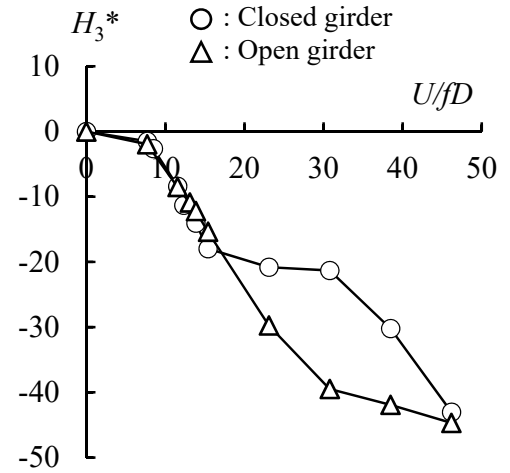
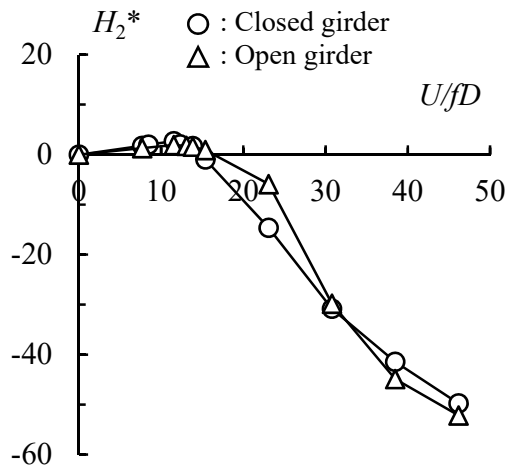


Fig. A 6 Flutter derivatives ($B/D = 3.24$, torsional 1DOF, $\alpha = 0^\circ$, $f = 2.6$ Hz, $2A\phi = 4^\circ$, smooth flow).

Aerodynamic response for $B/D = 5$ butterfly web girder at $\alpha = 0^\circ$ and $\alpha = -3^\circ$

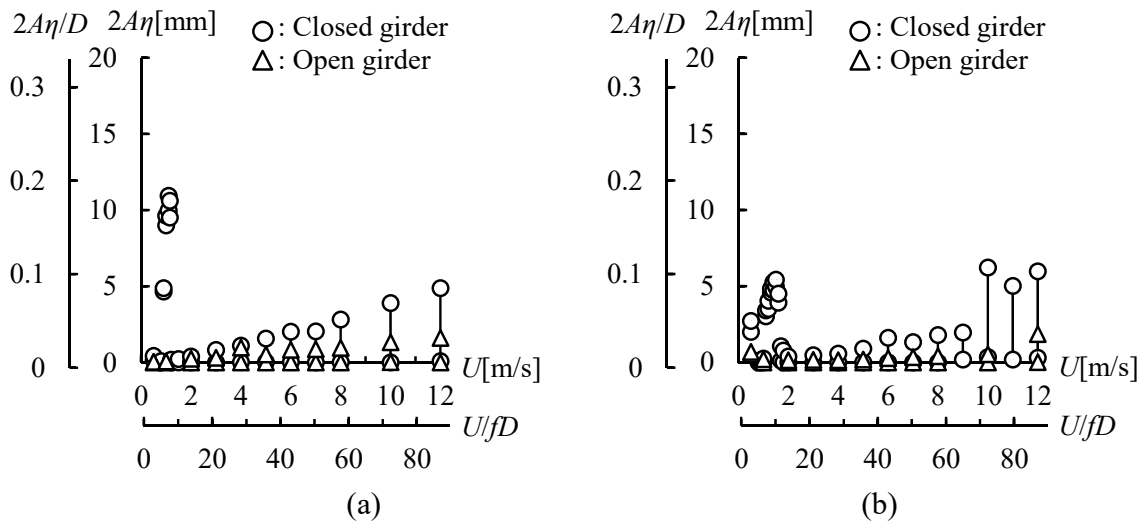


Fig. A 7 Aerodynamic response of the $B/D = 5$ model (vertical 1DOF, smooth flow): (a) $\alpha = +3^\circ$; (b) $\alpha = -3^\circ$.

Aerodynamic force coefficient for $B/D = 5$ butterfly web girder ($U = 8\text{m/s}$).

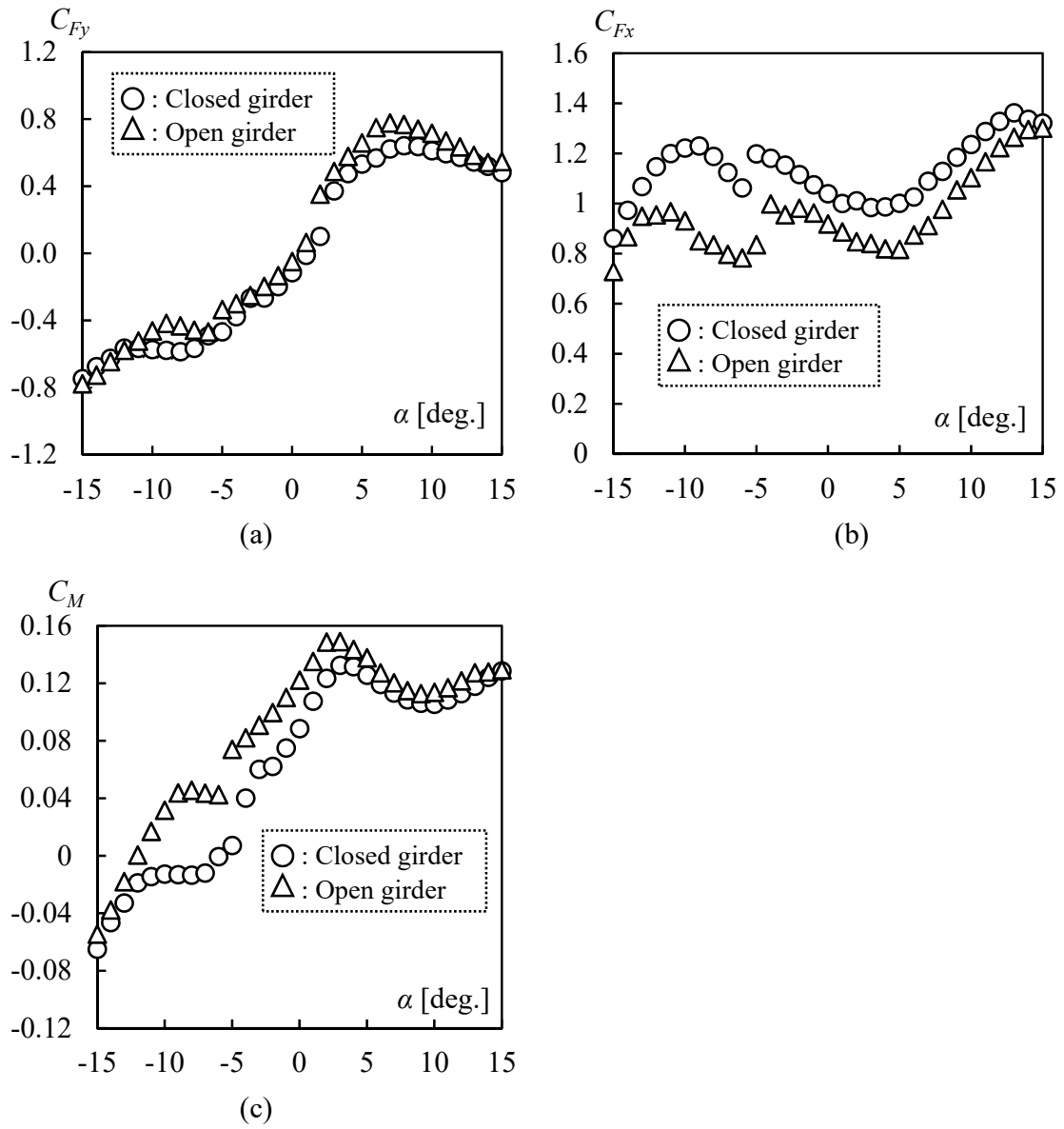


Fig. A 8 Aerodynamic force coefficients ($B/D = 5$ model, $U = 8\text{ m/s}$, smooth flow) for (a) lift force C_{Fy} ; (b) drag force C_{Fx} ; (c) pitching moment C_M .

Aerodynamic force coefficient for $B/D = 5$ butterfly web girder ($U = 12\text{m/s}$).

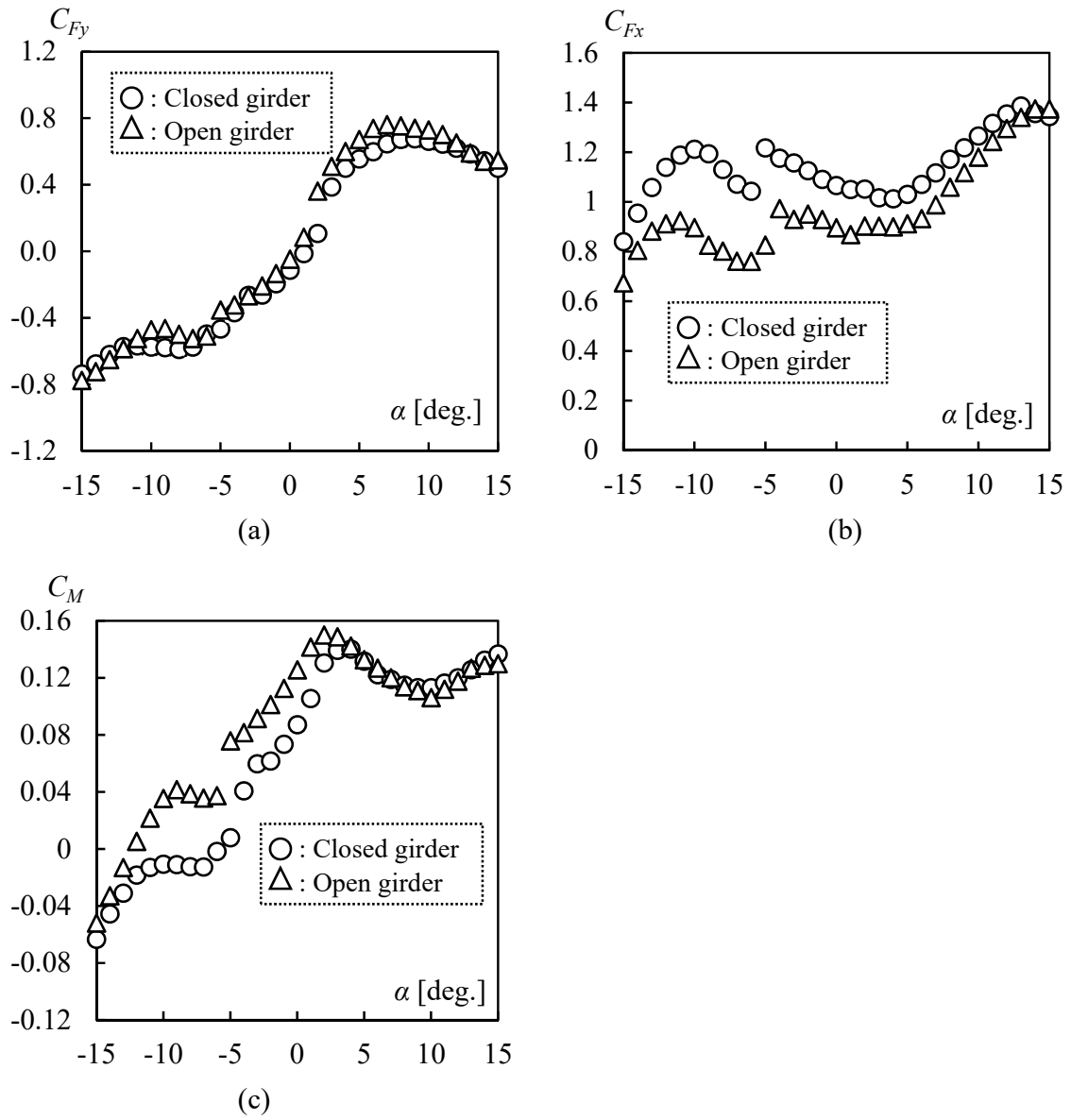


Fig. A 9 Aerodynamic force coefficients ($B/D = 5$ model, $U = 12\text{m/s}$, smooth flow) for (a) lift force C_{Fy} ; (b) drag force C_{Fx} ; (c) pitching moment C_M .

Flutter derivatives of the $B/D = 5$ butterfly web girder at $\alpha = 0^\circ$.

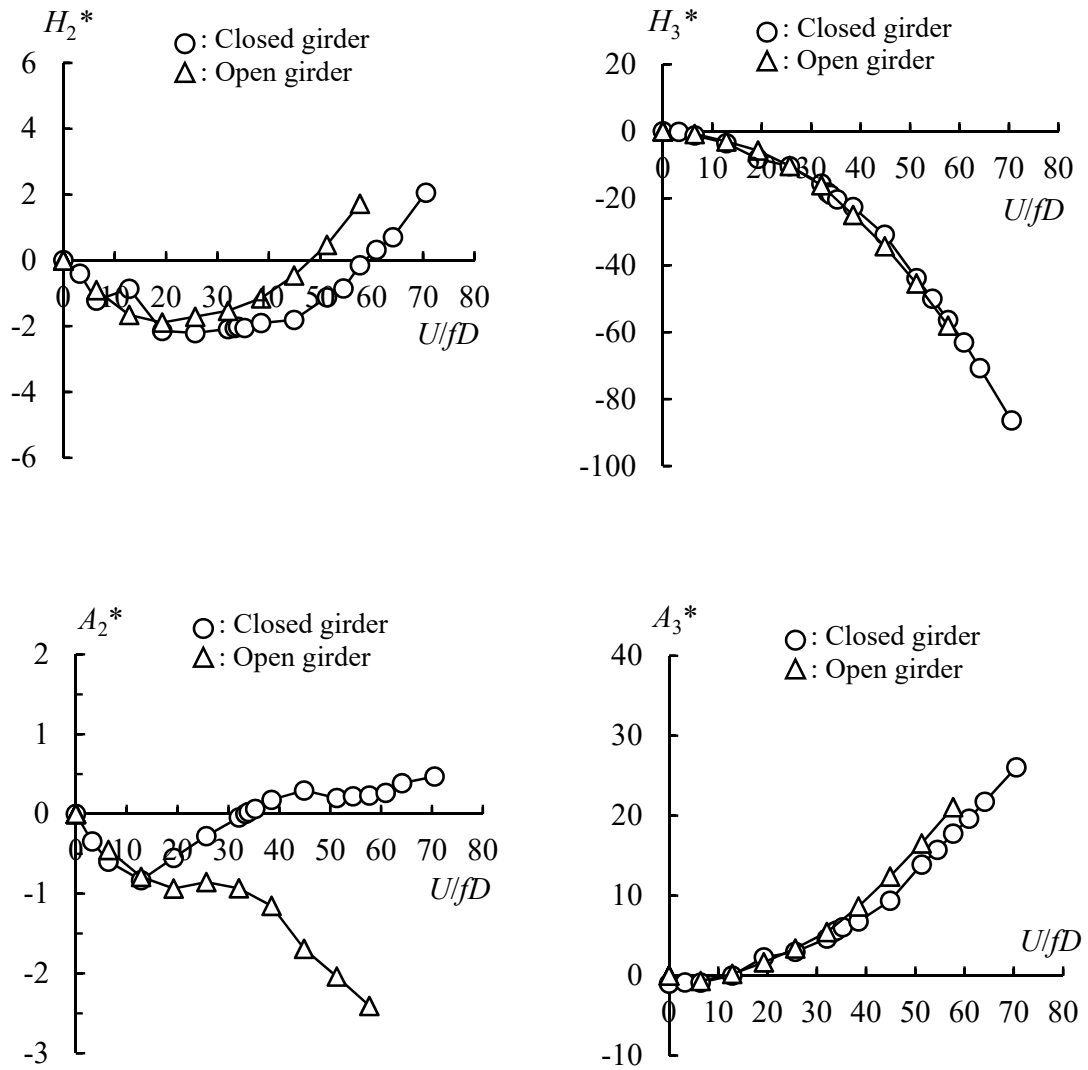


Fig. A 10 Flutter derivatives ($B/D = 5$, torsional 1DOF, $\alpha = 0^\circ$, $f = 2.6$ Hz, $2A\varphi = 4^\circ$, smooth flow).

Flutter derivatives of the $B/D = 5$ butterfly web girder at $\alpha = +3^\circ$.

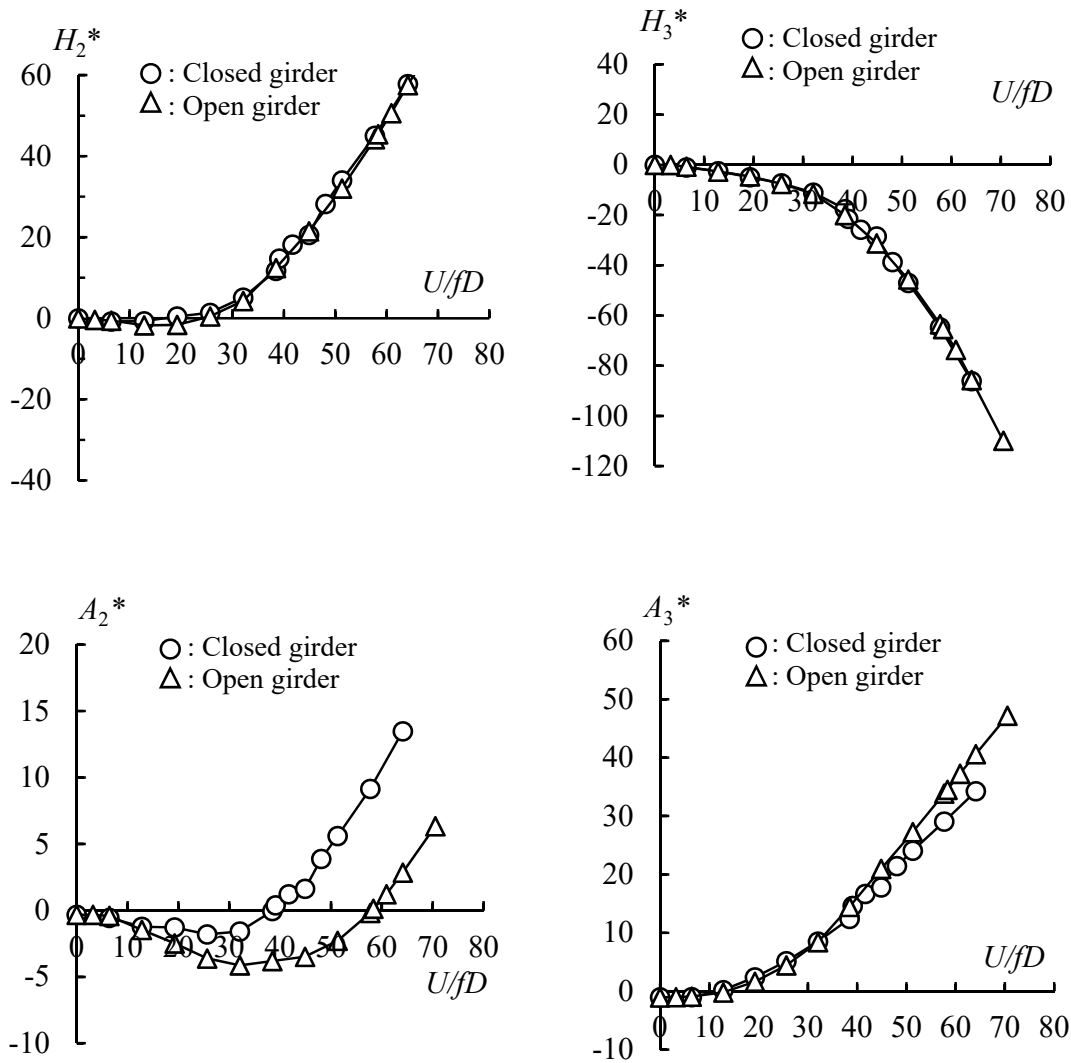


Fig. A 11 Flutter derivatives ($B/D = 5$, torsional 1DOF, $\alpha = +3^\circ$, $f = 2.6$ Hz, $2A\varphi = 4^\circ$, smooth flow).

Appendix B

Extensive results for the parallel $B/D = 3.24$ butterfly web girders

Aerodynamic force coefficients of the upstream girder

Table B 1 Upstream girder aerodynamic force coefficients (downstream girder fixed)

Upstream girder	Downstream girder	Attack angle	Wind velocity [m/s]	Drag force coefficient	Lift force coefficient	Moment coefficient	Fluctuating lift force coefficients	
Closed girder	Closed girder	0°	6	1.060	0.336	0.145	0.034	
			10	1.129	0.401	0.154	0.036	
		+3°	6	1.00	0.406	0.156	0.007	
			10	0.989	0.436	0.159	0.008	
		Open girder	0°	6	1.160	0.362	0.156	0.038
				10	1.135	0.395	0.154	0.041
	+3°		6	1.019	0.408	0.159	0.009	
		10	0.996	0.438	0.160	0.008		
	Open girder	Closed girder	0°	6	1.056	0.224	0.130	0.008
10				1.063	0.258	0.131	0.009	
+3°			6	0.846	0.220	0.126	0.009	
			10	0.914	0.274	0.134	0.011	
Open girder			0°	6	1.075	0.226	0.132	0.009
				10	1.067	0.254	0.131	0.009
		+3°	6	0.912	0.232	0.136	0.015	
10			0.920	0.257	0.134	0.023		

Table B 2 Upstream girder Strouhal number (downstream girder fixed)

Upstream girder	Downstream girder	Attack angle	Wind velocity [m/s]	Strouhal number	1/St	
Closed girder	Closed girder	0°	6	0.129	7.772	
			10	0.132	7.601	
		+3°	6	0.148	6.753	
			10	0.139	7.192	
		Open girder	0°	6	0.13	7.712
				10	0.135	7.399
	+3°		6	0.148	6.752	
		10	0.137	7.289		
	Open girder	Closed girder	0°	6	0.142	7.032
				10	0.148	6.77
			+3°	6	0.144	6.95
				10	0.141	7.108
Open girder			0°	6	0.147	6.796
				10	0.148	6.765
		+3°	6	0.146	6.837	

Aerodynamic force coefficients of the downstream girder

Table B 3 Downstream girder aerodynamic force coefficients (upstream girder fixed)

Upstream girder	Downstream girder	Attack angle	Wind velocity [m/s]	Drag force coefficient	Lift force coefficient	Moment coefficient	Fluctuating lift force coefficients
Closed girder	Closed girder	0°	6	0.476	-0.162	-0.010	0.355
			10	0.475	-0.185	-0.013	0.406
		+3°	6	0.263	0.127	0.019	0.083
			10	0.258	0.106	0.016	0.094
	Open girder	0°	6	0.447	-0.184	-0.013	0.295
			10	0.448	-0.195	-0.014	0.402
		+3°	6	0.212	0.091	0.018	0.067
			10	0.220	0.073	0.015	0.082
Open girder	Closed girder	0°	6	0.359	-0.136	-0.011	0.233
			10	0.354	-0.180	-0.015	0.186
		+3°	6	0.411	0.187	0.031	0.115
			10	0.388	0.177	0.029	0.107
	Open girder	0°	6	0.337	-0.154	-0.013	0.252
			10	0.355	-0.186	-0.018	0.167
		+3°	6	0.418	0.183	0.032	0.187
			10	0.402	0.169	0.031	0.267

Table B 4 Downstream girder lift force fluctuating frequency (upstream girder fixed)

Upstream girder	Downstream girder	Attack angle	Wind velocity [m/s]	Strouhal number	1/St
Closed girder	Closed girder	0°	6	0.131	7.645
			10	0.126	7.938
		+3°	6	0.148	6.772
			10	0.136	7.361
	Open girder	0°	6	0.129	7.758
			10	0.135	7.422
		+3°	6	0.14	7.145
			10	0.139	7.204
Open girder	Closed girder	0°	6	0.146	6.833
			10	0.145	6.904
		+3°	6	0.146	6.872
			10	0.141	7.078
	Open girder	0°	6	0.148	6.778
			10	0.142	7.064
		+3°	6	0.145	6.914
			10	0.139	7.175

Aerodynamic response of the upstream girder at $\alpha = 0^\circ$.

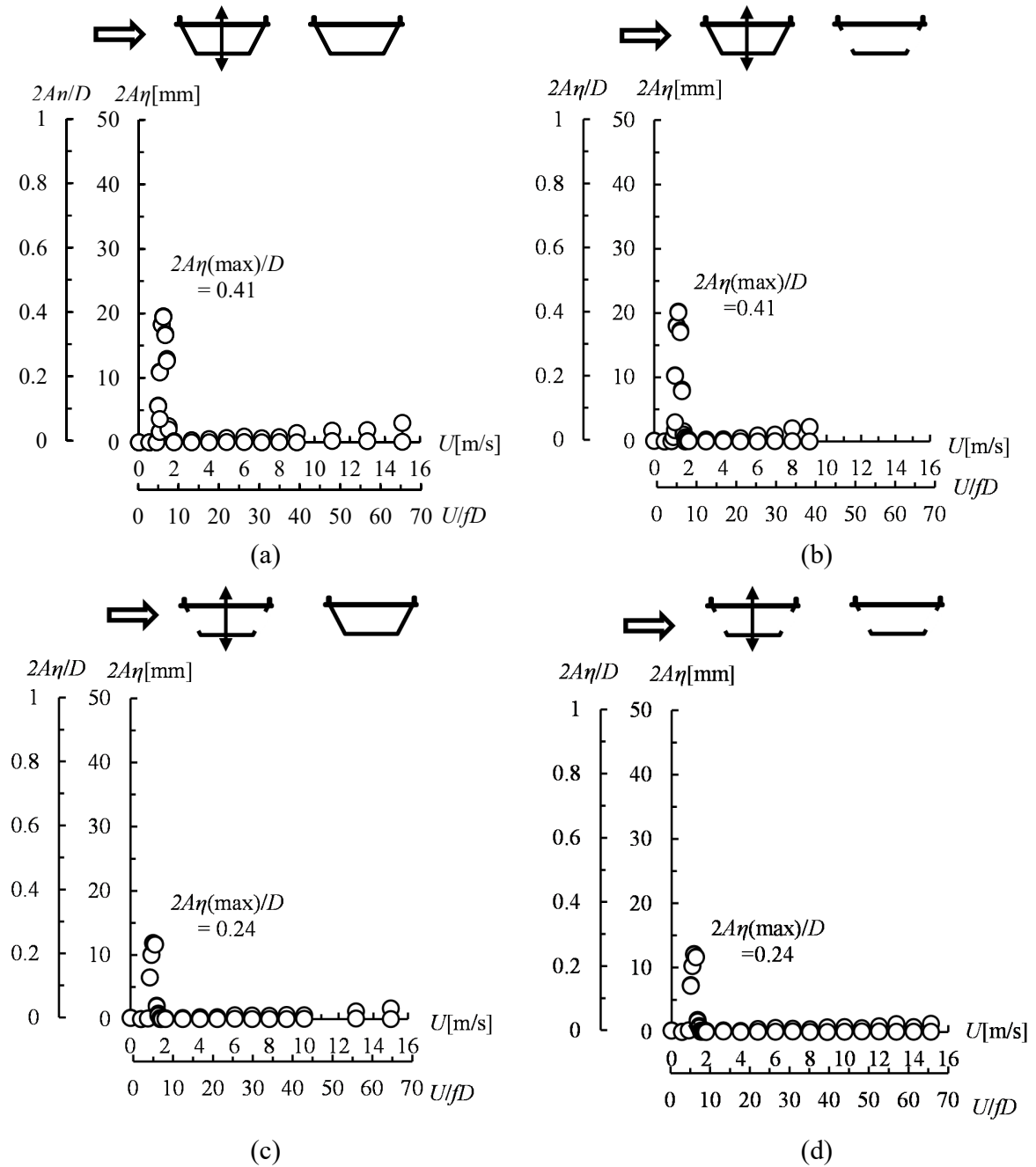


Fig. B 1 Aerodynamic response for (vertical 1DOF, $\alpha = 0^\circ$, smooth flow): (a) upstream closed girder with a fixed downstream closed girder; (b) upstream closed girder with a fixed downstream open girder; (c) upstream open girder with a fixed downstream closed girder; (d) upstream open girder with a fixed downstream open girder.

Aerodynamic response of the downstream girder at $\alpha = 0^\circ$.

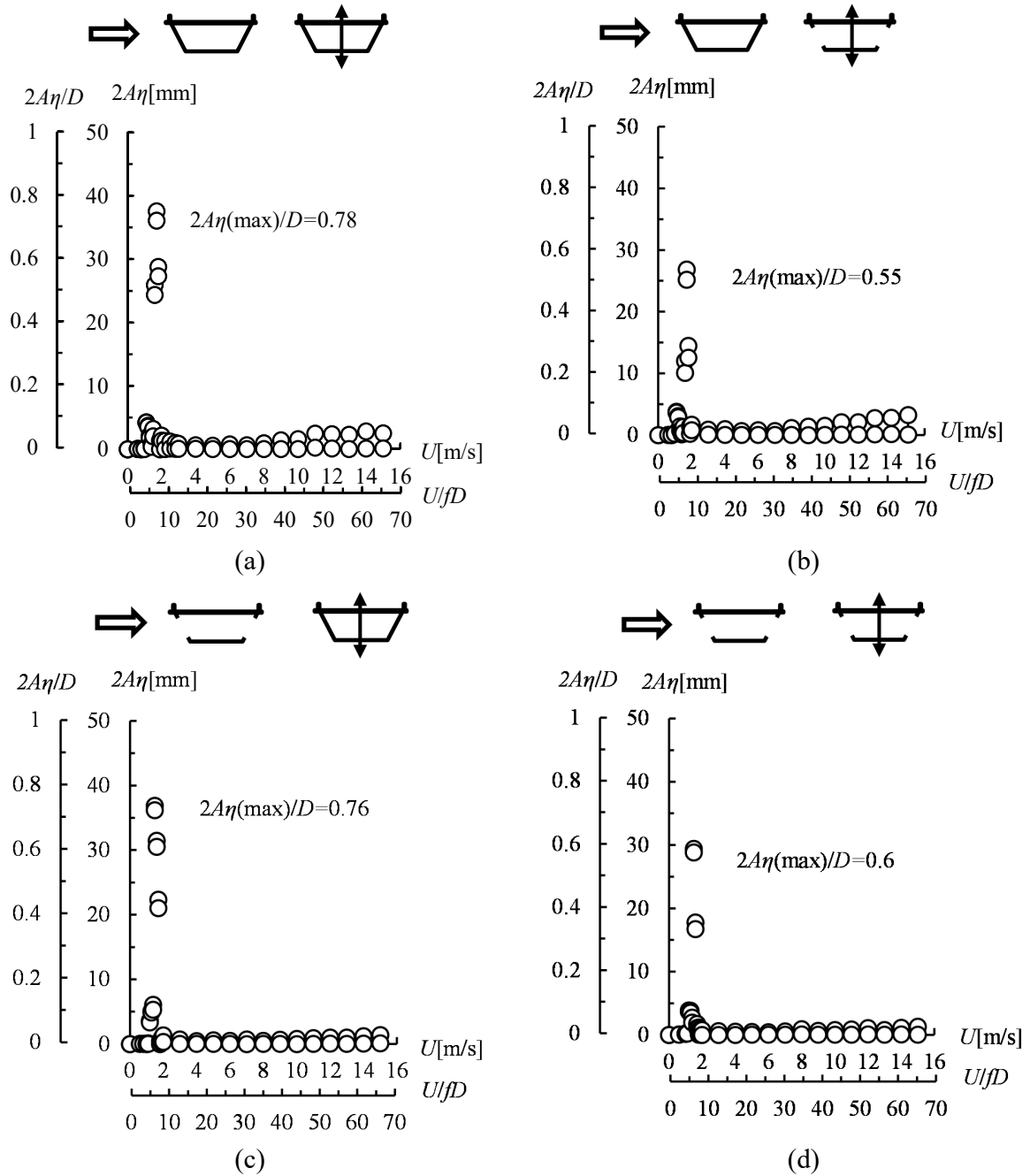


Fig. B 2 Aerodynamic response for (vertical 1DOF, $\alpha = 0^\circ$, smooth flow): (a) downstream closed girder with a fixed upstream closed girder; (b) downstream closed girder with a fixed upstream open girder; (c) downstream open girder with a fixed upstream closed girder; (d) downstream open girder with a fixed upstream open girder.

Role of the side-surface openings of the downstream girder on the flutter derivatives of the upstream closed girder ($\alpha = 0^\circ$)

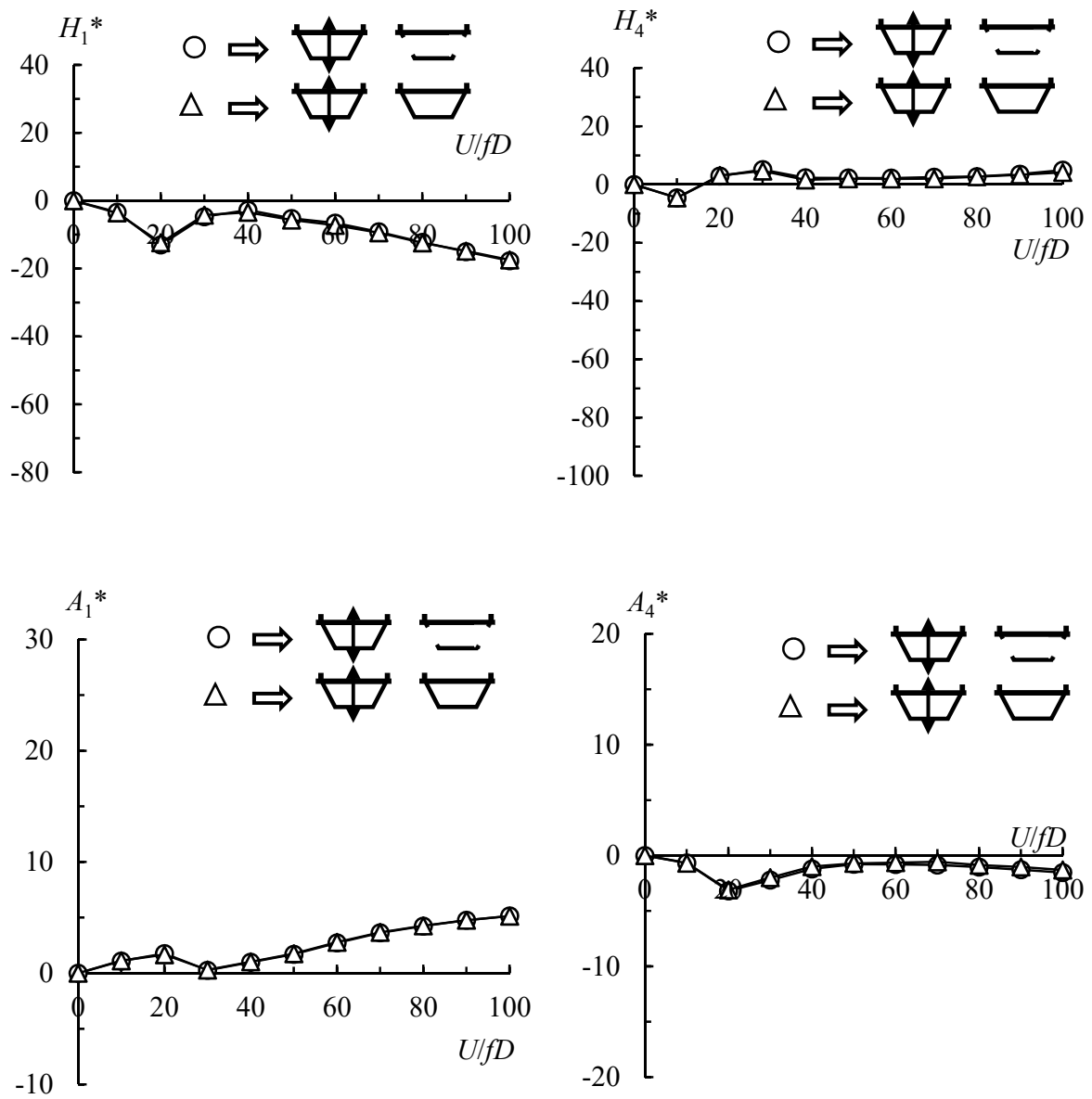


Fig. B 3 Flutter derivatives of the upstream closed girder ($B/D = 3.24$, vertical 1DOF, $\alpha = 0^\circ$, $f = 2.0$ Hz, $2A\eta = 20$ mm, smooth flow)

Role of the side-surface openings of the downstream girder on the flutter derivatives of the upstream open girder ($\alpha = 0^\circ$)

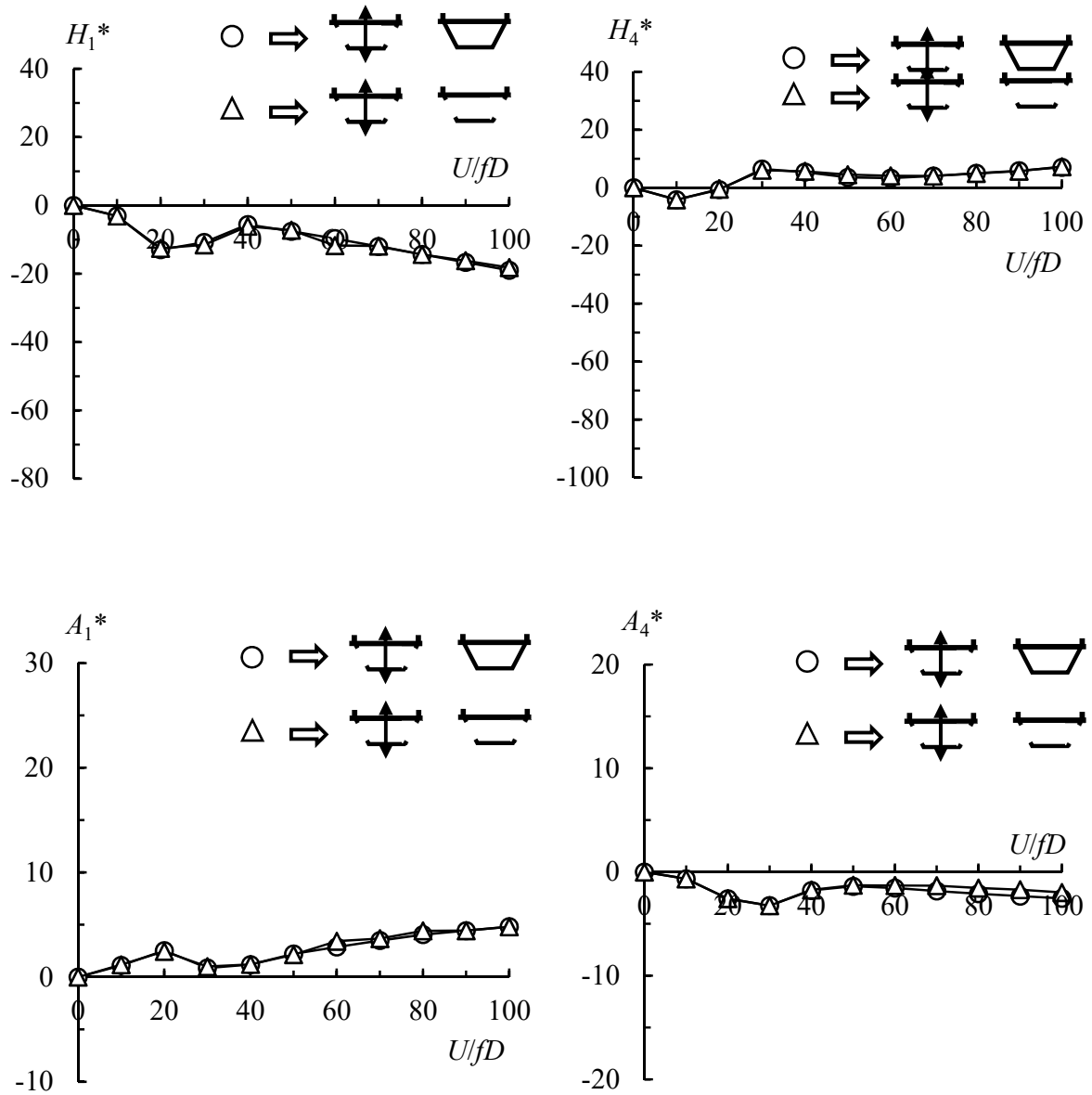


Fig. B 4 Flutter derivatives of the upstream open girder ($B/D = 3.24$, vertical 1DOF, $\alpha = 0^\circ$, $f = 2.0$ Hz, $2A\eta = 20$ mm, smooth flow)

Role of the side-surface openings of the upstream girder on the flutter derivatives of the upstream girder with a fixed downstream closed girder ($\alpha = 0^\circ$)

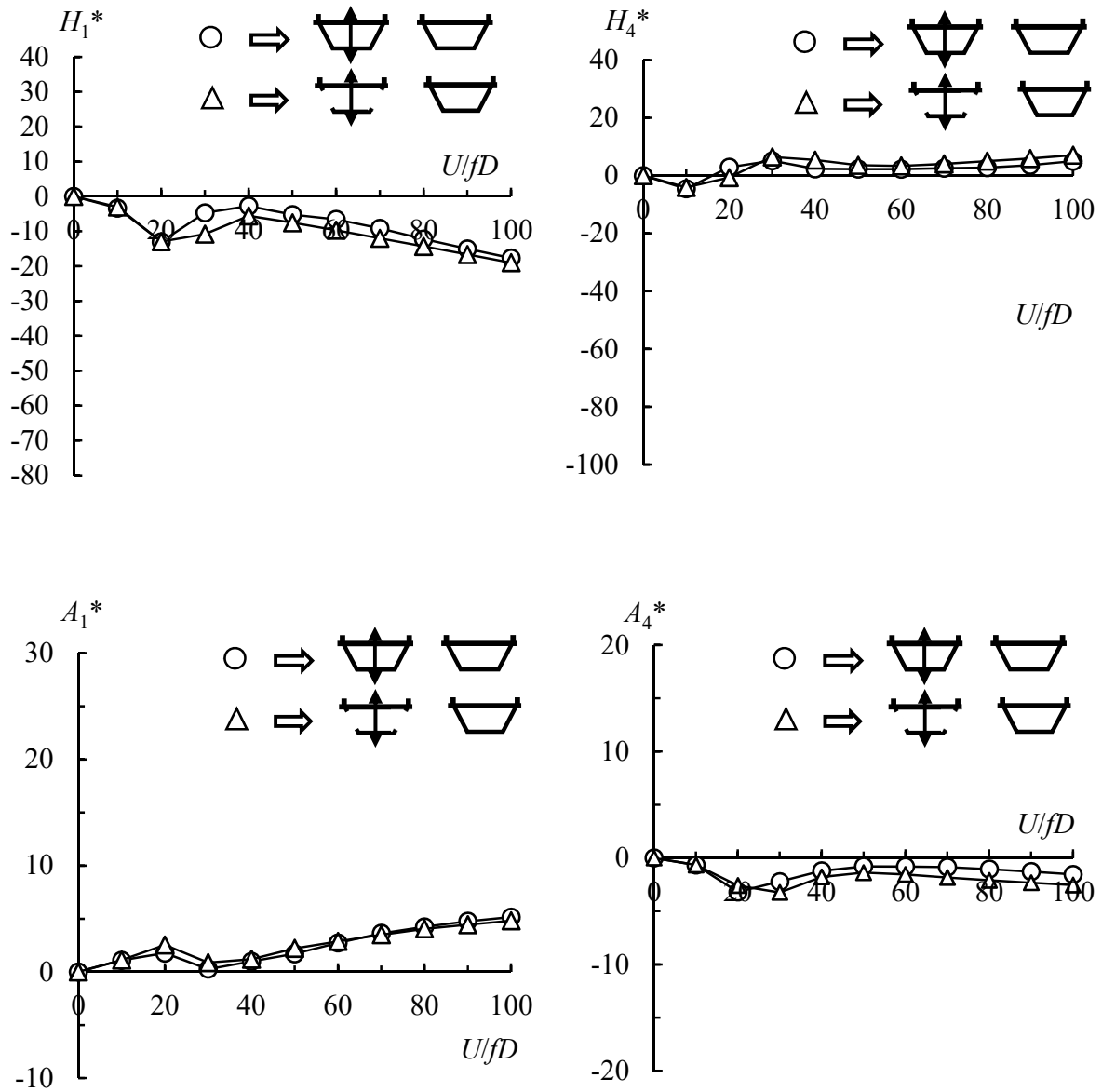


Fig. B 5 Flutter derivatives of the upstream closed girder and open girder with the fixed downstream closed girder ($B/D = 3.24$, vertical 1DOF, $\alpha = 0^\circ$, $f = 2.0$ Hz, $2A\eta = 20$ mm, smooth flow)

Role of the side-surface openings of the upstream girder on the flutter derivatives of the upstream girder with a fixed downstream open girder ($\alpha = 0^\circ$)

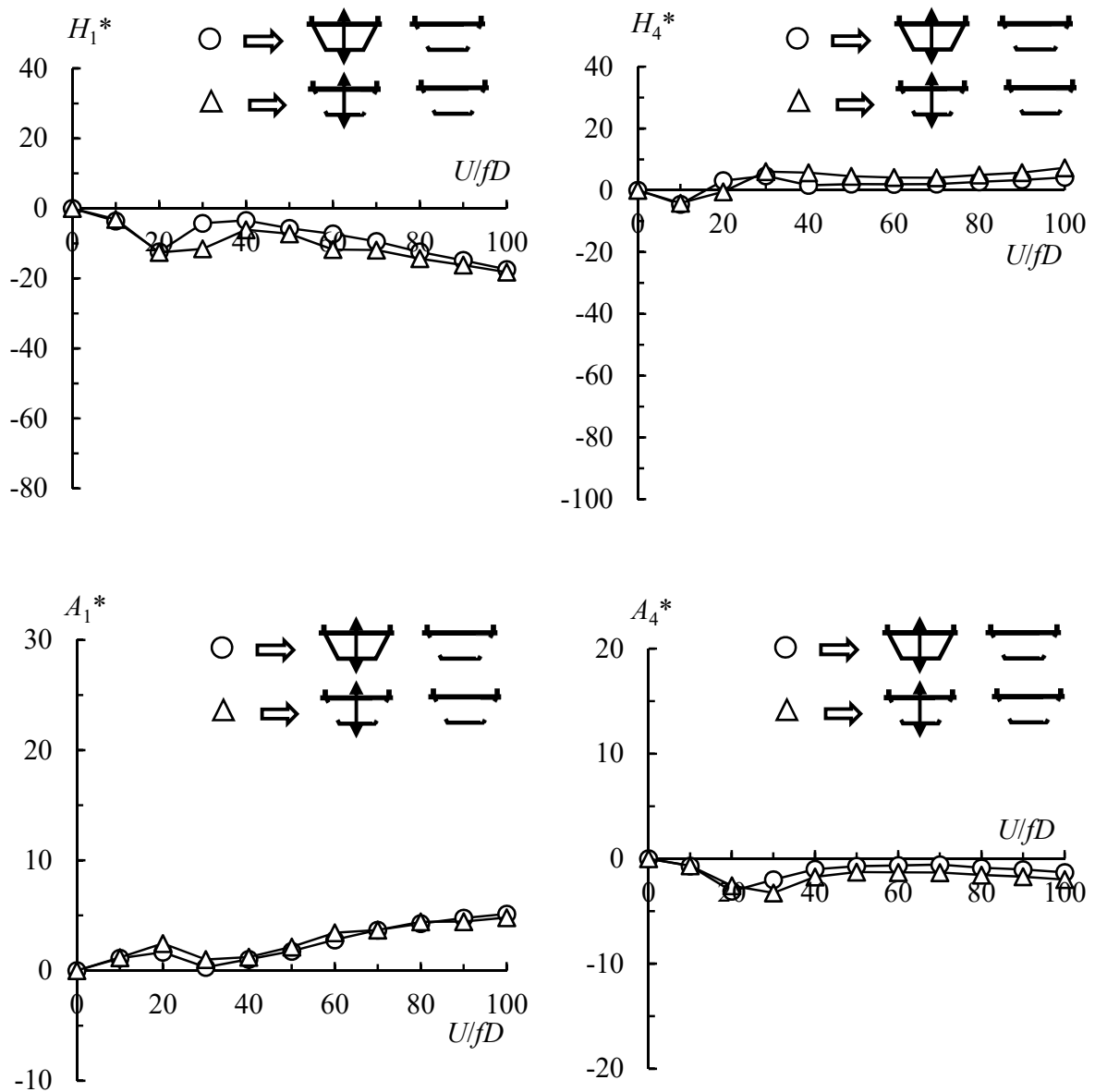


Fig. B 6 Flutter derivatives of the upstream closed girder and open girder with the fixed downstream open girder ($B/D = 3.24$, vertical 1DOF, $\alpha = 0^\circ$, $f = 2.0$ Hz, $2A\eta = 20$ mm, smooth flow)

Role of the side-surface openings of the downstream girder on the flutter derivatives of the upstream closed girder ($\alpha = +3^\circ$)

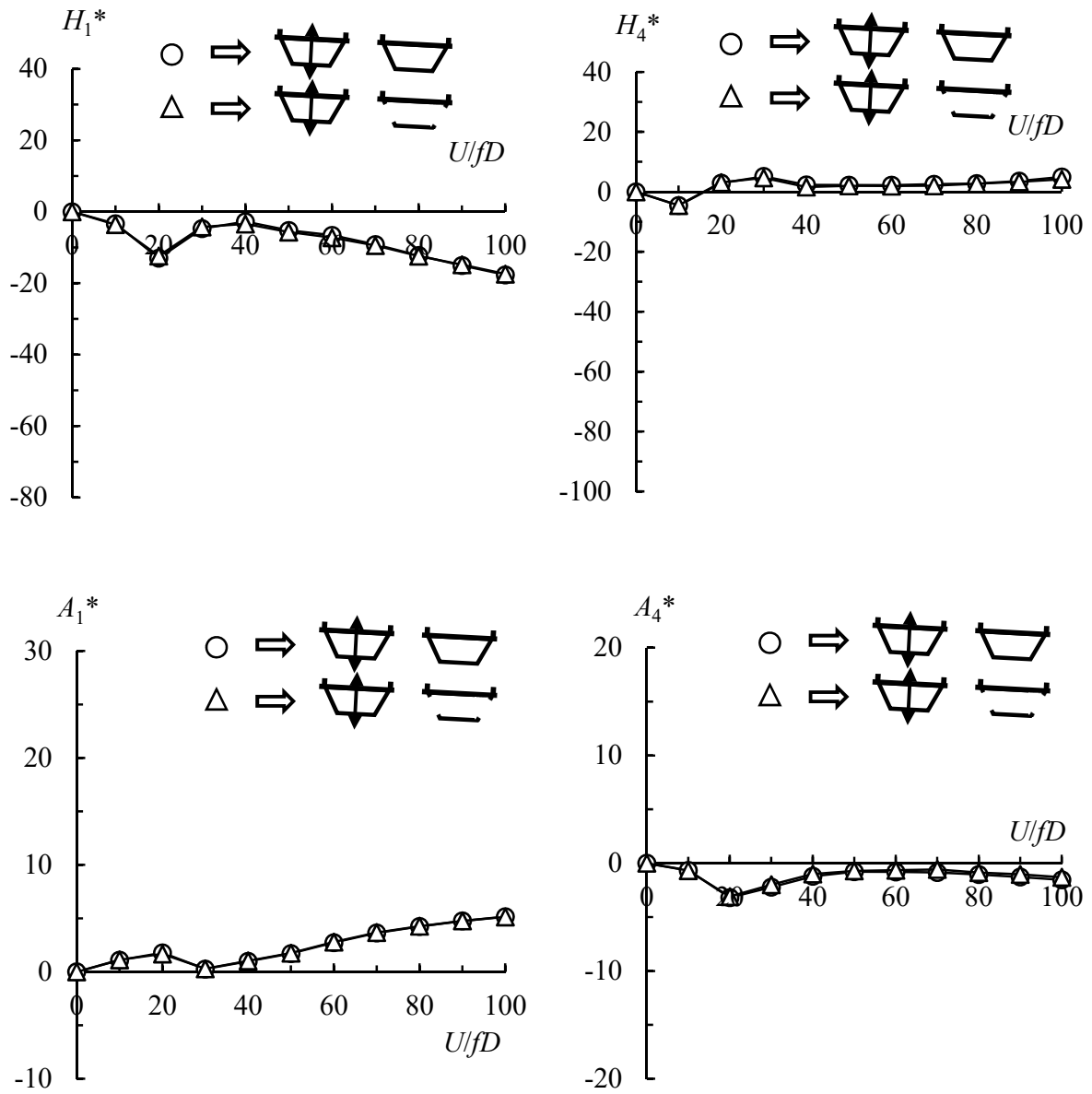


Fig. B 7 Flutter derivatives of the upstream closed girder ($B/D = 3.24$, vertical 1DOF, $\alpha = +3^\circ$, $f = 2.0$ Hz, $2A\eta = 20$ mm, smooth flow)

Role of the side-surface openings of the downstream girder on the flutter derivatives of the upstream open girder ($\alpha = +3^\circ$)

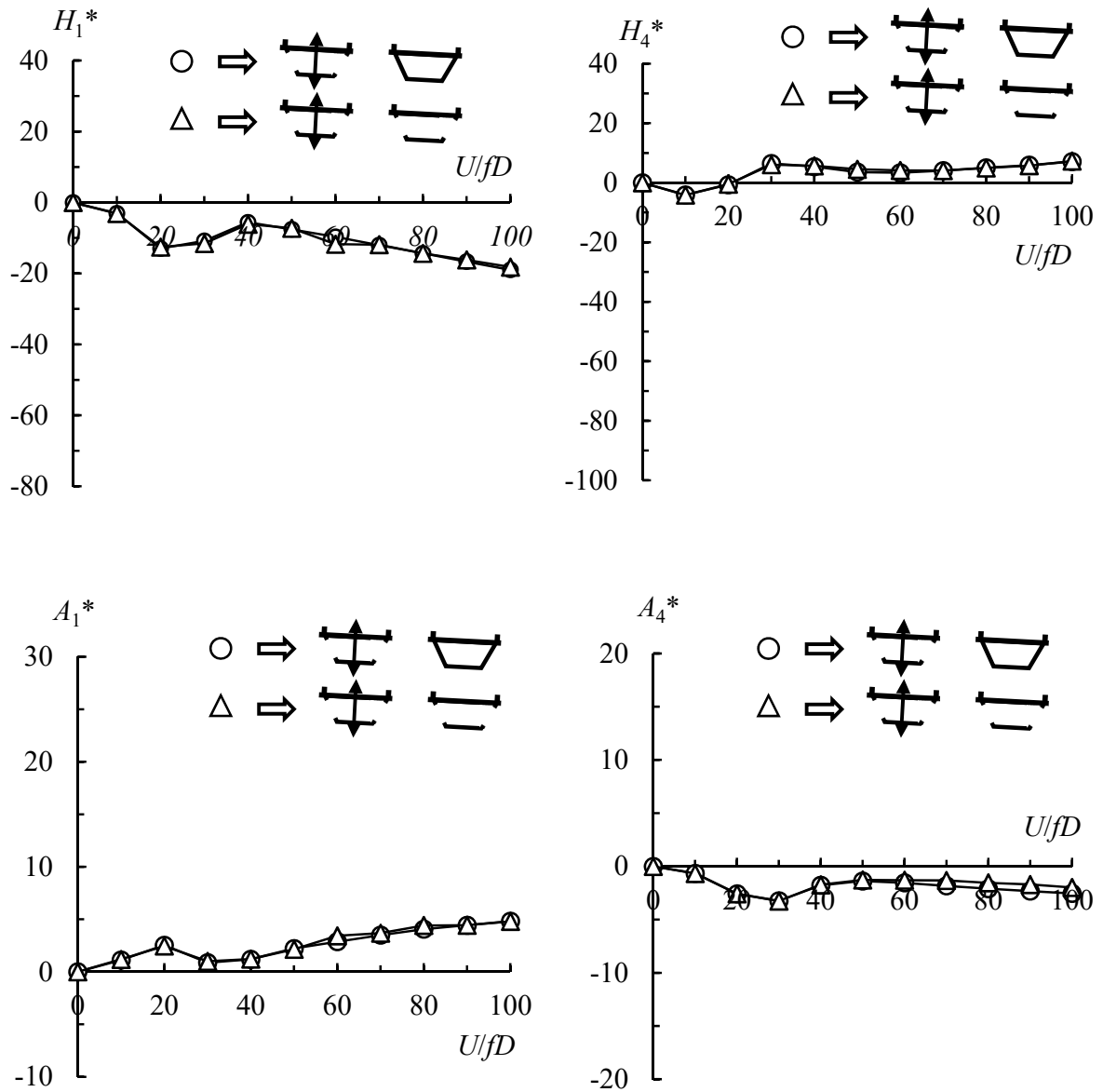


Fig. B 8 Flutter derivatives of the upstream open girder ($B/D = 3.24$, vertical 1DOF, $\alpha = +3^\circ$, $f = 2.0$ Hz, $2A\eta = 20$ mm, smooth flow)

Role of the side-surface openings on the flutter derivatives of the upstream girder with a fixed downstream closed girder ($\alpha = +3^\circ$)

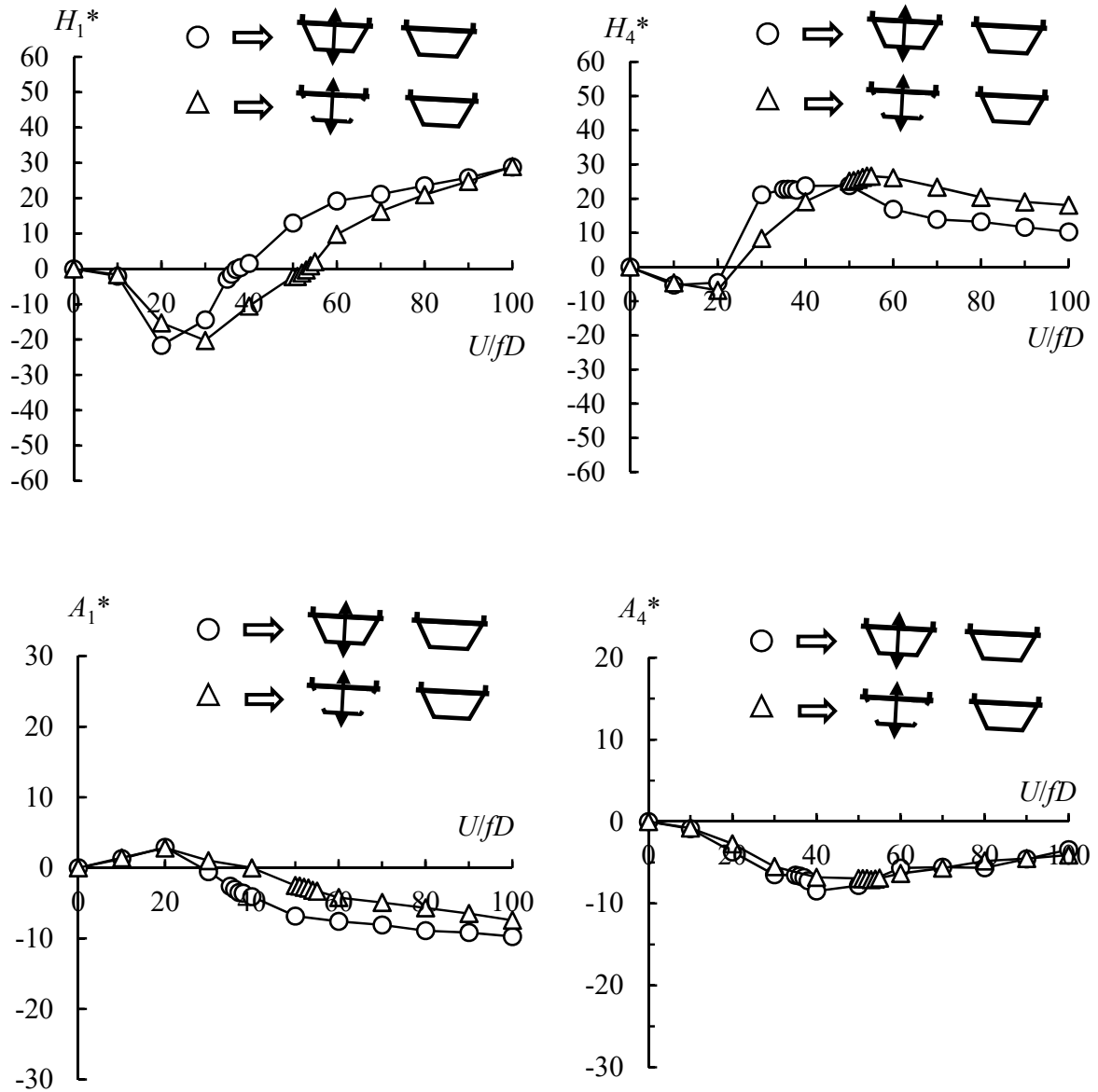


Fig. B 9 Flutter derivatives of the upstream closed girder and open girder with the fixed downstream closed girder ($B/D = 3.24$, vertical 1DOF, $\alpha = +3^\circ$, $f = 2.0$ Hz, $2A\eta = 20$ mm, smooth flow)

Role of the side-surface openings on the flutter derivatives of the upstream girder with a fixed downstream open girder ($\alpha = +3^\circ$)

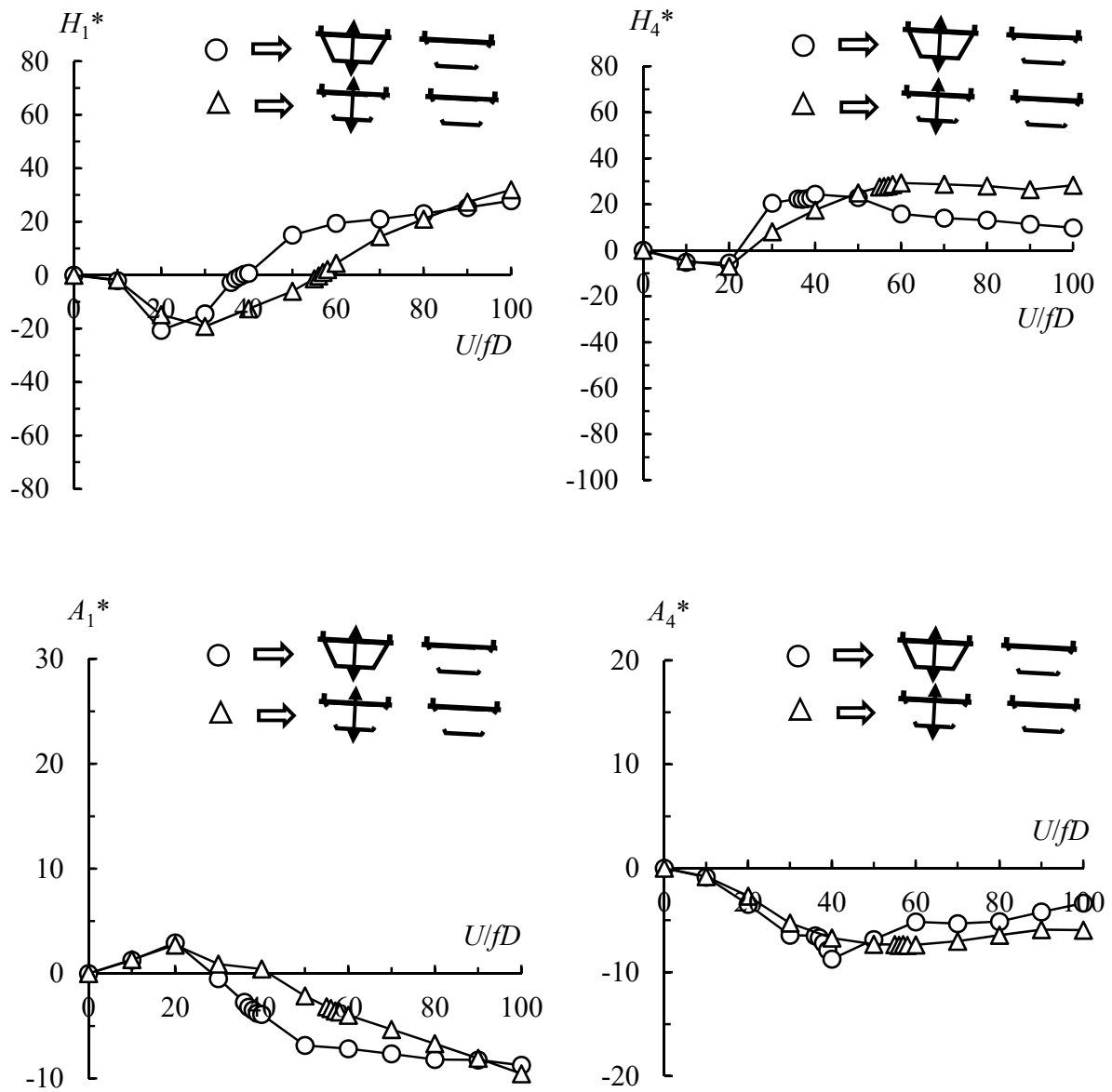


Fig. B 10 Flutter derivatives of the upstream closed girder and open girder with the fixed downstream open girder ($B/D = 3.24$, vertical 1DOF, $\alpha = +3^\circ$, $f = 2.0$ Hz, $2A\eta = 20$ mm, smooth flow)

Role of the side-surface openings of the upstream girder on the flutter derivatives of the downstream closed girder ($\alpha = 0^\circ$)

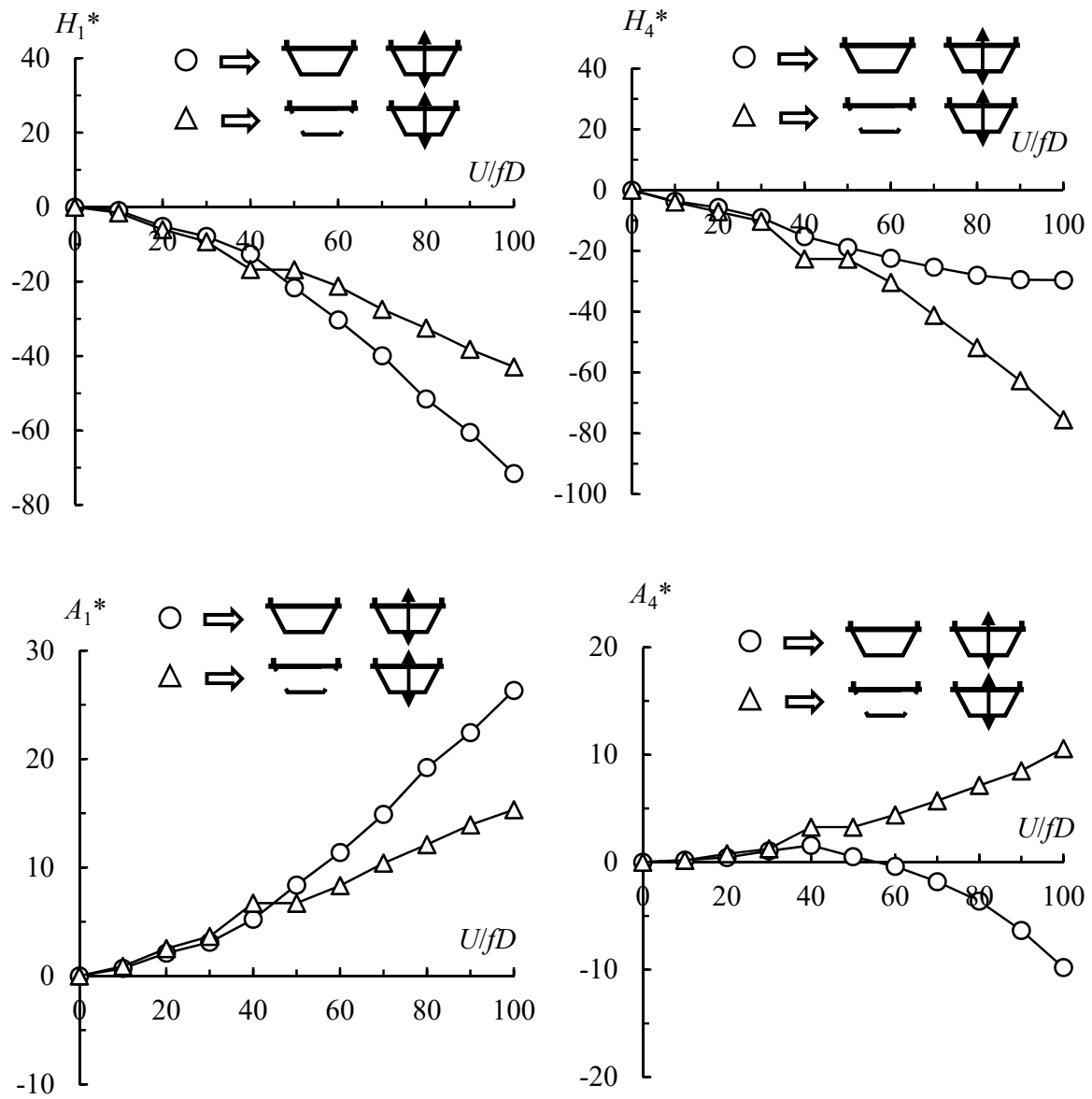


Fig. B 11 Flutter derivatives of the downstream closed girder ($B/D = 3.24$, vertical 1DOF, $\alpha = 0^\circ$, $f = 2.0\text{Hz}$, $2A\eta = 20\text{mm}$, smooth flow)

Role of the side-surface openings of the upstream girder on the flutter derivatives of the downstream open girder ($\alpha = 0^\circ$)

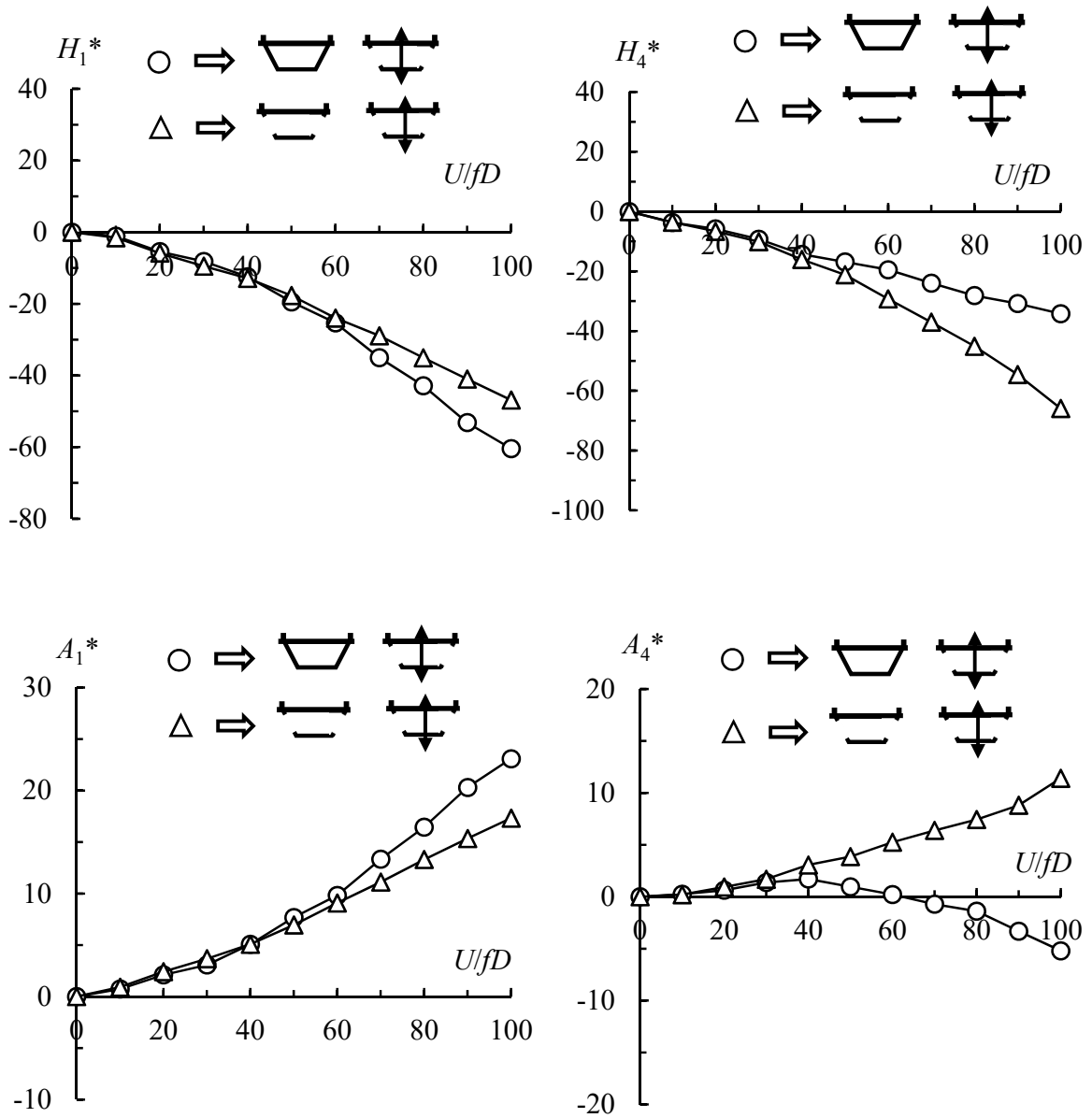


Fig. B 12 Flutter derivatives of the downstream open girder ($B/D = 3.24$, vertical 1DOF, $\alpha = 0^\circ$, $f = 2.0\text{Hz}$, $2A\eta = 20\text{mm}$, smooth flow)

Role of the side-surface openings of the downstream girder on the flutter derivatives of the downstream girder with a fixed upstream closed girder ($\alpha = 0^\circ$)

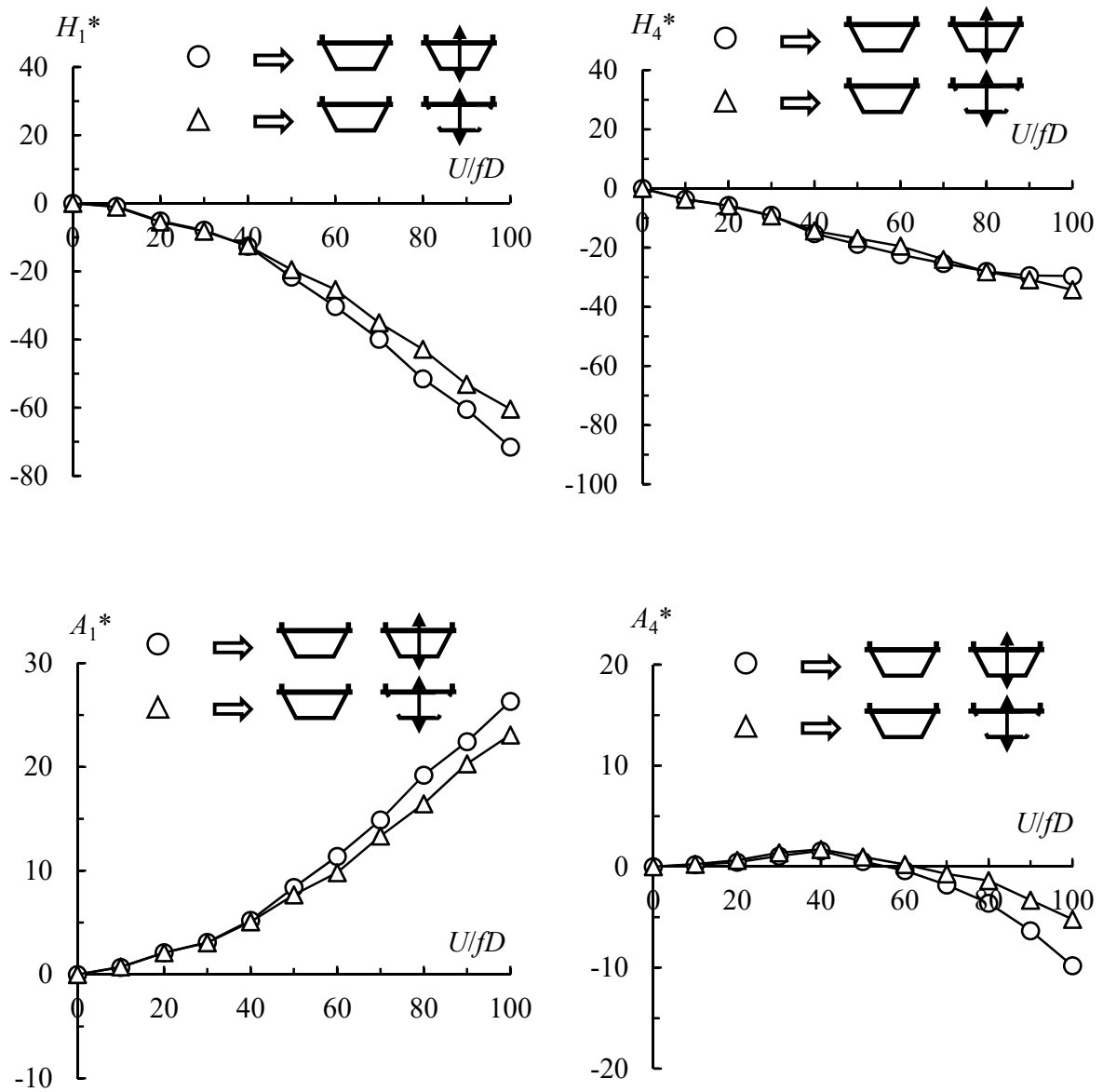


Fig. B 13 Flutter derivatives of the downstream closed girder and open girder with the fixed upstream closed girder ($B/D = 3.24$, vertical 1DOF, $\alpha = 0^\circ$, $f = 2.0$ Hz, $2A\eta = 20$ mm, smooth flow)

Role of the side-surface openings of the downstream girder on the flutter derivatives of the downstream girder with a fixed upstream open girder ($\alpha = 0^\circ$)

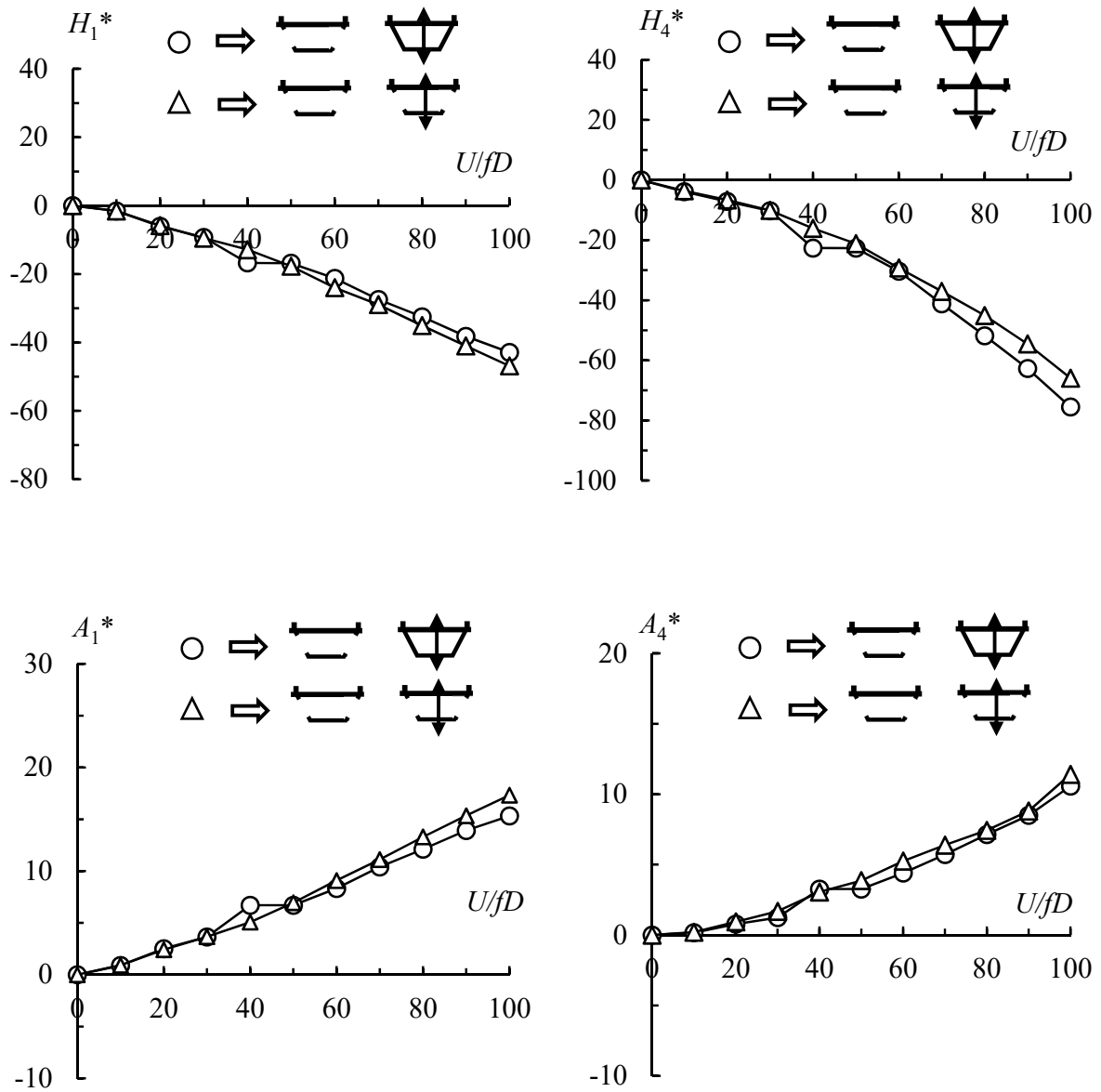


Fig. B 14 Flutter derivatives of the downstream closed girder and open girder with the fixed upstream open girder ($B/D = 3.24$, vertical 1DOF, $\alpha = 0^\circ$, $f = 2.0$ Hz, $2A\eta = 20$ mm, smooth flow)

Role of the side-surface openings of the upstream girder on the flutter derivatives of the downstream closed girder ($\alpha = +3^\circ$)

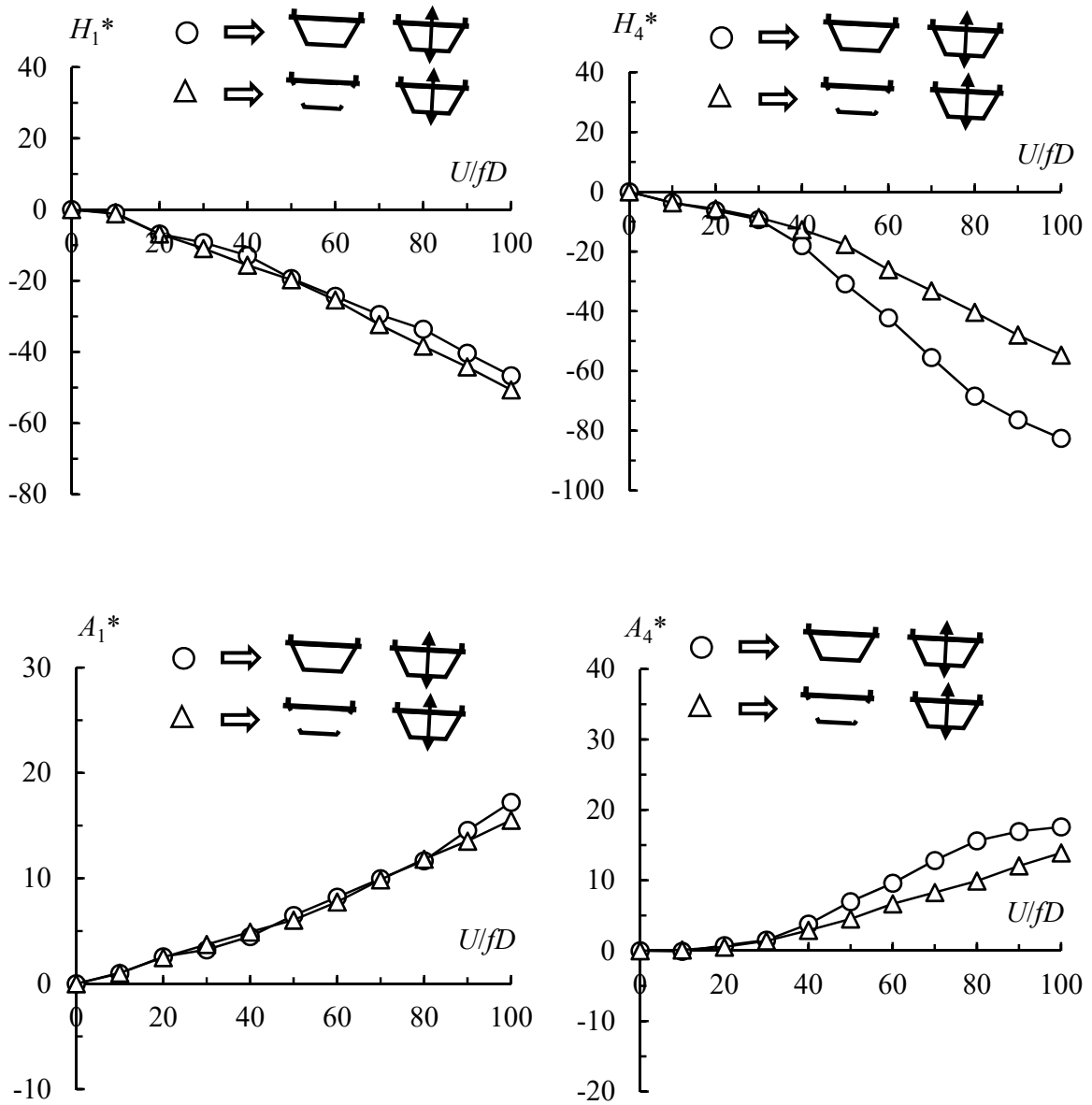


Fig. B 15 Flutter derivatives of the downstream closed girder ($B/D = 3.24$, vertical 1DOF, $\alpha = +3^\circ$, $f = 2.0\text{Hz}$, $2A\eta = 20\text{mm}$, smooth flow)

Role of the side-surface openings of the upstream girder on the flutter derivatives of the downstream open girder ($\alpha = +3^\circ$)

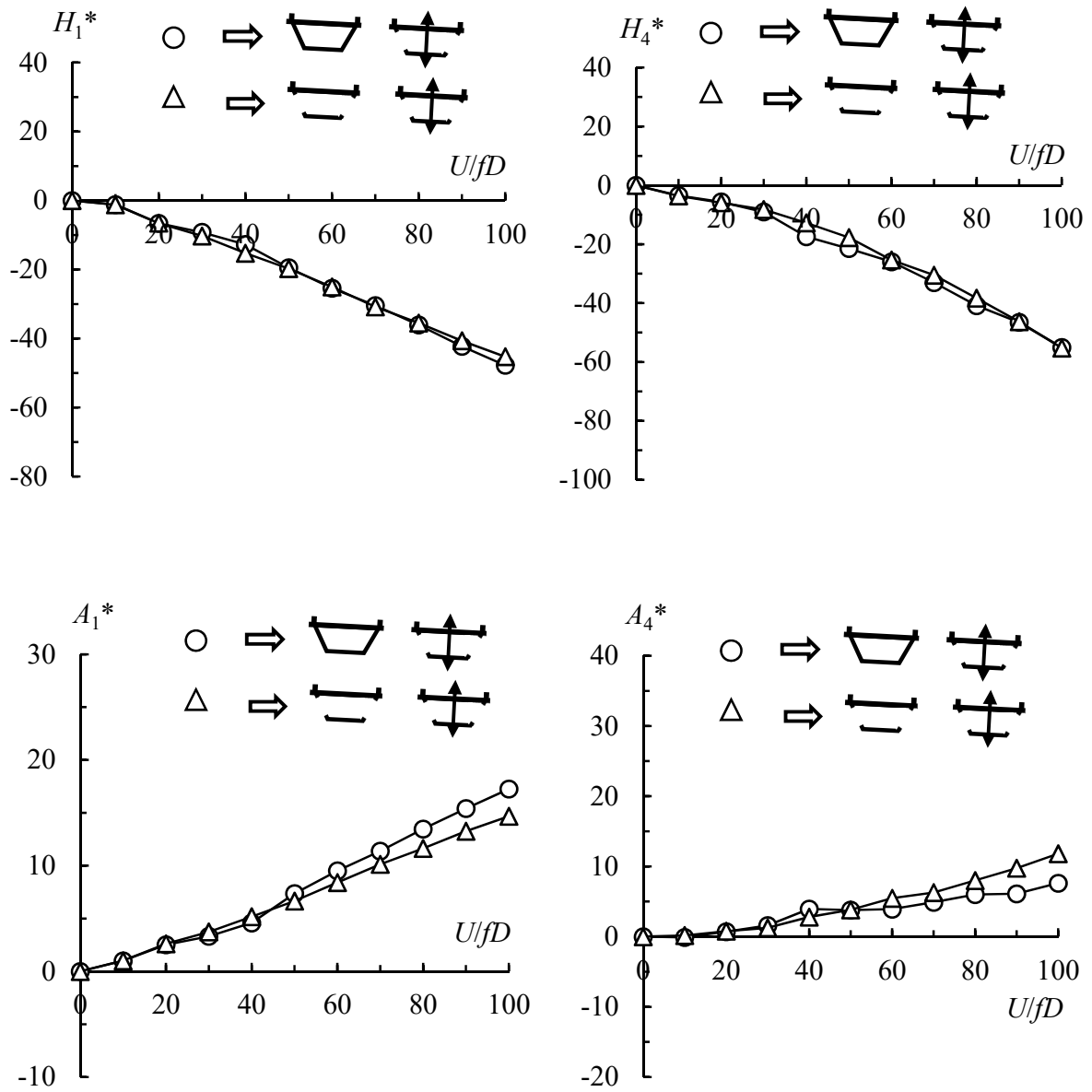


Fig. B 16 Flutter derivatives of the downstream open girder ($B/D = 3.24$, vertical 1DOF, $\alpha = +3^\circ$, $f = 2.0\text{Hz}$, $2A\eta = 20\text{mm}$, smooth flow)

Role of the side-surface openings of the downstream girder on the flutter derivatives of the downstream girder with a fixed upstream closed girder ($\alpha = +3^\circ$)

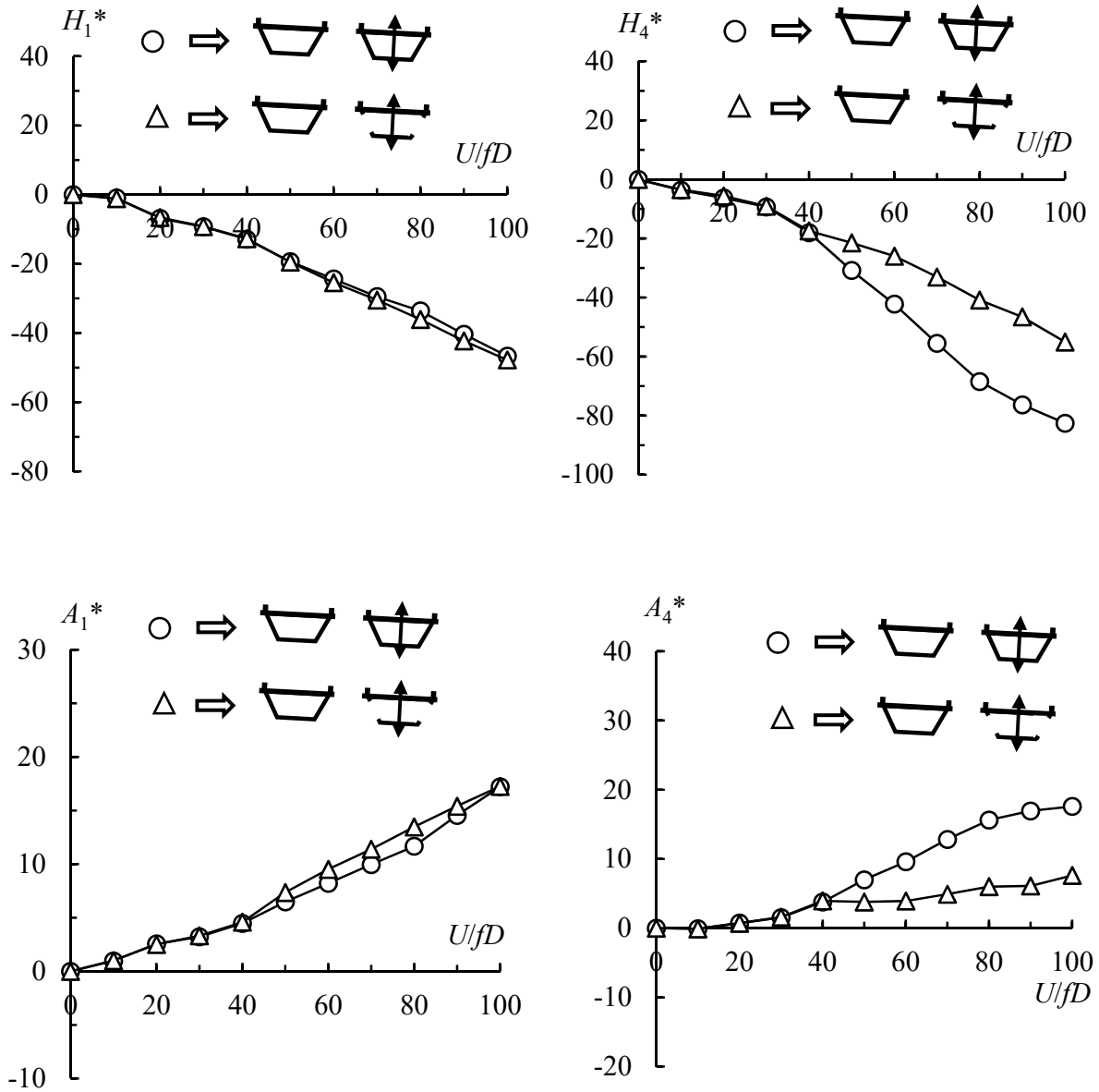


Fig. B 17 Flutter derivatives of the downstream closed girder and open girder with the fixed upstream closed girder ($B/D = 3.24$, vertical 1DOF, $\alpha = +3^\circ$, $f = 2.0$ Hz, $2A\eta = 20$ mm, smooth flow)

Role of the side-surface openings of the downstream girder on the flutter derivatives of the downstream girder with a fixed upstream open girder ($\alpha = +3^\circ$)

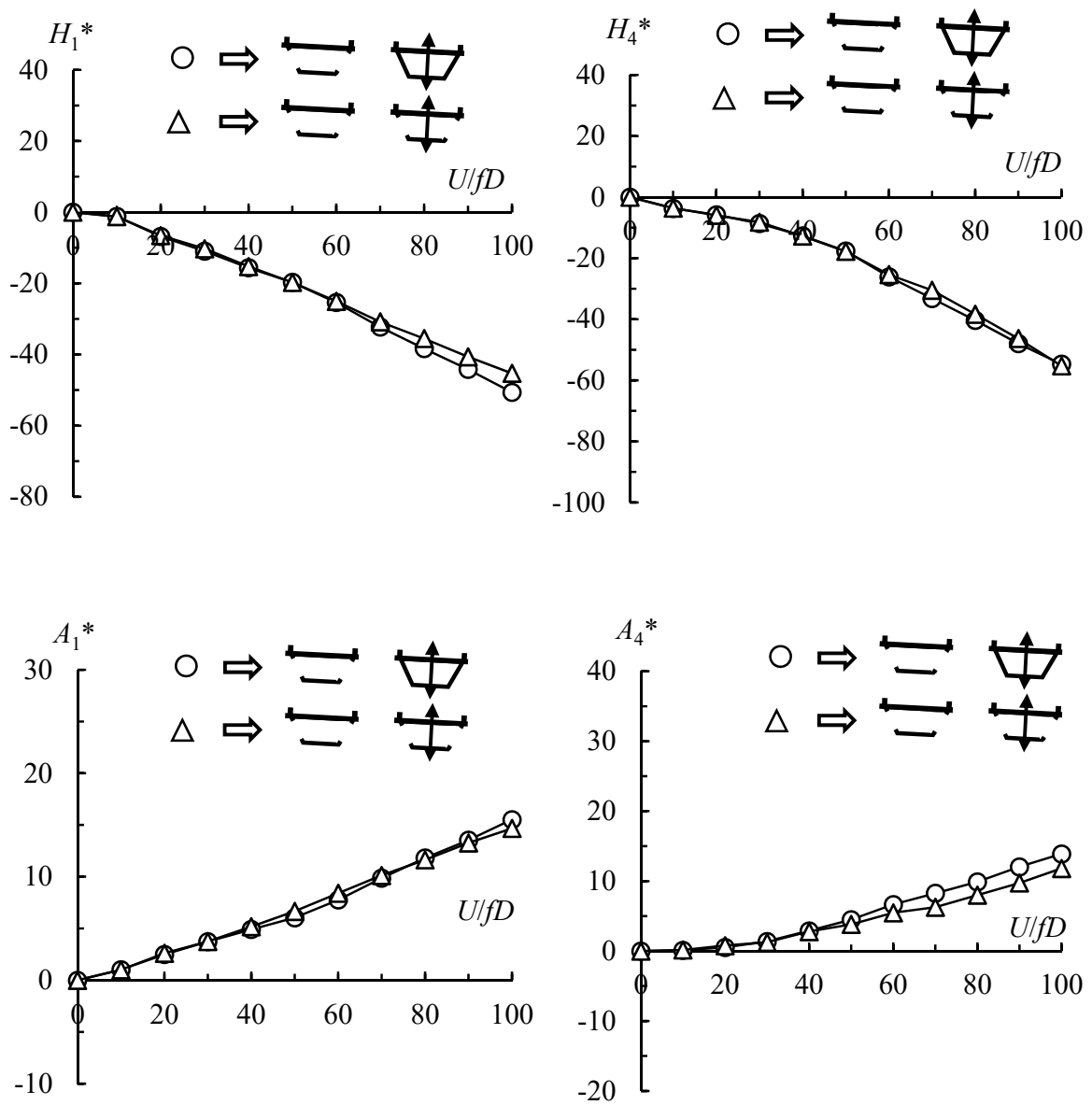


Fig. B 18 Flutter derivatives of the downstream closed girder and open girder with the fixed upstream open girder ($B/D = 3.24$, vertical 1DOF, $\alpha = +3^\circ$, $f = 2.0$ Hz, $2A\eta = 20$ mm, smooth flow)

Appendix C

Extensive results for the $B/D = 2$ rectangular cylinder

Unsteady lift force amplitude and phase lag

As shown in Eq. C 1, H_1^* is decided by the amplitude of unsteady lift force and the phase lag between the unsteady lift and the displacement. The phase lag was shown in Fig. A1. At high wind velocity, the phase lag gradually approached -90° . This is the reason why the quasi-steady theory is valid at the high wind velocity. If the phase lag gradually approached -90° at the high wind velocity, the H_1^* is actually the non-dimensional lift amplitude defined as Eq. C 2. Meanwhile, the H_1^* calculated based on the quasi-steady theory is the non-dimensional amplitude of the quasi-steady lift (Eq. C 3). At the high wind velocity the non-dimensional unsteady lift amplitude gradually approached the non-dimensional quasi-steady lift amplitude (Fig. C 2).

$$H_1^* = -\frac{L_\eta \sin \Psi_{L\eta}}{\rho b^2 \omega^2 \eta_0} \quad \text{Eq. C 1}$$

$$\overline{L_\eta} = -\frac{L_\eta}{\rho b^2 \omega^2 \eta_0} \quad \text{Eq. C 2}$$

$$\begin{aligned} \overline{L_{qs}} &= \frac{-\frac{1}{2} \rho U^2 B \frac{dC_{Fy}}{d\alpha} \dot{\eta}}{\rho b^2 \omega^2 \eta_0} = \frac{-\frac{1}{2} \rho U^2 B \frac{dC_{Fy}}{d\alpha} \eta_0 \omega |\cos(\omega t)|}{\rho b^2 \omega^2 \eta_0} = -\frac{U}{b\omega} \frac{dC_L}{d\alpha} \\ &= -\frac{1}{k} \frac{dC_L}{d\alpha} \end{aligned} \quad \text{Eq. C 3}$$

$$k = b\omega/U$$

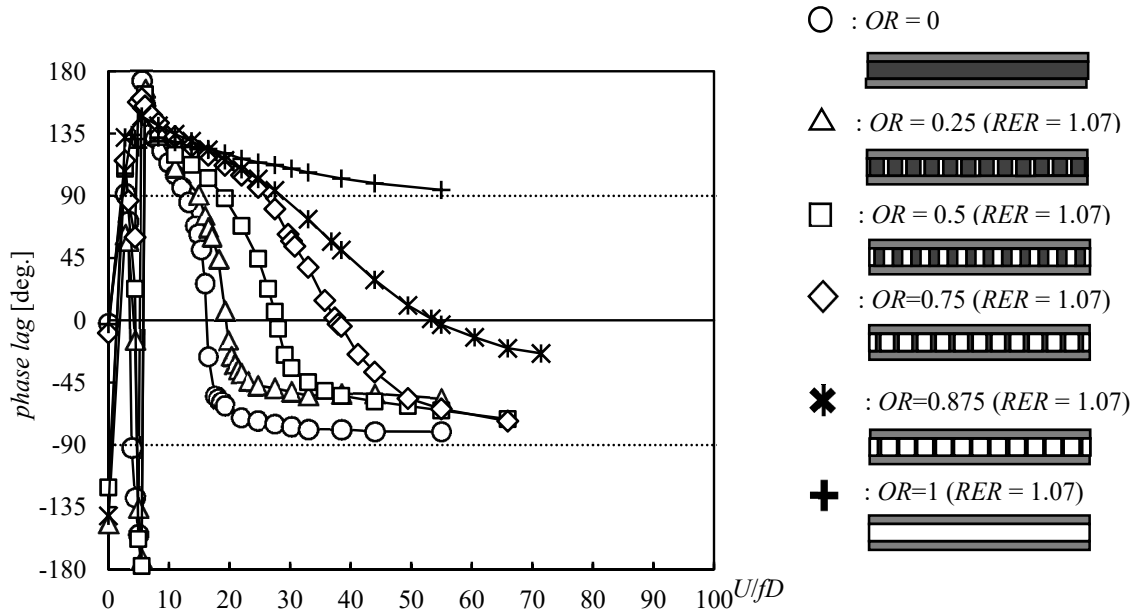


Fig. C 1 Phase lag of unsteady lift force relative to the displacement ($RER = 1.07$)

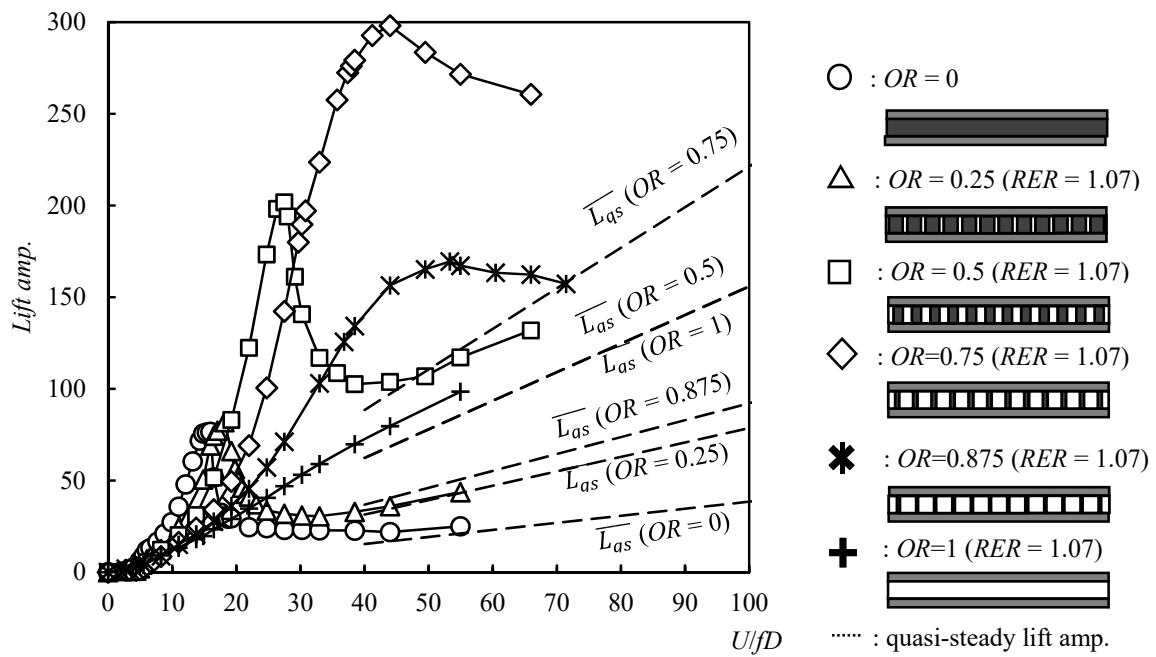


Fig. C 2 Amplitude of non-dimensional unsteady lift force ($RER = 1.07$)

The interaction between the outflow and flow entrainment in the wake

As shown in Fig. C3 (b) and (c), for $OR = 0.25$: The outflow from the downstream openings soon diffused into the near wake ($X < 180\text{mm}$). This kind of outflow from the downstream openings joined in the flow entrainment or the communication between the upside and downside shear layer in the near wake. The interaction between the outflow and the flow entrainment was dominated by the wake. According to Fig. C3 (d) and (e), for $OR = 0.5$: The outflow from the downstream openings was issued to a distance from the rear surface at $X < 210\text{mm}$, then broke up and dispersed into the wake. As shown in Fig. C3 (f)-(i), for $OR = 0.75$ and 0.875 : The outflow from the downstream openings penetrated with a high wind velocity and expanded a short distance ($X < 250\text{mm}$) into the wake with a relatively high wind velocity. As shown in Fig. C3 (j) $OR = 1$: The outflow from the openings penetrated into the wake with a high wind velocity into a long distance without any obvious expansion. The wake contributed strongly to the wake flow.

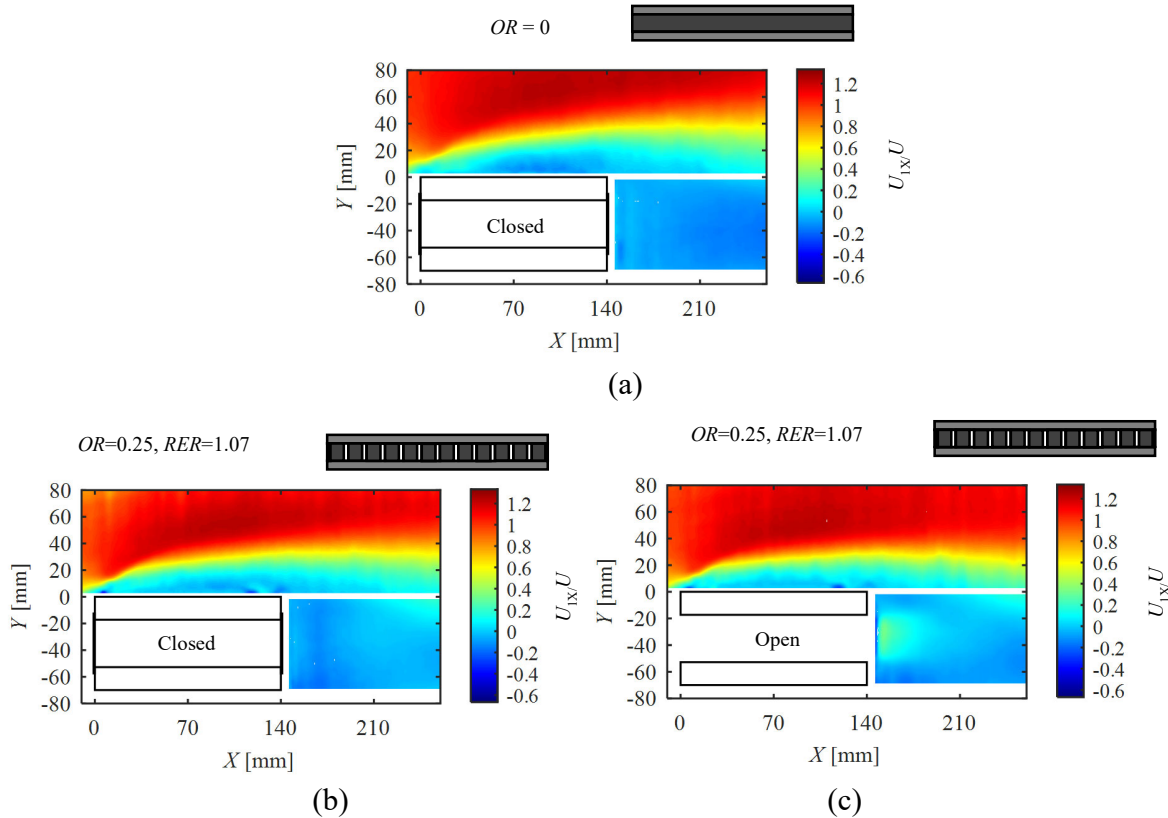


Fig. C 3 Contour map of the non-dimensional wind velocity (U_{1X}/U) of: (a) section of Case 1 ($OR = 0$); (b) closed section of Case 2 ($OR = 0.25$, $RER = 1.07$); (c) open section of Case 2; (d) closed section of Case 3 ($OR = 0.50$, $RER = 1.07$); (e) open section of Case 3; (f) closed section of Case 4 ($OR = 0.75$, $RER = 1.07$); (g) open section of Case 4; (h) closed section of Case 5 ($OR = 0.875$, $RER = 1.07$); (i) open section of Case 5; (j) section of Case 10 ($OR = 1$) ($U = 1.5\text{m/s}$, smooth flow).

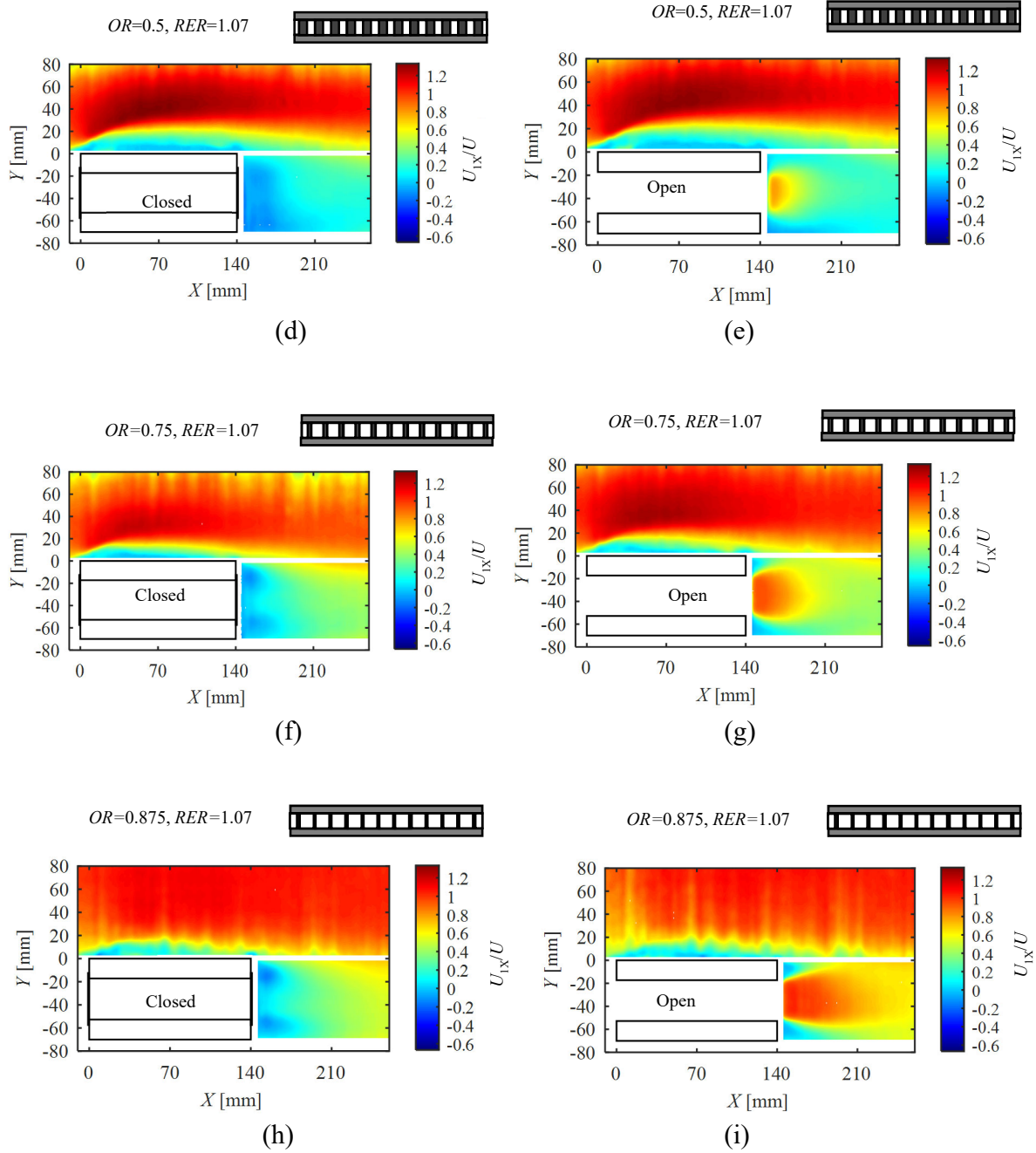
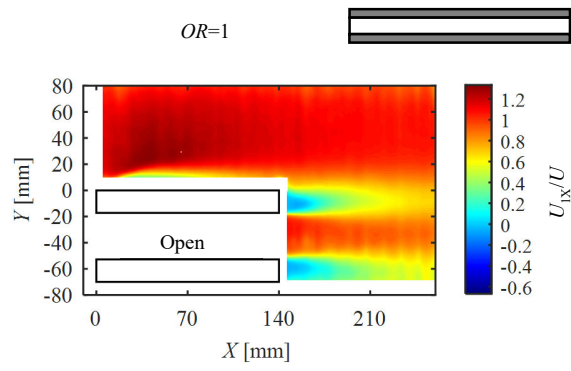


Fig. C 3 Continued



(j)

Fig. C 3 Continued

Role of outflow from side opening into wake on the aerodynamic performance

The flow rate through the inner space of the model into the wake and the interaction between the outflows from side openings with the flow entrainment in the wake both contributed to the flow field around the model. The role of the outflow on the aerodynamic performance was discussed. In order to investigate the effects of outflow into the wake on the aerodynamic performance on the model, the partition (Fig. C4) was introduced to limit the diffusion of the flow in span direction in the inner space and increase the wind velocity of the outflow.

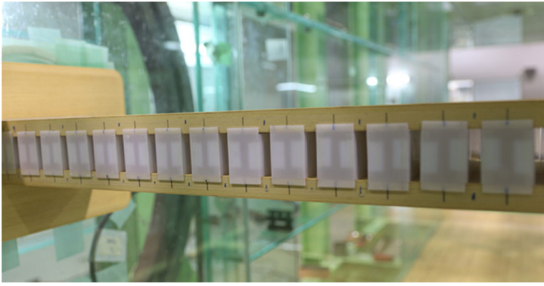
As shown in Fig. C5 (a) and (b), based on the results of Case 2 ($OR = 0.25$) and Case 4 ($OR = 0.75$), the wind velocity was almost the same at $-70 \text{ mm} < X < 0 \text{ mm}$ for the model with and without partitions, indicating that the flow amount/rate got into the model barely changed by introducing the partitions. However, as shown in Fig. C5 (a), at $0 \text{ mm} < X < 140 \text{ mm}$, the wind velocity of the flow between the partitions in the inner space of the model was obviously larger than that of the flow in the inner space of the model without partition. This indicates that by limiting the flow diffusion, the flow got through the inner space with a wind velocity of U (the approaching wind velocity) directly into the wake. At $140 \text{ mm} < X < 210 \text{ mm}$, the wind velocity of outflow from the model with partitions into the wake was slightly larger than that of the model without partitions. However, at $140 \text{ mm} < X < 210 \text{ mm}$, even though the wind velocity in the wake of the model with partition was slightly larger than that of the model without partition, because that the size of side openings was small, the wind velocity of both the models with and without partitions soon decreased due to the diffusion. According to Fig. C5 (b), for $OR = 0.75$, the wind velocity of the inner flow ($0 \text{ mm} < X < 140 \text{ mm}$) was slightly larger than that of the case without partitions. At $140 \text{ mm} < X < 210 \text{ mm}$, the wind velocity of outflow from the side openings of the model without partitions decrease gradually, while the wind velocity of the outflow from the side openings of the model with partitions keeps almost the same along X direction at $140 \text{ mm} < X < 210 \text{ mm}$. Therefore, by limiting the flow diffusion in the inner space of the model for $OR = 0.75$, the flow got through the inner space with a wind velocity of U (approaching wind velocity) directly into the wake. Meanwhile, owing to the limitation of the flow diffusion in the inner space by the partitions, the wind velocity of the outflow into the wake increased and subsequently the interaction between the outflow and the flow entrainment in the wake should be stronger due to the partitions. In summary, by limiting the flow diffusion in the inner space of the model, the flow got through the inner space of the model directly with a wind velocity of about U (approaching wind velocity), and the wind velocity of the outflow from the model with partitions was higher than that of the model without partitions.

Fig. C6 compares the lift force coefficients (C_{Fy}) of the model with partition and without partition for $OR = 0.25$ and 0.75 . As shown in Fig. C3 (a), for $OR = 0.25$, C_{Fy} of the model with and without partitions was almost the same, and $-dC_{Fy}/d\alpha|_{\alpha=0^\circ}$ was about 5 for both the models with and without partitions. In Fig. C6 (b), C_{Fy} of Case 5 ($OR = 0.875$) was also included for comparison. According to Fig. C6 (b), for $OR = 0.75$, the absolute value of C_{Fy} of the model with

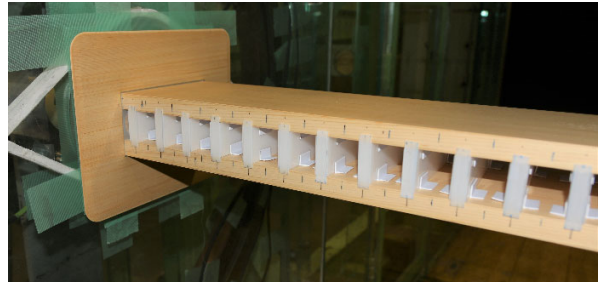
partitions was smaller than that of the model without partitions. Meanwhile, C_{Fy} of the model with partitions showed negative lift slope ($dC_{Fy}/d\alpha$) at $-2^\circ \leq \alpha \leq 2^\circ$, while C_{Fy} of the model without partitions showed negative lift slope at $-3^\circ \leq \alpha \leq 3^\circ$. Meanwhile, $-dC_{Fy}/d\alpha|_{\alpha=0^\circ} = 9.9$ of the model with partitions was smaller than $-dC_{Fy}/d\alpha|_{\alpha=0^\circ} = 13.9$ of the model without partitions. Therefore, by introducing the partitions, C_{Fy} barely changed for case of $OR = 0.25$, while absolute value of C_{Fy} decreased for $OR = 0.75$ by introducing the partitions. Furthermore, C_{Fy} of the model ($OR = 0.75$) with partitions was between C_{Fy} of the case of $OR = 0.75$ and 0.875 .

Fig. C7 shows H_1^* of the model with partitions and without partitions for $OR = 0.25$ and 0.75 . According to Fig. C7 (a), for $OR = 0.25$, H_1^* of the model with partition and without partition was almost the same. According to Fig. C7 (b), for $OR = 0.75$, the critical wind velocity of galloping for the model with partition was larger than that of the model without partition. This is also confirmed by the aerodynamic response shown in Fig. C7, which shows that the critical wind velocity of galloping increased owing to the introduction of the partition. Meanwhile, absolute value of H_1^* of the model with partition was relatively small than that of the model without partitions. Therefore, by introducing the partition, the galloping instability was not affected for $OR = 0.25$, while for $OR = 0.75$, the critical wind velocity of galloping increased by introducing the partitions, and H_1^* at the high wind velocity decreased by introducing the partitions. Furthermore, H_1^* of the model ($OR = 0.75$) with partitions was between H_1^* of the case of $OR = 0.75$ and 0.875 .

In summary, by introducing the partitions in the inner space of the model, the flow rate through the model barely changed, while the wind velocity of the outflow increased. For $OR = 0.25$, because the outflow from the side openings diffused soon into the near wake and the time-averaged separated flow is far from the model, the interaction between the outflow and flow entrainment in the wake was weak for both the model with and without partitions. Therefore, by introducing the partition to the model of small OR , the aerodynamic performance was barely affected. However, for $OR = 0.75$, because that the outflow from the side opening into the wake is with a high wind velocity and the shear layer was close to the trailing edge of the model, the interaction between the outflow from the side openings and the flow entrainment is strong. Therefore, the interaction between the flow entrainment and outflow into the wake would be sensitive to the increase of the wind velocity of the outflow into the wake. By introducing the partitions, the aerodynamic performance was barely affected for $OR = 0.25$, while for $OR = 0.75$, based on the aerodynamic performance, introducing the partitions equivalently increased OR .

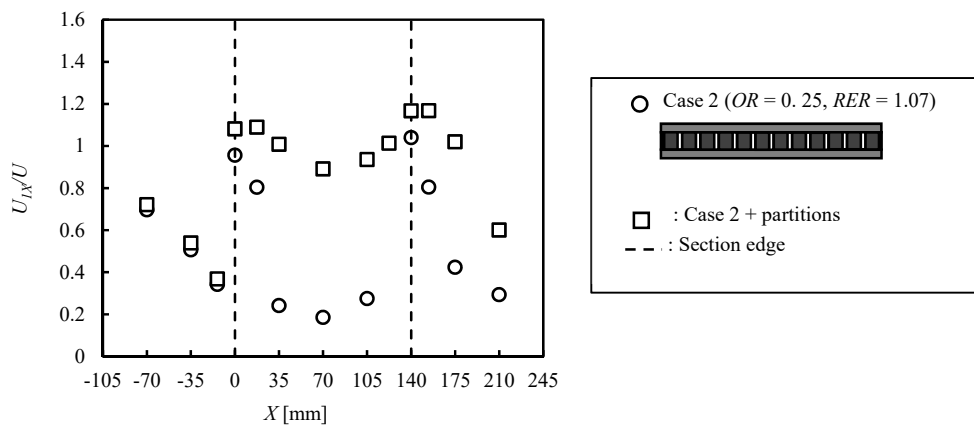


(a)

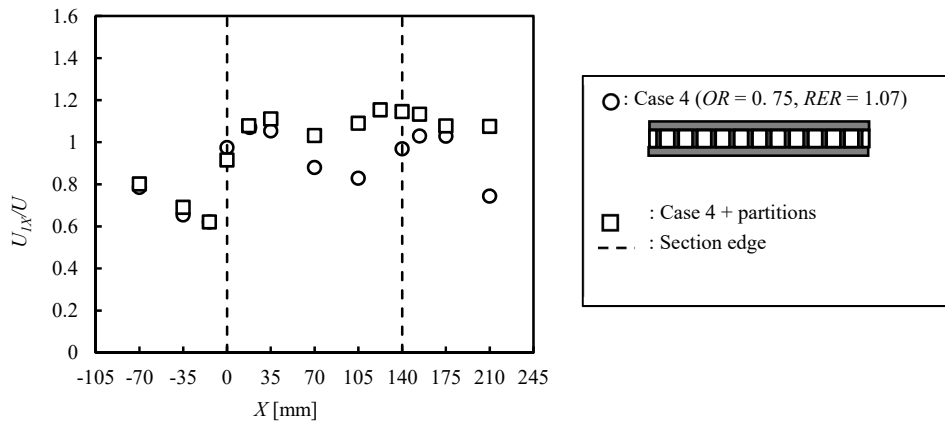


(b)

Fig. C 4 Partition for the model of (a) Case 2 ($OR = 0.25$, $RER = 1.07$), (b) Case 4 ($OR = 0.75$, $RER = 1.07$).



(a)



(b)

Fig. C 5 Comparison between non-dimensional X -direction wind velocity of flow getting through the model with and without partitions for (a) Case 2 ($OR = 0.25$, $RER = 1.07$), (b) Case 4 ($OR = 0.75$, $RER = 1.07$).

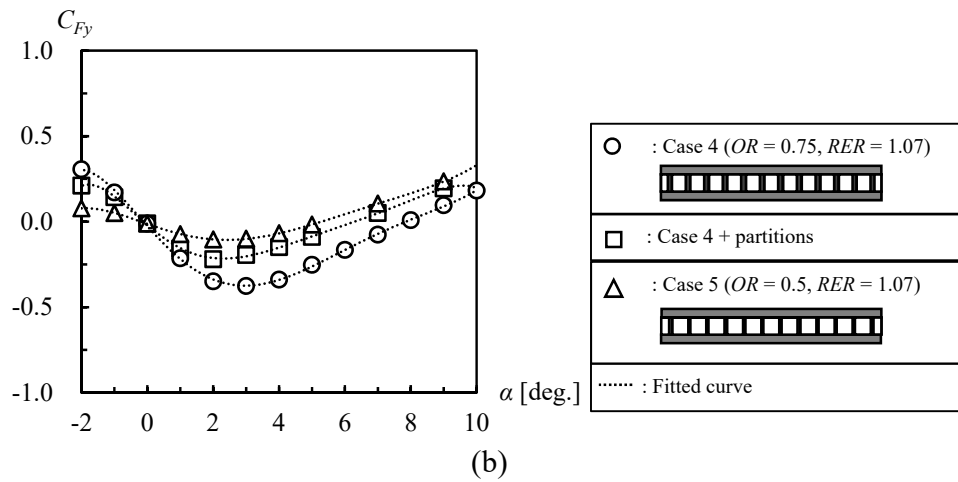
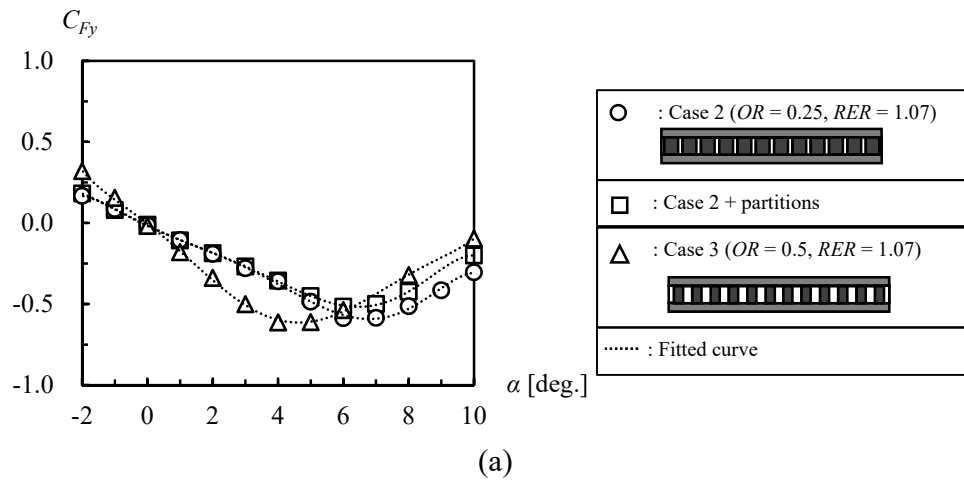
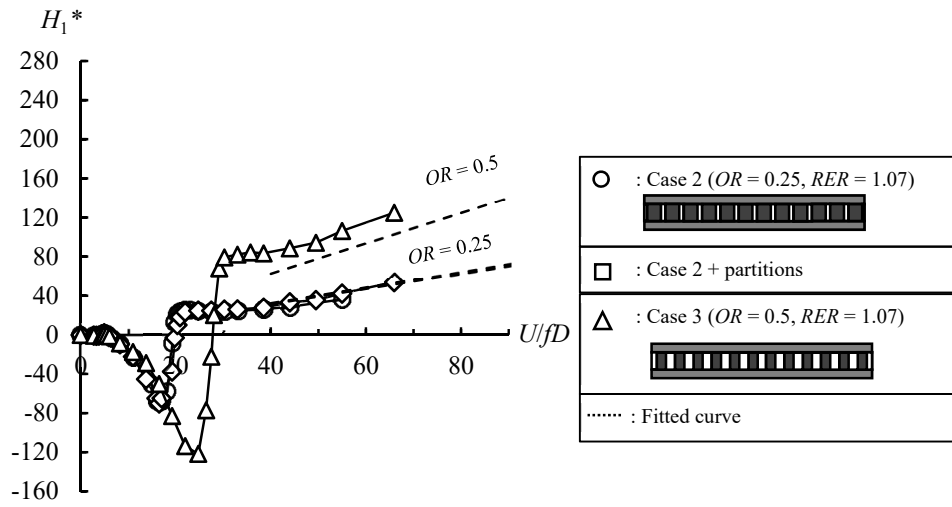
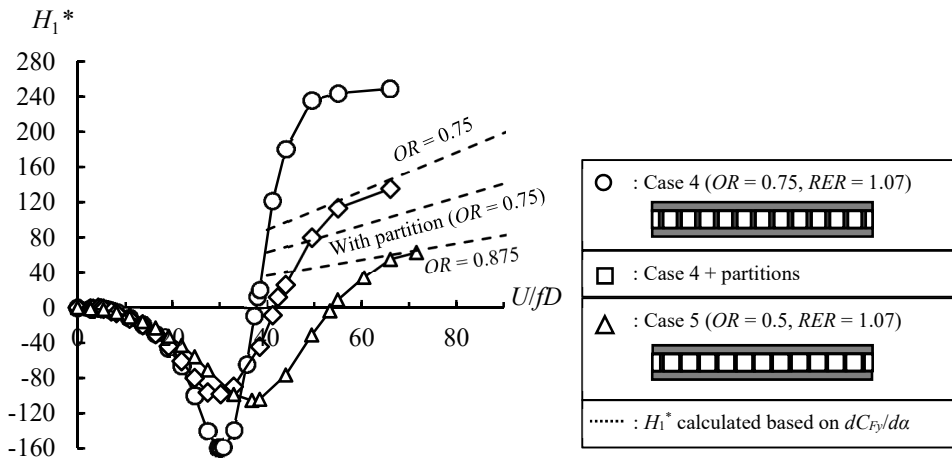


Fig. C 6 Comparison between lift force coefficients of the model with and without partitions for (a) Case 2 ($OR = 0.25, RER = 1.07$), (b) Case 4 ($OR = 0.75, RER = 1.07$).



(a)



(b)

Fig. C 7 Comparison between H_1^* of model with partition and without partition for (a) Case 2 ($OR = 0.25, RER = 1.07$), (b) Case 4 ($OR = 0.75, RER = 1.07$).

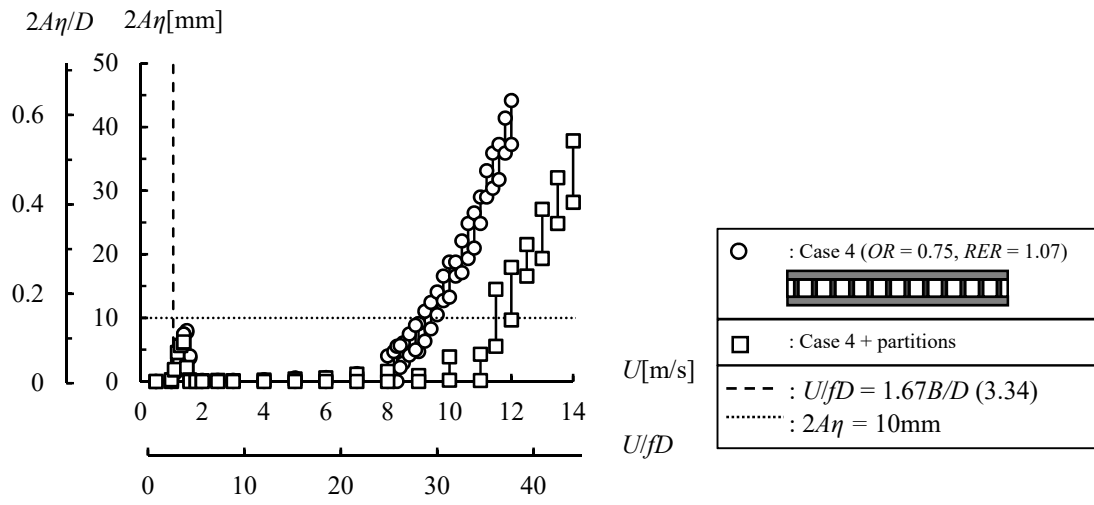


Fig. C 8 Comparison between the aerodynamic response of model with partition and without partition for case of $OR = 0.75$ ($RER = 1.07$).

Aerodynamic force coefficients

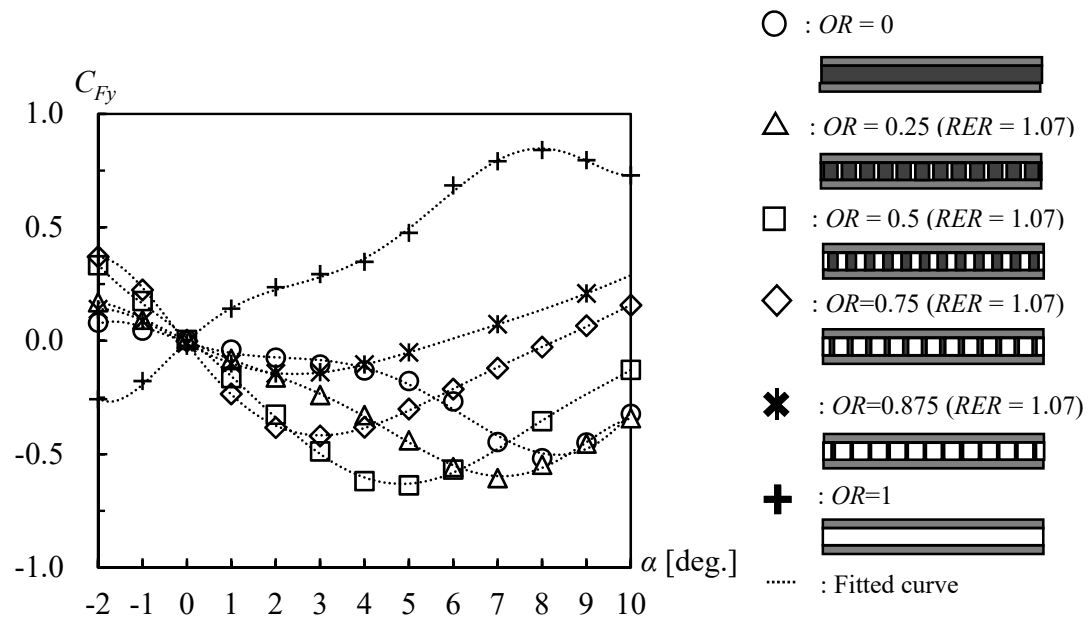


Fig. C 9 Change of lift force coefficients with OR ($OR = 0, 0.25, 0.5, 0.75, 0.875$ and 1) for $RER = 1.07$ ($U = 10\text{m/s}$, smooth flow).

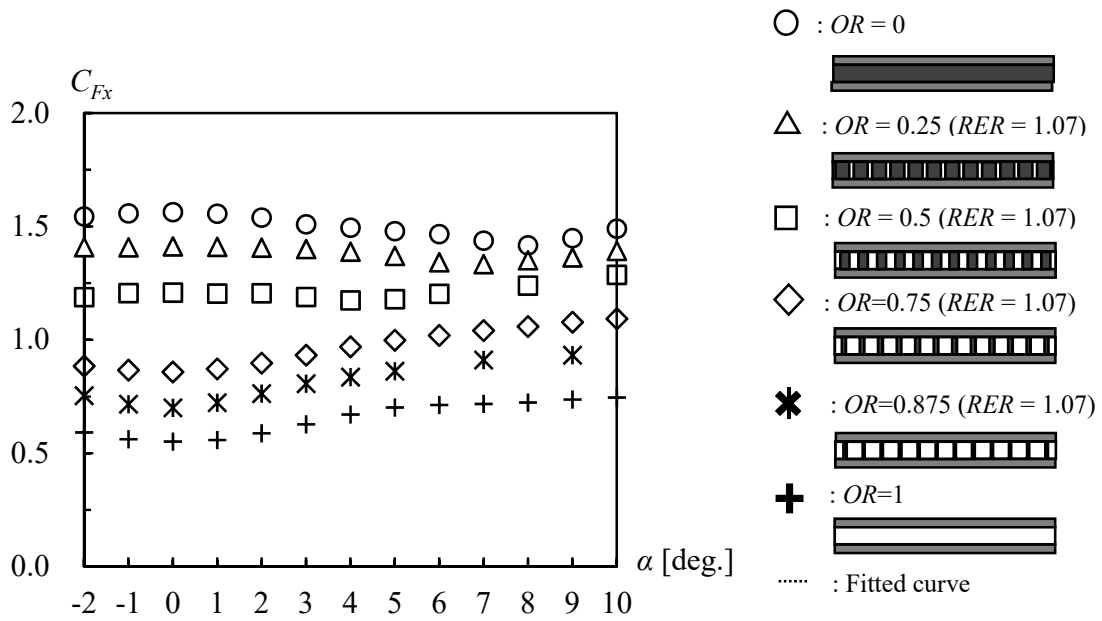


Fig. C 10 Change of drag force coefficients with OR ($OR = 0, 0.25, 0.5, 0.75, 0.875$ and 1) for $RER = 1.07$ ($U = 6\text{m/s}$, smooth flow).

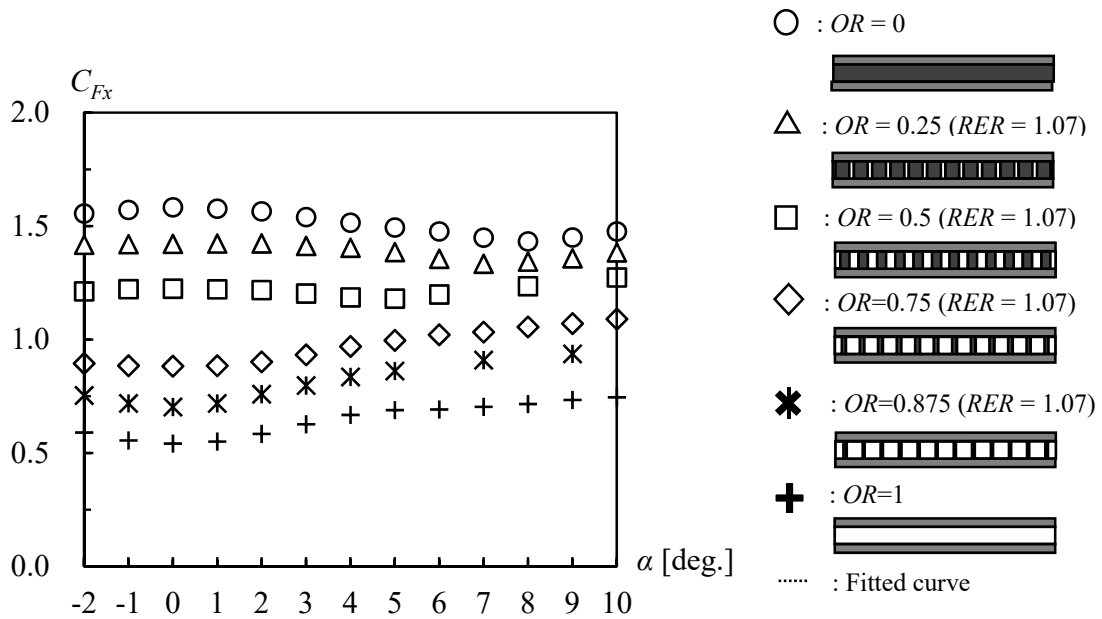


Fig. C 11 Change of drag force coefficients with OR ($OR = 0, 0.25, 0.5, 0.75, 0.875$ and 1) for $RER = 1.07$ ($U = 10\text{m/s}$, smooth flow).

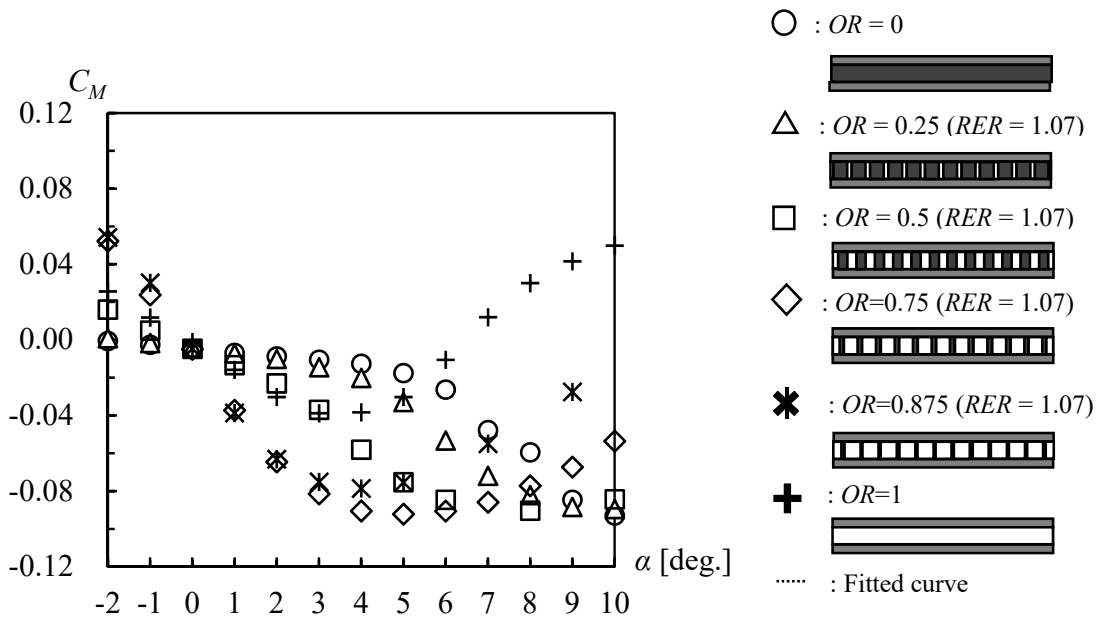


Fig. C 12 Change of pitching moment coefficients with OR ($OR = 0, 0.25, 0.5, 0.75, 0.875$ and 1) for $RER = 1.07$ ($U = 6\text{m/s}$, smooth flow).

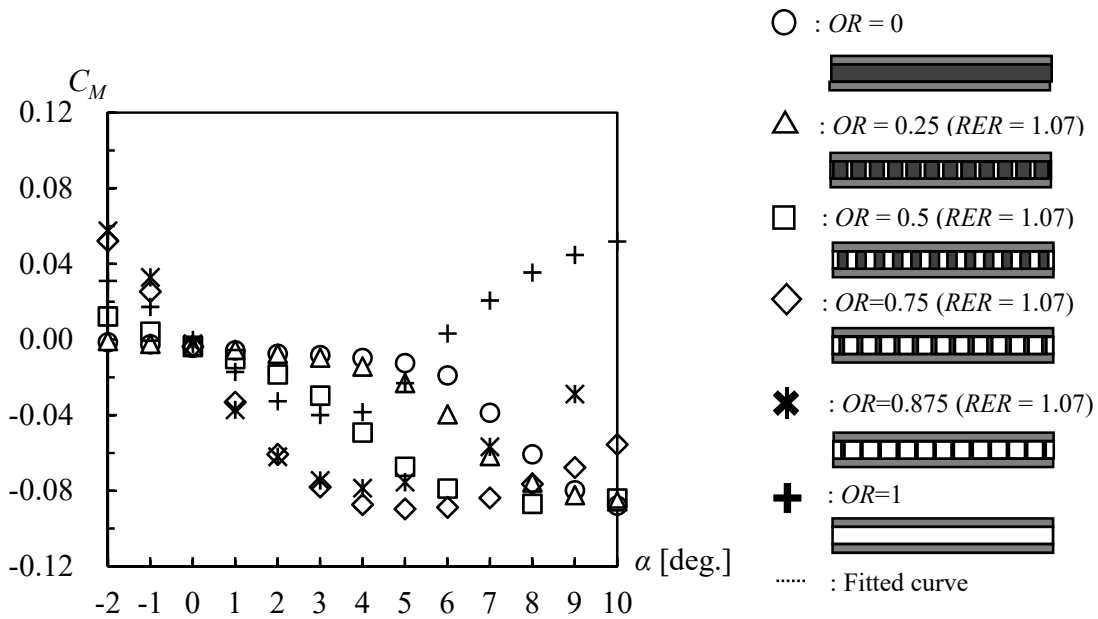


Fig. C 13 Change of pitching moment coefficients with OR ($OR = 0, 0.25, 0.5, 0.75, 0.875$ and 1) for $RER = 1.07$ ($U = 10\text{m/s}$, smooth flow).

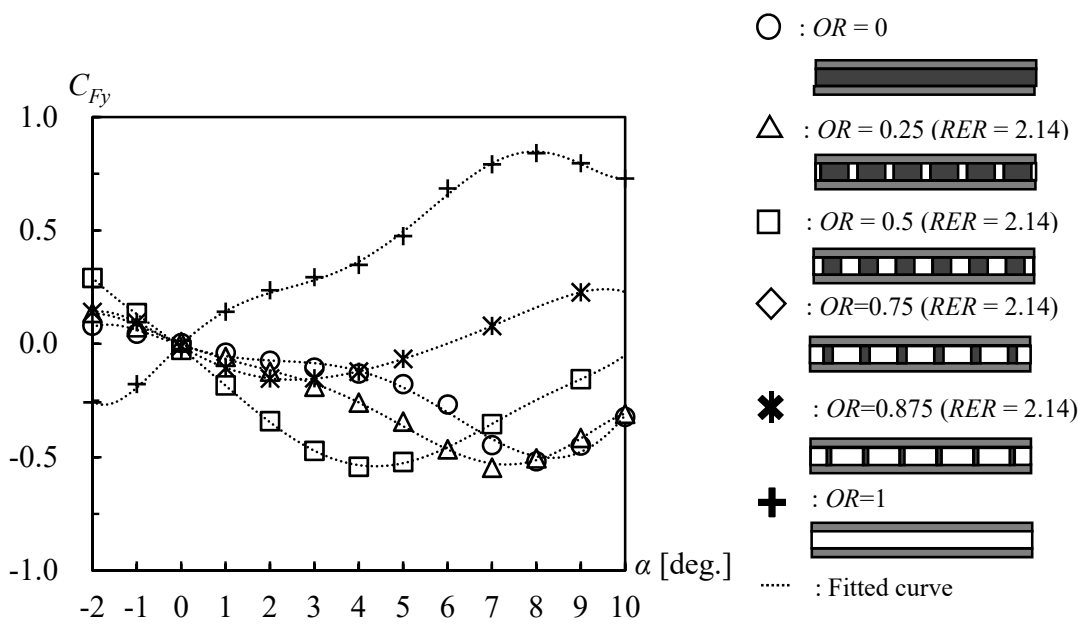


Fig. C 14 Change of lift coefficients with OR ($OR = 0, 0.25, 0.5, 0.75, 0.875$ and 1) for $RER = 2.14$ ($U = 6\text{m/s}$, smooth flow).

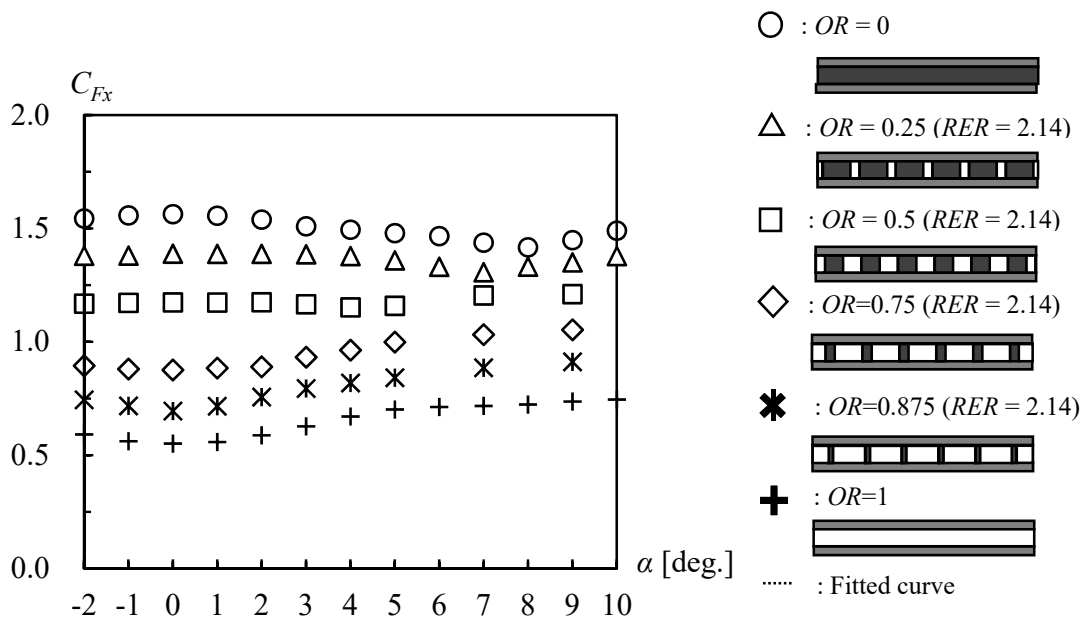


Fig. C 15 Change of drag force coefficients with OR ($OR = 0, 0.25, 0.5, 0.75, 0.875$ and 1) for $RER = 2.14$ ($U = 6\text{m/s}$, smooth flow).

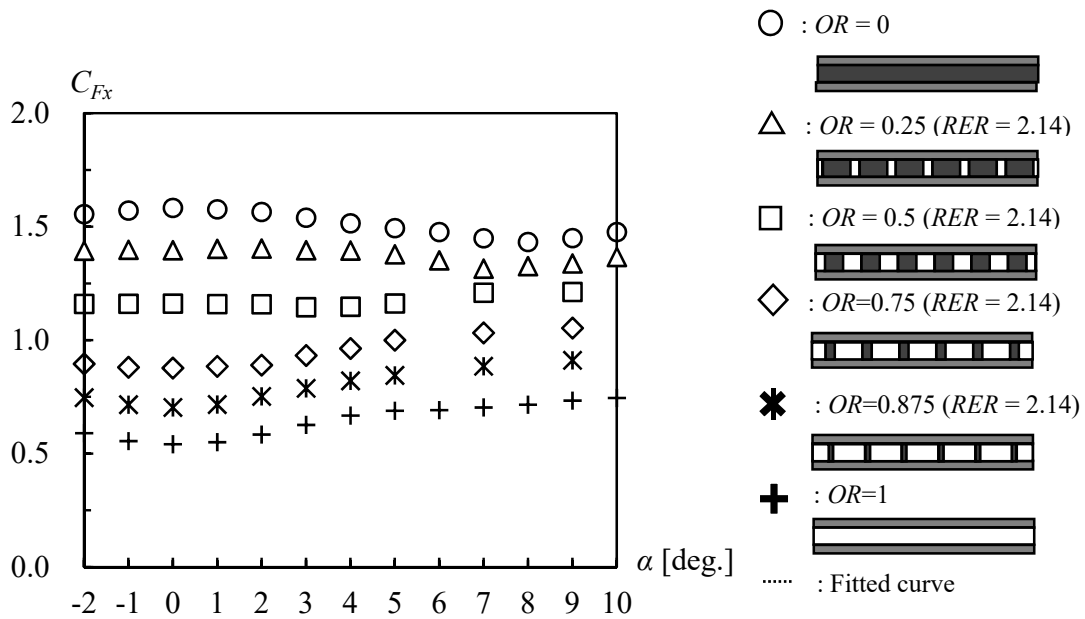


Fig. C 16 Change of drag force coefficients with OR ($OR = 0, 0.25, 0.5, 0.75, 0.875$ and 1) for $RER = 2.14$ ($U = 10\text{m/s}$, smooth flow).

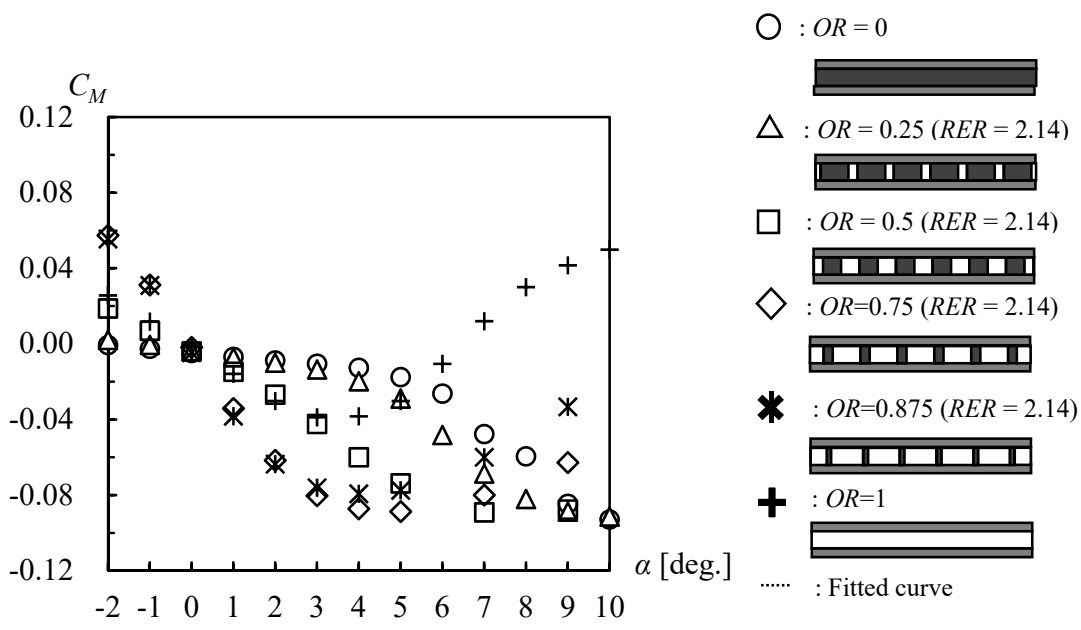


Fig. C 17 Change of pitching moment coefficients with OR ($OR = 0, 0.25, 0.5, 0.75, 0.875$ and 1) for $RER = 2.14$ ($U = 6\text{m/s}$, smooth flow).

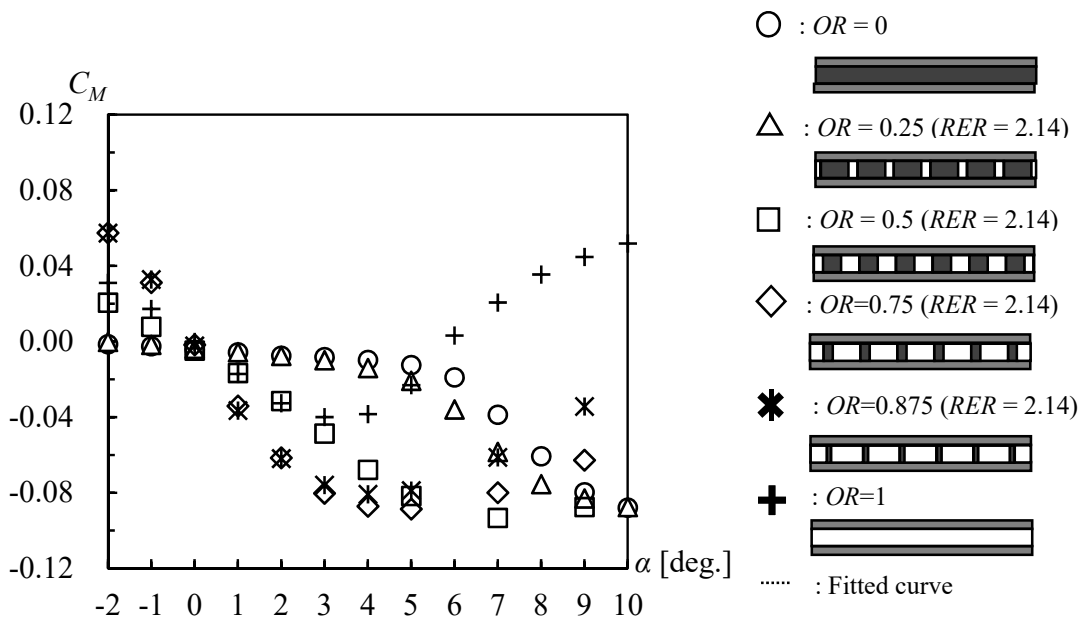


Fig. C 18 Change of pitching moment coefficients with OR ($OR = 0, 0.25, 0.5, 0.75, 0.875$ and 1) for $RER = 2.14$ ($U = 10\text{m/s}$, smooth flow).

Repeating Element-size Ratio (RER) and Aerodynamic damping H_1^*

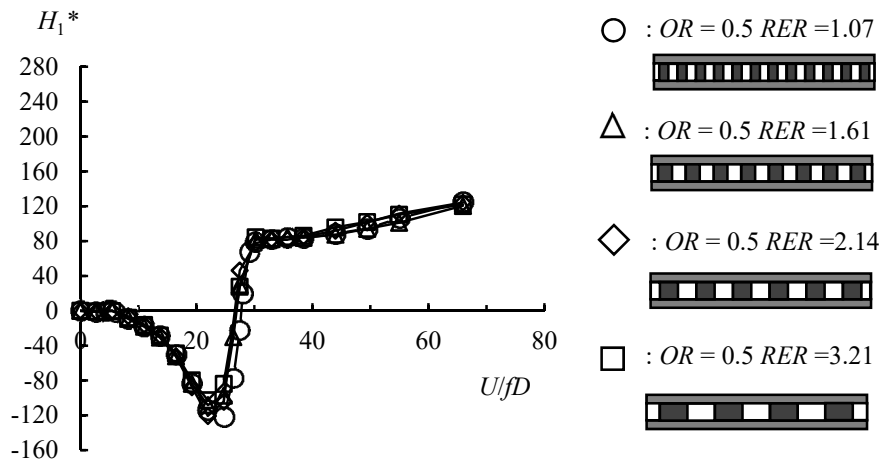


Fig. C 19 Comparison between H_1^* of Case 3 ($OR = 0.5$, $RER = 1.07$), Case 7 ($OR = 0.5$, $RER = 2.14$), Case 11 ($OR = 0.5$, $RER = 1.61$) and Case 12 Case 3 ($OR = 0.5$, $RER = 3.21$).

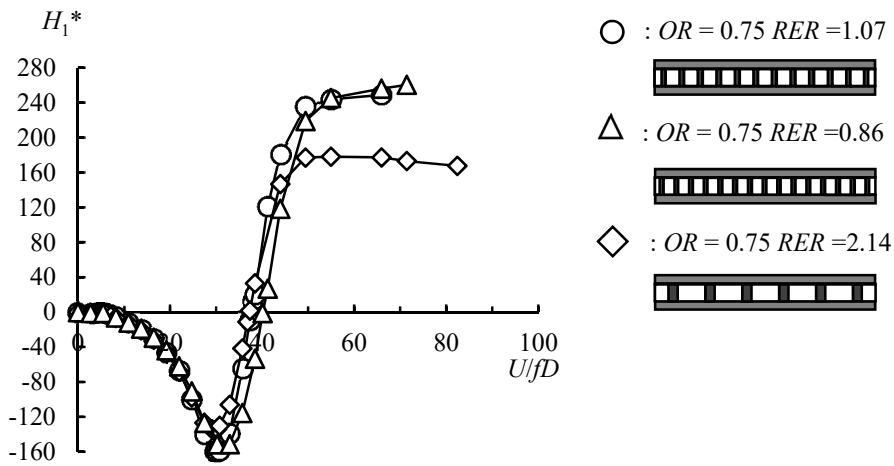
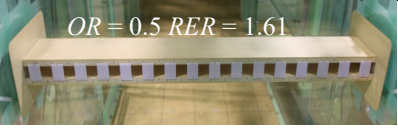
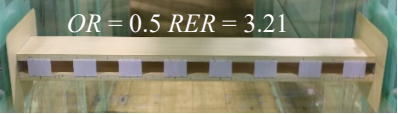


Fig. C 20 Comparison between H_1^* of Case 4 ($OR = 0.75$, $RER = 1.07$), Case 8 ($OR = 0.75$, $RER = 2.14$), Case 13 ($OR = 0.75$, $RER = 0.86$).

Table C1 Case lists of wind tunnel tests

Case name	Opening-area Ratio (<i>OR</i>)	Repeating Ratio (<i>RER</i>)	Element-size	Configuration
Case 11	0.5	1.61		
Case12	0.5	3.21		
Case 13	0.75	0.86		